# Design and Development of Components of a Modular Bioreactor

by

Craig Anthony Mascarenhas

Submitted to the Department of Mechanical Engineering
in partial fulfillment of the requirements for the degree of

Master of Science in Mechanical Engineering

at the

MASSACHUSETTS INSTITUTE OF TECHNOLOGY

June 2017



Signature redacted

Author .....
Department of Mechanical Engineering
May 12, 2017

Signature redacted

Certified by .....
J. Christopher Love
Professor of Chemical Engineering
Thesis Supervisor

Signature redacted

Certified by .....
Roger D. Kamm
Mechanical Engineering Faculty Reader

Signature redacted

Accepted by .....
Rohan Abeyaratne
Chairman, Department Committee on Graduate Theses

# Design and Development of Components of a Modular Bioreactor

Craig Anthony Mascarenhas

Submitted to the Department of Mechanical Engineering
on May 12, 2017 in partial fulfillment of the requirements
for the degree of Master of Science in Mechanical Engineering

## Abstract

Biologic drug manufacturing is traditionally conducted in large-scale, industrial bioreactors. The emergence of interest in disposable, bench-top bioreactors as a viable alternative is due to potential advantages such as lower contamination risk, time and cost savings, and ease of handling. The challenges associated with disposable, bench-top bioreactors include poor mixing, limited oxygen transfer, and a scarcity of non-invasive sensors for process control. This thesis investigates multiple aspects of a disposable, perfusion-capable bioreactor, in order to facilitate an optimal design.

In order to determine an impeller configuration that improves the mixing and mass transfer characteristics of a 1-liter bioreactor, Computational Fluid Dynamics (CFD) was used. The potential benefits of switching to a dual-Marine impeller system was revealed, which was then validated during fermentation experiments. Further predictions of a merging flow pattern in the 1-liter vessel was consistent with the literature based on the impeller spacing. A scaled-up 5-liter vessel was designed with Rushton impellers spaced so as to create a parallel flow pattern, which was later successfully predicted in the CFD simulations. Flow patterns were analyzed at various locations in both vessels to aid future design iterations.

Monitoring of process parameters, including liquid level, is important for automated control in bioreactors. Three novel, non-invasive, optical liquid level sensing methods were conceptualized, prototyped, and successfully tested. These solutions relied on self-developed image processing algorithms. Additionally, a magnetic liquid level sensor was also developed and tested that relied on a magnetic float and a series of reed switches.

In order to increase the perfusion membrane surface area and reduce complexity, the switch to a hollow-fiber harvest probe was examined. CFD studies guided design iterations by modeling the flow around the probe, giving insight into the stagnation properties and shear forces acting on the fibers. Additionally, experimental testing of the new harvest probe revealed its successful functionality and viability in the bioreactor.

Thesis Supervisor: J. Christopher Love
Title: Professor of Chemical Engineering

# Acknowledgements

My time at MIT has been more rewarding than I ever could have imagined, thanks to the amazing people I have had the privilege of knowing. I would like to thank my research advisor, Chris Love, for giving me the latitude to work on projects I find stimulating. I would also like to thank Roger Kamm, for his insight and perspective, and Amos Lu, without whom I would have been lost. And thanks to Leslie Regan, for perpetually looking after the MechE students like her own.

Thank you to my friends in Toronto, who changed my perspective on life. Seyon, Muneeb, and Kim, I know you will always be just a double-double from Timmies away. To the Wastemanz, for the ridiculous and random incidents that kept University hilarious, for never taking life too seriously, and for the soap, wherever she may be. And to my friends from OPG, for the lifelong friendships forged from the bureaucracy of government work. I am so grateful to all the people who made the trip to visit me in Boston – David, Jade, Martin, Kevin, Kristina, Allan, Gaurav, Matt, Zibran, A. Denise, U. Richard, and my family. You made sure I always had someone to look forward to seeing, and kept me going through stressful times.

Thank you to my friends at MIT, for creating the most fun-loving and intellectual community I've had the pleasure of being in. To the Haiti crew – David, Sterling, Janet, and Julia – for being the best group of people I have ever worked with, and for being so brilliant yet so humble. To my fellow GAME tennis players, for fostering global friendships over our mutual proclivity to hit a fuzzy, yellow, round object, may our legacy live on. To my friends at the Love Lab, may the Foos always be with you. And thanks to PK, and my roommates, Ben and Jorge, for all the debates, good times, and bantz.

Thank you Melanie, my little sister, for teaching me it's possible to love someone so annoying, so much. You inspired me with your hard work and maturity. It's LeviOsa, not LevioSA, you Muggle.

Mom, in the hours you spent helping me study for tests and do my homework as a kid, you taught me so much more than what was in those books. The unconditional support and love makes me feel so lucky, knowing at least one person always wants to hear about my day. Dad, I honestly don't think I would be here without you. You were the other half of the rock I could always lean on. You made education fashionable to me, and surrounded me with books and dreams for as long as I can remember. Thank you for teaching me to meet with triumph and disaster, and treat those two imposters just the same.

Together, you two have been the best parents anyone could ask for – my best friends and moral compass rolled into one. I love you, fam.

# Contents

# List of Figures

# List of Tables

# Chapter I
# Introduction

## 1.1 Background of Biotechnology & Biologic Drug Manufacturing

Biotechnology in the broadest sense is the field that studies, researches, and uses living organisms and cellular processes to make products. The earliest examples of biotechnology dates back to around 6000 BC to 4000 BC, where fermentation was used to make cheese and bread, from goat's milk and yeast respectively. In the 19$^{th}$ and 20$^{th}$ centuries, other products were commercially developed through fermentation, such as acetic acid, lactic acid, and alcohol [1]. More recently, the discovery of penicillin by Alexander Fleming in 1929 led to a further push of the biotechnology movement. An anti-toxin to diphtheria was manufactured from animals, although a side effect of it was that it was not always compatible with the human immune system. In the 1970s, the birth of genetic engineering coincided with the interest in biotechnology, culminating in the synthetic production of human insulin in 1982, the first biologic drug produced by recombinant DNA. Recombinant DNA usually refers to artificially formed DNA by combining a gene of interest with a plasmid within an organism that will express this gene to produce the intended protein product [2]. Since then, many of today's most popular pharmaceutical drug products are made using biotechnology.

Biologic drugs include proteins manufactured using DNA recombinant technology that are used as a drug for medicinal purposes. There are various steps to creating biologic drugs, starting with the cell line development, to upstream processing, bioreactor operation, and downstream processing to form the drug product. The host cells used can be microbial, insect, mammalian, or others, depending on the properties of the protein product required. Common cell lines include Chinese Hamster Ovary (CHO) cells and *E. coli* cells. In cell line development, an expression vector[1] is introduced into a target host cell. The cells that have integrated the vector are selected for, and a single clone is then selected and reproduced to form a master cell line. Considerations such as productivity, stability, scalability, impact on

[1] An expression vector is usually a plasmid that includes the gene of interest, along with a selectable marker, and a promoter and terminator for the gene of interest. Upon introduction into the cell, the vector causes the host cell to synthesize the protein encoded by the gene of interest.

purification, survivability at high densities, and adventitious contaminants are taken into account during selection. Multiple copies of the single clone cell are grown and cryopreserved in vials to form the master cell bank. Later, a vial may be thawed to form a working cell bank, which is then used for upstream production [2].

In upstream processing, cells are expanded from the vials into progressively larger vessels (such as shake flasks, wave bioreactors, stirred tanks) in order to increase the population of the cells. This is known as the seed train. Eventually, protein production is induced in the cell culture, with the goal of maximizing titers (protein concentration in bioreactor) and minimizing cost. The productivity of the cell culture depends on the composition of the media in the bioreactor, the feeding schedule, the culture environment, the age of the cells, and the accumulation of waste products. Ensuring the media contains sufficient nutrients, are at an optimal pH and temperature, and are properly mixed in order to promote oxygen transfer and homogeneity, are all part of appropriate cultivation of cells. The growth phase of the cell culture is called inoculation, followed by induction of protein by introducing additional media that will cause the gene to express it [2]. There are different types of bioreactor processes at this stage – fed-batch, chemostat, perfusion, etc. Fed-batch bioreactors require periodic feeding of nutrients, while the expressed protein, waste products, and cell culture remain together in the vessel until the end of the production run. In chemostat reactors, media and nutrients are continuously fed into the vessel, whereas spent cells and media are simultaneously harvested out of the reactor. Perfusion reactors retain cells by using a filtration mechanism, while continuously harvesting protein and waste products [1]. Upstream process development entails the identification and selection of parameters that have the largest influence on performance, and modifying the process to optimize for production while minimizing cost. Other than the selection of the host cell and cultivation mechanism, media development tries to optimize the cell performance based on the nutrient mix it receives. Microbial cells (e.g. *E. coli*) can make all 20 amino acids, but mammalian cells cannot. Therefore, the essential amino acids must be added in a stoichiometric manner for cell growth and production of proteins desired. Additionally, the media needs to be kept in the appropriate pH and

temperature range, have an appropriate salt concentration, carbon dioxide content, etc. During inoculation and induction, proper agitation of the bioreactors is required to ensure sufficient oxygen transfer and uptake by the cells, as well as a homogeneous mixture. The pH and temperature of the culture must also be maintained under optimal operating conditions.

After the protein product is expressed by the cells and collected, the downstream processing begins. The aim of downstream processing is the primary recovery of protein product during which it is stabilized and concentrated, followed by purification, polishing, and formulation wherein the product is prepared in its final buffer solution which stabilizes it for delivery. There are multiple techniques that may or may not be used to complete the downstream processing of protein product, dependent on the drug and upstream process. Sometimes, a synthetic post-translational modification (PTM) is added to a protein, such as adding polyethylene glycol to increase circulation in the body, or glycosylation of a protein. In some processes, the cells have not externally expressed the protein, and thus need to be disrupted, before some form of centrifugation separates the protein product from the rest of the cell matter. Filtration processes such as diafiltration or tangential flow filtration (TFF) are used for functions such as buffer exchange or separation of product. Chromatography is popularly used to separate protein product by relying on the difference in properties of the protein molecules from the other molecules. Examples of chromatography include gel permeation, hydrophobic interaction, affinity, and ion exchange chromatography [2].

## 1.2 Types of Bioreactors, Processes, Medium, and Host Cells

During the upstream process of biologic drug manufacturing, the protein product is expressed by cells that are being cultivated in a vessel known as a bioreactor. There are many types of bioreactors, with different advantages and disadvantages. The primary purpose of the bioreactor is to optimize the conditions that allow for maximum product yield. To that end, they have to optimally maintain process parameters such as aeration (oxygen/air input) rate, agitation (impeller speed) rate, temperature, pH, and other dimensions in order to maximize the yield conditions. There are trade-offs involved at every stage. For example, increasing the oxygen transfer rate (OTR) blindly by increasing the aeration and agitation rates, will lead to foaming as well as cell death due to shearing. On the other hand, trying to increase cell concentrations at a high growth rate may require high nutrient and oxygen feeding with good mixing. Similarly, the mechanical design aspect of the bioreactor also has bearing on the performance during upstream processing. The geometric ratios such as height-to-tank-diameter (H/T ratio), impeller-diameter-to-tank-diameter (D/T ratio), inclusion of baffles, the shape and curvature of the ends, etc. govern the quality of mixing, homogeneity, oxygen transfer, and gentleness on cells, all of which are important for good performance. It is also necessary to maintain aseptic conditions in the bioreactor [1].

There are many different kinds of bioreactors used in biopharmaceutical drug manufacturing. The continuous stirred-tank bioreactor is most commonly used in industry. In most stirred-tank bioreactors, a central shaft that supports agitators (such as impellers) rotates to mix the culture, while a sparger introduces air/oxygen into the vessel under pressure. Other probes like temperature, pH, dissolved oxygen, etc. are often present, along with inputs such as acid, base, antifoam, etc. to maintain the required conditions. Baffles are often included to prevent vortex formation and promote better mixing. Stirred-tank reactors usually have high oxygen transfer rates leading to high biomass productivity. They are also commercially abundant and thus have low investment and operating costs. Airlift bioreactors supply air from the bottom of the vessel, and the naturally buoyant bubbles rise to the top, whereas the design of the reactor creates a circulating fluid flow pattern. The

mixing in these reactors occurs without agitation, and thus lend themselves to applications where low shear and energy is required. Other examples of commercial bioreactors used for drug manufacturing include fluidized bed reactors, microcarrier or packed bed reactors, and photobioreactors, among others [1].

There is variance in the fermentation feeding regimes as well, such as batch, fed-batch, continuous, and perfusion fermentation. In batch fermentation, the materials required are present in the bioreactor from the start, and the products along with the remaining spent media and waste are removed at the end, and sent for downstream processing. In fed-batch fermentation, similar to batch fermentation, nothing is removed from the bioreactor until the end of the process run. However, the supply of nutrients can occur in different stages during the run, typically allowing for a cell growth phase followed by a protein production phase. In continuous fermentation, nutrients are continuously fed to the bioreactor, while spent medium and cells are continuously removed from the system as well. Perfusion fermentation systems extend on this concept, and also continuously feed cells, but use a filtration system to remove spent medium as well as protein product, while keeping cells in the bioreactor [1].

Similarly, multiple choices exist for the type of fermentation medium – the substance that enables the micro-organisms to grow and produce the intended products. The aim of optimizing fermentation medium is to maximize protein yield and concentration, minimize the production of undesirable metabolites, and produce consistent quality. Defined media consists of pure substrates in which the exact chemical ratios are known. In complex media, the exact composition is unknown as it is composed of enzymatic digests of animal, plant, or yeast cells. Other specific types of media such as selective media, differential media, and enriched media also exist [1].

In terms of host cells used to in the process of manufacturing biologic drugs, bacterial, yeast, mammalian, and insect cells have been commonly used. Bacterial hosts are usually cheaper, with fast growth rates. However, the yields are on the smaller side and they lack the ability to obtain the right post-translational modifications. *E. coli* is an example of a

popular bacterial host. Yeast hosts are typically slightly slower, but have higher yields. Animal and insect host cells are even slower but have almost identical gene representation and PTMs, thus offering more control.

## 1.3 Trends in Biotechnology

The already large field of biotechnology is projected to grow by 8% annually and make up a larger share of the market in the future [3]. As economic as well as social benefits of biotechnology are realized on a larger scale, the emergence of exciting new methods in biologic drug manufacturing can also be predicted. Some of these nascent technologies are can be expected to become mainstream in the near future.

Biologic drugs are typically complex molecules, and are sensitive to changes in the manufacturing process. Thus, drugs can be produced that are almost but not quite identical to a previously commercialized drug. These drugs are called biosimilars, and can be used after approval for treatment of the same condition as the previously commercialized biologic, upon patent expiration of the original biologic. The equivalent for small-molecule drugs are generics, which are exactly identical in structure. The first FDA approved biosimilar in the US was Sandoz's Zarxio, which like the original biologic drug Neupogen, is used to treat neutropenia [4]. It is expected that the biosimilar market is expected to grow in the coming years, with the expiration of a number of original biologic patents [3] [5].

Regarding production processes, a recent trend has been the use of single-use (disposable) systems for protein production [6]. The advantages of a smaller, single-use bioreactor are plenty, as well as having a few challenges. Recent developments attempt to make single-use systems commercially viable. These systems do not have to be concerned with turnover times and re-sterilization post-production. Additionally, potential cost savings present themselves with proper implementation of these systems. However, since this is a relatively less established area of research, off-the-shelf parts of the drug production chain that are also single-use, are sometimes hard to come by. Furthermore, current single-use systems are characterized by low mixing and oxygen transfer and poor foam management [7]. However, these parameters are not theoretically constrained for single-use systems, and are thus mere challenges on route to widespread commercial implementation of the technology, as interest in the field has been growing.

Other future potential developments in biotechnology include new host cells, improved recovery of high-producing cell lines, more efficient bioprocess development, improved media formulations, different bioreactor and membrane designs, transient gene expression, and many different developments to the field [8].

## 1.4 Motivation

This thesis aims to capitalize on the exciting growth in biotechnology, explore some of the recent trends, and enable a design for a continuous, perfusion-based, disposable bioreactor. The following chapters assess different parts of the bioreactor and conceptualizes, designs, tests, and/or assesses viable designs for components in the design of a modular bioreactor.

The workflow envisioned is to sift through theory of biotechnology, fluid mechanics, thermodynamics and product design, to develop potential solutions; then use CFD and other software tools to test these solutions; then rapid prototype the solutions that seem viable; and finally build the optimal solutions and subject them to experimental tests. The complete workflow is only partially represented in different parts of this work, but is a good framework for future development (Figure 1-1).

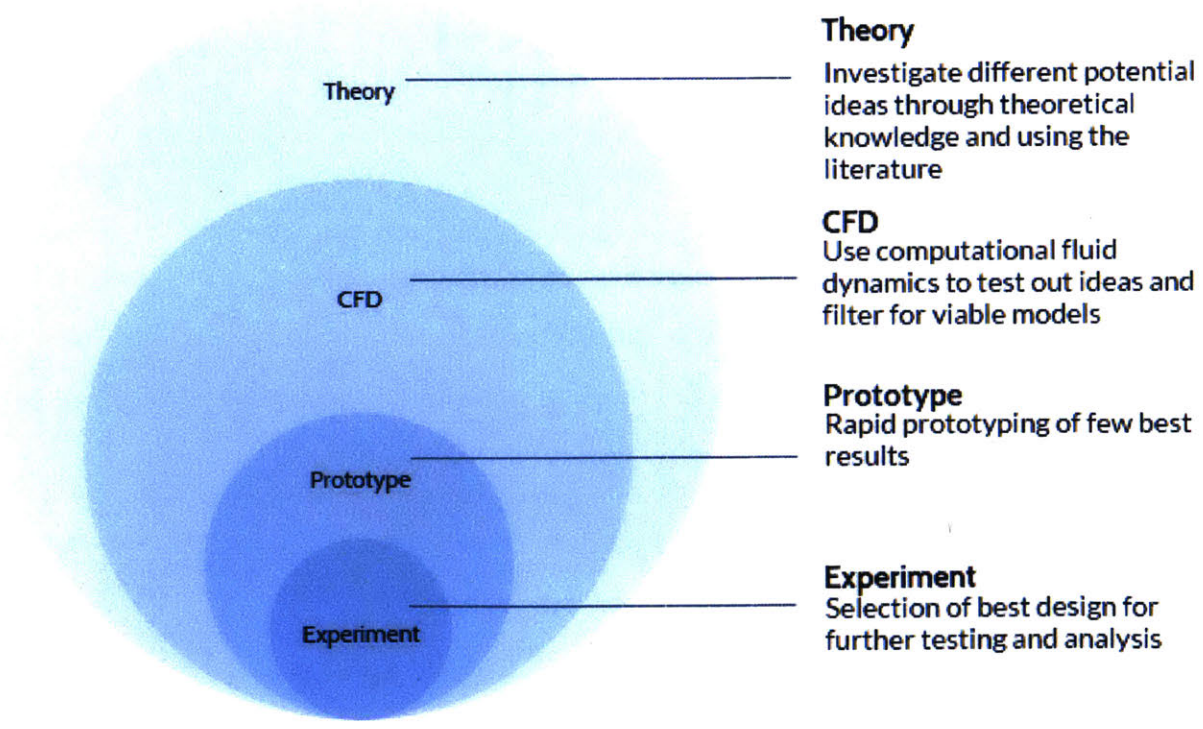


***Figure 1-1*** **Optimal design solution pathway**

## 1.5 Organization

The first chapter of this thesis (current chapter) is the Introduction. It introduces biotechnology through the history and background of the science. The basics of biologic drug manufacturing are explained, as well as the variance in the options of bioreactors, processes, host cells, or media, that affect the fermentation process. Further, recent and potential future trends in biotechnology are explored, as well as a description of the motivation for this work. The optimization of production of protein to cost of the process is key in improving bioreactor design, and will be explored through the various design parameters in this work.

Chapter 2 deals with the mixing and mass transfer in bioreactor kinetics. Ensuring sufficient mass transfer and continuously maintaining a homogeneous mixture is important in order to achieve a successful fermentation process. However, increasing mass transfer and decreasing mixing time without constraint leads to other problems. Balancing the mixing and mass transfer is vital to achieve optimal yield. In this chapter, computation fluid dynamics (CFD) simulations are run to compare the flow characteristics between different impeller types and configurations in a 1-liter vessel, followed by an experimental comparison of the impeller configurations based on protein production. Further, a similar CFD study is used to characterize the flow characteristics in a 5-liter vessel. Future work recommendations and further analysis is outlined in order to complete the study.

Chapter 3 explores bioprocess monitoring. Continuous fermentation requires process monitoring so as to be able to control the different operating parameters. These sensors include liquid level sensors, pH sensors, dissolved oxygen sensors, and so on, and pose unique challenges for implementation in disposable reactors. Non-invasive liquid level sensing technologies are designed and developed in this chapter, as well as tested and validated. Recommendations for other bioprocess sensing is also done.

Chapter 4 studies perfusion in the bioreactor. The advantages in switching to a different, novel harvest probe are explored. In order for a successful, iterative design and testing process to the new harvest probe, Computational Fluid Dynamics was conducted to

understand and study the flow around the probe as well as the bulk flow in the vessel. The CFD study was used to aid in designing experiments that tested the structural integrity of the harvest probe. Additionally, some testing of initial iterations of the harvest probe were conducted.

Chapter 5 conducts a partial market analysis for the completed concept design of the disposable bench-top scale bioreactor. With a "distributed manufacturing" value proposition, the study analyses the potential benefits of cutting the cold chain in biologic drug manufacturing, and understanding the current costs associated with it. It looks at the current landscape of the biopharmaceutical drug distribution network, in order to realize the benefits of the distributed manufacturing approach, as well as the market dynamics.

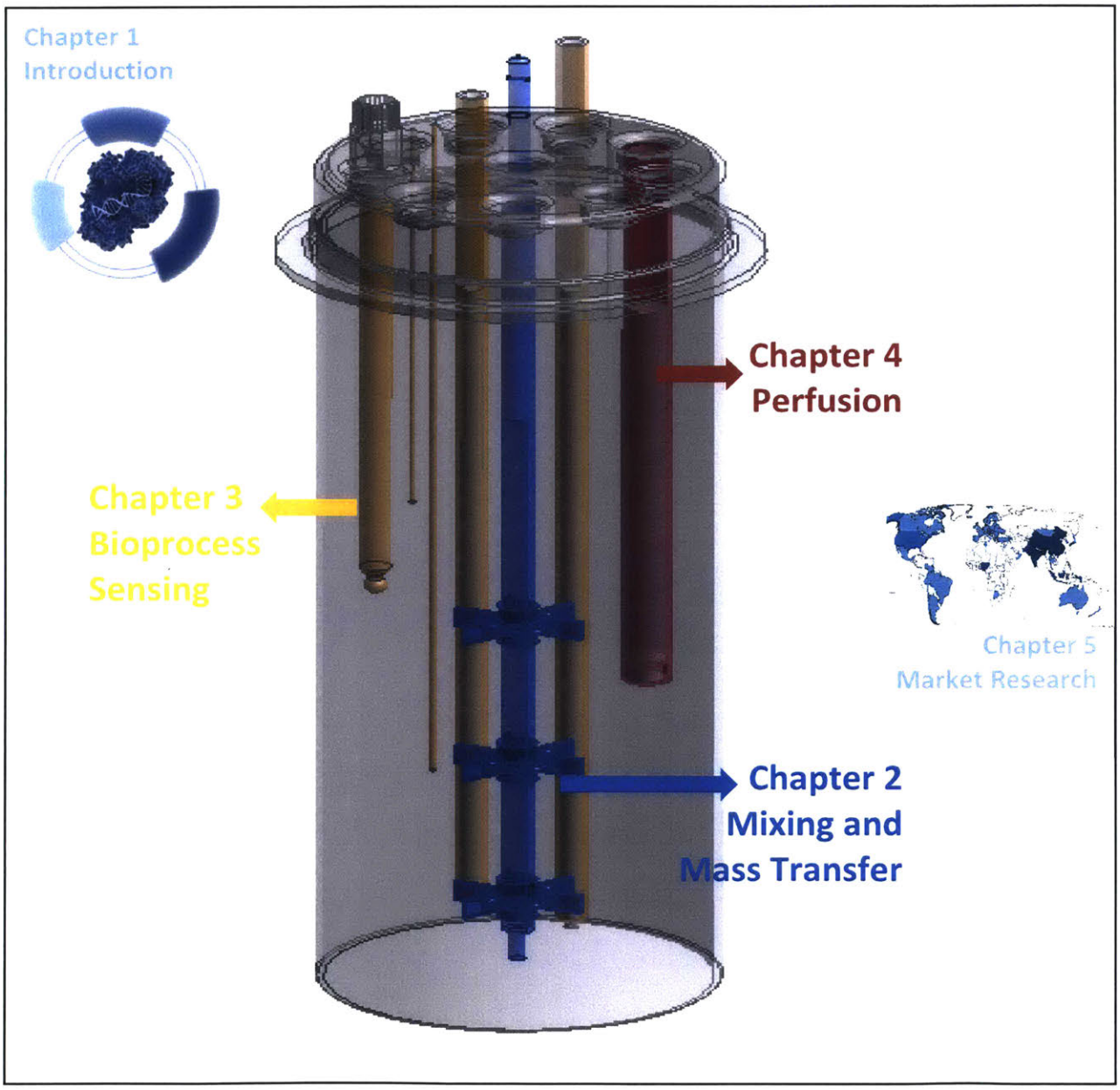


***Figure 1-2* Organization of the Thesis** (in order of Chapters 1 through 5): Introduction, Mixing and Mass Transfer, Bioprocess Sensing, Perfusion, Market Research

# Chapter II
# Mixing and Mass Transfer

# Abstract

Appropriate mixing and mass transfer is essential in bioreactors for the successful manufacturing of biologic drug products. In order to optimize protein yields and create conditions conducive to successful production runs, the design of the bioreactor so as to promote proper mixing and mass transfer is vital. To this end, Computational Fluid Dynamics (CFD) plays an important role in simulating the mixing and mass transfer characteristics within bioreactor geometries, without having to prototype different geometries to test them against each other. This chapter conducts certain comparative studies between bioreactor geometries using CFD simulations.

Three different impeller configurations are first compared in a 1-liter bioreactor geometry, using Rushton, Marine, and angled-Rushton impellers respectively. While the angled-Rushton simulations failed to converge, the Marine impellers showed distinctly higher axial velocities as compared to the Rushton impellers, which may indicate better mixing in a bioreactor such as the one used, due to the large axial clearance from the top impeller to the liquid surface. The impeller configurations were then experimentally used to produce protein, with the Marine impeller configuration leading to significantly larger biomass growth and protein production.

In the design of a larger 5-liter bioreactor, a 3-impeller Rushton configuration was spaced to create a parallel-flow pattern. The CFD simulations characterized the bulk flow patterns, which were consistent with the expected patterns from the literature. Furthermore, the flow velocities as a function of radial distance were plotted in various planes, based on similar studies in the literature, and were found to have good concurrence. These bulk studies can be used for further understanding of the flow dynamics of the vessel.

Future analysis should include multi-phase modeling and bubble dynamics, by advancing the current models. In spite of the results being consistent with previous computational and experimental work, experimental validation by techniques such as laser-doppler anemometry and particle image velocimetry should be conducted to compete the study.

## 2.1 Introduction

Successful biologic drug manufacturing often requires agitation and aeration of the bioreactor or vessel. For continuous cell growth and protein production, in addition to the nutrients and oxygen added to the vessel, proper dispersion of the materials (through ensuring a homogenous mixture) and mass transfer of oxygen to the culture is required. Thus, the agitation and aeration mechanisms are designed to try and optimize the process by maximizing production while minimizing cost and time. There are multiple factors affected by changes in agitation and aeration mechanisms. The trade-offs between agitation and aeration mean that cell damage, foaming, poor mixing, oxygen limitation and other factors can hinder the fermentation run and create non-optimal conditions at certain agitation speeds and aeration rates (Figure 2-1) [9]. Additionally, the cost due to power requirements and complexity of design is another consideration.

There are many parameters that can be adjusted in order to try and optimize fermentation conditions, including agitation method and speed, aeration method and rate, the geometric design of the vessel, cell retention, perfusion methods, chemical and thermodynamic conditions, bubble mechanics, and so on.

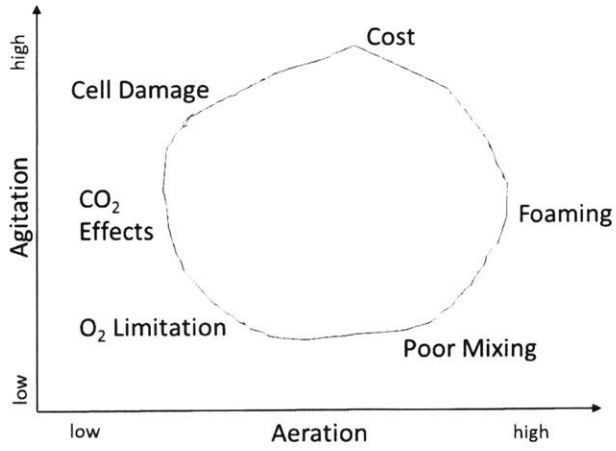


***Figure 2-3*** **Trade-offs between Agitation and Aeration** (Adapted from: [9])

Mixing and mass transfer studies typically focus on agitation and aeration mechanisms that aim to optimize the fermentation conditions in the bioreactor, by:

(1) reducing mixing time required for homogeneous broth, thus providing the entire cell culture with the required nutrients, as well as controls such as pH additives

(2) increasing the mass transfer of oxygen to the reactor fluid, thus satisfying the necessary aerobic requirements of the cell culture

This chapter will begin exploring these studies by characterizing the velocity profile using different impeller configurations. Further, the setup allows for future multiphase modeling and more complete simulations in the future, as well as future experimental validation.

## 2.2 Theoretical Basis

In order to enhance the growth and viability of the cells, and their ability to produce the protein of interest, proper cultivation conditions must be established. Sometimes, transport of nutrients to cells happens much faster than the biochemical reactions of the cells, in which case the biochemical reactions are the rate-limiting step. Mostly, however, the transfer of oxygen to cells is the limiting step. It is known that depletion of dissolved oxygen (DO) and accumulation of dissolved carbon dioxide is detrimental to cell growth and productivity [10]. Thus, the oxygen transfer rate (OTR) into liquid medium is important, as well as the complementary transfer of dissolved carbon dioxide to the bubbles. The transfer rate of oxygen to the reactor fluid, from the sparged bubbles, is often the governing link in productivity of the fermentation process. This oxygen transfer rate (OTR) is modeled by:

$$OTR = (k_l a) * (\mathrm{d}O_2^* - dO_2)$$

where $k_l a$ is the volumetric mass transfer coefficient, and the driving force ($dO_2^*$ - $dO_2$) refers to the gradient between the concentration of dissolved oxygen at the liquid-gas interface of a representative bubble, and the average dissolved oxygen of the bulk liquid [11]. Additionally, the mass balance of the dissolved oxygen in the bulk fluid, relating the OTR to the oxygen uptake rate (OUR) of the cells is given by:

$$\frac{d(dO_2)}{dt} = OTR - OUR$$

The oxygen uptake rate (OUR) refers to the rate at which the cells consume dissolved oxygen, and changes during the fermentation process [11].

Since the OTR is related to the volumetric mass transfer coefficient and the concentration gradient of the dissolved oxygen, it is important to understand those parameters and what

governs them better. Decoupling the volumetric mass transfer coefficient ($k_la$) into the mass transfer coefficient ($k_l$) and the interfacial area (a) between the phases allows for further understanding of the equations. However, it is important to realize that the predictions from theoretical calculations of these values have no universal applications, as there is much dependence on other parameters, and variability in operating conditions.

Higbie's penetration model is commonly used in determining a theoretical gas-liquid transfer prediction [12]. The penetration theory states that the small liquid eddies at the gas-liquid interface are continually attaching and detaching. During attachment, molecular diffusion causes interchange of solutes. Higbie's penetration theory predicts the mass transfer rate based on the exposure time for mass transfer ($t_e$) and the oxygen diffusion coefficient in the liquid layer ($D_L$) is [13]:

$$k_l = 2 * \sqrt{\frac{D_L}{\pi * t_e}}$$

The exposure time which refers to the residence time of the eddies at the gas-liquid interface, is unknown, but governed by the dissipation of energy ($\varepsilon$) in the liquid per unit mass, and is predicted by various models. For non-Newtonian fluids, the Ostwald-de Waele model for flow yielded the development of the following equation [14]:

$$k_l = \frac{2}{\sqrt{\pi}} * \sqrt{D_L} \left(\frac{\varepsilon * \rho}{k}\right)^{\frac{1}{2(1+n)}}$$

where is $\rho$ the density, k refers to the consistency index in a power-law model, and n is the flow index in a power-law model.

In Newtonian fluids, this equation reduces to [14]:

$$k_l = \frac{2}{\sqrt{\pi}} * \sqrt{D_L} \left(\frac{\varepsilon * \rho}{\mu}\right)^{\frac{1}{4}}$$

where $\mu$ is the viscosity.

The interfacial area (a) between the gas bubbles and the bulk liquid is predicted based on the total gas hold-up ($\phi$) and the average bubble diameter ($d_b$), by the equation [15], [16]:

$$a = \frac{6\phi}{d_b}$$

Multiple factors affect these parameters that govern the interfacial area. For example, the average bubble diameter is a function of the sparger geometry and the bubble sizes created, the presence of baffles, other geometry, bubble breakup due to impellers, bubble coalescence, and so on. Similarly, the gas hold-up is also affected by the mechanical design of the bioreactor, turbulence in the bioreactor, operating conditions, and so on.

In stirred tank bioreactors, gas hold-up was estimated using isotropic turbulence theory to develop the following equation [17]:

$$\frac{\phi}{1-\phi} = 0.5\left(\frac{V_s^{\frac{2}{3}}}{(gl)^{\frac{1}{3}}}\right)\left(\frac{\rho_L}{\rho_L - \rho_G}\right)$$

where $V_s$ is the superficial gas velocity, g is the gravitational constant, $\rho_L$ and $\rho_G$ refer to the densities of the liquid and gas phases respectively, and l is Kolmogorov length scale, which was modeled in an equation that assumes the size of the bubbles is affected by the stirred speed [18]:

$$l = \left(\frac{\sigma}{\xi\rho_L}\right)^{\frac{3}{5}}\left(\frac{L^{\frac{2}{5}}}{w^{\frac{6}{5}}}\right)\left(\frac{\rho_L}{\rho_G}\right)^{0.1}$$

where $\sigma$ is the interfacial tension, $\xi$ is the coefficient of resistance (and is 0.4 for 1000 < Re < 200000), w is the velocity of the blade and is given by $w = \pi*T*N$ (where T is the stirrer diameter and N is the stirrer speed), and L is the usually $1/6^{th}$ the blade height (h) of the stirrer for standard configurations [12]. Thus, the equation for gas hold-up can be expanded to [12]:

$$\frac{\phi}{1-\phi} = 0.819\left(\frac{V_s^{2/3} * N^{2/5} * T^{4/15}}{g^{\frac{1}{3}}}\right)\left(\frac{\rho_L}{\sigma}\right)^{1/5}\left(\frac{\rho_L}{\rho_L - \rho_G}\right)\left(\frac{\rho_L}{\rho_G}\right)^{\frac{-1}{15}}$$

The complex bubble mechanics have created further divergence in the theory regarding bubble diameter based on the breakup mechanics, coalescence, and other parameters. One equation proposed for the average bubble size in stirred tank bioreactors with Newtonian fluids is as follows [19]:

$$d_b = 0.7 * \left( \frac{\sigma^{0.6}}{\left(\frac{P}{V}\right)^{0.4} \rho_L{}^{0.2}} \right) * \left(\frac{\mu_L}{\mu_G}\right)^{0.1}$$

where $\mu_L$ is the liquid viscosity, $\mu_G$ is the gas viscosity, P is the pressure and V is the volume of the liquid in the bioreactor.

Thus, the above equations are attempts to capture the relationship between bioreactor mechanical and operating parameters with the volumetric mass transfer coefficient that affects the oxygen transfer rate.

Operational conditions such as the stirrer speed and gas velocity, geometric parameters such as the height and diameter of the bioreactor, physical properties such as viscosity, density, and interfacial tension, are all influential in affecting the mass transfer coefficient ($k_l a$) and the concentration gradient of dissolved oxygen, that ultimately influence the OTR [12].

While bubbles have a positive influence on cell culture due to the gas transfer they introduce, there are negative effects as well. Bubbles can cause cell death in many ways:

(1) Bubble breakup and coalescence can shear cells in the vicinity of the bubbles [20]
(2) Local rapid oscillations from bubble activity can also kill cells due to acceleration forces [21]
(3) Bubble bursting at the free surface can kill cells [20] [22]
(4) Bubble trends that increase mass transfer have also been shown to increase cell death in some cases [21]

The implication is that simply increasing mass transfer is not the solution to achieve optimal product yield. Bubble-based predictions to guide mass transfer calculations is

notoriously difficult, as the microscale physics of bubbles are probability based. Population balance models (PBMs) are commonly used, that cluster bubbles by diameter size ranges, and are then modeled computationally. In order to create computational simulations, these theoretical models of bubble activity were developed in the literature. A caveat to all models developed is that multiple simplifications and assumptions have been made in order. One of the better models developed is shown here [23]. They assume isotropic turbulence, binary breakage of fluid particles, the breakage volume fraction to be a stochastic variable, the breakup occurrence being determined by the energy level of the arriving eddy, and that only eddies of smaller or equal to length scale of the particle diameter can induce particle oscillations [23]. The model recommends a general rate model for fluid particle breakage [23]:

$$\Omega_B(v: vf_{BV}) = \int_{\lambda_{min}}^{d} P_B(v: vf_{BV}, \lambda)\dot{w}_{B,\lambda}(v)d\lambda$$

where $\Omega_B(v: vf_{BV})$ is the breakage rate of particles of size $v$ into a fraction between $f_{BV}$ and $f_{BV} + df_{BV}$, where $f_{BV}$ is the breakage volume fraction, $P_B(v: vf_{BV}, \lambda)$ is the probability for a particle of size $v$ breaking into two particles, one with volume $vf_{BV}$ when the particle meets eddy of length scale $\lambda$, and $\dot{w}_{B,\lambda}(v)$ is the frequency of arriving eddies of length scale between $\lambda$ and $\lambda + d\lambda$. After developing models for probability and frequency, the paper creates an extended model for breakup rate of particles of size $v$ or $d$ into particle sizes of $vf_{BV}$ and $v(1 - f_{BV})$ [23]:

$$\frac{\Omega_B(v: vf_{BV})}{(1 - \epsilon_d)n} = c_4\left(\frac{\epsilon}{d^2}\right)^{1/3}\int_{\xi_{min}}^{1}\frac{(1+\xi)^2}{\xi^{1/3}}\exp\left(\frac{-12c_f\sigma}{\beta\rho_c\epsilon^{2/3}d^{5/3}\xi^{11/3}}\right)d\xi$$

where:

$$\epsilon \rightarrow \textit{energy dissipation rate per unit mass}$$

$$\epsilon_d \rightarrow \textit{local fraction of the dispersed phase}$$

$$n \rightarrow \textit{number of bubbles per unit dispersion volume}$$

$$c_4 \cong 0.923 \rightarrow \textit{constant}$$

$$\xi = \frac{\lambda}{d} \rightarrow size\ ratio\ between\ an\ eddy\ and\ a\ particle$$

$$c_f = f_{BV}^{2/3} + (1 - f_{BV})^{2/3} - 1$$

$$\beta = 0.6\Gamma\left(\frac{1}{3}\right)\alpha\ ;\alpha = 1.5 \rightarrow constant$$

In order to aid computational numerical simulations, the model went on to create an equation that governed the particle size distribution of the daughter bubbles formed upon breakage of bubbles [23]:

$$\eta(v: vf_{BV}) = \frac{2\int_{\xi_{min}}^{1}(1+\xi)^2\xi^{-11/3}e^{X_c}d\xi}{v\int_0^1\int_{\xi_{min}}^{1}(1+\xi)^2\xi^{-11/3}e^{X_c}d\xi df_{BV}}$$

where $\eta(v: vf_{BV})$ is the fraction of particles that break into particles of size between $v$ and $vf_{BV}$, and $X_c$ is the critical dimensionless energy for breakup modeled by [23]:

$$X_c = \frac{12c_f\sigma}{\beta\rho_c\epsilon^{2/3}d^{5/3}\xi^{11/3}}$$

While these prediction models are useful in gaining a theoretical understanding of the mechanics of the reactor, its real use is in creating numerical simulation models that are solved computationally to predict reactor performance. However, with the simplifications and assumptions in creating a numerical solution, the most accurate way is repeated empirical results. However, computational simulations still allow for a relative understanding of the different reactor geometries and operation conditions, and the effect they have on fermentation performance.

## 2.3 Computational Fluid Dynamics (CFD) Studies

CFD was used to conduct a comparison between impeller types in two different studies. The first study compared impeller types in a two-impeller system for a 1 L bioreactor. With future plans to develop a larger bioreactor, the second study focused on analysis of the fluid kinetics in a three-impeller system.

### 2.3.1 CFD Theory and Equations

Computational Fluid Dynamics (CFD) is a way to numerically estimate a solution to the Navier-Stokes equations of fluid mechanics, using simulations. CFD numerical software typically uses a finite volume method, or an infinitesimal finite element method as control regions upon which to apply the Navier-Stokes equations. The ANSYS Fluent solver used in this work is a finite volume method. The governing Navier-Stokes equations for viscous flow (the continuity, momentum, and energy equations) are described here.

The conservation of mass (continuity) in a control volume approach leads to [24]:

$$\frac{\partial}{\partial t}\iiint_{\mathcal{V}} \rho d\mathcal{V} + \oiint_{S} \rho \boldsymbol{V}.d\boldsymbol{S} = 0$$

where S is the control surface, $\mathcal{V}$ is the control volume, **V** is the flow velocity vector at elemental surface area d**S**, and $\rho$ is the density [24]. This integral form of the conservation of mass equation is reduced to [24]:

$$\frac{\partial \rho}{\partial t} + \nabla.(\rho \boldsymbol{V}) = 0$$

Similarly, the momentum equations in conservation form are [24]:

$$\frac{\partial(\rho u)}{\partial t} + \frac{\partial(\rho u^2)}{\partial x} + \frac{\partial(\rho uv)}{\partial y} + \frac{\partial(\rho uw)}{\partial z} = -\frac{\partial p}{\partial x} + \frac{\partial}{\partial x}\left(\lambda \nabla.\mathbf{V} + 2\mu\frac{\partial u}{\partial x}\right) + \frac{\partial}{\partial y}\left[\mu\left(\frac{\partial v}{\partial x} + \frac{\partial u}{\partial y}\right)\right] + \frac{\partial}{\partial z}\left[\mu\left(\frac{\partial w}{\partial x} + \frac{\partial u}{\partial z}\right)\right] + \rho f_x$$

$$\frac{\partial(\rho v)}{\partial t} + \frac{\partial(\rho v^2)}{\partial y} + \frac{\partial(\rho uv)}{\partial x} + \frac{\partial(\rho vw)}{\partial z} = -\frac{\partial p}{\partial y} + \frac{\partial}{\partial x}\left[\mu\left(\frac{\partial v}{\partial x} + \frac{\partial u}{\partial y}\right)\right] + \frac{\partial}{\partial y}\left(\lambda \nabla.\mathbf{V} + 2\mu\frac{\partial v}{\partial y}\right) + \frac{\partial}{\partial z}\left[\mu\left(\frac{\partial w}{\partial y} + \frac{\partial v}{\partial z}\right)\right] + \rho f_y$$

$$\frac{\partial(\rho w)}{\partial t}+\frac{\partial(\rho w^2)}{\partial z}+\frac{\partial(\rho uw)}{\partial x}+\frac{\partial(\rho vw)}{\partial y}$$
$$= -\frac{\partial p}{\partial z}+\frac{\partial}{\partial x}\left[\mu\left(\frac{\partial u}{\partial z}+\frac{\partial w}{\partial x}\right)\right]+\frac{\partial}{\partial y}\left[\mu\left(\frac{\partial w}{\partial y}+\frac{\partial v}{\partial z}\right)\right]+\frac{\partial}{\partial z}\left(\lambda\nabla.\mathbf{V}+2\mu\frac{\partial w}{\partial z}\right)+\rho f_z$$

where x, y, and z define the 3-dimensional space, and u, v, and w are the velocity components in those directions, $f_i$ is the $i^{th}$ component of the body force per unit mass acting on the fluid element, $p$ is the pressure force, $\mu$ is the molecular viscosity coefficient, and $\lambda$ is the bulk viscosity coefficient [24].

Finally, the conservation of energy equation is written as [24]:

$$\frac{\partial}{\partial t}\left[\rho\left(e+\frac{V^2}{2}\right)\right]+\nabla.\left[\rho\left(e+\frac{V^2}{2}\boldsymbol{V}\right)\right]$$
$$= \rho\dot{q}+\frac{\partial}{\partial x}\left(k\frac{\partial \mathrm{T}}{\partial x}\right)+\frac{\partial}{\partial y}\left(k\frac{\partial \mathrm{T}}{\partial y}\right)+\frac{\partial}{\partial z}\left(k\frac{\partial \mathrm{T}}{\partial z}\right)-\frac{\partial(up)}{\partial x}-\frac{\partial(vp)}{\partial y}-\frac{\partial(wp)}{\partial z}$$
$$+\frac{\partial(u\tau_{xx})}{\partial x}+\frac{\partial(u\tau_{yx})}{\partial y}+\frac{\partial(u\tau_{zx})}{\partial z}+\frac{\partial(v\tau_{xy})}{\partial x}+\frac{\partial(v\tau_{yy})}{\partial y}+\frac{\partial(v\tau_{yz})}{\partial z}+\frac{\partial(w\tau_{xz})}{\partial x}$$
$$+\frac{\partial(w\tau_{yz})}{\partial y}+\frac{\partial(w\tau_{zz})}{\partial z}+\rho\boldsymbol{f}.\boldsymbol{V}$$

where $e$ is the internal energy, $\dot{q}$ is the heat transferred per unit time per unit area, T is the temperature, k is the thermal conductivity, and $\tau_{ij}$ are the viscous stress terms [24].

CFD is used to approximate a solution to these set of equations, upon input of some flow variables, boundary conditions, and a defined geometry.

The RNG k-$\epsilon$ viscous model was used in all numerical simulations carried out in this work. The transport equations for this and other specific models are documented widely available.

## 2.3.2 Impeller Comparison Study in 1.0 L bioreactor

This study compared three impeller types for use in the 1.0 L Infors-2 vessel currently being used by the project. The impellers types are standard Rushton impellers, Marine impellers,

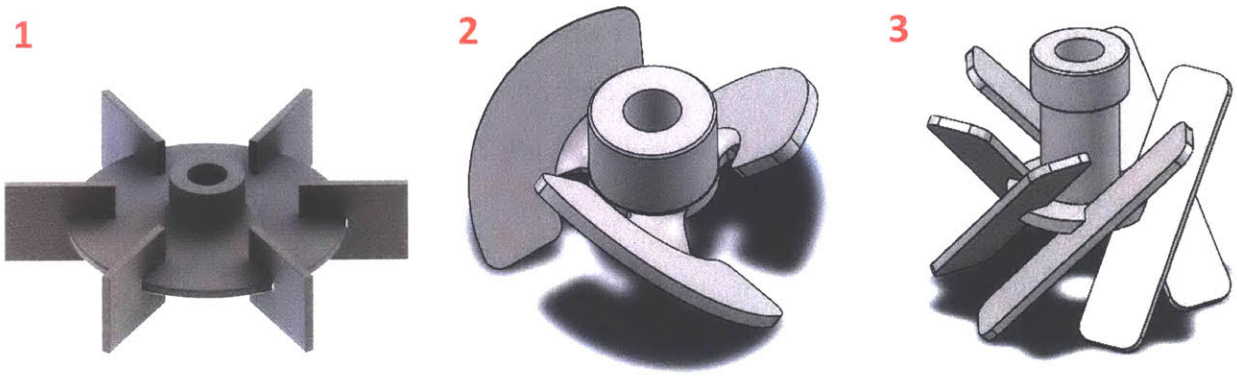


*Figure 2-2* **The three impeller types (1) Rushton (2) Marine (3) Angled-Rushton**

and angled-Rushton impellers. Figure 2-2 depicts a single impeller of each type. The 1-liter vessel uses a two-impeller agitation shaft. Thus, the three impeller configurations are referred to as "dual" Rushton, "dual" Marine, and "dual" angled-Rushton. The impeller spacing is fairly close as demanded by the constraints of the other probes and parts in the bioreactor.

The main objective of this study was to characterize the bulk flow patterns induced by each of the different configurations and compare them to each other. The hope is that future work will expand upon this basis and use the reactor and impeller models to:

(1) solve two-phase population balance models to predict gas holdup, mass transfer, shear, bubble activity, and completely characterize the mixing quality of each vessel

(2) compare different kinds of configurations to study $k_l a$ dependence on geometry

### 2.3.2.1 Geometry

The geometries used in the setup included only the agitation shaft along with the impellers of interest, as well as a probe that was added to ensure the vessel had eccentricity and non-symmetry, to aid in analysis of bulk flow. The Multiple Reference Frame model is used, as is standardly done in the literature to achieve a good compromise between physical accuracy and lower computational costs [25] [26] [27] [28] [29]. In order to enable the Multiple Reference Frame (MRF)[2] model, the geometries were divided into *Fixed Air*, *Fixed Fluid*, and *Rotating Fluid* regions (Figure 2-3) [30] [31]. There are multiple other probes and

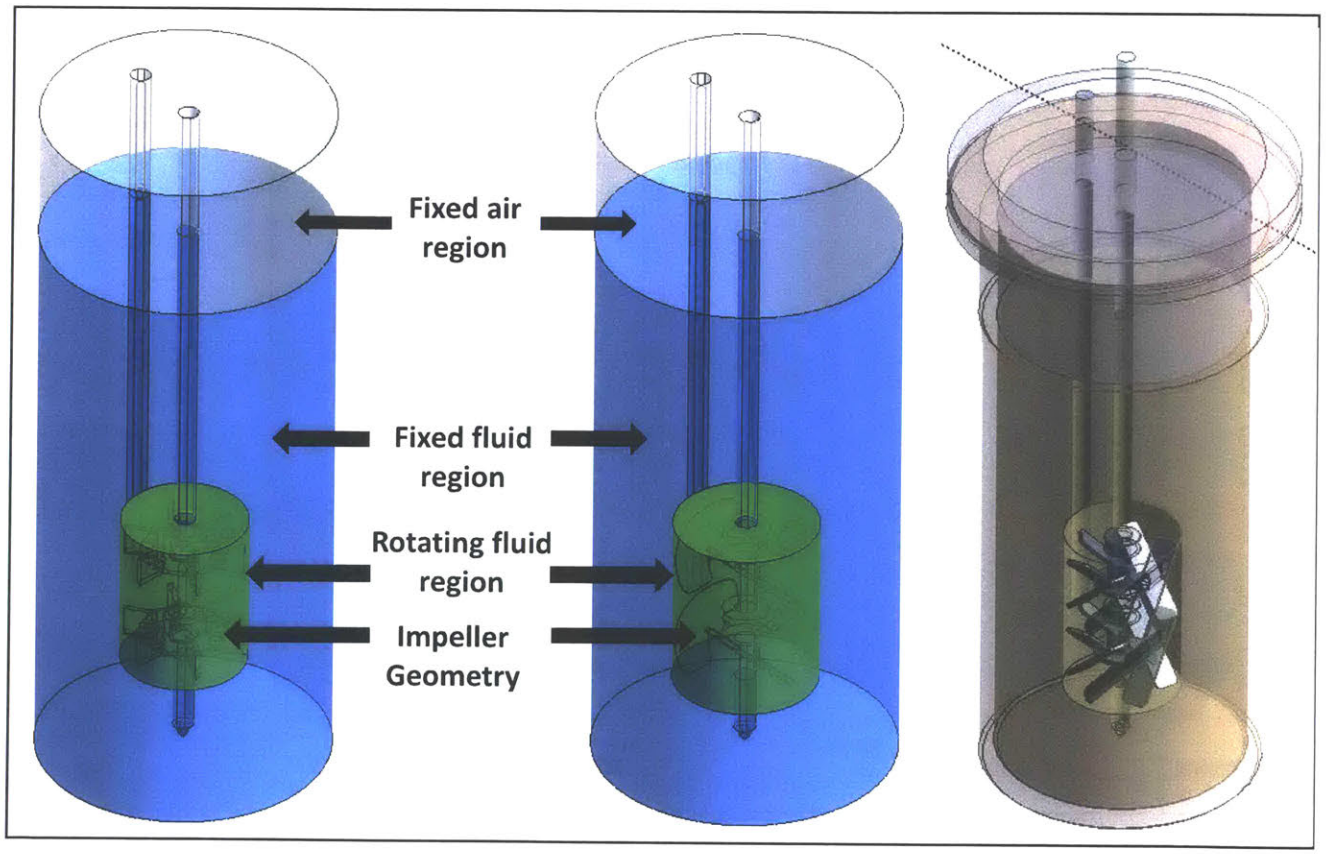


***Figure 2-3* Geometry and MRF Regions in Impeller Study** Left-to-right: Geometry and regions for the dual-Rushton, dual-Marine, and dual-angled-Rushton impellers; the dual-angled-Rushton (greyed out) simulations were unsuccessful

[2] The Moving or Multiple Reference Frame (MRF) model in CFD is a steady-state approximation model. Cell zones are defined within the geometry, and these zones move at different speeds. The flow in the moving zone is solved independently using moving reference frame equations, and the interface of zones are transformed to allow for variables across zones to calculate boundary fluxes [30]. The MRF model was developed to solve the two sets of equations and then was applied to impeller-induced flows [31].

parts in the vessel, but for the sake of simplicity in this comparative initial analysis, these were excluded.

### 2.3.2.2 Mesh

The geometries were then meshed using the in-built ANSYS Meshing Software. The mesh minimum element size was set to 0.50 mm, a maximum size of 1.00 mm, high smoothing, medium relevance center, using the CutCell method. The meshes can be seen in Figure 2-4.

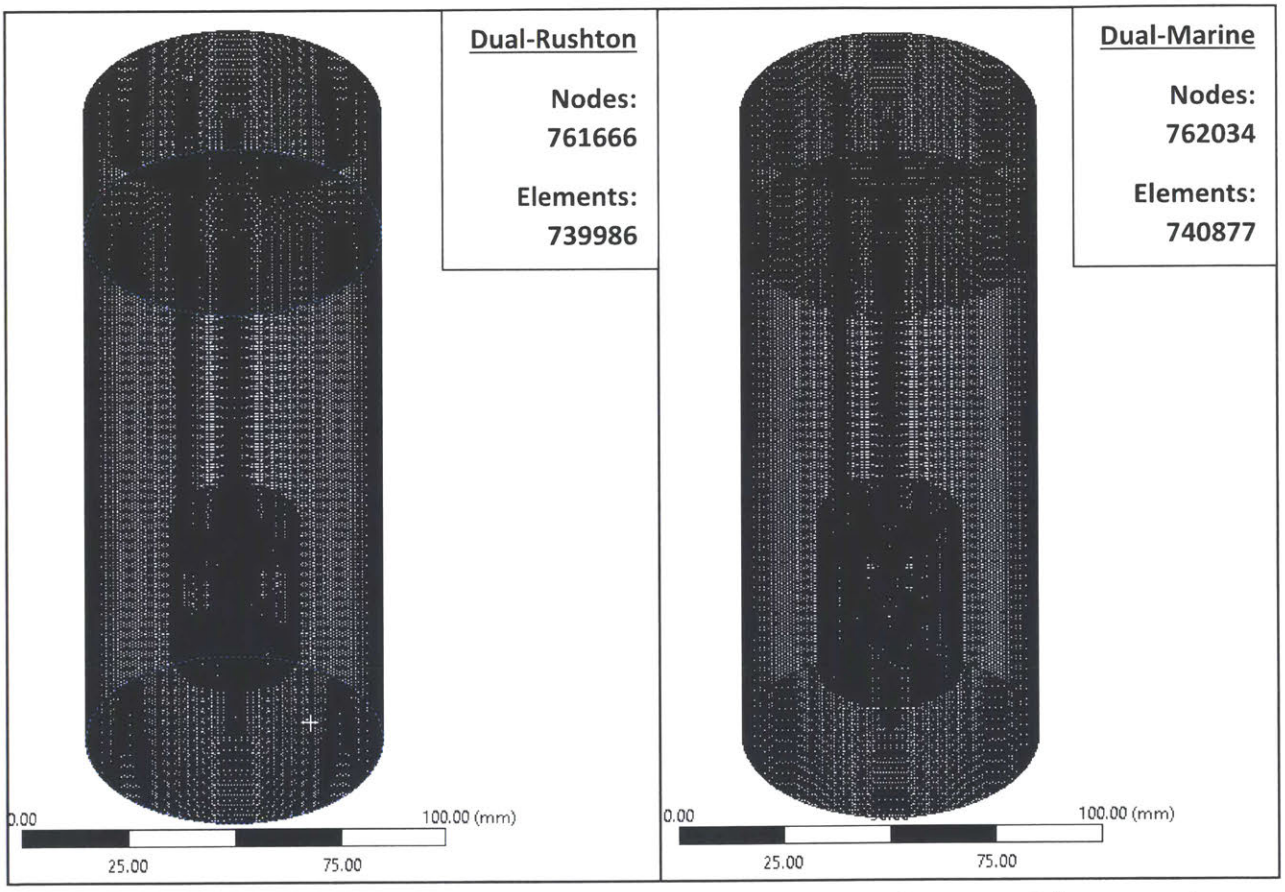


***Figure 2-4* Meshes in Impeller Study** Meshes of the two impeller configurations that successfully converged

### 2.3.2.3 Solver Setup

The meshes were then imported into the ANSYS Fluent Solver. For a stirred tank, the Reynolds number is defined as:

$$Re = \frac{\rho N D^2}{\mu}$$

where ρ is the density of the fluid, N is the agitator speed, D is the impeller diameter, and μis the dynamic viscosity of the fluid [32]. For stirred bioreactors, the laminar region is generally considered when Re < 10, whereas the start of the turbulence region has wide variance in the literature, from Re > 480 [33] to Re > 1200 [34].

The Reynolds number for the slowest impeller case (300 rpm) is in the early turbulent regime, with Re = 5000, and the 1000 rpm case has Re = 16700. Models that account for lower Reynolds numbers have been shown not necessarily provide better results than turublent models [33]. Previous studies have shown that bioreactor modeling in the transition regime with Re = 1700 can be successfully modeled using turbulent models [35]. Some studies model any stirred bioreactor flow with Re > 50 using a turbulent model [36]. Thus, the k-epsilon model was used for the Viscous Model, commonly used for similar studies in bioreactor simulations [32] [37] [28] [25] [38]. First-order models such as the standard k-epsilon or renormalization group theory (RNG) k-epsilon models that assume isotropic turbulence, have historically given good predictions of the mean flow and hydrodynamic quantities [39] [40] [41], as well as well qualitatively predicted turbulence results [42] [43] [41].

The *Rotating Fluid Region*, the *Fixed Fluid Region*, and the *Fixed Air Region* were defined as walls with a "No Slip" condition, except for the interface between the *Fixed Fluid* and the *Fixed Air* region, which was simulated as a static free surface by defining it as a wall with zero-shear to properly simulate the boundary conditions. Within the cell zones, the rotational zone was set to the desired rpm (multiple simulations run with different speeds), whereas the other zones were set to having no frame motion. This properly enables the MRF model to simulate impeller rotation within the vessel. The fluid in all zones was set to

water at standard temperature and pressure (STP) conditions, which has properties that are fairly similar to the fluid mix within the bioreactor.

The SIMPLE pressure-velocity coupling solver was used, with a Least Squares Cell Based gradient, second order pressure and momentum equations, and first order turbulent equations. The under-relaxation factors to achieve convergence are shown in Table 2-1. A Standard Initialization was used with default settings, and the solution was accepted as having converged when all the residuals were below 10 e-03.

| | |
|---|---|
| Pressure | 0.3 |
| Density | 1 |
| Body Forces | 1 |
| Momentum | 0.1 |
| Turbulent Kinetic Energy | 0.1 |
| Turbulent Dissipation Rate | 0.1 |
| Turbulent Viscosity | 1 |

***Table 2-1*** **Under-relaxation Factors in the Impeller Study Simulation**

### 2.3.2.4 Results and Discussion

The two impeller configurations that achieved successful convergence were the dual-Rushton and the dual-Marine impellers. They were each simulated at two impeller speeds – 300 rpm and 1000 rpm, both in the typical operating range. The static pressure profiles of the impellers viewed from above show clear high-pressure leading edges and low-pressure lagging edges (Figure 2-5), which validates the simulation, as this is consistent with the literature as well as with theoretical fluid mechanics.

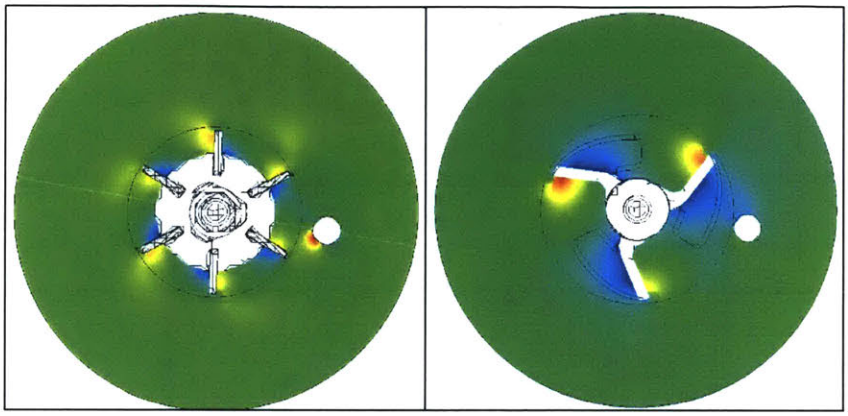

***Figure 2-5* Pressure Profiles in Impeller Study** High-pressure leading edges and low-pressure lagging edges in the Rushton (left) and Marine (right) impellers for the 1000 RPM cases

The velocity profiles for the different speeds and configurations are shown in Figure 2-6. For the case of the dual-Rushton impellers, it can be seen that the simulation predicts the impellers to pump in "merging flow", as described by Rutherford et al [44]. This is consistent with the literature (computational and experimental) that shows Rushton impellers spaced close to each other will have a "merging flow" pattern [44]. In spite of the consistency with literature, future work should experimentally verify these computational results.

For turbulent flow, rigorous theoretical analysis has shown that in stirred bioreactors, the average shear rate γ in the fluid is [45]:

$$\gamma = constant * N^{3/2}$$

where N is the impeller speed and the proportionality constant is dependent on the flow index and consistency index [45]. This theoretical relationship is consistent with well-known empirical results [46] [47] [45]. Shear rate is important because of mixing as well as cell viability, as mentioned earlier. The constant depends on the geometry of the impellers

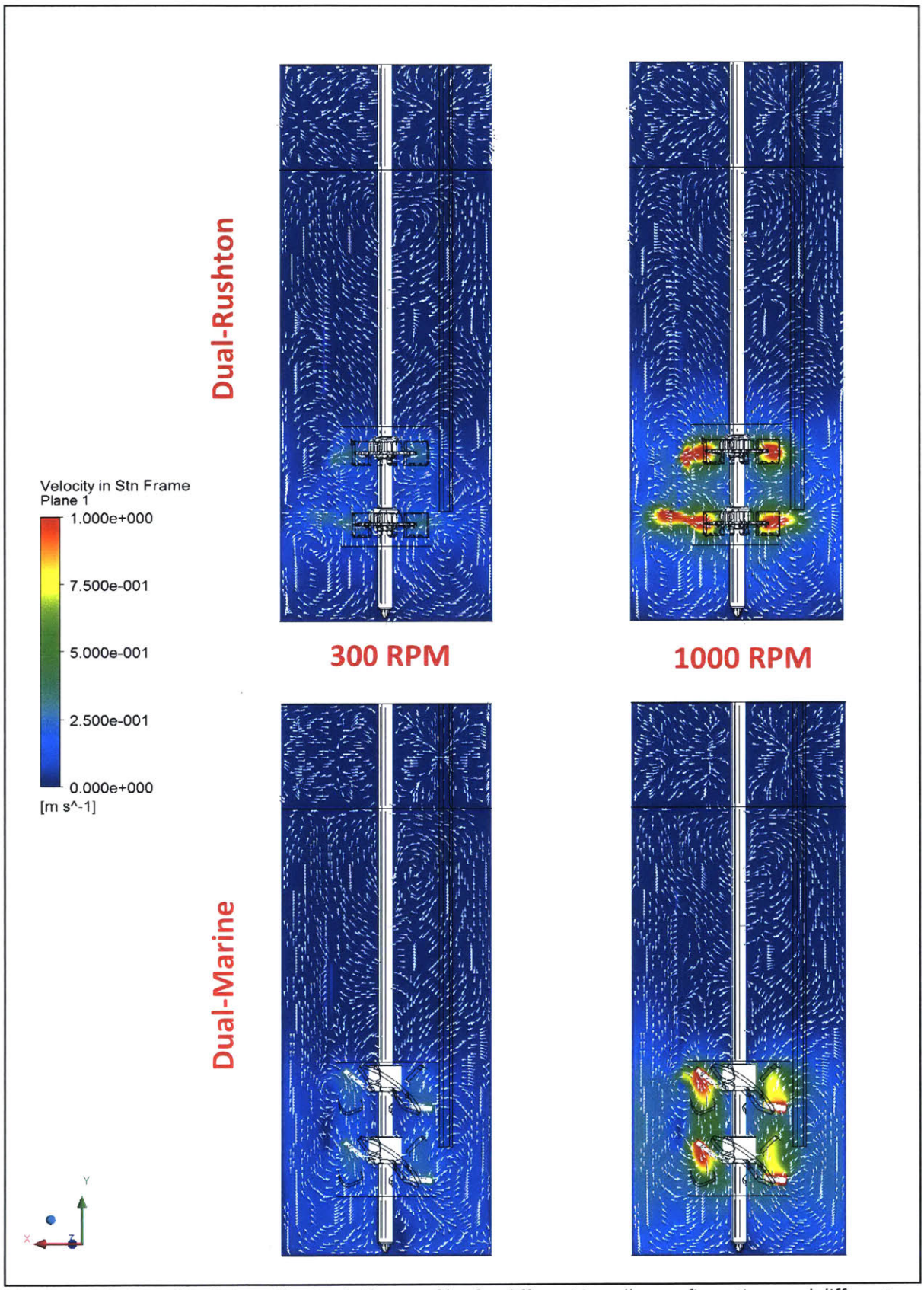


***Figure 2-6* Flow Profiles in Impeller Study** Flow profiles for different impeller configurations and different impeller speeds

and the bioreactor itself, and the computational results can be used to determine it in future analyses.

Similarly, the dimensionless power number can also be calculated [29]:

$$Ne = \frac{P}{\rho N^3 d^5} = \frac{2\pi M_R}{\rho N^2 d^5}$$

where $M_R$ is the torque acting on the stirrer and the shaft [29].

Using the bulk flow velocity results, the compartment model can then be used to accurately predict the mixing time ($t_{95\%}$) required for homogeneity [48]. These models use the velocity results from CFD analysis to numerically solve a transient mass balance of the system of ordinary differential equations of tracer concentration in each compartment [49] [50] [51] [52]. There is good agreement between experimental results and those done using theory [48].

Exporting the results from the simulation predicting the velocity flow field in the bioreactor, the radial and the axial flow velocities, as well as the overall velocities, are shown as a function of radial distance, at specific axial planes. Apart from the absolute values, the normalized dimensionless values are also plotted so as to be consistent with the style of similar studies in the literature [44] [29] [53] [54] [33]. The absolute value are normalized against the impeller tip speeds, shown in Table 2-2.

| Rotation Speed (RPM) | $V_{tip}$ (m/s) |
|---|---|
| 300 | 0.471 |
| 600 | 1.571 |

***Table 2-2*** **Impeller Tip Speeds vs RPM for the Impeller Study**

The radial and overall velocity profiles generated in the simulation where plotted as a function of radial distance away from the centerline (agitator shaft), at a height of 0.056 m from the bottom of the vessel, so as the be in line with the centerline of the top impeller. The axial velocity as a function of radial distance was probed at heights of 0.049 m and 0.063 m, so as to be just above and below the top impeller. The distance was based of the

study from Kaiser et al, probing at a consistent location with regards to the distance from the impeller height [29].

The overall velocity profile as a function of radial distance has a very similar shape to the study conducted by Ng et al [53]. The velocity starts of low, peaks near the blades, and then gradually decreases (Figure 2-7). This similarity helps validating the results, and also points out useful flow characteristics in the bioreactor. The radial velocity profiles (absolute and dimensionless) are shown in Appendix A.

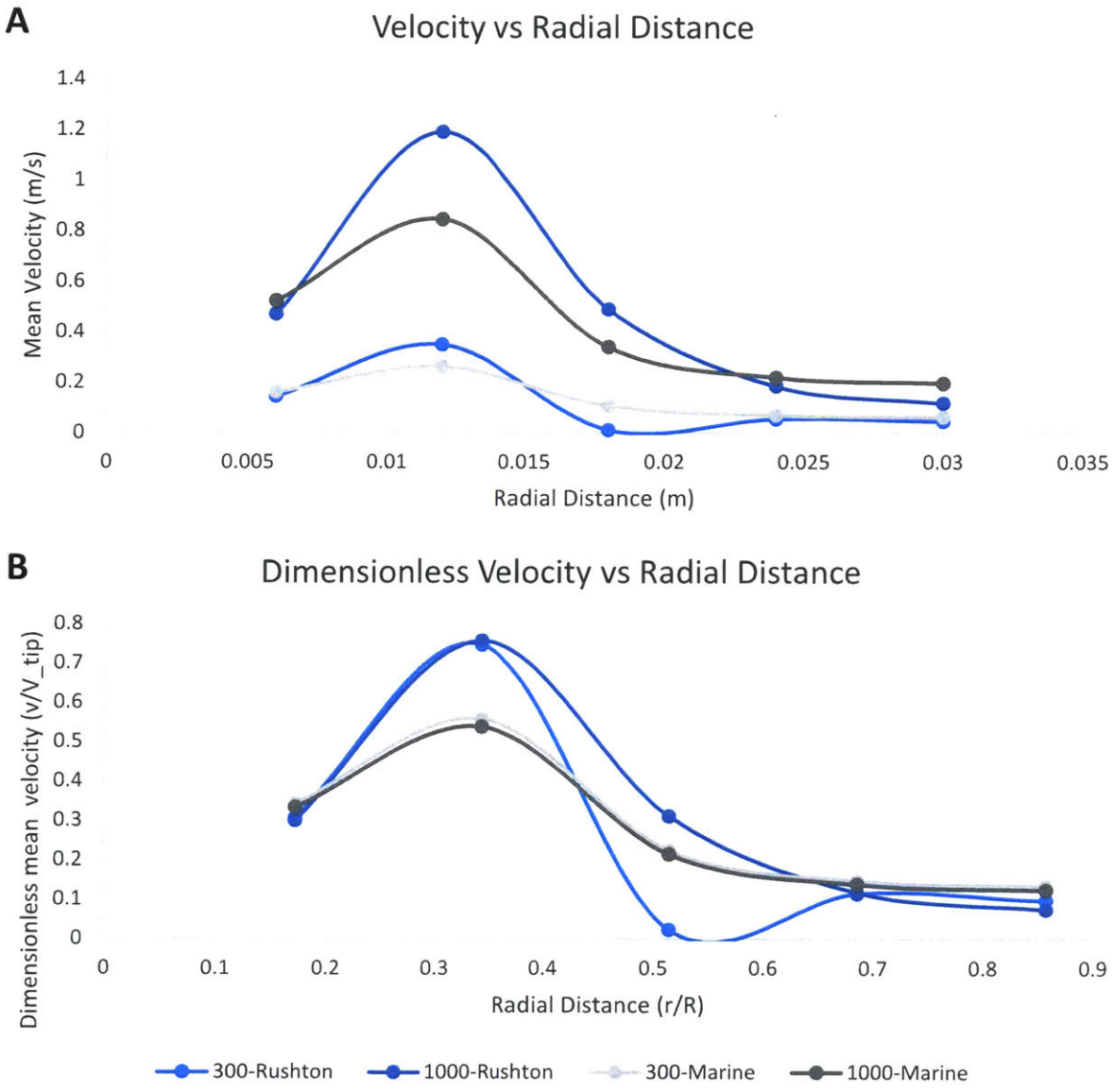


***Figure 2-7* Velocity vs Radial Distance in Impeller Study** (A) Absolute and (B) Dimensionless mean velocity as a function of radial distance from the center of the of vessel for each rotational speed, at a height of 0.056 m from the bottom of the vessel

The dimensionless axial velocity profiles as a function of radial distance from the center shaft, is shown in Figure 2-8 (the absolute profiles are shown in Appendix A). The dual-Rushton configuration pumps towards from the blades axially at the top and bottom, consistent with typical Rushton flow profiles. Whereas the dual-Marine configuration is an upward-pumping setup, consistent with the experimental study of Odeleye et al [55]. Furthermore, the dual-Marine configuration has much higher dimensionless axial velocity performance than the dual-Rushton configuration.

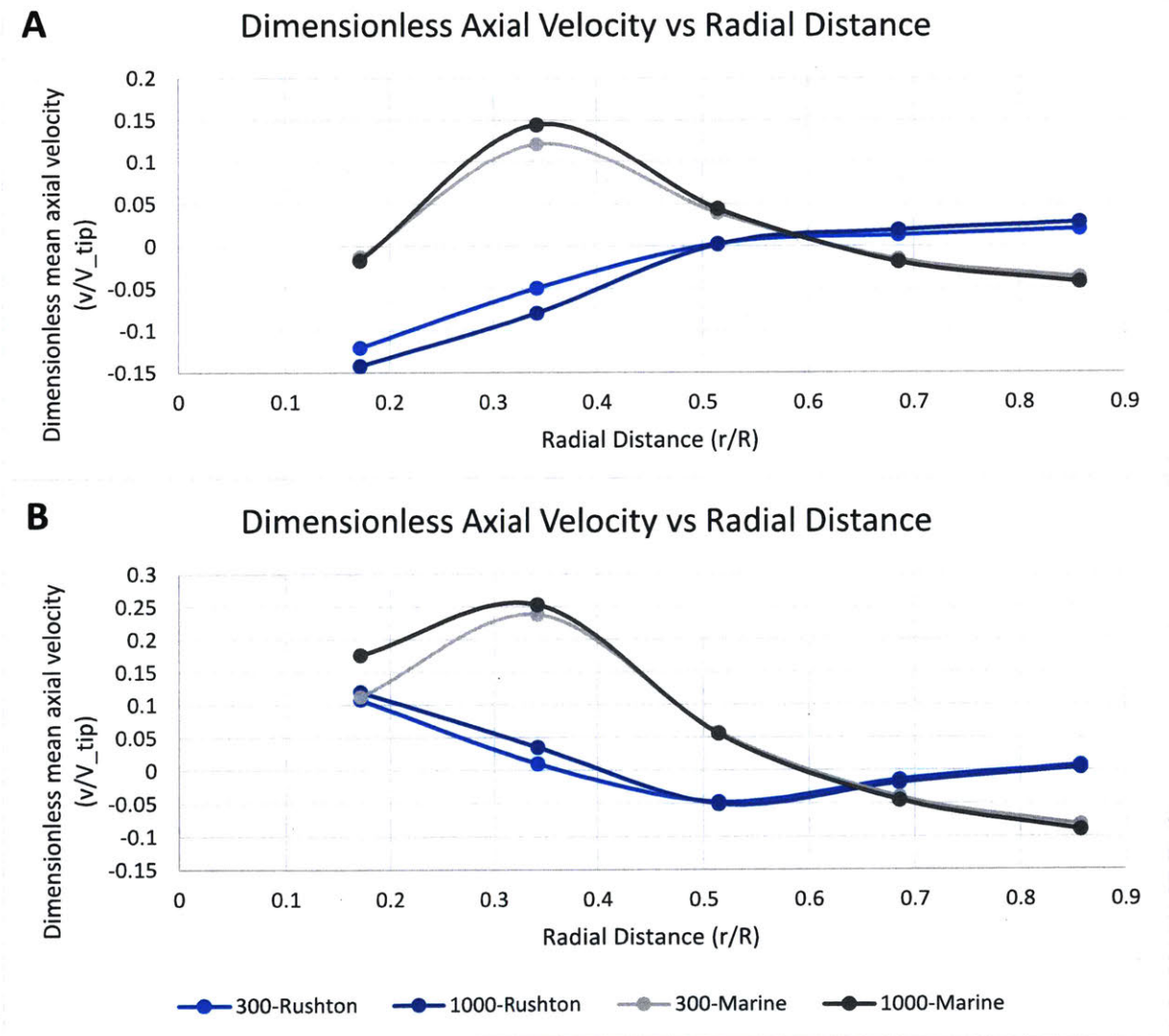


***Figure 2-8* Axial Velocity vs Radial Distance** Dimensionless mean axial velocity as a function of radial distance from the centerline, at a height of (A) 7 mm above and (B) 7 mm below the top impeller

The overall results signify that the dual-Marine configuration may be beneficial for bulk mixing in the vessel, as it has good overall flow velocities in all directions, combined with

the fact that the bioreactor impellers (in both setups) are near the bottom of the vessel, which could mean axial mixing is vital. To further the study, experimental validation techniques such as particle image velocimetry (PIV) and laser-doppler anemometry (LDA) can be considered as next steps. In the interim, however, experimental testing of the reactor configurations to produce protein was conducted.

#### 2.3.2.5 Experimental Testing

An experimental impeller configuraiton study was later conducted in the lab to determine the different configurations have on product yield (design of experiments and implementation by: Laura Crowell, William Doherty, Alexandra Boneyman [Love Lab]; Amos Lu [Braatz Lab], hereon referred to as Team InSCyT, after the project name). For the study, the host cell line used is *Pichia pastoris* as that is what the lab project uses. *P. pastoris* has been identified as having immense potential in the biologic drug manufacturing field, due to their faster growth rates to a high density compared to CHO [56], as well as their simple, 4-chromosomal genome [57]. The first set of experiments compared the traditionally used dual-Rushton configuration, to the dual-Marine and the dual-angled-Rushton impeller configurations. The protein produced in testing was granulocyte-colony stimulating factor (G-CSF), which is sometimes administered to chemotherapy patients to increase their ability to produce white blood cells.

The first round of testing compared the dual-Rushton, dual-Marine, and dual-angled-Rushton configurations at the same operating conditions. 60 $OD_{600}$ of strain $P_{ADX1}$ G-CSF H1 was injected, re-suspended in 10 ml of BMGY. Biomass was accumulated for 32 hours (BMGY-fed) at an oxygen sparge rate of 0.04-0.2 standard liters per minute (SLPM), at a stirred speed between 500-1500 RPM, to a dissolved oxygen (DO) set-point of 100%. The transition to production at 32 hours reduced the DO set-point to 40%, with continuous G-CSF production for 5 days (BMMY). The bioreactor traces are shown in Figure 2-9. The

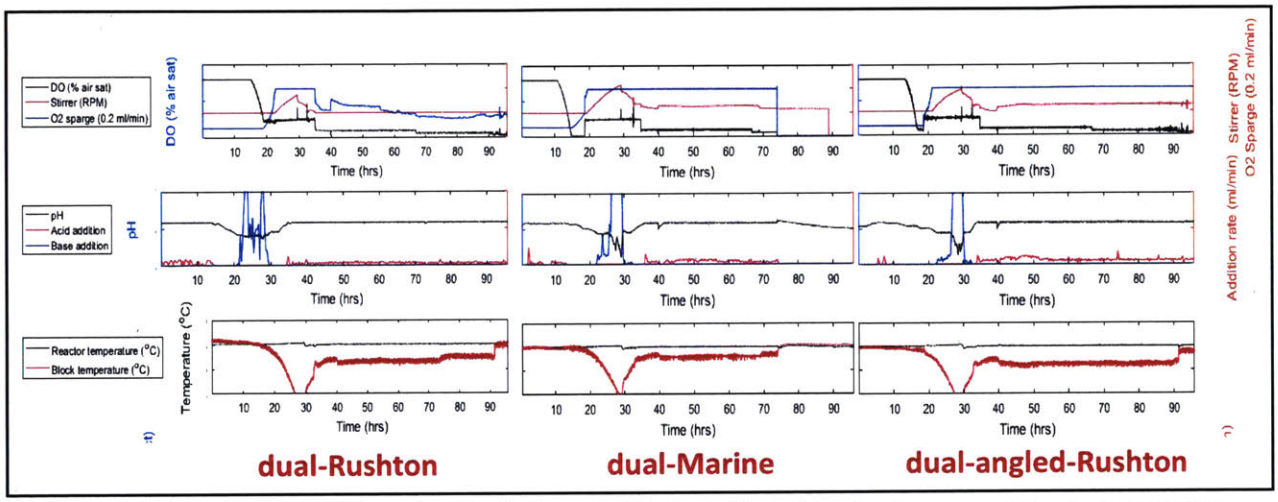


***Figure 2-9* Bioreactor Traces in Impeller Study** Traces of the growth and production runs of the three impeller configurations (Image Credit: Team InSCyT)

results of the run show can be seen in the gel electrophoresis[3] samples conducted (Figure 2-10). These qualitative results clearly show that the dual-Marine had strikingly larger protein yield than the dual-Rushton and dual-angled-Rushton configurations. Similarly the biomass sampling done throughout the process shows that the dual-Marine configuration led to the highest cell concentration (and thus, best cell growth) by a factor of around 2, compared to the other two configurations (Figure 2-11). The increased cell growth would be a major factor in the higher protein yield, although other factors also potentially played a part.

[3] Gel electrophoresis is a method used to separate DNA, RNA, or proteins based on their molecular size. The protein of interest is used a Standard against which to measure against, and the darker the band along the Standard line, the higher the concentration of the protein of interest.

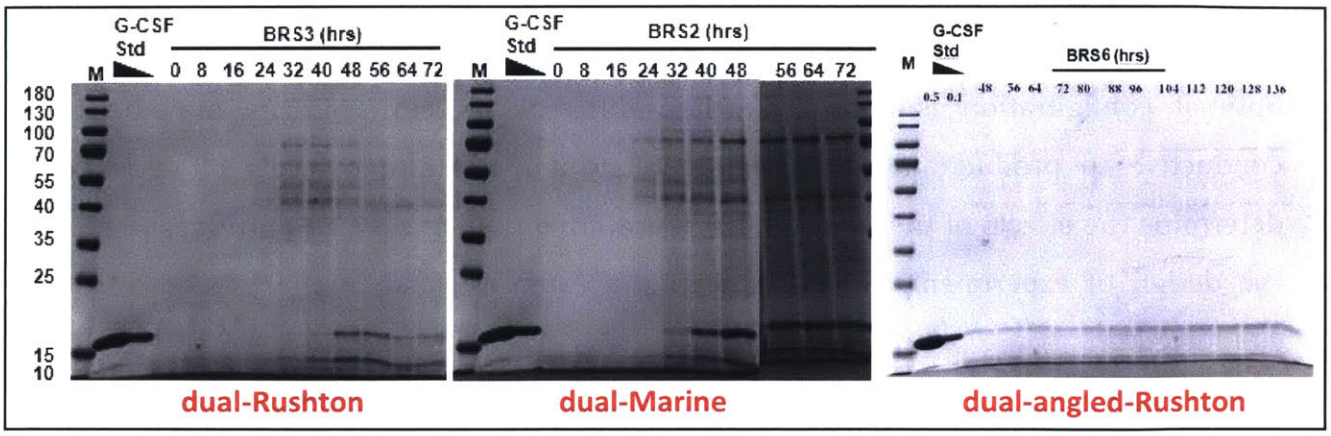


***Figure 2-10* Gel Electrophoresis Samples in Impeller Study** Samples for the three impeller configurations with the standard as the protein of interest (Image Credit: Team InSCyT)

The better cell growth conditions in the dual-Marine setup could be due to the higher predicted axial velocities from the computational simulations, in a tank that has large axial distances without impellers. Further simulations such as two-phase modeling (as well as experimental validation) will help in the future in determining more accurately the internal dynamics of the bioreactor.

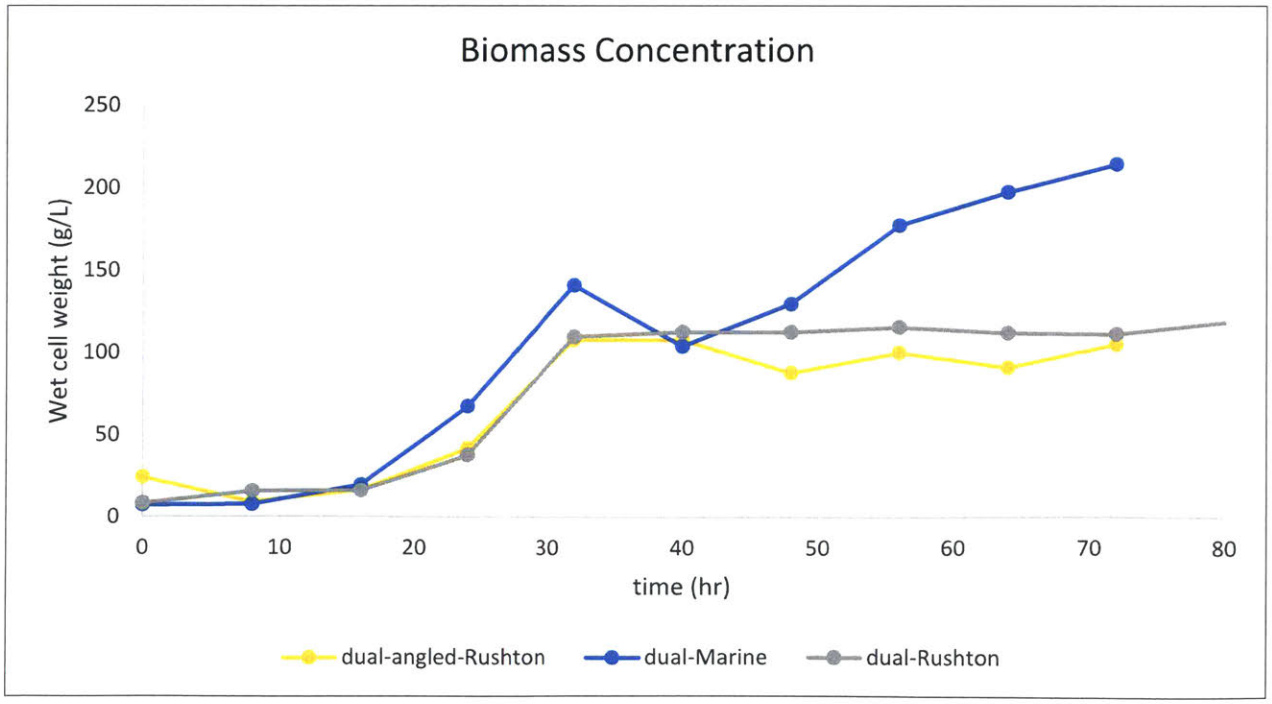


***Figure 2-11* Biomass Concentration in Impeller Study** Wet cell weight by hour since start of inoculation; induction at 32 hours (Image Credit: Team InSCyT)

Future rounds of testing plan to mix-and-match impeller types to determine whether the optimal configuration is hybrid. Further, different protein products may be more conductive to production in different configurations. Multiple levels of testing will determine the effects of the impeller configuration on cell growth and product yield, and the design of experiments for such testing is extensive, and in the process of being conducted.

### 2.3.3 Flow analysis in 5.0 L bioreactor

Future plans to switch to protein production in a larger, 5-liter vessel motivated this flow analysis. The objective of this study was:

(1) Develop a CFD model for easy future iterations and analysis
(2) Study the flow profiles of the proposed 5-liter bioreactor
(3) Enable downstream 2D simulation analysis to study any part of the bioreactor microscopically, such as shear and stagnation characteristics around the perfusion probe (Chapter 4)

#### 2.3.3.1 Design

Designing an impeller configuration was the first step of the future model. The study hopes to create a base model upon which iteration and optimization can be conducted. Thus, for a base design, traditional design recommendations for bioreactors from the literature are followed. The diameter of the impellers was chosen to be one-third the diameter of the vessel, as recommended in the literature [44] [39]. This value is an impeller diameter of 50 mm in this case, as the vessel diameter is 150 mm.

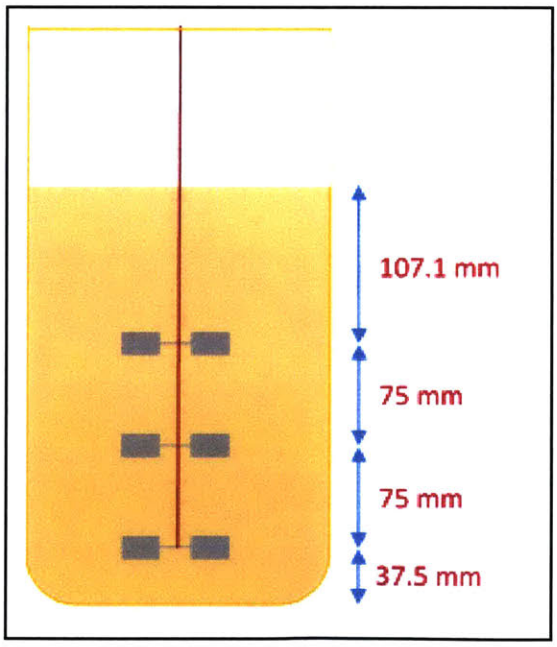


***Figure 2-12* Impeller Spacing in 5-liter Vessel**
Design of impeller spacing for initial iteration

To produce a flow pattern that promoted the "parallel flow" pattern from Rutherford's study [44] as a starting point for a design, the space between the bottom of the vessel and the lowest impeller should be a 0.25T, the spacing between the impellers should be 0.5T, and the submerged depth of the top impeller should be at least 0.25T, where T is the vessel diameter. The height of the fluid is 294.6 mm. Thus, a three-impeller system was chosen, with the space between the bottom of the vessel and the bottom (first) impeller L1 = 37.5 mm, the space between the first and second impellers L2 = 75 mm, the space between the second and third impellers

$L_3$ = 75 mm, and the submerge distance of the top (third) impeller C = 107.1 mm (Figure 2-12). The minimum recommended submergence distance was 0.25T = 37.5 mm, but a higher distance was chosen because a fourth impeller would not leave sufficient submergence distance at the top, and additionally, the possibility of vortex formation had to be considered, and a higher clearance allows for non-interference between the vortex and the highest impeller.

Rushton impellers were chosen as they are the most commonly used impellers in the biotechnology field, and thus can provide good data as an initial design, coupled with the fact they were used to produce the "parallel flow" pattern from Rutherford's study [44]. For similar reasons, a 6-blade design was chosen as opposed to also commercially offered 8-blade designs. Another reason for avoiding an 8-bladed design was to decrease the chance of flooding that can be caused by trailing vortices being as long as the spacing between the blades, and the adherence of large bubbles creating air gaps between the blades.

Baffles are often used in bioreactor to promote better mixing by breaking up a "solid-body rotation" movement of the fluid. However, with the number of functional probes immersed in the vessel, the use of baffles was deemed redundant.

### 2.3.3.2 Geometry

The geometry of the bioreactor used in the simulation mimics the scaled-up concept of the 5-liter vessel set for development for use in the lab, adapting the design of the impeller shaft from the previous section (Figure 2-13). The only notable difference was the change from the actual hollow-fibers to a cylinder that would have enclosed all the fibers if they were present. This is only done in the 3D simulation, and is a valid assumption in solving bulk flow profiles, as multiple fibers arranged cylindrically have the same bulk flow pattern as flow around a cylinder. This is later validated in the 2D analysis. The geometry was modeled in SolidWorks and exported to ANSYS Design Modeller. An area enclosing the three impeller shafts was defined as the *Rotating Fluid Region*, while the rest of the bioreactor was defined as the *Fixed Fluid Region*. This was done so as to use the Multiple Reference Frame model in simulating the 3D solution, as is commonly done in the literature [25] [26] [27] [28]. The top surface of the bioreactor was defined separately as a named selection called *Static Free Surface*, so as to assign it different boundary properties.

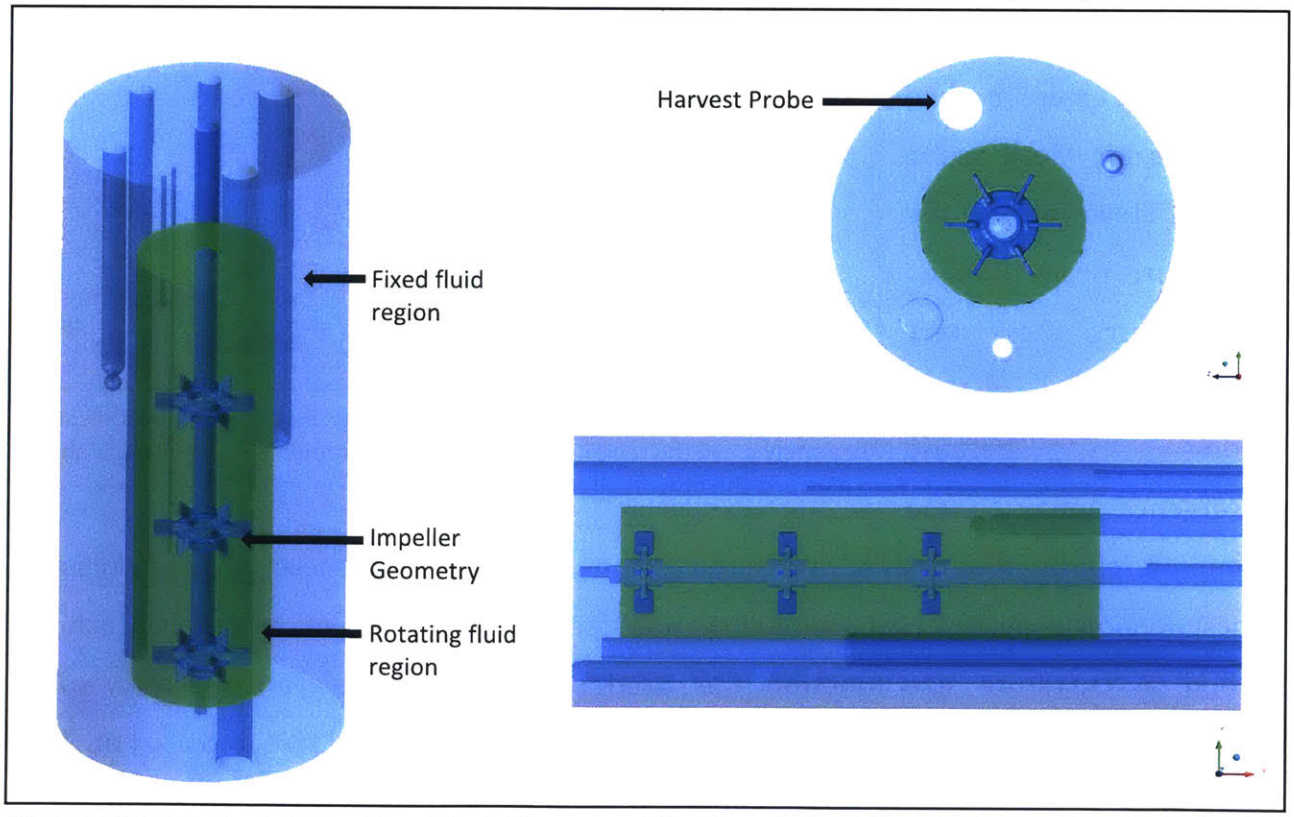


***Figure 2-13* Geometry in 5-liter Vessel Study** Geometry of the bioreactor with the rotating region shown in green

### 2.3.3.3 Mesh

The mesh was divided into 3 regions – the impellers blades, the probes/shafts, and the bulk (rest of the geometry). Region 1 (impeller blades) was meshed using the Mesh Sizing option. It consisted of 735 faces (highlighted in blue in Figure 2-114) soft meshed with an element size of 2 e-03 m and a minimum size of 1 e-03 m. Region 2 (probes and shafts) was also meshed using the Mesh Sizing option. It consisted of 24 faces (highlighted yellow in Figure 2-14) soft meshed with an element size of 2 e-03 m and a minimum size of 1 e-03 m. In this case, both Region 1 and 2 were meshed with the same Mesh Sizing options. However, to aid with future projects using this geometry, there were separated into distinct regions because convergence may often depend on refining the mesh of one of the regions, depending on where the gradients are highest. Region 3 (the rest of the geometry) was sized using the Cut Cell Assembly Meshing Method. A curvature size function was used, with medium relevance center, high smoothing, a minimum size of 1 e-03 m, and a maximum tetrahedral size of 8 e-03 m. The overall mesh of the geometry resulted in 567,764 nodes, and 506,233 elements. The total

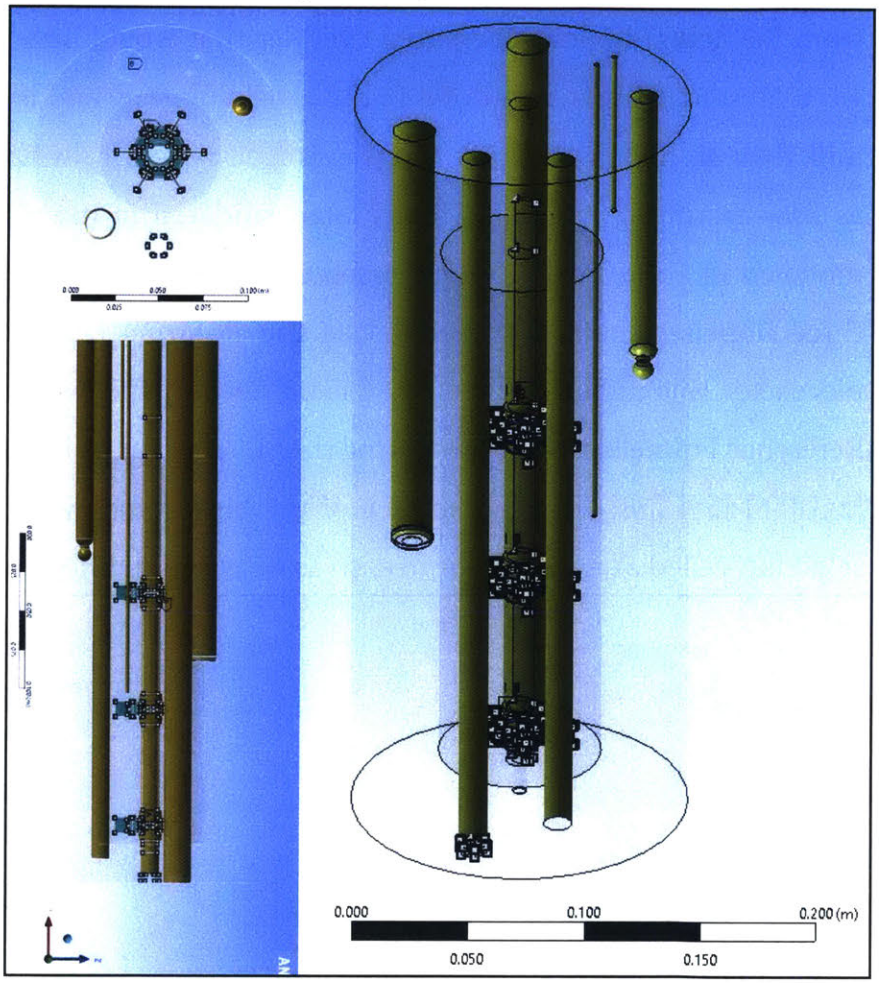


***Figure 2-14*** **Mesh Sizing in the 5-liter Vessel Study** Sizing was used to separately mesh the regions of expected sharp gradients – one group is shown in blue and the other is shown in yellow

mesh can be seen in Figure 2-15, including with some section cuts to show the internal meshing.

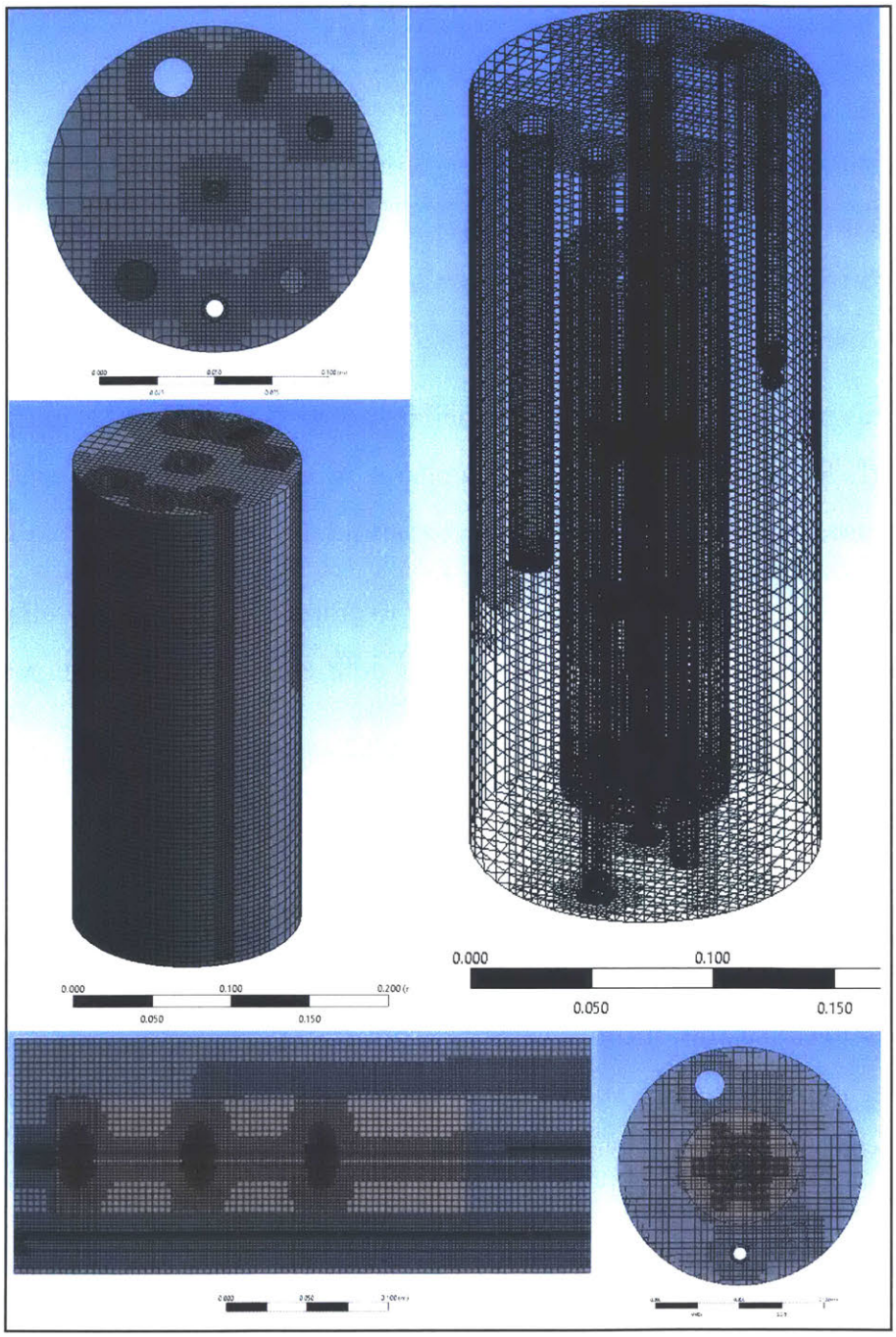


***Figure 2-15* Mesh in the 5-liter Vessel Study** The entire mesh is shown in the top three images. The bottom two images are cross-sections of the mesh to display the interior meshing.

### 2.3.3.4 Solver Setup

The mesh was then imported into the ANSYS Fluent Solver. For a stirred tank, the Reynolds number is defined as:

$$Re = \frac{\rho N D^2}{\mu}$$

where ρ is the density of the fluid, N is the agitator speed, D is the impeller diameter, and μis the dynamic viscosity of the fluid [32]. For stirred bioreactors, the laminar region is generally considered when Re < 10, whereas the start of the turbulence region has wide variance in the literature, from Re > 480 [33] to Re > 1200 [34].

The Reynolds number for the slowest impeller speed case (300 rpm) is in the fully turbulent regime, with Re = 14,000. Thus, the k-epsilon model was used for the Viscous Model, commonly used in this regime for bioreactor simulations [32] [37] [28] [25] [38].

The *Rotating Fluid Region* and the *Fixed Fluid Region* were defined as walls with a "No Slip" condition, whereas the *Static Free Surface* was defined as a wall with zero-shear conditions to properly simulate the boundary constraints within the working of the MRF model. Although the harvest probe (hollow-fibers) is actually pulling protein product and therefore have minor mass and velocity flow associated with it, it is modeled as a wall. This is because the outflow velocity from the fibers is negligibly slow (on the order of $10^5$ to $10^7$ times slower than the velocities around the impellers) at typical operating conditions to not affect the bulk flow profile of the bioreactor. Within the cell zones, the rotational zone was set to the desired rpm (based on the impeller speeds being simulated), whereas the other zones were set to having no frame motion. This properly enables the MRF model to simulate impeller rotation within the vessel. The fluid in all zones was set to water at

| | |
|---|---|
| Pressure | 0.3 |
| Density | 1 |
| Body Forces | 1 |
| Momentum | 0.1 |
| Turbulent Kinetic Energy | 0.1 |
| Turbulent Dissipation Rate | 0.1 |
| Turbulent Viscosity | 1 |

***Table 2-3* Under-relaxation Factors in the 5-liter Vessel Study Simulation**

standard temperature and pressure (STP) conditions, which has properties that are fairly similar to the fluid mix within the bioreactor.

The SIMPLE pressure-velocity coupling solver was used, with a Least Squares Cell Based gradient, second order pressure and momentum equations, and first order turbulent equations. The under-relaxation factors to achieve convergence are shown in Table 2-2. A Standard Initialization was used with default settings, and the solution was accepted as having converged when all the residuals were below 10 e-04.

### 2.3.3.5 Results and Discussion

The pressure profiles of the appartus at the different impeller speeds are show in Figure 2-16. A slice of the vessel at a height of 0.184 m was the plane used to view the pressure profile, as this As can be seen, there is a clear presence of high-pressure leading edges and low-pressure lagging edges.

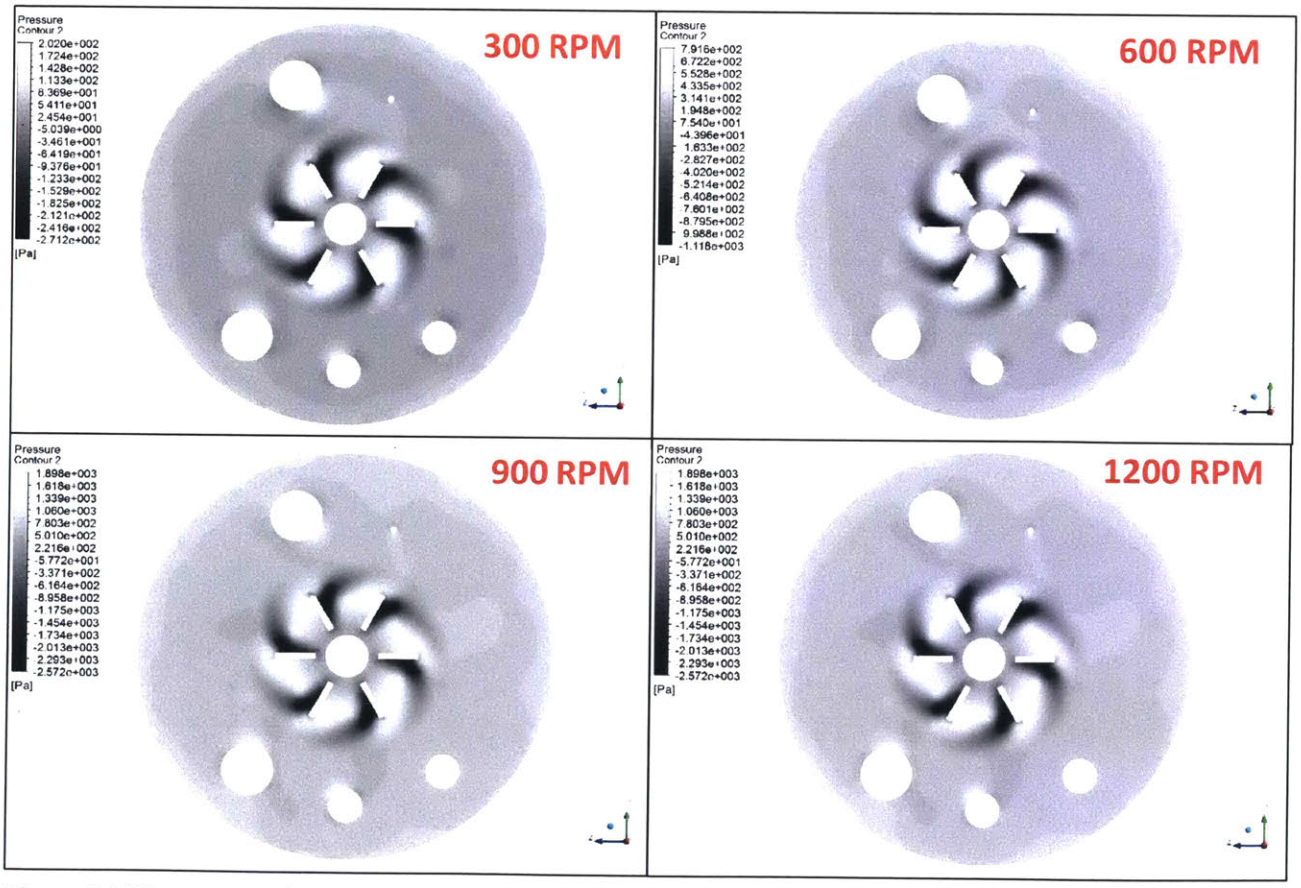


***Figure 2-16*** **Pressure Profiles in the 5-liter Vessel Study** Static pressure slice at a height of 0.184 m in the vessel (at the impeller height) shows the high-pressure leading edges and low-pressure lagging edges

Figure 2-17 shows the flow profiles of the bioreactor at the different impeller speeds, with flow vectors. The flow velocity contour scale is localized to each case, thus this figure informs the flow patterns seen in the bioreactor. Although the velocity magnitudes are different, the emergence of the "parallel flow" demonstrated experimentally and computationally by Rutherford et al [44] is evident at all four impeller speeds tested. Thus, the empirical evidence in the literature is used to validate the qualitative resutls. However, future work should to further this study should conduct experimental testing in the form of laser-doppler anemometry (LDA) or particle image velocimetry (PIV) to validate the computational results as well. Figure 2-18 depicts the four impeller speeds on the same scale, for comparison of velocities induced in the bioreactor.

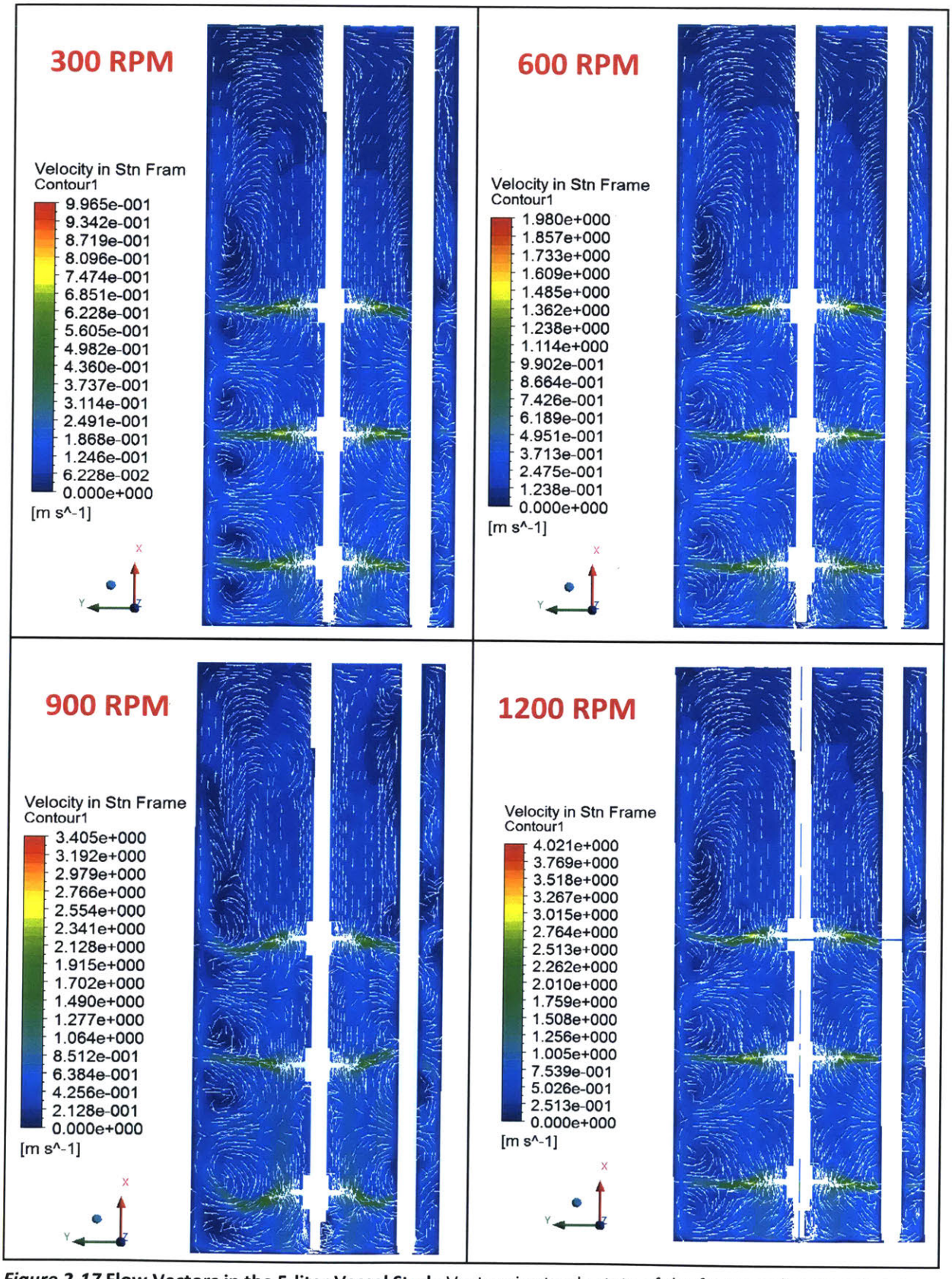


***Figure 2-17* Flow Vectors in the 5-liter Vessel Study** Vectors in steady state of the four impeller speeds, seen in the vertical plane, with velocity vectors. The "parallel flow" pattern is evident at all speeds, although the velocities are notably different.

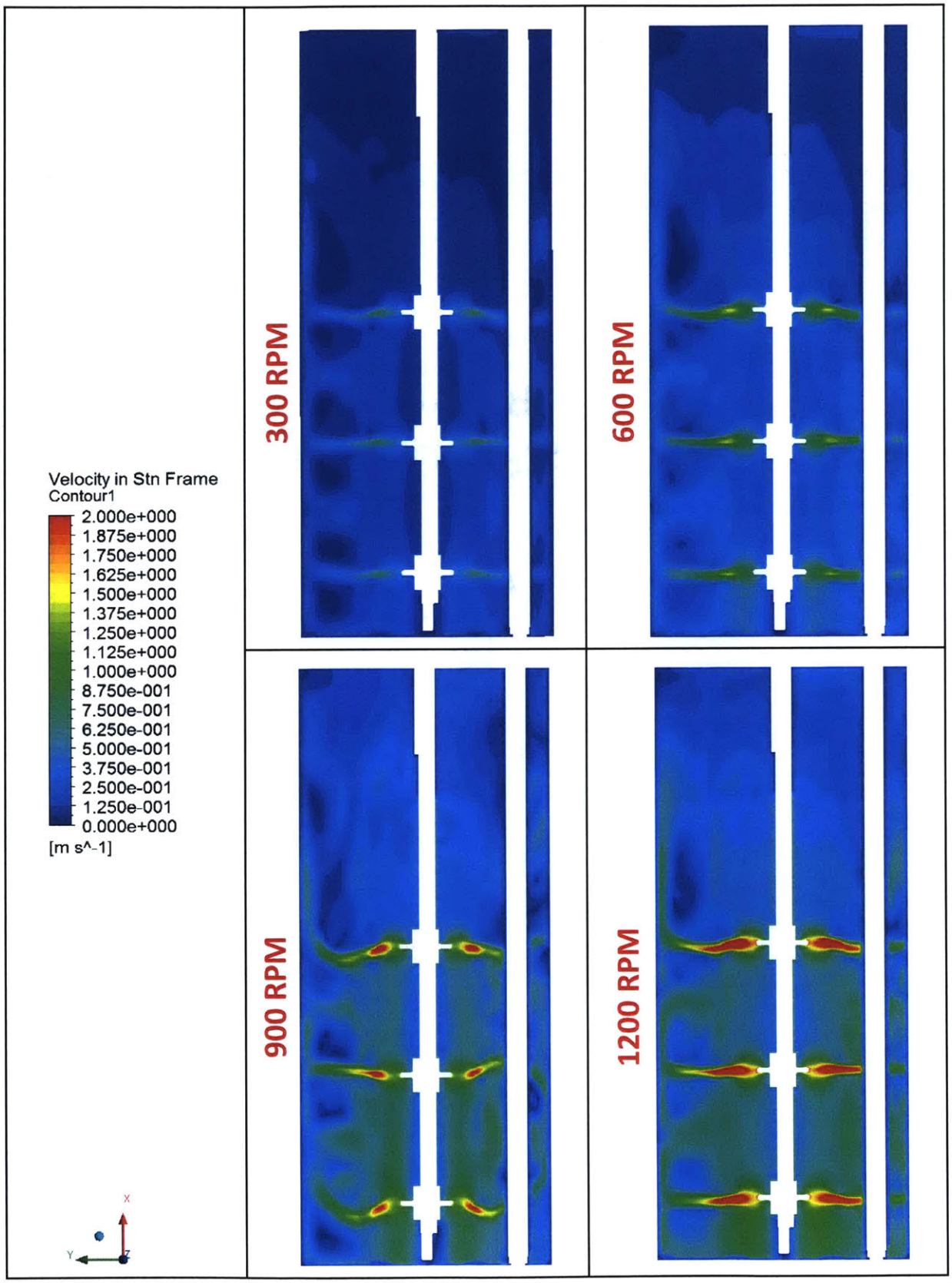


***Figure 2-18* Velocity Profiles in the 5-liter Vessel Study** Flow profiles steady state of the four impeller speeds to a normalized scale, seen in the vertical plane. The difference in induced velocities is evident here.

Exporting the results from the simulation predicting the velocity flow field in the bioreactor, the radial, axial, and the tangential flow velocities, as well as the overall velocities, are shown as either a function of radial or axial distance, at specific axial or radial planes. Apart from the absolute values, the normalized dimensionless values are also plotted so as to be consistent with the style of similar studies in the literature [44] [29] [53] [54] [33]. The absolute value are normalized against the impeller tip speeds, shown in Table 2-2. Further, different literature studies are used to compare the results against, since no single study was found that published all radial, tangential, axial, and overall velocity profiles for a Rushton stirred-tank, leading to the need to use multiple studies.

| Rotation Speed (RPM) | $V_{tip}$ (m/s) |
|---|---|
| 300 | 2.58 |
| 600 | 5.15 |
| 900 | 7.73 |
| 1200 | 10.30 |

***Table 2-4*** **Impeller Tip Speeds vs RPM for the 5-liter Vessel Study**

The overall velocity as a function of distance from the agitation shaft is depicted in Figure 2-19, at a height of 0.187 m from the bottom of the vessel[4], which coincides with the topmost impeller. It can be seen that the velocity (for the height in-line with the top impeller) starts of low, peaks early near the impeller blades, and then gradually decreases towards the outer edges of the vessel. This profile is very consistent with the Rushton computational and experimental data in Ng et al (Figure 2-20), also measured in line with the impeller [53]. This helps validate the overall results, and additionally, offers some insight into the flow characteristics. The velocity as a function of axial distance is shown in Appendix B, at a distance of 0.03 m radially away from the center shaft.

[4] For a radial distance of 0.01 m away from the centre, a height of 0.184 m was used (slightly lower), as the solid impeller was present at 0.187 m, thus giving no fluid velocity results

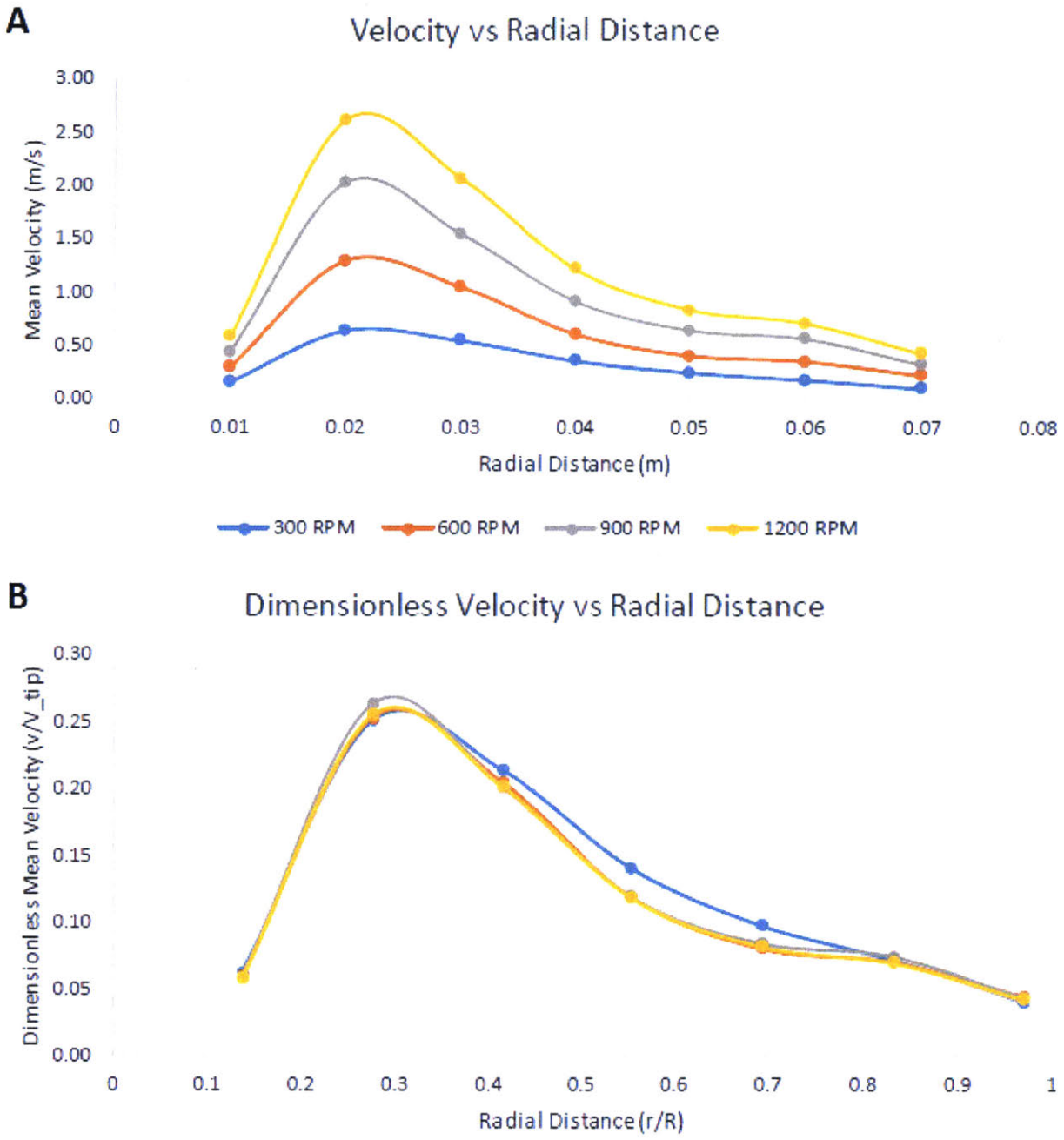


***Figure 2-19*** **Velocity vs Radial Distance in the 5-liter Vessel Study** (A) Absolute and (B) Dimensionless mean velocity as a function of radial distance from the center of the of vessel for each rotational speed, at a height of 0.187 m from the bottom of the vessel

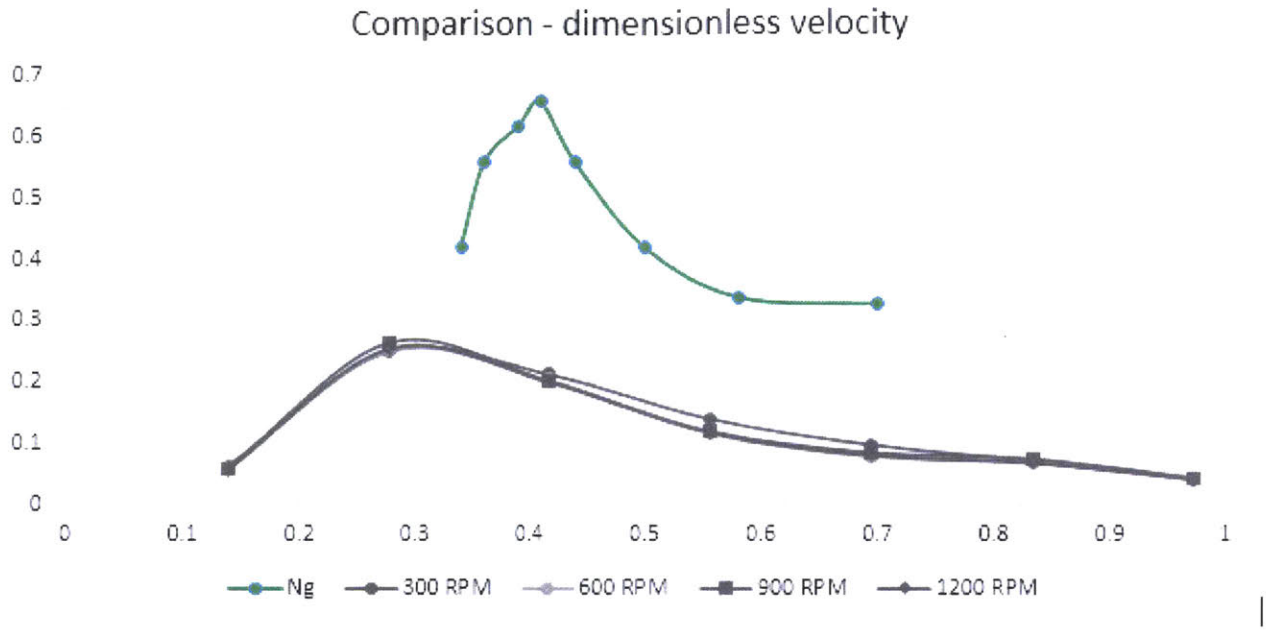


***Figure 2-20*** **Experimental Comparison of Velocity in the 5-liter Vessel Study** Comparison to experimental data by Ng et al who probed velocity data at the in-line with the impeller

Similarly, the radial velocity as a function of radial distance is depicted at a height of 0.177 m in absolute and dimensionless form (Figure 2-21). The height of 0.177 m was chosen to match the probe location of the Zadghaffari study [54], which probed at a height of $\Delta z = -1.18*b$ away from the centerline of the top impeller, where b is the blade height.

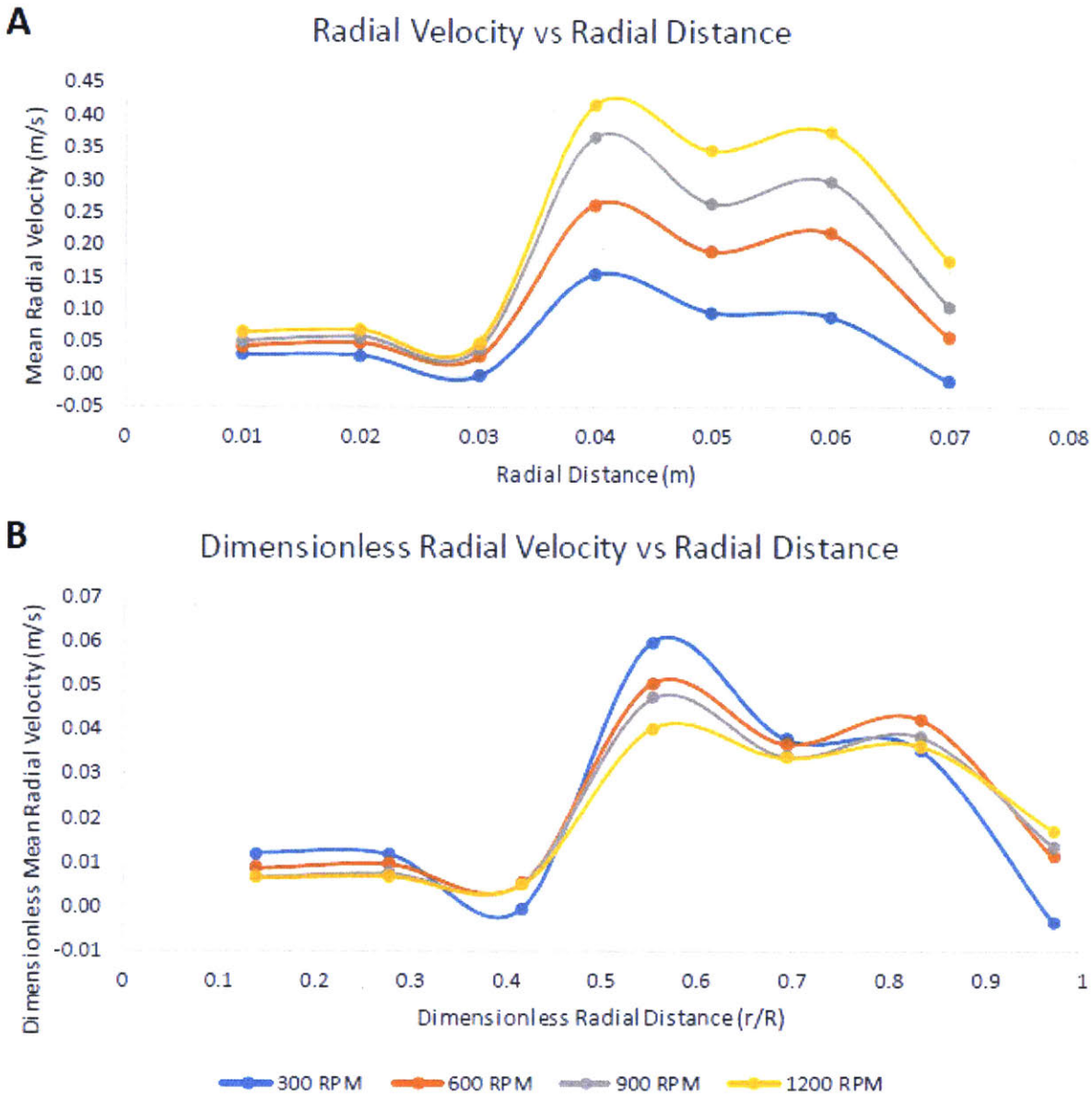


***Figure 2-21* Radial Velocity vs Radial Distance in the 5-liter Vessel Study** (A) Absolute and (B) Dimensionless Mean radial velocity as a function of radial distance from the center of the vessel for each rotational speed at a height of 0.187 m

This radial velocity profile is in good agreement with that of the top-impeller (at the same location probe) of the Zadghaffari study [54]. The study was a computational simulation comparison to experimental results, which had good agreement with each other. The experimental values from their study are shown compared to the numerical results here (Figure 2-22).

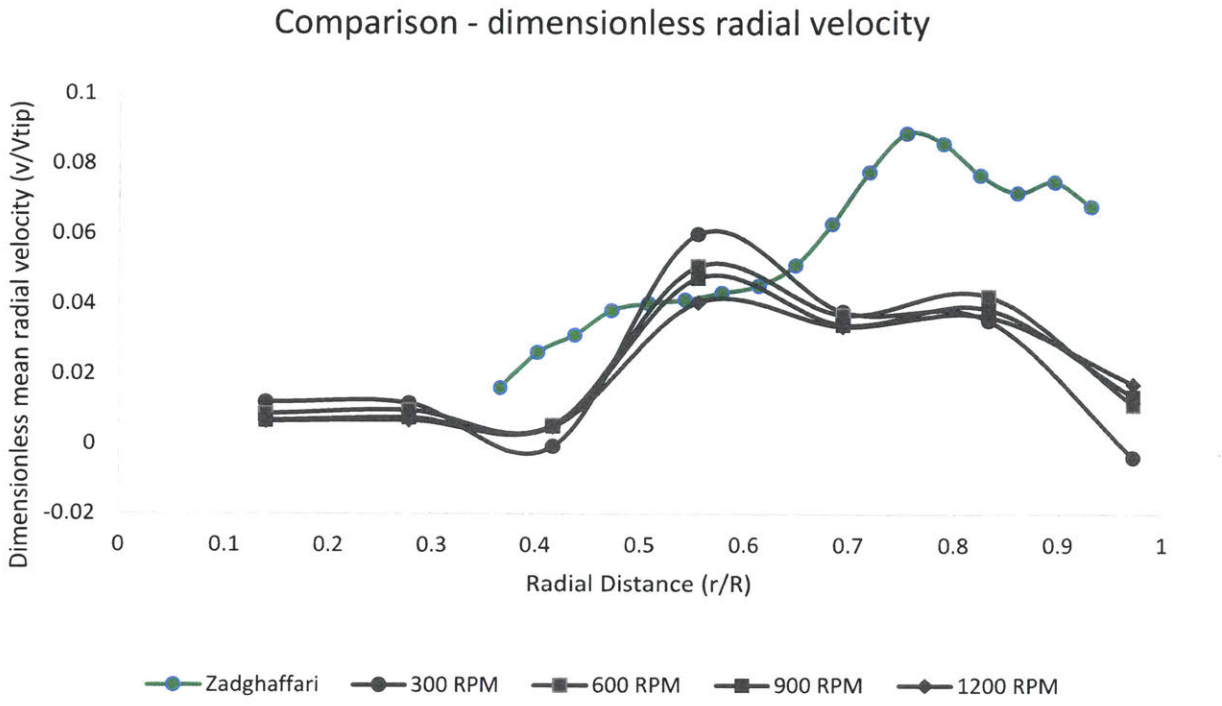


***Figure 2-22*** **Experimental Comparison of Radial Velocity in the 5-liter Vessel Study** Comparison to experimental data by Zadghaffari et al who probed radial velocity data at the same location ($\Delta z$ = -1.18*blade-height, where $\Delta z$ is the distance from the centerline of the top impeller)

Noticably, two distinct peaks are formed, a larger initial one followed by a smaller secondary one. However, the location of the peaks are slightly transposed across studies, potentially due to the inclusion of probes within the vessel that are excluded in the Zadghaffari study. A similar double peak is seen in the radial velocity profile of the study conducted by Yu et al [32]. However, they use different agitators, and the location of the probe is unknown.

The dimensionless axial velocity profiles are shown as a function of distance from the agitator shaft (center of the vessel) in Figure 2-23. The two heights were at a distance of 0.180 m, and 0.194 m from the bottom of the vessel, so as to be just below and just above the top impeller by a distance of 7 mm each. The reason this distance was chosen was because the separation of heights probed is 14 mm, giving a $\Delta z/d = 0.27$ (z is the distance from the impeller centerline to the probe location, and $d$ is the diameter of the impeller), which is what is used in a simulation by Kaiser et al [29]. However, their data is probed next to the top impeller, which is an "elephant ear" impeller, unlike the Rushton setup here.

No axial velocity study for Rushton impellers was found. The normalized velocities are shown in Figure 2-23, and the absolute values are shown in Appendix B.

The axial velocities have a distinctly symmetrical shape above and below the impeller, as it draws fluid towards it near the blades. This is similar to the dual-Rushton configuration

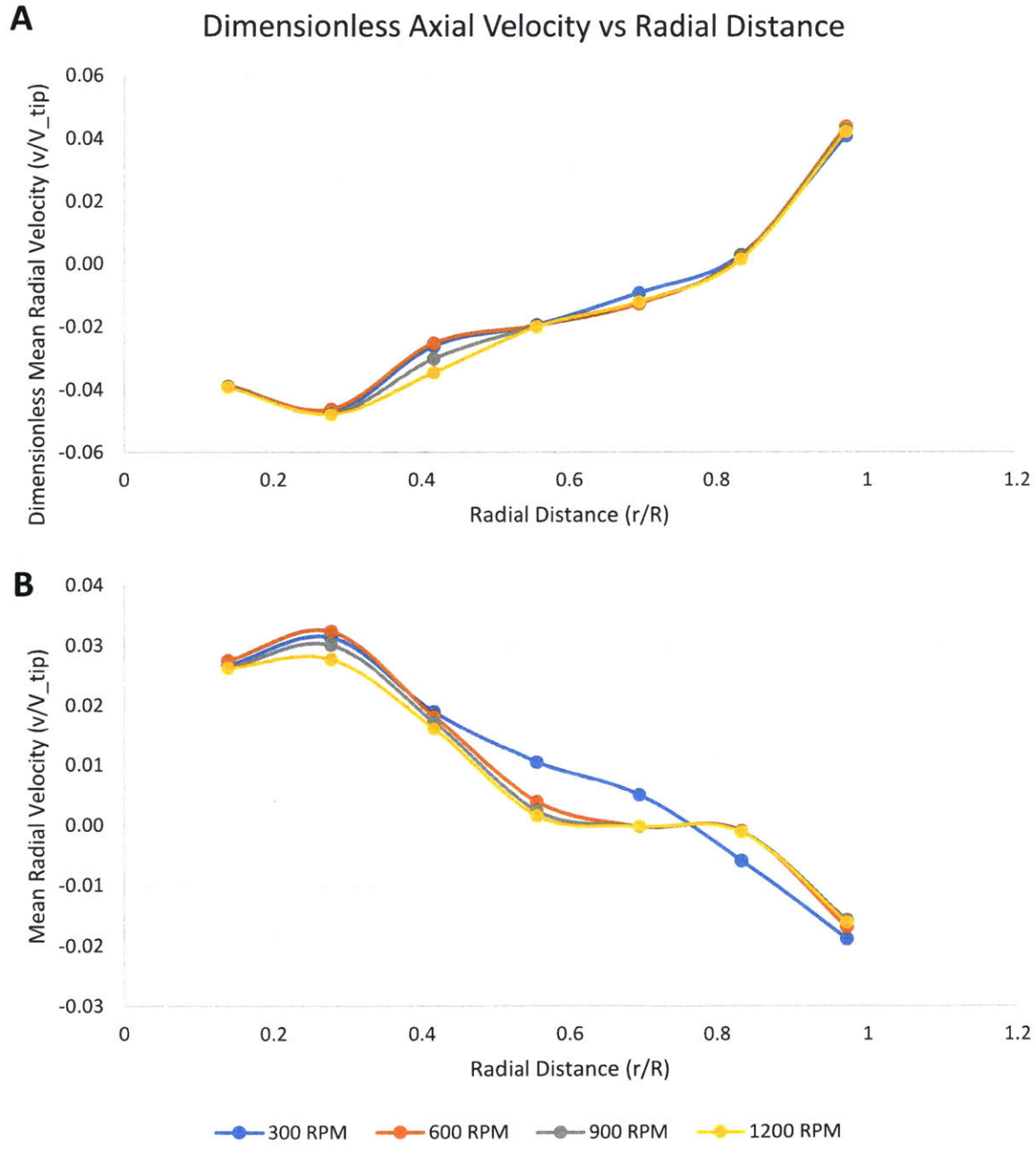


***Figure 2-23*** **Axial Velocity vs Radial Distance in the 5-liter Vessel Study** Dimensionless mean axial velocity as a function of radial distance from the centerline, at a height of (A) 7 mm above and (B) 7 mm below the top impeller

studied in the first part. The elephant ear impeller used by Kaiser et al is a downward pumping impeller, with the axial velocities negative near the impeller (above and below) [29].

The tangential (absolute and dimensionless) velocity profiles as a function of radial distance at the height of 0.0318 m is shown in Appendix B.

Overall, although consistency with the empirical and computational data in the literature is evident, future continuation of this work would ensure that these results were validated experimentally so as to appropriately complete the study. Particle image velocimetry (PIV) and laser-doppler anemometry (LDA) techniques can be used as done for bioreactors in the literature [44] [54] [53].

## 2.3.4 Other Work and Future Analysis

In order to aid future studies and two-phase modeling, another study that was conducted is detailed here. Using a bioreactor geometry that was previously used in protein production in the lab, a pilot CFD study was conducted. The geometry and mesh are shown in Figure 2-24. The velocity profiles at three impeller speeds (300, 600, and 1000 RPM) are shown in Figure 2-25.

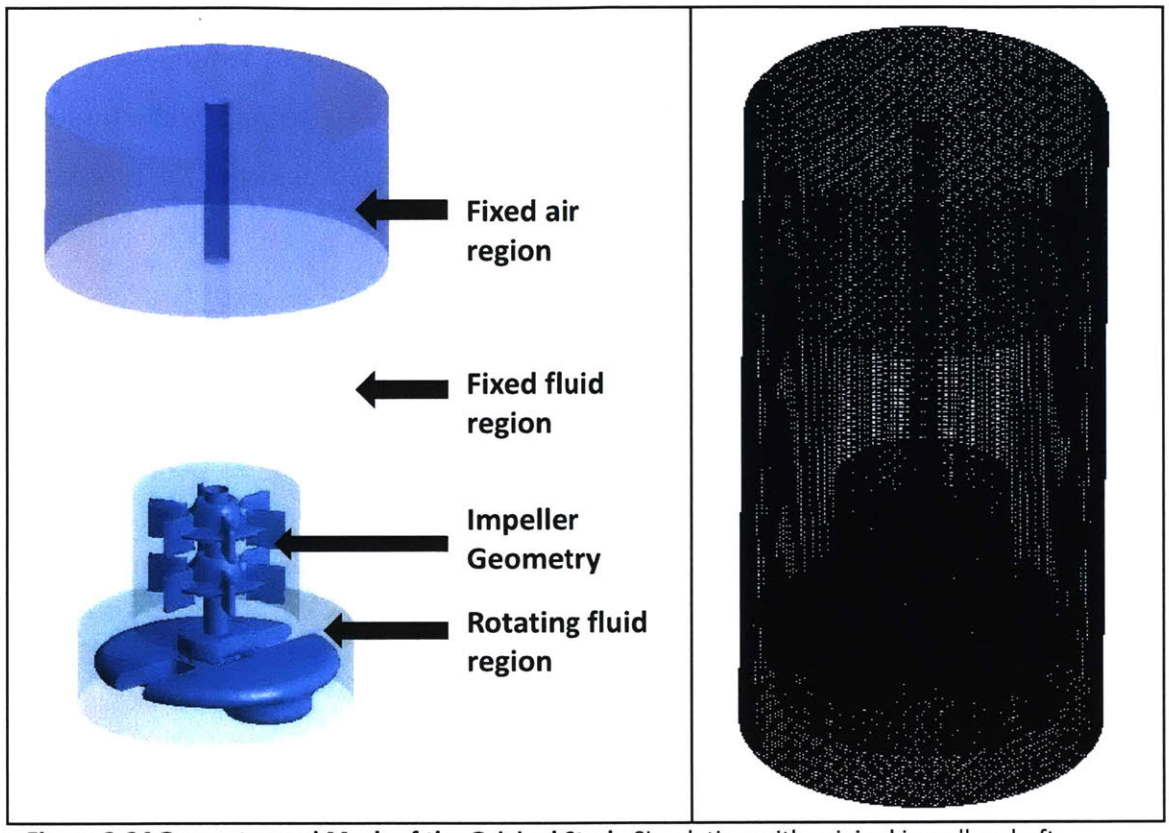


***Figure 2-24* Geometry and Mesh of the Original Study** Simulation with original impeller shaft

To achieve further understanding of the mass transfer environment, Amos Lu (Braatz Lab, MIT) conducted a multiphase CFD simulation with population balance models (PBM) that enabled the prediction of the mean Sauter diameter in the bioreactor (Figure 2-26), the dissolved oxygen (Figure 2-27), and ultimately the localized mass transfer coefficient ($k_La$) in the bioreactor (Figure 2-28), depicted for the simulation conducted at 800 RPM [58]. These are the recommended types of studies that can be done as a secondary step beyond the work in this chapter.

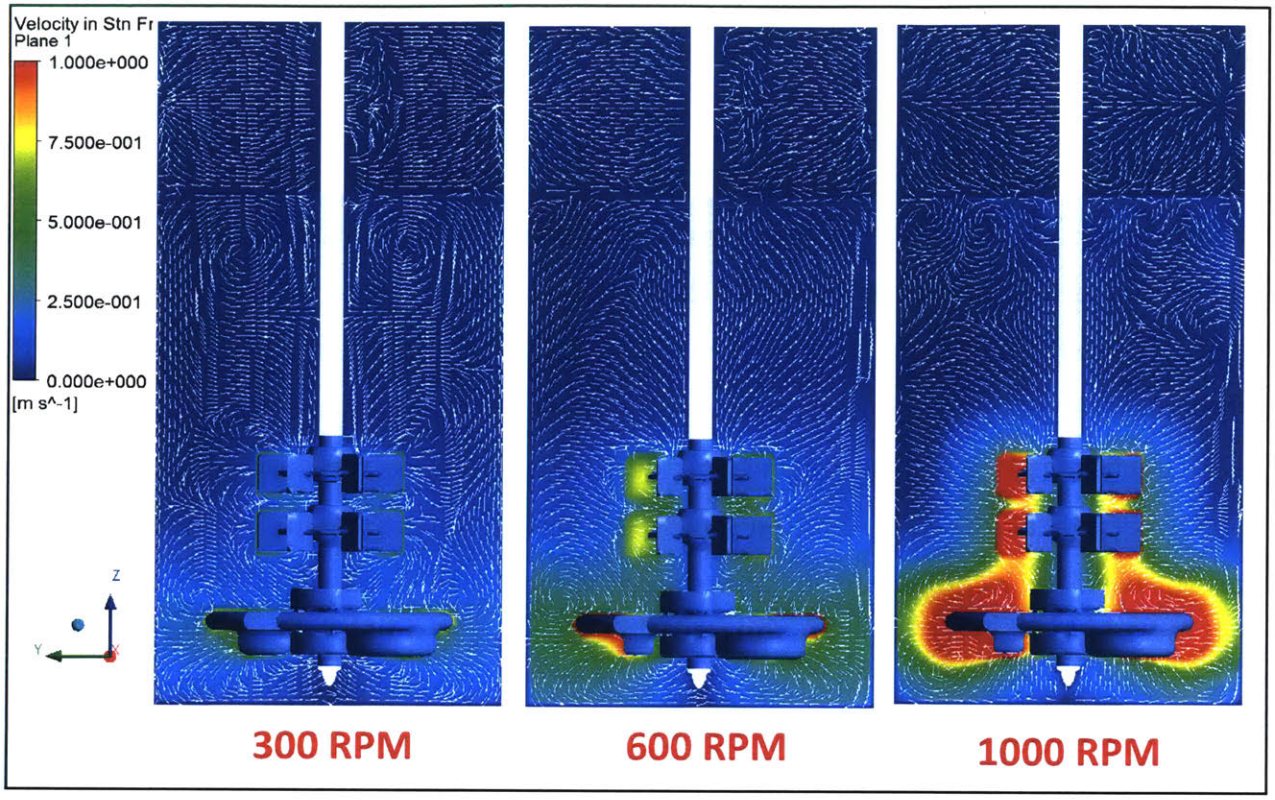


***Figure 2-25* Velocity Profiles of the Original Study** at three impeller speeds on the same velocity scale

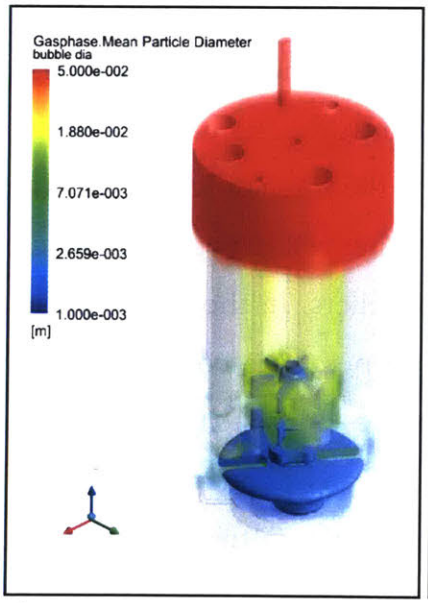


***Figure 2-26* Mean Sauter Diameter Profile** in the bioreactor at 800 RPM (Amos Lu) [58]

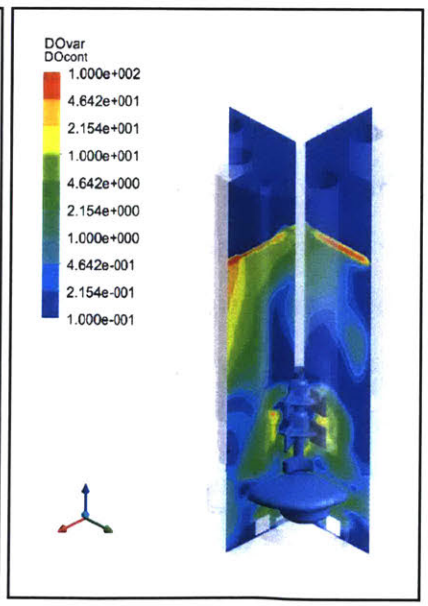


***Figure 2-27* Dissolved Oxygen Profile** in the bioreactor at 800 RPM (Amos Lu) [58]

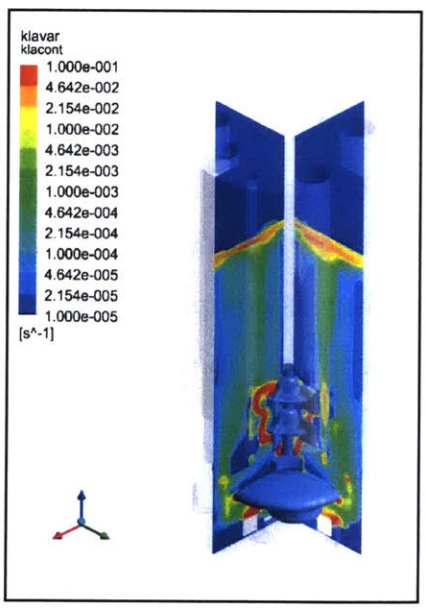


***Figure 2-28* $k_La$ Profile** in the bioreactor at 800 RPM (Amos Lu) [58]

The future work recommended after this study includes computational and experimental paths. Computationally, the study of different kinds of impeller configurations in the 5-liter vessel can be carried out. Further, for both sizes of vessels, more advanced fluid dynamic studies that involve two-phase modeling and bubble population modeling will allow for studies that can characterize the volumetric mass transfer coefficient in different bioreactors, as well as gas holdup and other important parameters. All the data simulated computationally, here and in future work, should be validated experimentally with different methods such as particle image velocimetry (PIV) and laser-doppler anemometry (LDA) for flow patterns, colorimetric mixing time studies, $k_la$ measurements, as well as biopharmaceutical drug production under controlled environments to measure how different bioreactor configurations affect product yield, cell density, etc. in real empirical data.

## 2.4 Conclusions

Mixing and mass transfer studies conducted through computational simulations provided insights into the flow profiles of the 1-liter and 5-liter bioreactors. A comparison between impeller configurations showed good agreement with the simulations and expected flow profiles from the literature. The Marine impeller configuration was shown to have higher axial velocity, which may be responsible for better mixing due to the high axial distance without an impeller in the 1-liter bioreactor. Experiments using the three different impeller configurations showed the Marine configuration to promote higher cell growth and protein product as compared to the Rushton and angled-Rushton impellers. In the 5-liter vessel, the computational simulations depicted a parallel flow pattern that is consistent with literature, with further agreement upon probing the velocities in specific directions. Additional multiphase modeling and bubble dynamics modeling can be conducted to more accurately predict the flow characteristics in future design iterations. Future work should also ensure these results are validated with experimental techniques.

# Chapter III
# Bioreactor Process Sensing

# Abstract

Bioprocess monitoring is an essential part of continuous drug production runs in bioreactors. Various process parameters such as temperature, pH, cell concentration, and liquid level, among others, need to be sensed in order to control the production process. In the design of a disposable, continuous, perfusion-based bioreactor, the sensors are required to be either disposable themselves, or non-invasive and placed outside the vessel.

Multiple liquid level sensing solutions were conceptualized for bioreactors. From these, three optical methods and one magnetic method were designed, prototyped, and tested. For all the optical methods, image processing algorithms were developed in order to recognize the object of interest based on color and size. A camera hooked up to a computer monitors the bioreactor on-line, runs the algorithms, and predicts the liquid level. The first optical method is discrete, and uses different colored bands painted along the agitator shaft, where the bands visible above the liquid surface are seen by the camera. The second optical method is continuous, and uses a colored float that moves with the level, where the liquid level is predicted by determining the location of the float. The third optical method is also continuous, and involves a painted agitator shaft, where the amount of colored shaft visible (above the liquid surface) is used to predict the liquid level. Finally, the magnetic level sensor relies on a magnetic float near the vessel wall on the inside, that rises and falls with liquid level. Externally, a series of reed switches are activated based on proximity to the float, and can thus be correlated to the liquid level. All four designs were prototyped and successfully tested. Future work will aim to further characterize these sensors by measuring their performance through varying light conditions and liquid optical densities.

Recommendations for other bioprocess sensing, such as pH, temperature, cell concentration, and dissolved oxygen monitoring, was also made. All solutions mentioned were either disposable or non-invasive, in keeping with the overall design of the bioreactor.

# Part I
# Liquid Level Sensing

# 3.1 Initial Liquid Level Sensing Designs

## 3.1.1 Introduction

Liquid level sensing is essential for process control in a continuous-perfusion bioreactor. For the single-use scenario, there are a number of factors to be considered. Although the research and designs explores options for single-use bioreactors, this does not limit the level sensor to be disposable. The distinction is simple – anything inside the sterile disposable vessel should be disposable as well, whereas external options can be reused (due to lack of the requirement of sterility) and can be thus be more expensive. Further considerations include the nature of sensing – discrete vs continuous, and relating that to what degree of control is required for process control. Similarly, whether the design invasive or external to the process, which will largely affect price as well, is to be considered, along with whether it has a disruptive impact on the rest of the design of the bioreactor. Reliability and accuracy is of course a major factor, and to some sense is affected by whether the level sensor is hard-sensing or soft-sensing (directly reading level, or dependent on other properties).

Two major complications related to sensing liquid levels in bioreactors are the surface and fluid agitation, as well as the change in liquid properties (such as ionic conductivity and density) with time. These render simpler level sensing methods unusable in this scenario.

### Density-Compensation

Some of the methods outlined below will require the use of some density-compensation method. For example, since the density of the fluid changes with time, it causes complications in some of the methods. There are a few ways to conduct density-compensation externally, but it has to be noted that this would add complexity and potentially additional equipment and cost. Furthermore, some methods require coupling with other sensing that is being conducted, for it to work. The density compensation methods themselves are note explored here.

### 3.1.2 Theoretical First-Order Designed Solutions

Nine different approaches to sensing level are outlined below, with simplified schematics. Some of these designs have been used in industry, whereas some were conceptualized specially for the project. Their characteristics differ based on being discrete or continuous designs, hard or soft-sensing, invasive or non-invasive designs, and designs that have a major "ripple effect" on the rest of the bioreactor design, and some that have none at all. Discrete level sensing is used to measure a single-point or a few points of liquid level, and can either be used for point-level applications, or to know the liquid level within range but without knowing the exact level. Continuous level sensing would predict the exact liquid level throughout the range of the vessel. Hard sensing refers to leveraging the actual position of the liquid level in order to make the prediction, whereas soft sensing relies on secondary parameters. Invasive designs include solutions that sense level by using equipment that is placed in the vessel from the outside, whereas non-invasive sensing predicts level either completely from the outside, or by using parts that are pre-placed internal to the vessel, and do not breach the vessel. The ripple effect of the design refers to how much modification is required to be made to the rest of the bioreactor design in order to accommodate the level sensing technology. The optimal design will be continuous, non-invasive, have minimal ripple effect, and be inexpensive.

The designs presented in order: Capacitive Level Sensor, Colored Float Sensor, Magnetic Sensor, Optical Density Absorbance Differential Sensor, Load Cell, Force Transducer, Time of Flight Methods, Painted Band Method, Colored Shaft Method.

### Capacitive Liquid Level Sensor

Traditional capacitive level sensing methods fail due to change in ionic conductivity of solution changing the dielectric constant. The capacitive level sensor – which usually changes voltage output value with level – also changes value due to change in constant. In this design, a reference sensor that is always below level can be used to continuously correct for the changing constant. Another sensor can then accurately output level after being corrected for change in constant. This method is continuous, soft-sensing, non-invasive, with no ripple effect, and inexpensive.

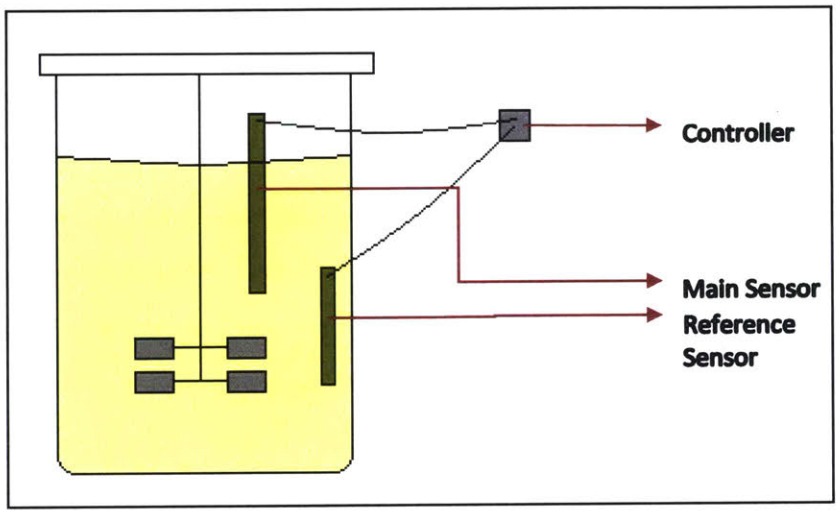


*Figure 3-4* **Capacitive Liquid Level Sensor Schematic**

### Colored Float Sensor

In this design, a colored float rises and falls with level. The annular float is a different color from the liquid and is around an existing probe. A camera embedded into the head plate from above is hooked up to a computer/controller. Live-time chrominance filtering and binarization can be done to detect the presence and coordinates of the red pixels, which can be correlated to liquid level. The float will be disposable and cheap. This method is continuous, hard-sensing, non-invasive, with minimal ripple effect, and inexpensive.

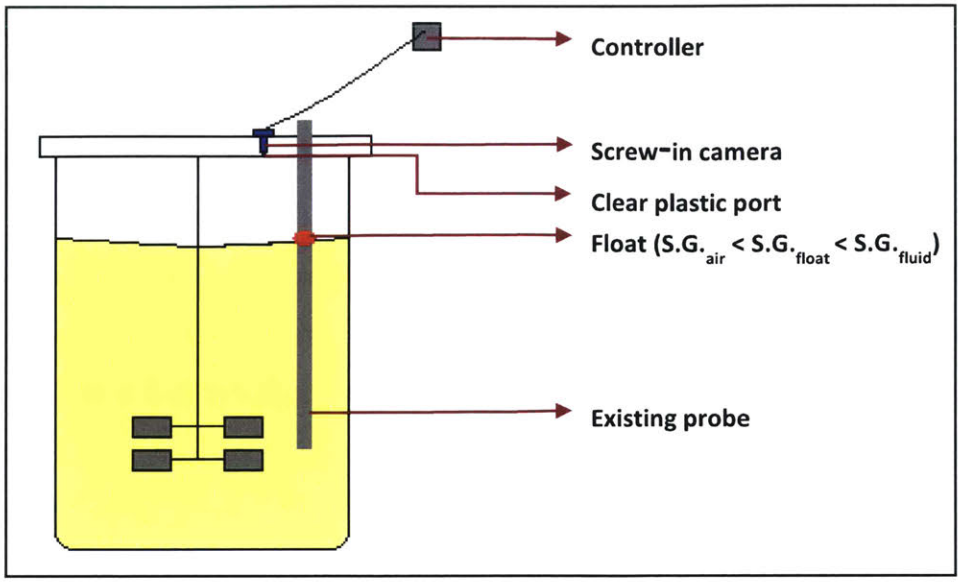


*Figure 3-5* **Colored Float Liquid Level Sensor Schematic**

## Magnetic Level Sensor

A magnetic float on a baffle near the wall of the bioreactor rises and falls with liquid level. Reed switch turns "on" and "off" when the magnet is at the desired level or away. May require multiple reed switches externally to know if level is above or below desired level. Alternatively, could use Hall Effect sensor for continuous results instead of pseudo-continuous/discrete level. The magnet is disposable and is mounted on a non-magnetic baffle. This method is discrete/continuous, hard-sensing, non-invasive, with minimal ripple effect, and inexpensive.

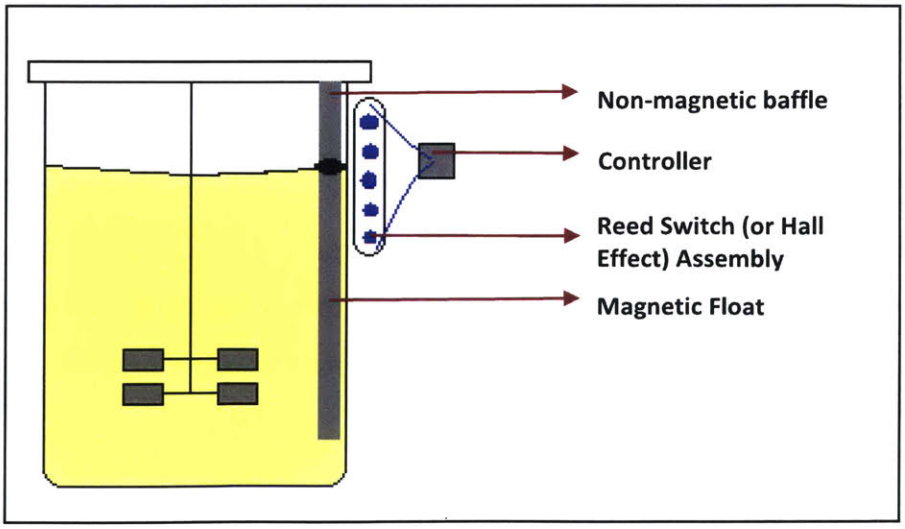


*Figure 3-6* **Magnetic Float Liquid Level Sensor Schematic**

### Optical Density Absorbance Differential Level Sensor

In this method, two optical density measuring instruments are used. One optical density measurement apparatus (OD1) calculates absorbance and relates it to cell concentration, as path length is always "submerged". OD2 varies as a function of liquid level AND cell concentration. OD1 corrects OD2 for cell concentration, so OD2 calculates only level. Since optical density measurements are already used in bioreactors for cell growth measurements, this method enables 2 process control parameters with one technique. However, there are potential complications with foaming at surface, path length too long, etc. This method is continuous, soft-sensing, non-invasive, causes large ripple effect, and expensive.

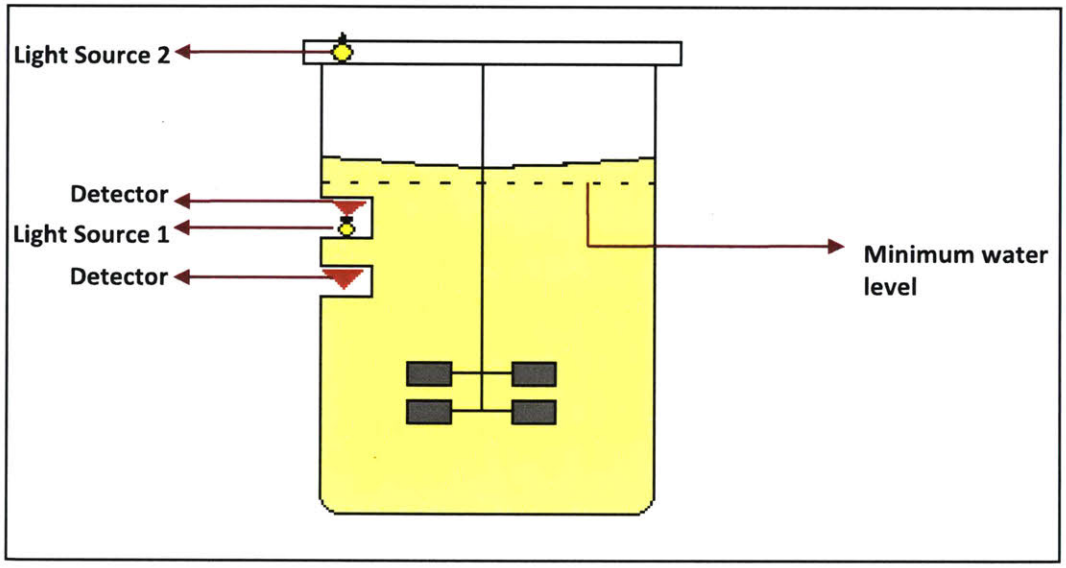


***Figure 3-7*** **Optical Density Differential Liquid Level Sensor Schematic**

### Load Cell Level Sensor

A change in load (weight measured) corresponds to change in level in an ideal scenario. However, density of the fluid changes during process. Thus, density-compensation is required – which adds complexity and cost. Vibration-damping or adjustment in process control would likely also be required as the measurements would be jarring due to agitation

of the apparatus. This method is continuous, soft-sensing, non-invasive, with moderate ripple effect, and may be expensive (due to density-compensation).

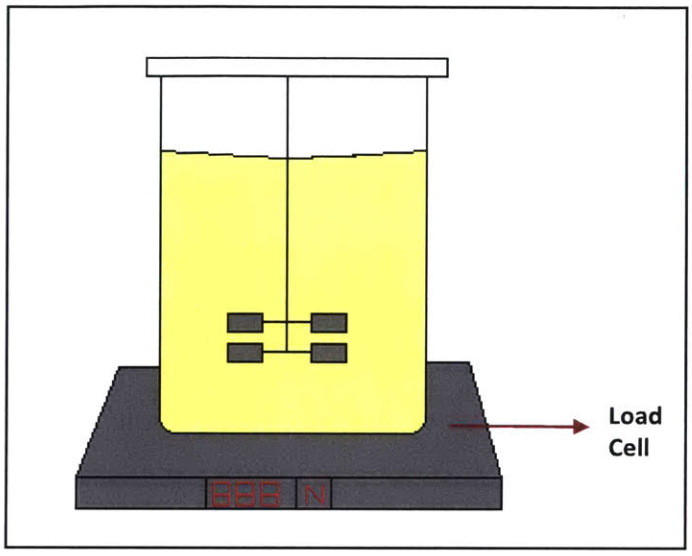


***Figure 3-8*** **Load Cell Liquid Level Sensor Schematic**

### Force Transducer Level Sensor

The density of the suspended baffle is greater than fluid. As level changes, buoyancy force does too, changing read out on force transducer, which is attached to the top of the baffle. This force is read out and correlated to the liquid level. Density-compensation required for this method (as hydrostatic pressure increases with liquid density) – which leads to increased complexity and cost. Noise due to conditions could potentially alter readings.

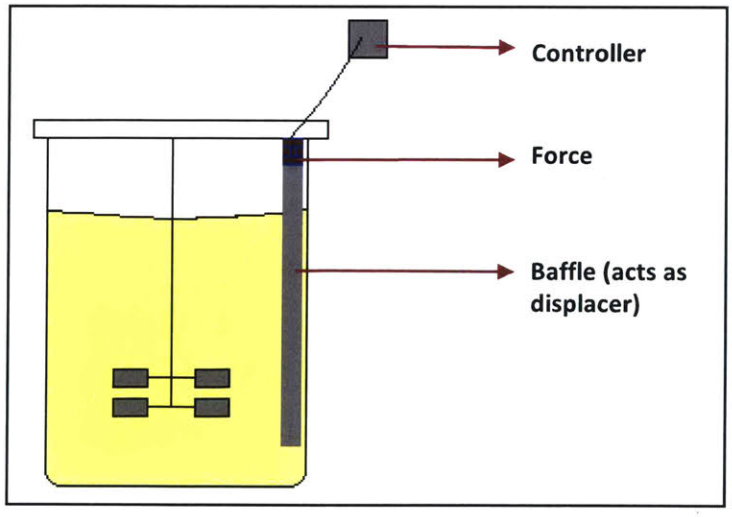


***Figure 3-9*** **Force Transducer Liquid Level Sensor Schematic**

This method is continuous, soft-sensing, invasive, with moderate ripple effect, and may be expensive (due to density-compensation).

### Time-of-Flight Methods

Ultrasonic or light (LASER) waves are emitted and reflected off the surface and received. The time-of-flight (TOF) determines distance travelled and thus the level of fluid. However, there are potential problems with an agitated surface. Additionally, highly accurate measurements are required since the TOF is on the order of milliseconds. This method is continuous, hard-sensing, non-invasive, with minimal ripple effect, and expensive.

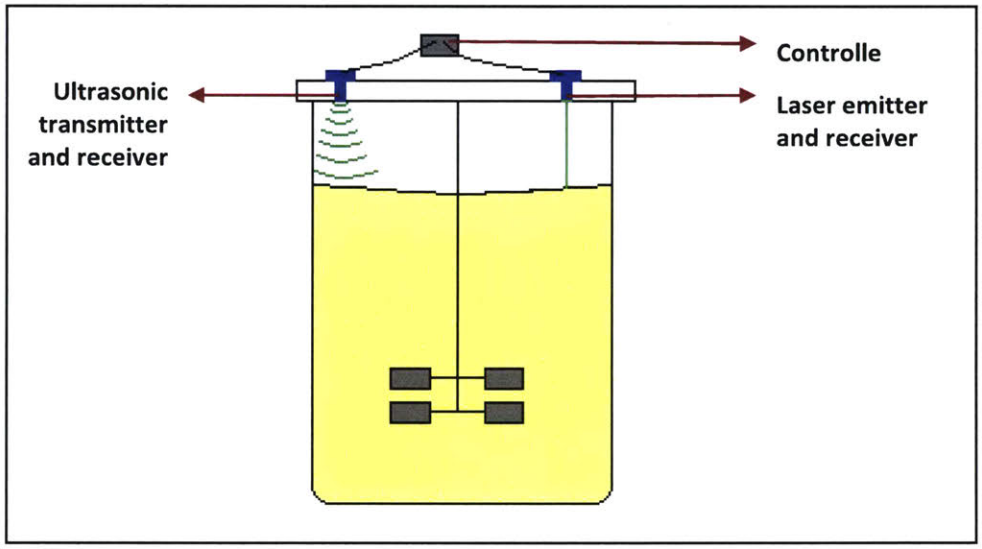


***Figure 3-10*** **Time-of-Flight Methods Liquid Level Sensor Schematic**

### Painted Bands Level Sensor

Painted bands of different colors along the impeller shaft. A camera with a sensor above senses the presence or absence of different colors. Process control can be carried out based on these instances. This method is "single-point" level sensing if only one band used. Multiple bands offer more control. The presence of a vortex may prematurely expose bands. The degree of accuracy required in this design is key. This method is discrete, hard-sensing, non-invasive, with minimal ripple effect, and inexpensive.

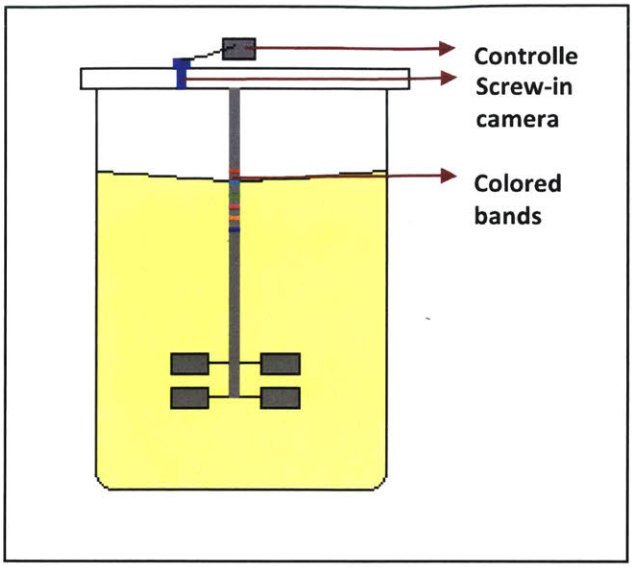


*Figure 3-11* **Painted Bands Liquid Level Sensor Schematic**

### Colored Shaft Method

The colored shaft is an extension of the colored float idea, in that it aims to leverage color sensing to determine the liquid level. The agitator shaft is colored red, and the opacity of the liquid ensures that the submerged part of the shaft is not visible. The part above the water is sensed by the camera, and image processing is done to evaluate the amount of shaft visible, which is then correlated to liquid level. The presence of a vortex may slightly

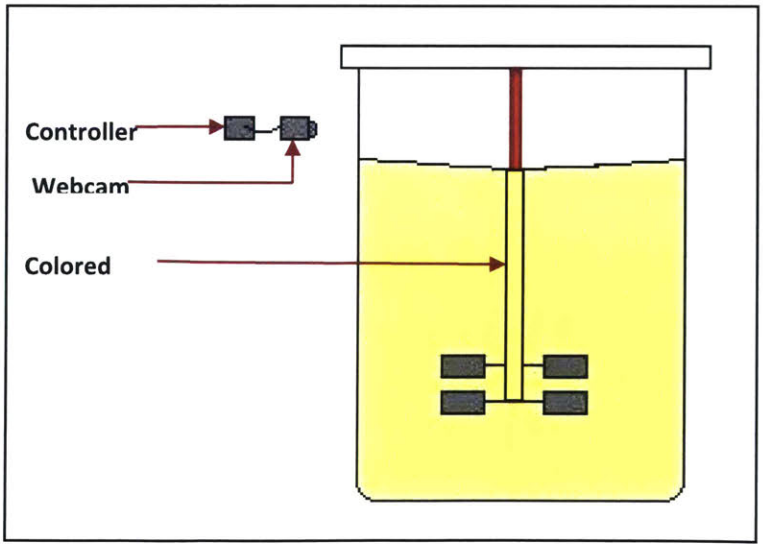


*Figure 3-12* **Colored Shaft Liquid Level Sensor Schematic**

alter results. This method is continuous, hard-sensing, non-invasive, with minimal ripple effect, and inexpensive.

### Developing Liquid Level Sensing Methods

From the ideas outlined above, a few were chosen based on their advantages to be developed and tested. The following sections will explore the development and testing of three optical liquid level sensing methods (the Colored Float, Colored Shaft, and the Painted Bands) and the magnetic level sensor.

## 3.2 Optical Level Sensing Methods – Development and Testing

### 3.2.1 Introduction

Single-use bioreactors offer potential advantages such as high flexibility, easy handling, lower risk of cross-contamination, and savings in time and cost over traditional reusable bioreactors, primarily due to pre-sterilized components [6]. Some of the restrictions regarding rapid adoption of single-use bioreactors include detection of leachables from the container which can interact with the product [59], poor scalability as of now, as well as the lacking prevalence of widely available disposable sensors [60]. There are, however, multiple factors motivating their use in manufacturing as well as R&D [61]. These include public pressure on pricing, the emergence of biosimilars, increase in number of low-volume biopharmaceutical products, and multiproduct facilities, among others.

There is also an increased use of perfusion-enabled bioreactors due to improved equipment reliability, wider range of operational skills in the biomanufacturing industry, and greater awareness of its advantages, the prevalence of perfusion bioreactors is experiencing an upward trend [62]. Compared to traditional fed-batch bioreactors, where cells, media, and products remain in the bioreactor until the end of the run, perfusion bioreactors use specific filtration or membrane systems to continuously culture, feed, harvest product, and dispose of waste and spent media [63]. The expressed protein can be immediately available for purification, which can save time and money, and could allow rescue of product in the event of contamination [63]. Due to the much higher concentrations of cell culture [10x-30x] [63], perfusion bioreactors can be much smaller than comparable fed-batch reactors, for the same total productivity. The smaller size makes perfusion bioreactors a good candidate for single-use, disposable systems in biomanufacturing.

To enable perfusion in small-scale bioreactors, there is an opportunity for advancing systems for real-time, online monitoring of various process parameters such as temperature, dissolved oxygen, pH, and cell growth, for process control [64]. Liquid level in the reactor is another parameter that can be monitored for controlling the rate of

perfusion, the rate of nutrient feed, or in any step that requires volume control. Depending on the nature and requirements for process control, the liquid level sensor could sense a single point, multiple discrete points, or continuous levels.

Stirred single-use bioreactors configured for perfusion, currently use invasive liquid level sensors such as conductive level probes [65] [66] [67]. Having non-invasive alternatives way to sense liquid level, could offer several advantages, including reduced vessel and headplate complexity, reduced risk of contamination, and increased cost savings by enabling another disposable element.

A few non-invasive level sensing methods exist, but are usually unsuitable to use in bioreactors. Externally-mounted capacitive level sensors that sense the changing dielectric constant of the fluid are sensitive to changes in ionic conductivity of the reactor fluid during a bioreactor run [68] [69] [70]. Methods such as load cells and pressure transducers are subject to variations in the density of the reactor fluid, as well as altered by vibrational noise. Time of flight methods such as ultrasonic or lasers require very high resolution due to the small geometries, and are susceptible to change due to a wide range of parameters, thus needing to be fairly expensive in order to work in this scenario, negating the benefits of the non-invasive method [71].

### 3.2.2 The Design Concepts

Three optical liquid level sensing methods were conceptualized and developed for the purpose of this investigation. Two methods are continuous to offer complete process control, whereas one method is discrete, lending itself to point-level applications in biotechnology. The reason for this diverse approach is to characterize different solutions as being more appropriate in different scenarios. For example, if refined and commercialized, the discrete solution will be cheaper to implement than its continuous counterparts, though they offer more control if required. Schematics for the conceptualized methods are shown in Figure 3-10, 3-11, and 3-12.

### Discrete Optical Level Sensor: Painted Bands

The agitator shaft of the bioreactor has bands of different colors along its length. The number of bands depends on the amount and resolution of process control required. Each color is far away on the spectrum from the reactor fluid, and different enough from each other. A camera on the outside of the reactor is pre-position and calibrated, taking live images of the vessel. As the liquid level rises and falls, different colored bands will become visible or disappear. The presence or absence of certain colors is detected by the camera (hooked up to a processor), and the liquid level is known to be below or above certain thresholds.

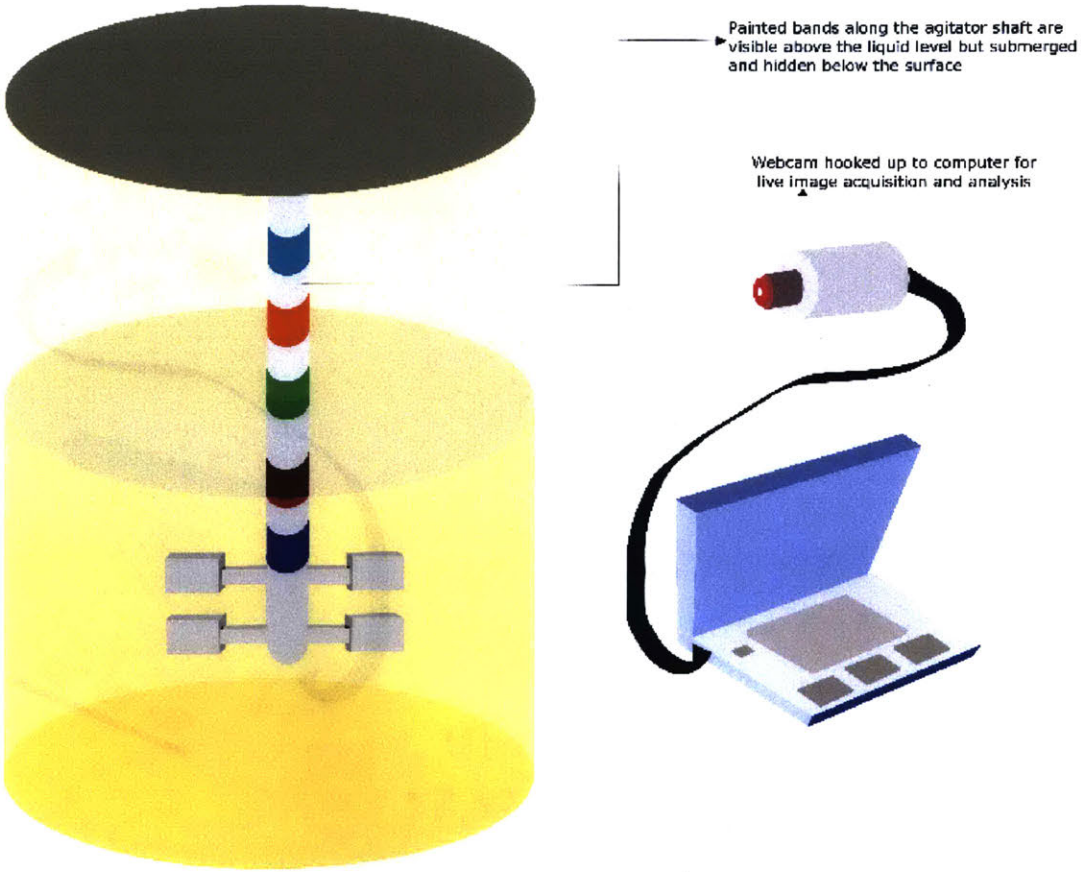


***Figure 3-13*** **Discrete Optical Liquid Level Sensor (Painted Bands) Concept Schematic**

### Continuous Co-ordinate-based Liquid Level Sensor: Colored Float

A disposable, pre-sterilized float comes with the disposable reactor vessel. The float is around a probe near the wall of the reactor, and is of a starkly different color than the reactor fluid, for example, a bright red float in contrast to the shades of cream-yellow experienced by the fluid during a run. A camera on the outside of the reactor is pre-positioned and calibrated, taking live images of the vessel. As the float rises and falls with liquid level, the camera (hooked up to a processor) detects the position of the red float, and correlates it to liquid level.

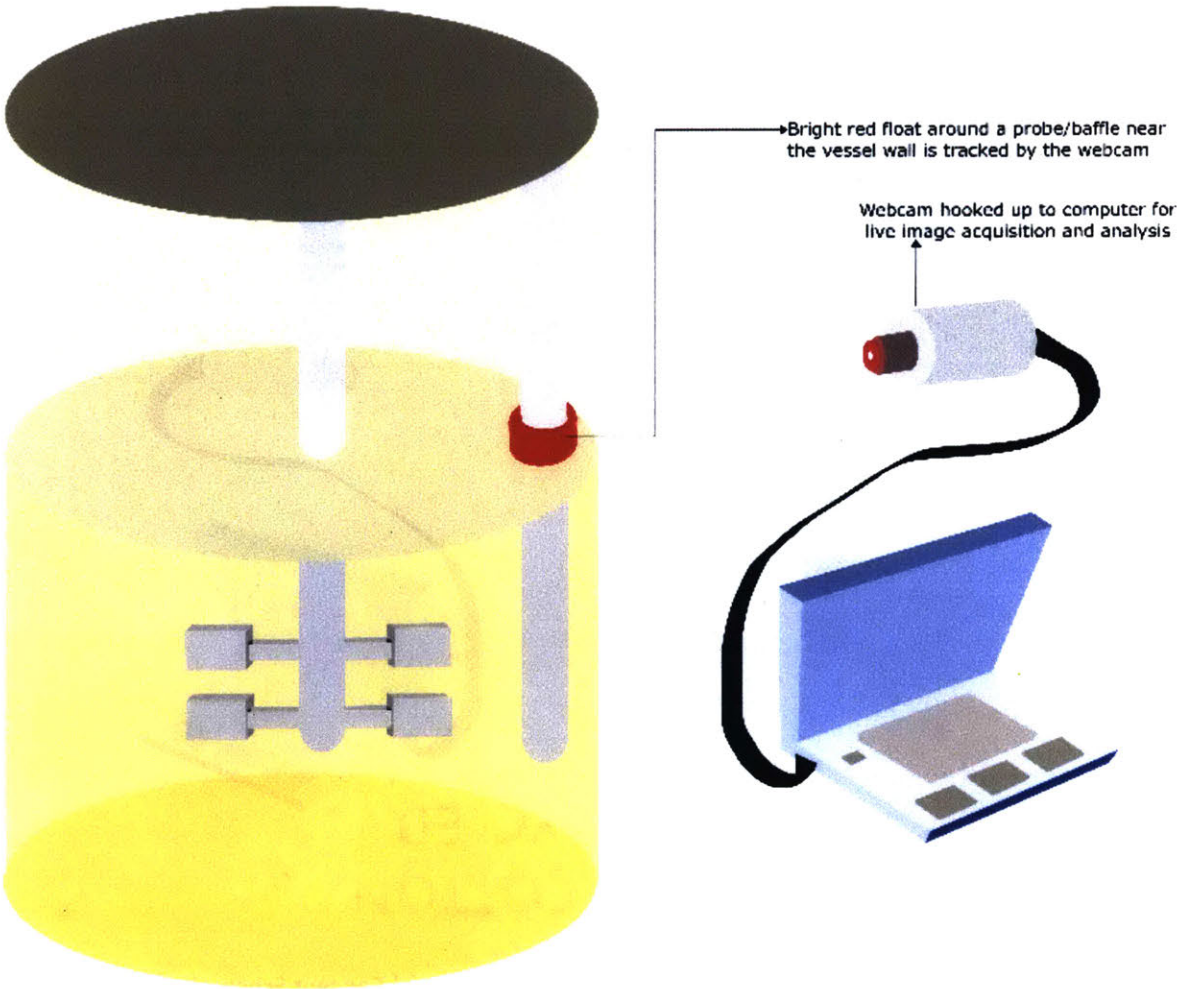


***Figure 3-11*** **Continuous Co-ordinate-based Liquid Level Sensor (Colored Float) Concept Schematic**

### Continuous Area-based Liquid Level Sensor: Colored Shaft

The agitator shaft of the bioreactor is a contrasting color to the reactor fluid, for example, bright red. A camera on the outside of the reactor is pre-positioned and calibrated, taking live images of the vessel. As the liquid level rises and falls, more or less of the red shaft is hidden by the opaque reactor fluid. Thus, the visible portion is detected by the camera (hooked up to a processor), and the amount of visible shaft is correlated to liquid level.

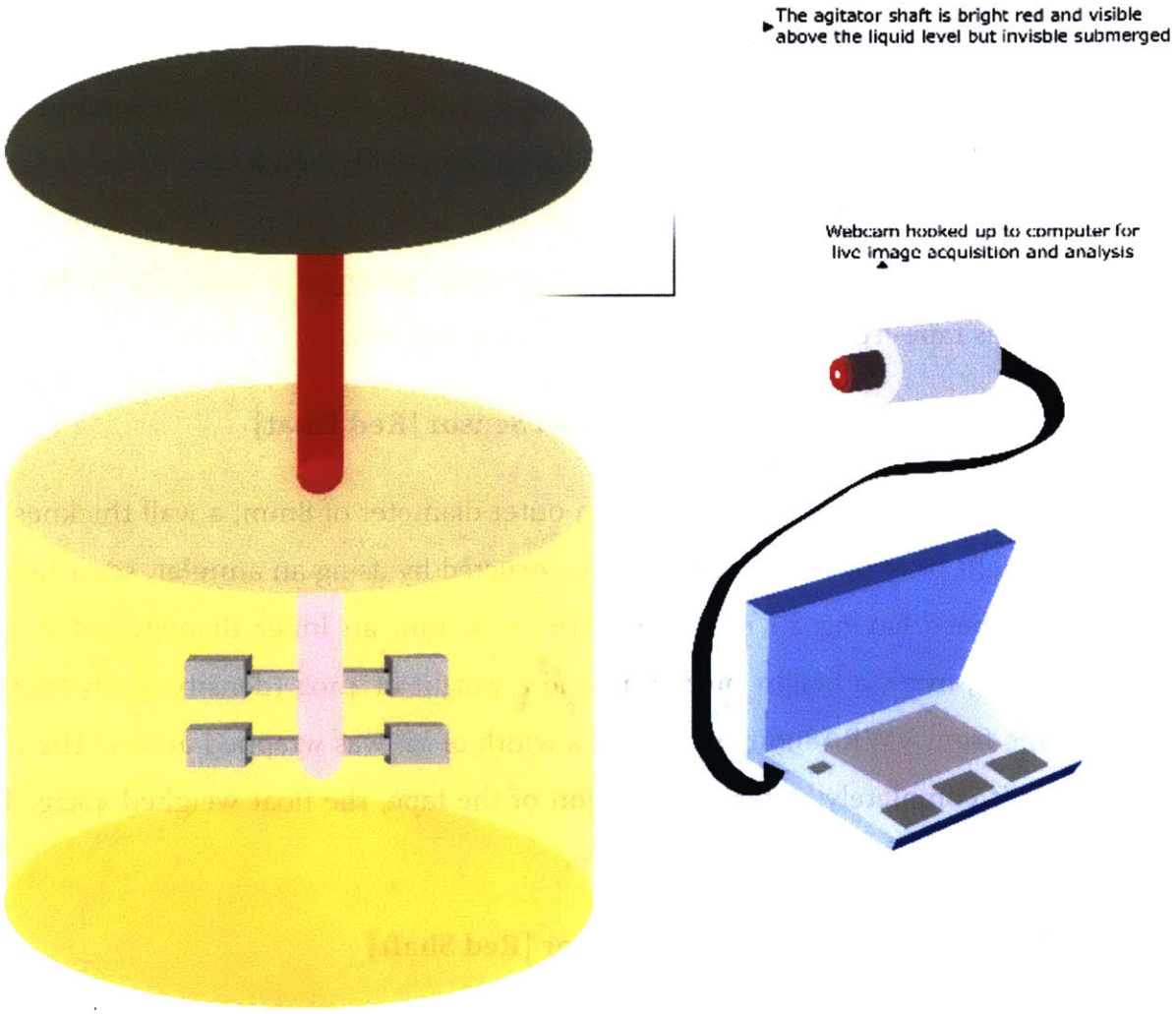


***Figure 3-14*** **Concept Schematic for the Continuous Area-based Liquid Level Sensor (Colored Shaft)**

### 3.2.3 Experimental Setup and Construction of Elements

The elements unique to each method were constructed as follows.

**Discrete Optical Level Sensor [Painted Bands]**

A clear plastic probe was constructed with an outer diameter of 8mm, a wall thickness of 1mm, and a height of 13 inches. At a distance of 3.5" from the bottom of the probe, bright blue tape from VWR (89097-936) with a width of ½" was wrapped around the length of the plastic probe once, to cover exactly ½" of height. After a spacing of 1/8" below the end of the blue tape, orange tape from VWR (89097-934) with a width of ½" was wrapped the length of the plastic probe once, to cover exactly ½" of height. Similarly, with the spacing and length consistent, green tape (VWR: 89097-930), bright red tape (VWR: 89097-932), and lavender tape (VWR: 89097-906) were respectively wrapped around the probe. The plastic probe was tape-free for the last half-inch at the bottom.

**Continuous Co-ordinate-based Optical Level Sensor [Red Float]**

A clear plastic probe was constructed with an outer diameter of 8mm, a wall thickness of 1mm, and a height of 13 inches. A float was constructed by using an annular, semi-hollow polypropylene piece having an outer diameter 27.5 mm, an inner diameter of 11 mm (thickness of 8.25 mm), a height of 12 mm, and a weight of 4.19g (density of 175 kg/m$^3$). Bright red tape from VWR (89097-932) with a width of ½" was wrapped around the float so as to cover it completely. After the addition of the tape, the float weighed 4.52g. The float was then placed around the plastic probe.

**Continuous Area-based Optical Level Sensor [Red Shaft]**

A clear plastic probe was constructed with an outer diameter of 8mm, a wall thickness of 1mm, and a height of 13 inches. Bright red tape from VWR (89097-932) with a width of ½" was wrapped around the length of the plastic probe to cover 10 inches of height. The tape was overlapped such that the plastic was not visible along the 10 inches. Above 10 inches, the clear plastic was visible.

## Experimental Setup

A 1000 ml glass beaker with wall thickness of 0.15 inches (0.38 cm) was used to resemble the bioreactor. The beaker was filled with *Pichia pastoris* cell culture post-run that is stirred at 600 rpm using a VWR mini-magnetic stirrer and plate, thus simulating an agitated bioreactor. Along with the image-capturing camera and process control computer, the elements constructed for each level sensing method were then introduced into the assembly respective of the experiment being conducted (Figure 3-13).

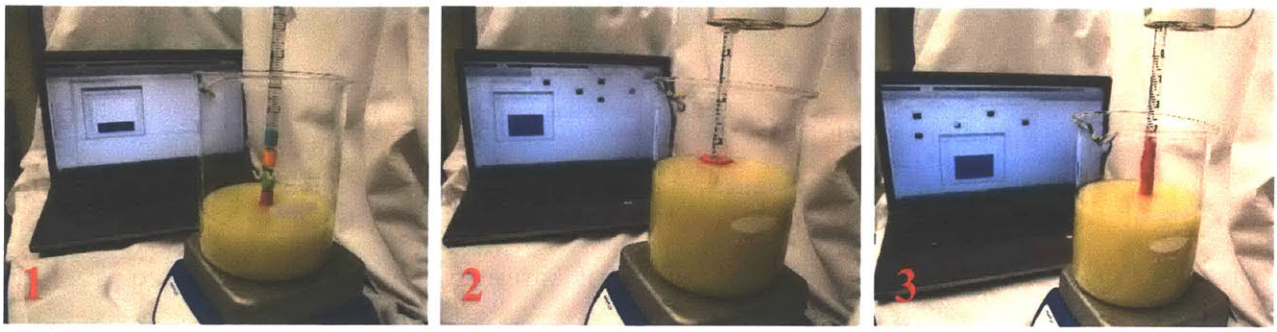


***Figure 3-13*** **Experimental Setups for the optical liquid level sensors** (1) Discrete Optical Liquid Level Sensor [Painted Bands] (2) Continuous Co-ordinate-based Liquid Level Sensor [Red Float] (3) Continuous Area-based Liquid Level Sensor [Red Shaft]; the live image processing predicts the level based on the images captured, and can be visualized on the computer screens here for demonstration purposes

### 3.2.4 Image Processing Algorithms

A laptop running MATLAB R2015b (Windows 8.1), with an Intel® Core™ i7-3630QM CPU @ 2.40 GHz processor with 8.00 GB of installed memory RAM, was used for its in-built webcam for image acquisition, and to run the MATLAB image processing algorithms online, in real-time. The liquid level was then varied as required, while the process computer's webcam acquired images. For all three methods described here, the algorithms developed (explained below) were then run continuously using the acquired images, and the level was predicted. Figure 3-14 shows an example of the algorithms working to predict level.

*Chrominance-based Binarization (CBB) Algorithm*

A CBB algorithm was developed to create a binary (black and white) image from the original image, by selecting for the colors of interest. The acquired image was first converted from the RGB (red, green, blue) space to the HSV (hue, saturation, value) space. The H-value provides a truer representation of the color of the object, and is less sensitive to environmental lighting conditions, unlike the RGB values in which the color and luminance information are coupled [72]. The HSV image is then filtered using thresholding of the different hue, saturation, and value data against the known ranges of the colors of interest. To remove optical and physical noise, the holes in the binary image are then filled by using a function that fills sets of background pixels that cannot be reached by filling in the background from the edge of the image.

*Colored Object Detection (COD) Algorithm*

The binary image generated from the CBB algorithm is then converted into discrete objects. The COD algorithm applies a Gaussian blur and filter to the binary image, to smooth erroneous pixels, physical, and optical imperfections, and to reduce vibrational noise [73]. This transformation was done by clustering binary data, and creating "blobs" that represent objects of the specific color in the original image. To avoid flecks of the specific color in the image, and other minor objects of the same color that may interfere with the process, an

area-based filter was then applied to only retain objects within a certain pixel area range. For the geometric setup and camera resolution (640x800 pixels) implemented, the allowed range of area was set to filter objects smaller than 40 pixels when searching for the colored float or the painted bands, and 500 pixels when searching for the colored shaft. This range is determined by knowing the positioning of the camera in relation to the setup, as well as the camera resolution, which allow correlations to the range of sizes of the binary objects expected.

The retained objects of the specific color are then counted. Within the specified range, only one object should remain for each color of interest, since the choice of apparatus and geometry is designed to leave us with one remaining object per color. These visualized objects are leveraged in different ways for each sensor method described here.

*Painted Bands (PB) Algorithm*

The PB algorithm used the COD algorithm to extract information from the binary images it created. The objects for each band color were counted in the COD algorithm, and fed to the PB algorithm. The PB algorithm used these counts to detect the presence or absence of the specific painted band in the image, and correlated that to the point-level being above or below certain values associated with the bands at those levels.

*Red-colored Float (RCF) Algorithm*

The RCF algorithm used the COD algorithm to extract information from the binary image it created. The algorithm detected the location of the red object, and determined its centroid. By pre-determined geometrical calculations and knowledge of camera-acquired image specifications, the centroid of the red float that was detected was then used to correlate to liquid level. An average of five level readings was conducted at each point, and the calculated mean value is the resulting predicted level value. In case of an erroneous zero reading, the code disregards this value in calculating the mean.

*Red-colored Shaft (RCS) Algorithm*

The RCS algorithm used the COD algorithm to extract information from the binary image it created. This algorithm detects the residual size of the red probe. By pre-determined geometrical calculations and knowledge of camera-acquired image specifications, the area was then used to determine the liquid level. An average of five level readings was conducted at each point, and the calculated mean value is the resulting predicted level value. In case of an erroneous zero reading, the code disregards this value in calculating the mean.

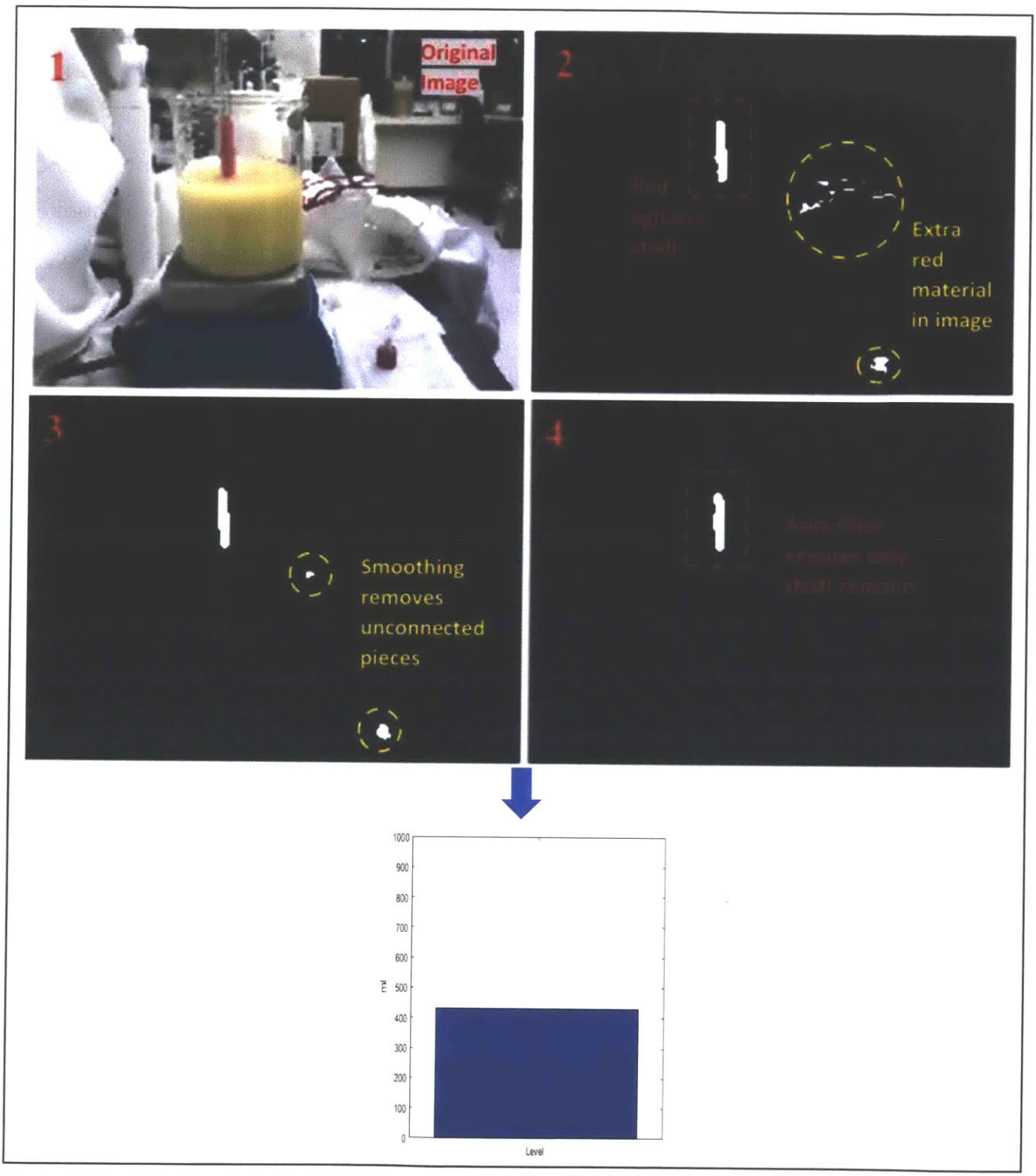


***Figure 3-14*** **Image Processing Algorithms** producing level results (1) Original Image (2) Binary image of red parts of image detected using the CBB algorithm (3) Smoothing and Gaussian blur done during part of COD algorithm (4) area filtering and object detection to finish COD algorithm. The last image is then used to predict liquid level. In this case (Red Shaft Sensor), the final step involves correlation of area of red object to liquid level based on calibrated geometric relationships. The original image was done in an environment of flawed lighting and obscure objects to demonstrate how the algorithm deals with potentially destabilizing objects, since a bioreactor's environment may also have minor red objects.

## 3.2.5 Experimental Testing – Results and Discussion

### Discrete Optical Level Sensor

In lieu of an in-vessel point level sensor, an optical method consisting of painted bands along the impeller shaft was conceptualized. A live, image-acquiring camera was hooked up to the process control computer. Taking advantage of the typical opacity of the reactor fluid, the camera can only see the colored bands above the surface. The idea behind this is to be able to sense certain critical level measurement points, which is where the colored band will be located. As soon as the camera sees that color, the process computer can trigger the point-level reading associated with that color. To ensure the image processing algorithms worked robustly, the colors chosen needed to be different enough from each other and from the reactor fluid. In this experiment, five colors are used – blue, orange, green, red, lavender. The experiment was built and setup as detailed in the previous section. To test the Discrete Optical Level Sensor, the vessel volume was varied from 0 ml to 1000 ml while the camera and computer sensed the presence or absence of the five colors and predicted the point level. In this experiment, the process control assumed the level was *above* the associated level when a color was detected. However, depending on the desired function, the reverse can be programmed.

The results of testing are shown in Figure 3-15. The sensor triggered the level above "X" to which it was assigned, accurately for each level, with the highest absolute mean error being 4 ml, and the highest percentage mean error being 0.67%. Each individual calculation took an average of 1.4 seconds to complete. In this case, as soon as a specific color is detected, the associated level alarm is triggered, but depending on the application, an easy conservative step can be added that necessitates detecting the specific color five times in a row before triggering the alarm of being above the corresponding value.

### Continuous Co-ordinate-based Optical Level Sensor

While a point-level sensor is appropriate in some applications, in order to provide more control in the process, while keeping the benefits of a non-invasive optical level sensor, a

continuous level sensor was conceptualized. The idea was to track liquid level directly by using a float. As the float varies directly with the level of liquid in the vessel, capturing the co-ordinates of the float enables prediction of the level as well. To ensure the float is easily detectable by the image processing algorithms, its color must be different from that of the liquid. In this case, a red float was used, and the experiment was setup and built as detailed in the previous section. The test the Continuous Coordinate-based Optical Level Sensor, the vessel volume was varied from 400 ml to 1000 ml while the camera and computer sensed the position of the red float and used it to predict the liquid level.

The results of the experiment are shown in Figure 3-16. There were no erroneous zero readings in the primary experiment conducted, due to good lighting conditions. The average time taken for each individual level calculation using the current setup was 1.6 seconds, with 7.9 seconds required to predict level using five averaged readings. To assess the accuracy of the predicted values, we measured a range of liquid level values (between 400 ml and 1000 ml). The highest absolute error was 10.8 ml, with a highest percentage error of 2.38%. The standard deviation for the individual level readings had a highest value of 8.7 ml, and a highest standard error value of 2.6 ml.

**Continuous Area-based Optical Level Sensor**

The benefits of a non-invasive, continuous liquid level monitoring system were achieved using the previous setup. However, the use of an additional part (the float) was necessary to achieve the desired functionality. In order to try and achieve the same functionality without the addition of added parts, we created a different continuous level sensor using the agitator shaft that is already in the vessel. By detecting the amount of visible shaft area using a camera, the computer predicts the level by assuming the liquid in the vessel blocks the rest of the agitator shaft. To ensure the shaft is easily distinguishable so that the image processing algorithms work appropriately, the agitator shaft of the bioreactor is a contrasting color to the reactor fluid – bright red is used in this case. In order to test the Continuous Area-based Optical Level Sensor, the experiment was built and setup as detailed in the previous section. The vessel volume was varied from 400 ml to 1000 ml,

while the camera and computer sensed the amount of visible shaft area, and correlated it to liquid level.

The results of the experiment are shown in Figure 3-17. There were no erroneous zero readings in the primary experiment conducted, due to good lighting conditions. The average time taken for each individual level calculation using the current setup was 1.5 seconds, with 7.7 seconds required to predict level using five averaged readings. To assess the accuracy of the predicted values, we measured a range of liquid level values (between 400 ml and 1000 ml). The highest absolute error was 15.0 ml, with a highest percentage error of 2.34%. The standard deviation had a highest standard deviation value of 5.0 ml, and a highest standard error value of 1.5 ml.

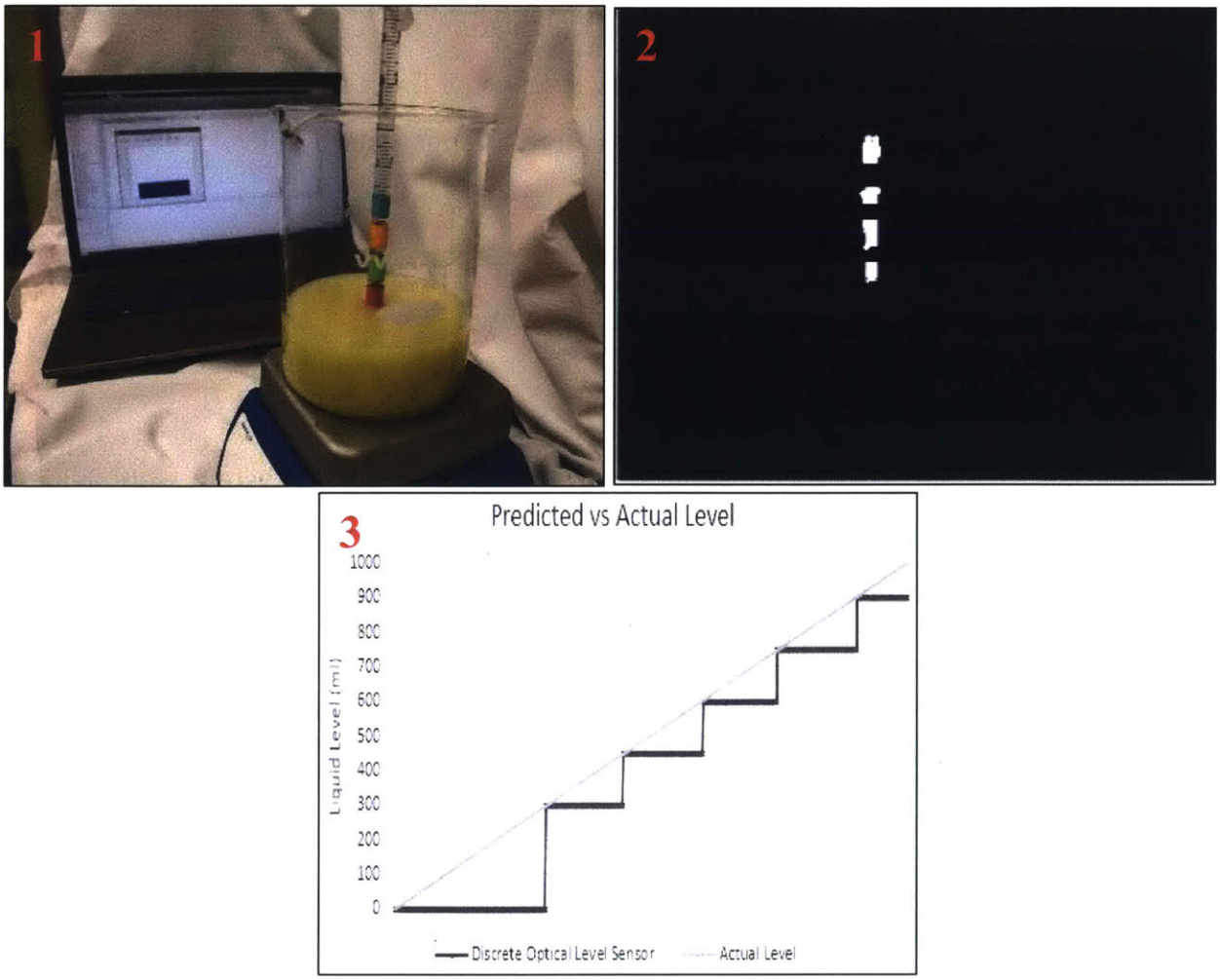


***Figure 3-15*** **Discrete Optical Level Sensor (Painted Bands) Results** (1) Experimental Setup (2) Post-image-processing – binarization, chrominance filtering, smoothing, area-filter (3) Predicted level results in relation to actual liquid level

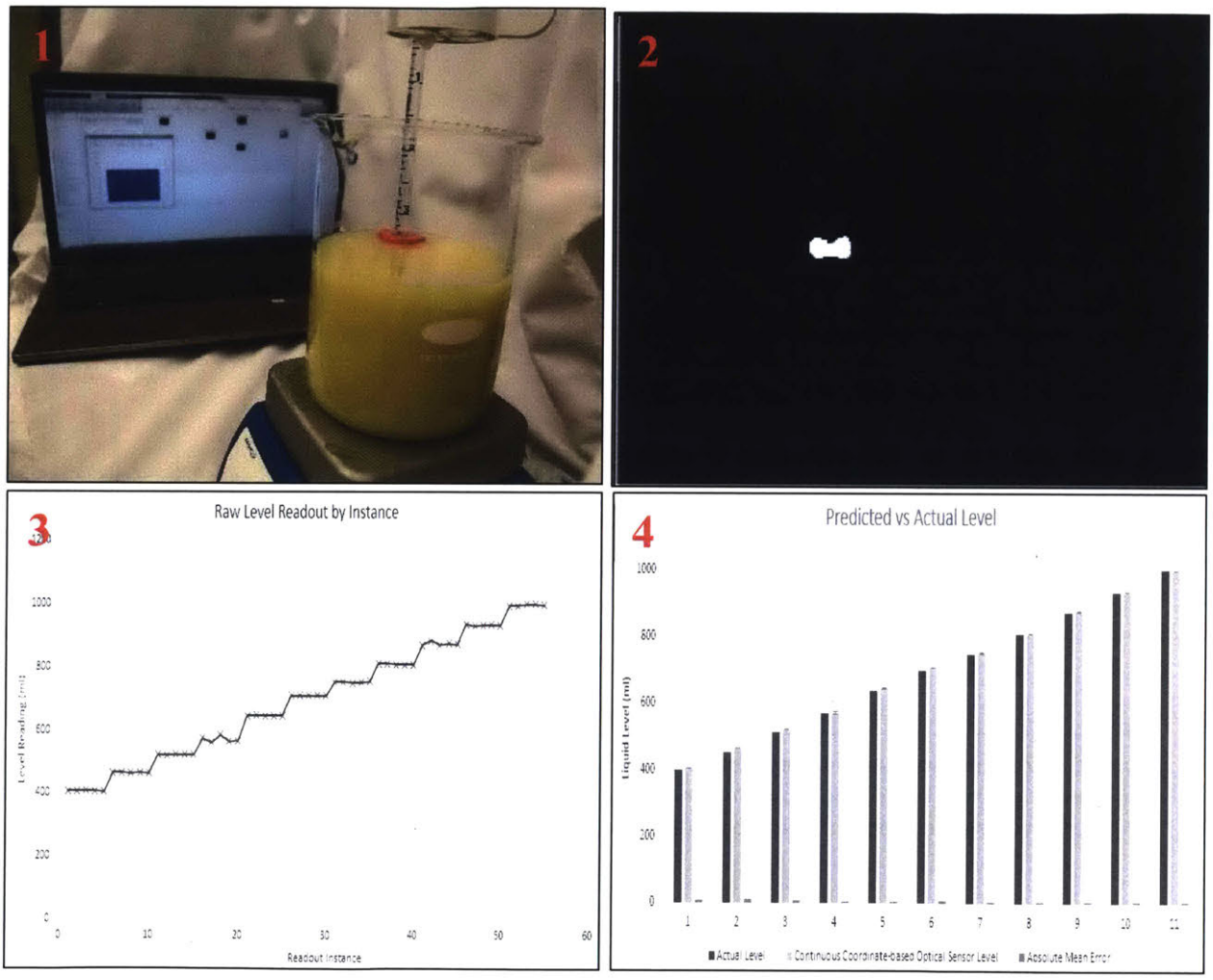


***Figure 3-16*** **Continuous Co-ordinate-based Optical Level Sensor (Colored Float) Results** (1) Experimental Setup (2) Post-image-processing – binarization, chrominance filtering, smoothing, area-filter (3) Raw Level Readout by Instance (4) Predicted level results in relation to actual liquid level

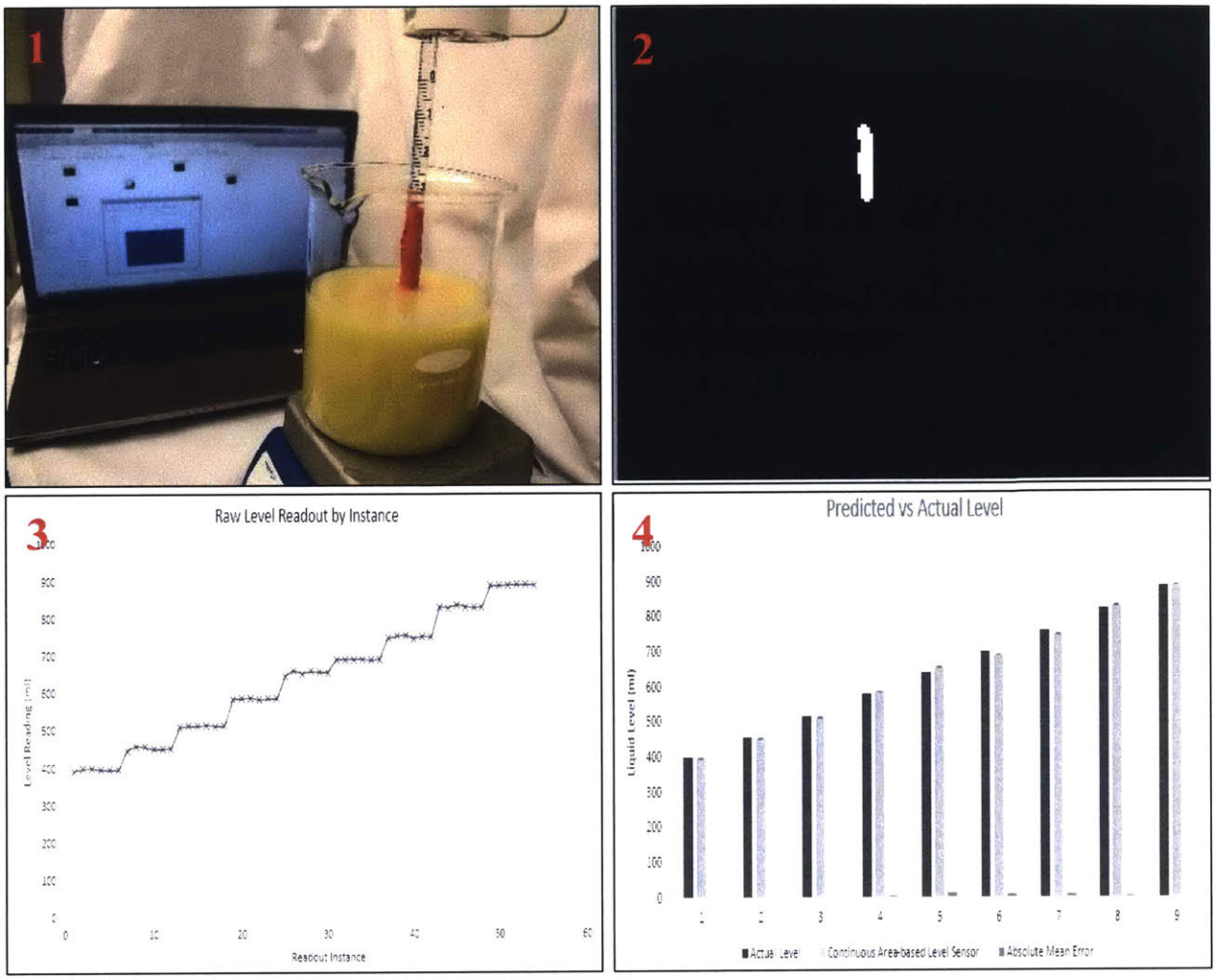


***Figure 3-17*** **Continuous Area-based Optical Level Sensor (Colored Shaft) Results** (1) Experimental Setup (2) Post-image-processing – binarization, chrominance filtering, smoothing, area-filter (3) Raw Level Readout by Instance (4) Predicted level results in relation to actual liquid level

## Discussion

The successful testing of the optical level sensors validates a novel solution to process control using level sensing in bioreactors. There is no longer a requirement for an invasive sensor that inconveniences the setup as well as introduces a potential sterility concern. An external sensor allows for reusability even in the case of disposable bioreactors, and is cost effective in the long run. Two of methods created are continuous to offer complete process control, whereas one method is discrete, lending itself to point-level applications in biotechnology.

As seen in the results, the sensors work on the order of seconds. The reactor fluid volume changes at a rate of 15-30 ml/hour, which means the sensors developed are adequate for process control. Typically, the rate of fluid flux incoming or outgoing in perfusion bioreactors is not fast enough to alter the liquid level faster than the sensor calculates the level. The Continuous Coordinate-based Optical Level Sensor requires the addition of the float as a piece of equipment, whereas the other two methods use an existing part of the setup (the shaft) to achieve functionality. Since the Discrete Optical Level Sensor only gauges the presence or absence of a specific color band, it is more robust for its application, as opposed to the continuous level sensors. However, the continuous sensors offer more control due to the ability to predict level to a closer degree.

Since all methods use optical sensing and chrominance filtering to achieve their respective results, after a certain point, the drastically changing light conditions make the optical level sensors vulnerable to stop working, as can be seen in the results. This problem can be circumvented in future designs, by using a more sophisticated setup with a controlled and consistent light source inside a closed environment. Alternatively, a slightly less robust but cheaper modification to the current setup would be to use a "gray card" approach, where the code uses the known gray card HSV values as a reference, and corrects the image for changing lighting before implementing the algorithms [74]. The formation of a vortex at certain stirrer speeds could potentially slightly skew the level sensors since the liquid surface becomes concave and has different heights at different points. If the formation of a

vortex is a concern to proper process control, and very precise level sensing is required, the two continuous techniques can be used in tandem to correct for the vortex. With the float level at the wall, and the agitator shaft level at the center, the two methods will experience opposite effects of the vortex level change, and can be combined to correct to the true level (volume) of the vessel. Alternatively, knowledge of the vortex formed with stirrer speed can be used to correct and recalibrate the level sensor.

**Future Work**

Since the density of cell culture varies during the course of a run, the opacity of the reactor fluid may also be affected. In order to ensure that the level sensor worked throughout the process, the experiment should be repeated at varying optical densities (OD) of reactor fluid. Similarly, another concern is the fact that a possible changing light source could interfere with optical measurements. To test the robustness of the optical level sensors with changing light surroundings, the experiment should also be repeated by changing the lux hitting the bioreactor setup, while the percentage of failed readings (no detection of desired objects, or a zero reading) is measured. These experiments are the planned as future work to further characterize the level sensors.

## 3.2.6 Conclusions

The optical level sensing methods described in this paper have myriad applications in industry, and especially in biotechnology. They offer a non-invasive way to accurately gauge liquid level for process control. This is especially useful in continuous-perfusion, disposable bioreactors. These methods can be applied in any scenario where liquid level sensing are required.

The Discrete Optical Level sensor lends itself to applications where point-level sensing is required. Similarly, the continuous level sensors can be used in applications where the exact level value is required. Other industries where level sensing is prevalent, and have the same geometric characteristics, include the wastewater or water treatment industry, food industry, packaging and bottling industries, and so on.

Overall, the methods and algorithms developed as described in this paper work effectively to gauge liquid level for the purpose of process control in running a single-use, continuous perfusion bioreactor, and offer plenty of advantages over traditional level sensors. The optical methods offer a non-invasive alternative that do not cause sterility concerns, avoid added reactor complexity and cost, and are reusable even in a single-use bioreactor setup.

## 3.3 Magnetic Optical Level Sensor – Development and Testing

### 3.3.1 Introduction

Continuous perfusion bioreactors offer various advantages over traditional fed-batch reactors such as higher cell concentrations (and product yields), lower accumulated waste products, immediate availability of protein products for purification, more consistent expression profiles, and a host of other benefits [75]. Additionally, single-use (disposable) bioreactors are becoming a common alternative to the stainless steel reactor for manufacturing [61]. Some of their advantages include lower cross-contamination risk, easier handling, higher flexibility, and savings in time and cost [76]. The adoption of disposable or continuous perfusion bioreactors signals a growing opportunity for the development of new techniques for process control and other peripheral aspects of fermentation or cultivation.

Sensing the level of liquids in bioreactors provides one measure for enabling process control since the rate of perfusion and feeding can be regulated as required by the operator to create the optimized production conditions in the vessel. Current approaches for perfusion bioreactors use in-vessel level probes for this purpose [66] [67]. Non-invasive sensing offers multiple benefits, including reduced risk of contamination, reduced geometric complexity, and potential cost savings. For disposable bioreactors, non-invasive sensors could allow for reuse of the sensor, facilitating rapid turnaround of process equipment without necessitating sterilization.

The few non-invasive technologies for sensing liquid level that exist in other industries do not typically lend themselves to applications in bioreactor vessels. For example, external capacitive level sensors work by measuring the change in dielectric constant through the vessel wall. The ionic conductivity of the fluid in fermentation changes during the course of the run, however [68] [69] [70], and interferes with these measurements. Here, we report a non-invasive liquid level sensing technique using a magnetic float and externally-

mounted reed switches, that does not depend on fluid properties, but instead leverage the fluid level itself to allow direct measures of the fluid level in the reactor.

### 3.3.2 The Design Concept

A magnetic float is suspended around a non-magnetic shaft placed in the vessel. This shaft can be one of the other probes used for process control, or a baffle. The proximity to the edge of the vessel ensures that the magnetic field penetrates the outer surface of the vessel. The strength of the magnet can be adjusted to compensate for position, and can be disposable. On the outside of the vessel, close enough to be affected by the magnetic field, an array of reed switches is attached vertically. Thus, when the magnetic float rises and falls with level, different reed switches will be turned on. These switches can be connected in a circuit to indicate to the process control computer which switch is on and experiencing current, and by extension indicate the position of the magnetic float, which can be used to predict the liquid level. The schematic for this concept is depicted in Figure 3-18.

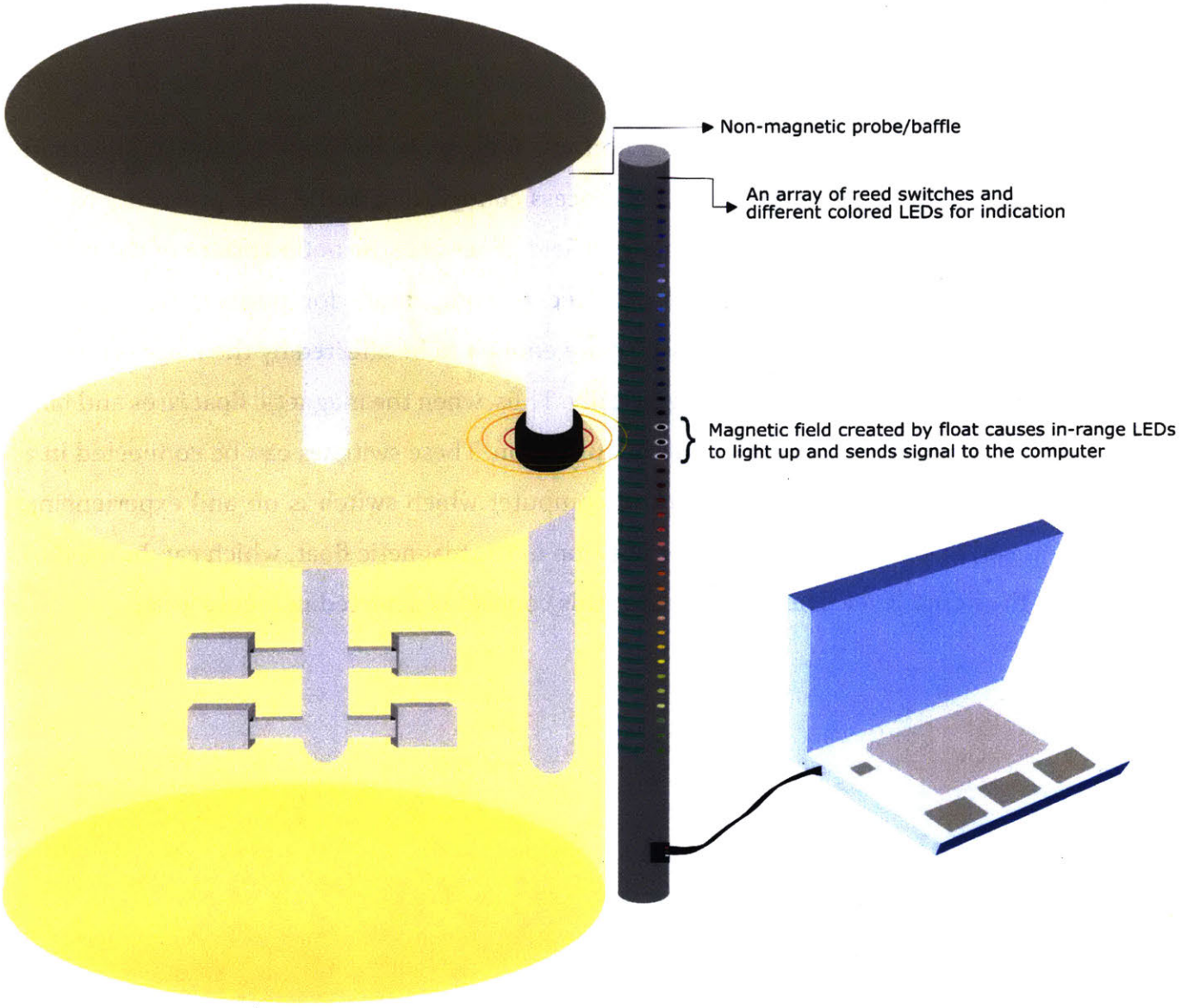


***Figure 3-18*** **Magnetic Liquid Level Sensor Concept Schematic** with multiple reed switches to accurately predict liquid level

### 3.3.3 Experimental Setup and Construction of Elements

To achieve a specific gravity less than that of the reactor fluid (approximately that of water), we used a foam polystyrene floatation ring as the float. Four nickel-coated neodymium [NdFeB] magnets were equidistantly spaced and embedded in the float. The magnets were of a ½" disc diameter and ¼" thickness, with an individual pull force of 6.1 pounds. External to the vessel, we placed an array of reed switches. Reed switches are electric switches that turn on in the presence of a magnetic field. Depending on the specific reed switch and magnet strength, the distance and orientation required to turn them on will vary. In this case, the reed switches used are SPST-NO, with a magnetic sensitivity of 12-18 Ampere-turns. The probe holding the magnetic float is simply a plastic shaft in this case, whereas the vessel is a glass beaker with a diameter of 4.25 inches (10.80 cm) and a wall thickness of 0.15 inches (0.38 cm). The vessel geometry is important in regards to evaluating sensor performance, since level sensing resolution is based on height, and a smaller diameter vessel leads to increased resolution for the same volume change. One configuration tested

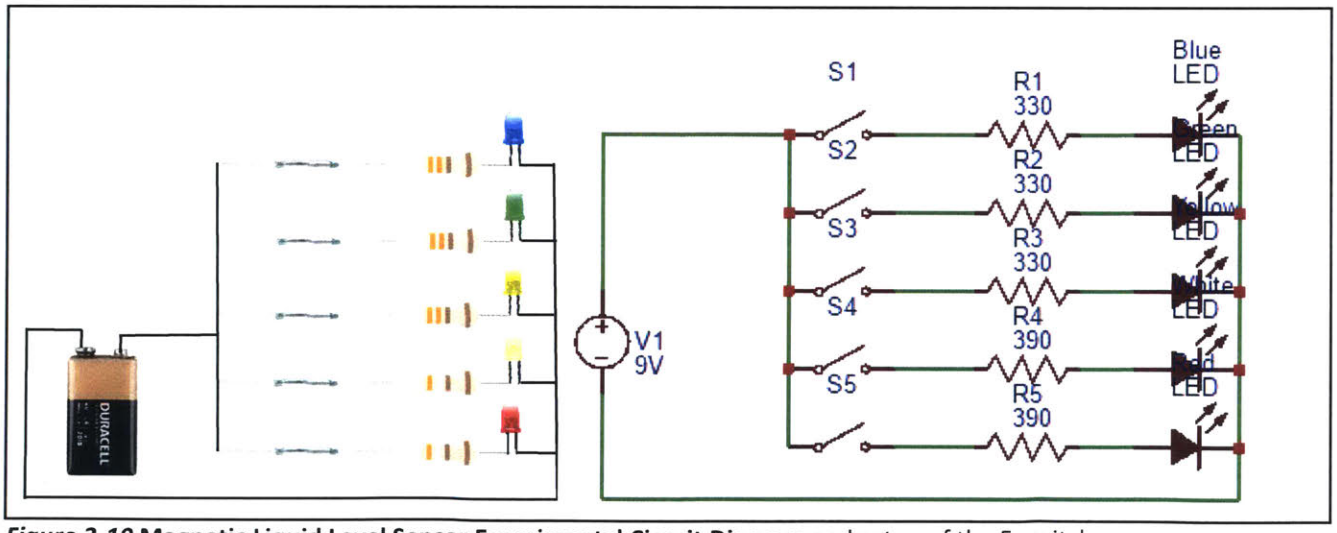


***Figure 3-19*** **Magnetic Liquid Level Sensor Experimental Circuit Diagram** and setup of the 5-switch array

here included an array of 5 reed switches, that was assembled according to Figure 3-19. To provide visual feedback on the system for the active switch, each of them are placed in series with a different colored light emitting diode (LED). In a setup for process control, other means of communications such as current sensors or a direct voltage or current signal can be sent to the processor, instead or in addition to LEDs. In this case, the spacing of the

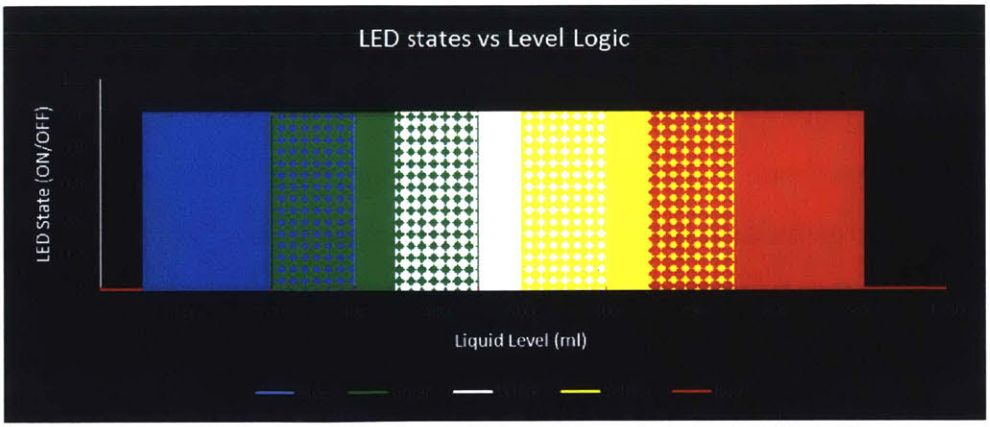


***Figure 3-20* LED Level Logic** Solid areas indicate the sole LED that will be on at a certain liquid level, whereas argyle pattern of two colors corresponds to those two LEDs being on in that liquid level range

reed switches was intended to turn on either one or two LEDs at a table, based on the logic diagram (Figure 3-20). The schematic of the setup constructed is shown in Figure 3-21.

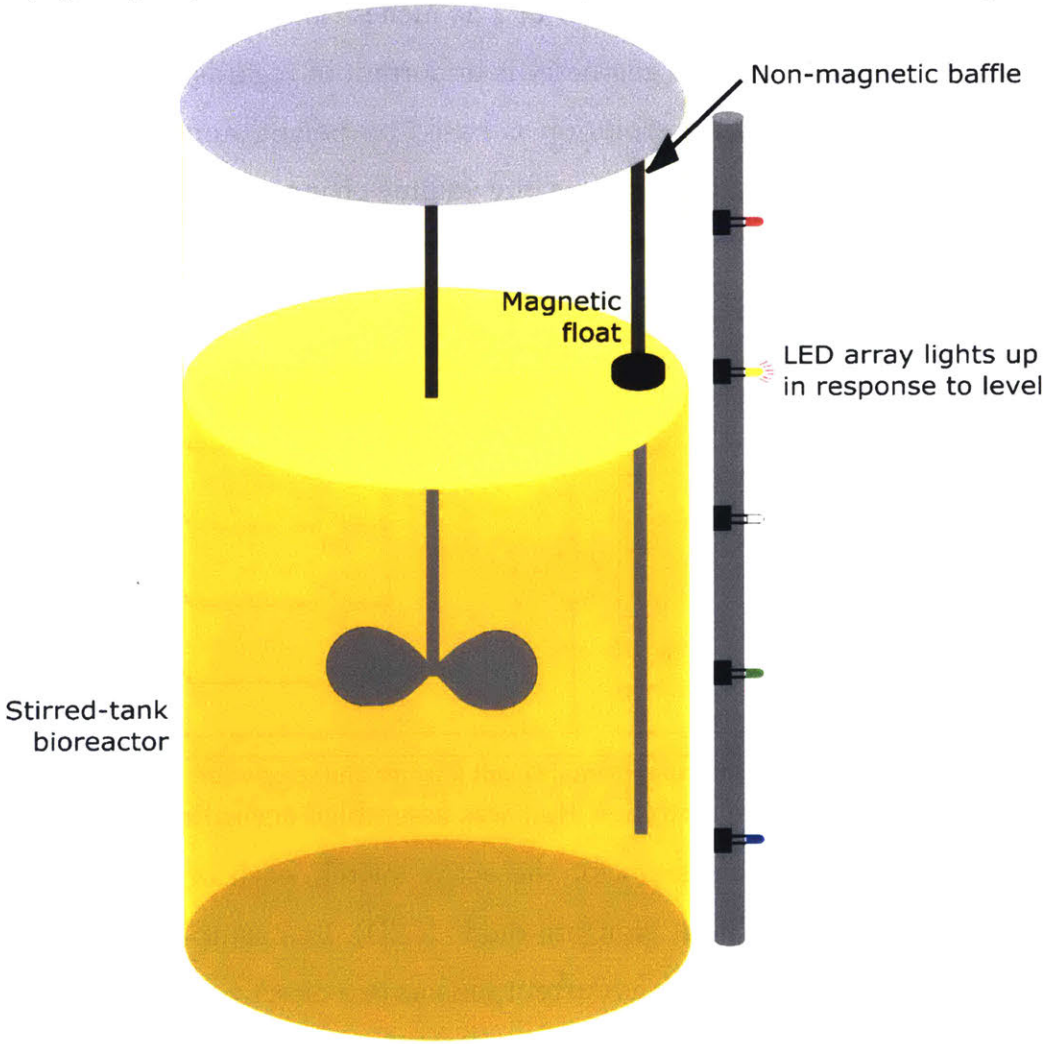


***Figure 3-21* Magnetic Liquid Level Sensor Experimental Schematic**

### 3.3.4 Experimental Testing – Results and Discussion

The liquid level was varied between 0 ml and 1000 ml. Figure 3-22 shows the experiment at two instances indicating liquid level by the different LEDs that are on.

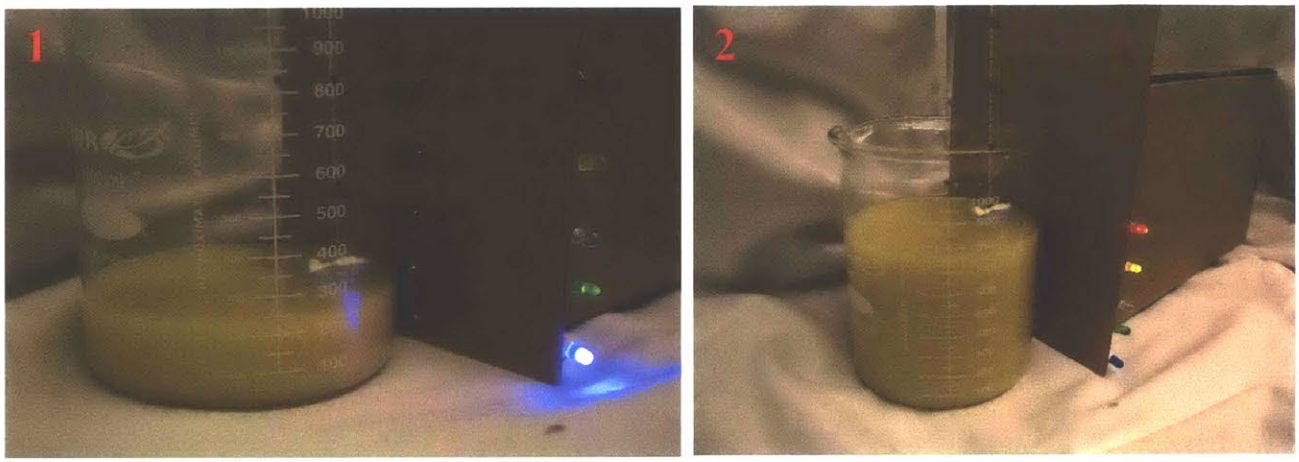


***Figure 3-22*** **Magnetic Liquid Level Sensor Experimental Setup** during a test (1) Volume of about 275 ml turns the blue and green LEDs on (2) Volume of about 725 ml turns the yellow and red LEDs on

The results of testing the Magnetic Float Sensor are shown in Figure 3-23. To minimize negate the effect of LEDs flickering on and off due to the magnetic field only temporarily reaching the reed switches, the reading was allowed to stabilize for 10 seconds before the LED was said to be ON. This mimics a process control step that verifies positive signal for a 10 seconds before processing the level. As can be seen, the results correspond very closely to the designed logic. The discrepancies occur due to lack of robustness of the experimental setup, and the fluctuations and instabilities introduced due to testing.

In a stable bioreactor environment, with a commercially prototyped array of reed switches, and knowing the exact magnetic field environment, as well as the interference from surrounding objects, a precise sensor can easily be developed to follow its assigned logic perfectly. Additionally, the discrete level sensor can transform into a pseudo-continuous sensor by adding reed switches and increasing the amount of steps (n). As *n* goes to infinity, the sensor will overlap the actual level exactly, and the sensor will become continuous. Depending on the resolution of liquid level sensing required, *n* will need not go to infinity, but instead be high enough to achieve sensing to the accuracy desired. Assuming the logic dictates that each step is evenly spaced (which is not the case in the current setup due to

leveraging combinations of ON states to achieve more steps), then $n$ equals the number of reed switches, and the number of different level states that can be predicted. Figure 3-24 shows the logic for different values of $n$, from 5 to infinity, along with their capable resolution in this setup.

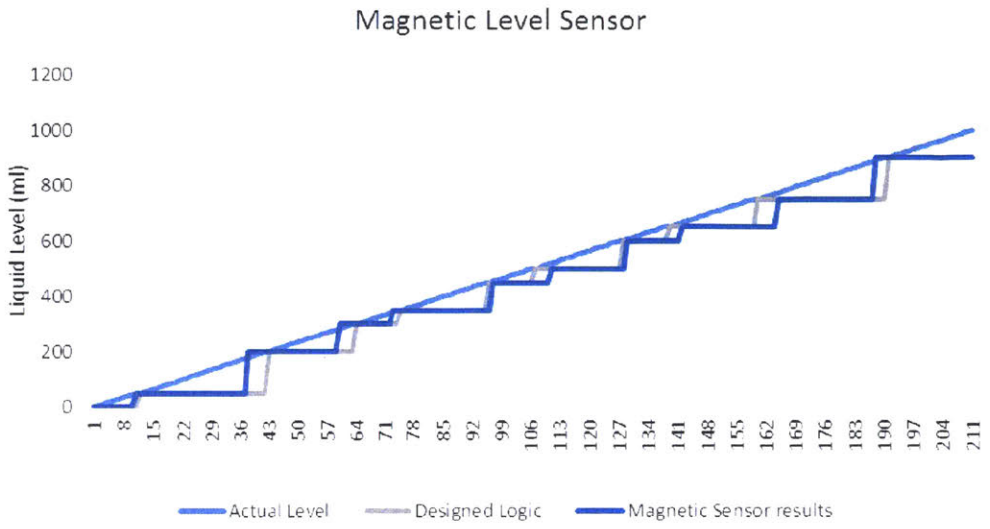


***Figure 3-23*** **Magnetic Liquid Level Sensor Results** The designed logic (gray) is a stepwise discrete function that combines electric signals to realize the position of liquid level using a combination of reed switches. The actual experimental results (dark blue) follow this logic with some fluctuations due to the imperfect equipment and instabilities of testing.

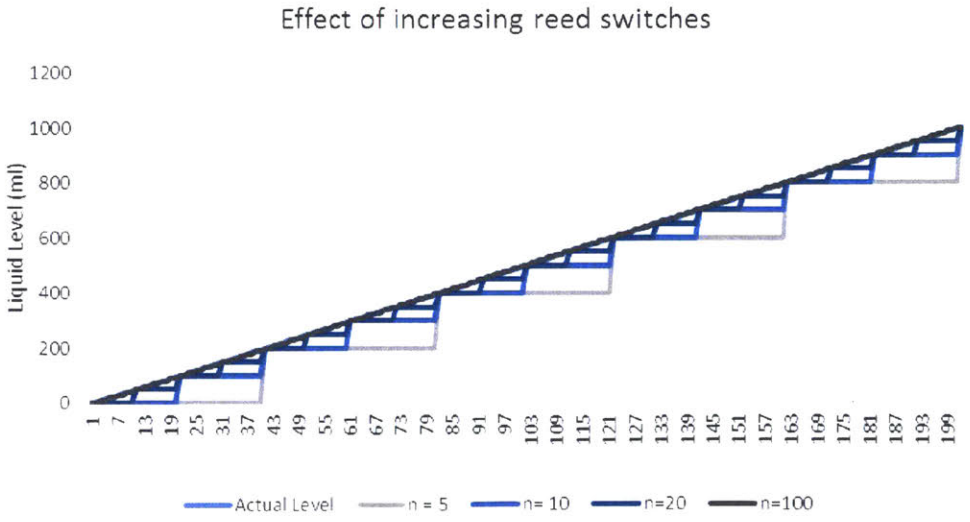


***Figure 3-24*** **Effect of Increasing the Number of Reed Switches** (n) from 5 to 1000. As $n$ increases, the resolution is fine enough to resemble a continuous sensor, as can be seen in the n =100 case where it overlaps with the true level.

A more sophisticated, improved version of the Magnetic Float Liquid Level Sensor would comprise a custom-made adhesive strip of reed switches that attaches externally to the vessel. All the necessary information regarding which switch is sensing current, will be parsed through to one end of the strip, and output to the processor. The strip is carefully manufactured so that the switches are equidistant but also with the knowledge of the rest of the system (such as the magnetic float, vessel wall properties, etc.) so as to ensure perfect relay of logic as the magnetic float changes with level. The magnetic float itself will have a uniform distribution of magnetic material so that rotation of the float does not change the magnetic field. An alternative to reed switches that can also be used are Hall Effect sensors, which are similar to reed switches in that they react to a magnetic field. However, they can act as a continuous sensor, due to their ability to increasing output voltage (until saturation) linearly with increasing magnetic field density. This is a good modification if a truly continuous sensor is required. However, the binary nature of reed switches makes them more reliable and robust.

### 3.3.5 Conclusions

A liquid level sensor using a magnetic float and an array of reed switches was successfully tested in this work. This non-invasive option to liquid level sensing has a wide range of applications in biotechnology as well as other industries in which non-invasive fluid sensing would be beneficial. Further development and modifications to the technology would enhance the robustness, reliability, and resolution of the sensor. While the magnetic level sensor is primarily a discrete sensor that lends itself to point-level alarm control, with increased resolution (or implementation of Hall Effect sensors), they can also be used for process control when continuous level sensing is required. Using an external magnetic level sensor allows for reduced reactor complexity, reduced risk of contamination, increased cost savings from re-use, and other benefits when used for process control in a single-use, continuous perfusion bioreactor.

# Part II
# Other Sensing

## 3.4 pH Sensing

pH sensing is another important aspect of process control in biologic drug manufacturing. Controlling pH is essential for cell growth and viability. Different micro-organisms grow in different pH ranges. Thus, it is important to be able to continuously sense the pH of the culture, and adjust it in real time with base and acid addition. Most process control pH sensors are invasive due to the nature of pH sensing. With regards to designing a sensing mechanism with the overall bioreactor design outlined in the document, no new novel technologies were developed. Rather, an assessment of the current methods was undertaken, along with a recommended designs and future potential solutions.

The overall motivation of this work is the design of a continuous, disposable, perfusion-capable bioreactor. Thus, in order to fit within the design parameters, any sensor must be either disposable or non-invasive. Non-invasive sensors present outside the vessel can be re-used even with disposable bioreactors, with no need for sterilization due to fact that they do no interact with the medium. Similarly, disposable sensors themselves can be used because they will be disposed of along with the bioreactor itself.

Non-invasive pH sensors rely on pH patches inside the vessel, which react to changes in chemistry of the solution. These changes can be exploited from outside the vessel to determine pH. This optical-based pH sensing relies on patches placed on the internal vessel wall (of a transparent vessel), that are pre-calibrated. The patches are externally illuminated, and a spectrometer is used to determine the pH [77] [78] [79].

Multiple options for disposable, invasive pH sensing methods exist. Most commonly, a measuring electrode and a reference electrode combine to measure the voltage potential induced by the hydrogen potential (pH) of the solution, in a battery form [80]. Many industrially available pH sensing probes exist for disposable applications [81] [82].

## 3.5 Dissolved Oxygen Sensing

Dissolved oxygen (DO) monitoring is vital for process monitoring, as product yield is a function of multiple parameters, but arguable none more important than oxygen transfer rate to the cells. Thus, in order to optimize cell growth, viability, and productivity, it is essential that the optimal dissolved oxygen levels are maintained in the reactor fluid. No novel DO sensing technologies were developed in this work. Rather, an overview of the current available options is analyzed. Similar to pH sensors, for a disposable continuous bioreactor, either disposable DO sensors are required, or non-invasive sensors.

Similar to non-invasive pH monitoring, DO patches have also been developed for external sensing. Patches are placed on the inside of a transparent bioreactor vessel wall, and are typically excited by optical fibers, after which the detection of fluorescence by a phase fluorometer is used to determine the DO level [83] [84] [85]. However, most of these non-invasive methods are expensive and require peripheral equipment, although they can be used through multiple fermentation cycles.

With regards to disposable, invasive methods, plenty of options exist for DO sensing. The most common method is the use of a polarographic (Clark) cell, where the amount of current entering the cells directly correlates to the amount of oxygen entering the cell, as a partial pressure gradient is induced across the membrane based on pre-calibration [86] [87] [88]. Sensors that use methods such as fluorescence quenching also exist, in which a dye is illuminated, followed by the capture of the dye's emission fluorescence. The fluorescence lifetime is related to the oxygen concentration of the aqueous solution, and this the DO is determined [89].

## 3.6 Temperature Sensing

Temperature monitoring and control is important in biologic applications because cell cultures are typically more viable between certain temperatures. Thus, ensuring the temperature of the fluid in the bioreactor is known is necessary. For disposable bioreactors, either disposable temperature sensors, or non-invasive ones, would be required.

Many disposable temperature sensors exist on their own [90]. Most commonly, temperature is measured with an RTD, thermocouple, or thermistor [91]. However, it is common to find temperature sensing conducted on a pH or DO monitoring probe [92] [81].

Non-invasive temperature sensing has not been adapted in bioprocessing, due to the complexity of sensing internal temperature remotely. However, optical thermal sensors based on thermal imaging and infrared technology are plausible. Although infrared sensors are surface temperature imaging tools, calibration and further development of the setup apparatus can lead to externally mounted thermal imaging sensors. Further, the infrared camera may be screwed into a port on the headplate of the bioreactor, thus able to detect the fluid surface temperature. However, contamination concerns are still not eliminated, although they are minimized.

## 3.7 Cell Concentration Monitoring

Process control in biologic drug manufacturing often requires the monitoring of cell density or concentration. Additionally, academic or research and development causes require cell concentration monitoring in order to gain an understanding of the performance of the process and optimize future experimental procedures. Thus, a sensor to measure cell concentration online is important.

The most common cell density measurement technique is the measurement of the optical density of the fluid. While traditionally this measurement is done separately, recent technology has enabled online, continuous, real-time optical density (and thus, cell concentration) monitoring [93]. Additionally, non-invasive monitoring cell concentration monitors that do not measure optical density have been developed, such as permittivity measurements based on coplanar transmission lines [94], and flow-through (disposable, invasive) broth viscosity measurements [95].

Any of the alternate methods can be used in process sensing in the bioreactor, as long as the elements are non-invasive or disposable.

# Chapter IV
# Perfusion

# Abstract

Perfusion is the process of retaining cells in the bioreactor while removing protein product and waste materials. In order to do this, a membrane is typically used through which fluid passes due to a pressure differential created. In moving to a larger bioreactor, and also to improve potential perfusion work rate, a different perfusion probe is considered, called the harvest probe, which consists of multiple hollow-fiber membranes in parallel. In order to assess the characteristics of the new membrane, Computational Fluid Dynamics (CFD) and testing is employed.

A preliminary 2D CFD study informs the initial iteration of the spacing of the hollow-fibers, based on the stagnation point characteristics of the flow. After the first prototype is manufactured, testing is conducted at typical operating conditions, and the initial harvest probe is found to perform successfully at operating conditions, although fouling of the membrane still occurs at the same conditions where fouling in previous membranes occurs. A concern that arises from the initial round of testing is the fragility of the membrane, as some damage to the fibers occurred during the testing. Thus, in order to create a second design iteration, understanding the forces acting on the individual hollow-fibers was necessary, so as to replicate such conditions in structural integrity testing during development. To that end, a 3D CFD study was conducted in which the harvest probe was simulated in the bioreactor macroscopically as a single cylinder, so as to aid with convergence in the bulk flow. These bulk flow profiles were then exported to a 2D microscopic analysis, where the individual hollow-fibers were all accurately modeled, and the flow conditions surrounding the fibers, as well as the forces on them, were predicted. These results were then used to design testing setups for the design iterations by the contracted company manufacturing the harvest probe, to ensure it can withstand the flow conditions within the bioreactor, without compromise of form of function.

Further, these models can be used to analyze other aspect about the design and conduct future analysis.

## 4.1 Introduction

Continuous perfusion bioreactors require a sufficient membrane filter area to effectively perfuse volume from the vessel at the appropriate rate to maintain equilibrium. The currently used 1 litre Infors-2 vessel allows for 0.5 ml/min perfusion rate through the use of 2 FISP[5] membranes [96]. The opportunity to increase the efficiency and capability of perfusion presented itself. At the same time, a shift in the reactor volume to 5.0 liters was proposed. Instead of scaling up with the use of FISP membranes, the opportunity to increase the efficiency and capability of perfusion presented itself. The use of a hollow-fiber harvest probe membrane is proposed, which is a probe that runs vertical in the reactor fluid, composed of multiple parallel hollow-fibers membrane strands spaced apart within the probe through which the perfusion takes place. The probe will require only 1 port (PG 13.5) in the headplate of the bioreactor, and increase the filter surface area to 338 $cm^2$ due to the numerous small hollow-fiber membranes. The perfusion volume capability due to the added surface area will increase to 7 ml/min (10.08 L/day). In contrast, a scaled up double-FISP membrane would have achieved 2.5 ml/min perfusion at the standard flux. Thus, with the change in the use of membrane technology, the perfusion capability of the system can be increased, along with a decrease in the number of working parts.

In order to gauge the viability of the concept and tweak design parameters, the use of Computational Fluid Dynamics (CFD) is used. There are multiple qualitative and quantitative learnings that can occur from CFD, which can inform the design process, and can aid in guiding rapid design iterations. The areas of interest that govern the quality of perfusion in the bioreactor are its propensity to fouling, the fluid flow profiles around the perfusion harvest probe, the strength of the harvest probe against cross-flow, and other such issues. In this study, these parameters of interest are studied through the shear experienced by the hollow-fibers in the harvest probe, the velocity profile of the bioreactor, and the fouling properties (location of stagnation point, etc.).

[5] FISP refers to the perfusion membranes developed by Flownamics [96]

## 4.2 2D Computational Fluid Dynamics (CFD) Study and Testing

A 2D CFD study conducted by Amos Lu (Braatz Lab, MIT) evaluated certain properties of the reactor in the vicinity of the proposed harvest probe. Using a slice of the bioreactor at a point where the impellers are located, a 2D geometry of the impeller was created. Using the Moving Reference Model[6], the 2D model was simulated as having a rotating impellers at various rotational velocities [30]. The utility of such a 2D model is in allowing for rapid decision-making regarding design parameters. However, the learnings are qualified by drawbacks such as the fact that the 2D model over-simplifies the geometry in the z-domain. It assumes the impellers and all probes run the whole height of the vessel. Clearly this is not the case, with a lot of variance in the z-direction. Hence, the results get more inaccurate in more remote areas of the reactor. That said, there is plenty of useful information to be gained in running such an analysis, most notably qualitative understanding of the flow in such a reactor.

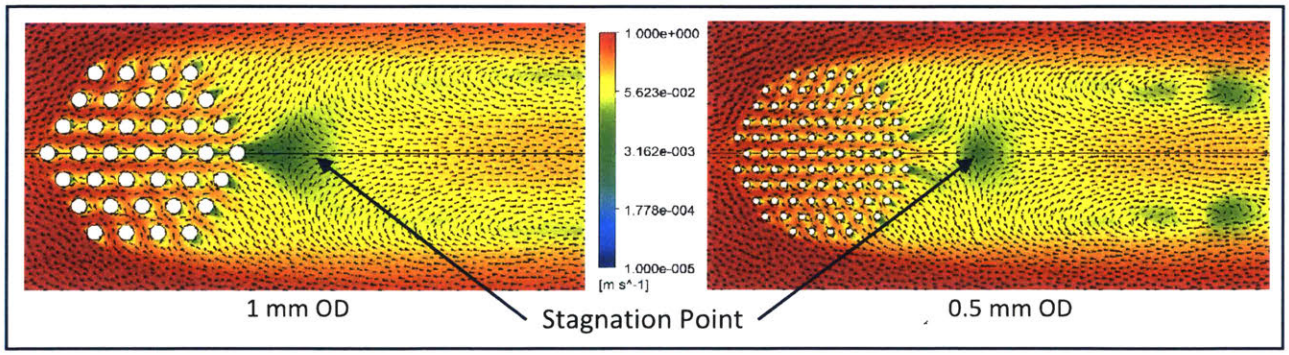


***Figure 4-1* 2D CFD Comparison of Hollow-fiber Diameters** A close up look of the velocity profile of the hollow-fibers in the 2D infinite flow field simulation with the velocity plotted logarithmically to a max of 1 m/s (the input, shown in red). The arrowheads indicate the direction of the velocity vectors at those points. *(Amos Lu)*

First, the harvest probe geometry with all the hollow fibers were modeled in a 2D infinte flow field simulation, with an inlet condition of 1 m/s and a pressure outlet far downstream. As can be seen from Figure 4-1, the stagnation point for the flow in the case with 1 mm outer diameter (OD) fibers is much closer to the cluster than in the case of 0.5 mm OD.

[6] The Moving or Multiple Reference Frame (MRF) model in CFD is a steady-state approximation model. Cell zones are defined within the geometry, and these zones move at different speeds. The flow in each zone is solved independently using moving reference frame equations, and the interface of zones are transformed to allow for variables across zones to calculate boundary fluxes [30].

This indicates a higher propensity to fouling under the flow conditions by the 1 mm OD fibers. The smaller 0.5 mm fibers are less likely to foul, as well as have increased filter surface area by means of their geometry. However, there is a fragility trade-off as they are more likely to compromise their integrity. This would be catastrophic and allow for the filter to have a path of least resistance for the cells to accidently perfuse thorugh, rendering the membrane useless. Thus, further studies to test the structural integrity and the shear experienced by the fibers are also conducted later in this study.

Second, the MRF model was implemented to determine the average shear rates experienced by the hollow fibers, and compare it to the average shear rates experienced by the FISP. A higher shear rate near the surface of the harvest probe allows for the de-fouling due to the tangential flow filtration (TFF) mechanism. However, higher shear also indicates higher forces acting on the fibers, and thus, higher likelihood of fracture or other failure.

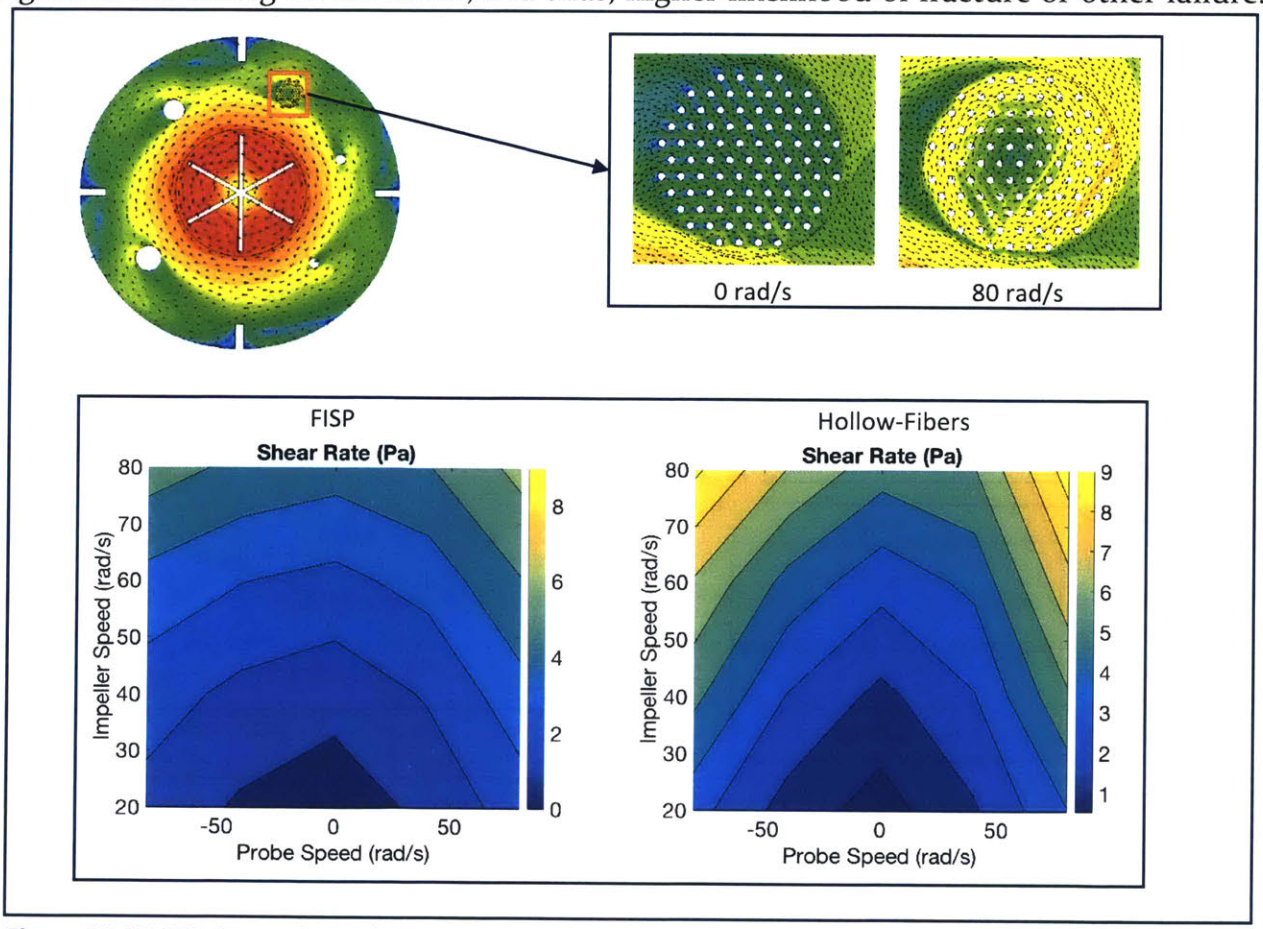


***Figure 4-2* 2D CFD Comparison of Shear Rate on FISP vs Harvest Probe** The 2D simulation indicates lower average shear rates for the hollow fibers as compared to the FISP, for the same impeller speeds. Allowing the hollow-fibers harvest probe to also rotate allows for higher shear rates. *(Amos Lu)*

As can be seen in Figure 4-2, the harvest probe itself needs to be rotated at about 50 rad/s to achieve the same shear rate as the stationary FISP does.

At this point, developing a rotating harvest probe was not possible. Thus, the development of the stationary probe focused on proper spacing of the hollow-fibers to decrease the propensity of fouling. Informed by the results in the 2D analysis (Figure 4-1), the hollow-fibers were spaced at 1 mm and developed by Goddard Technologies for the purpose of this investigation. After the development of the initial prototype, the hollow-fiber harvest probe was physically tested according to the setup shown in Figure 4-3. The headplate of the 1 L Infors 2 bioreactor was modified as shown in Figure 4-3, and equipped with a downstream flow meter and pressure sensor and a syringe pump assembly to control the flow. For the initial round of qualitative testing, no pressure and flow data was recorded (Table 4-1). For the second round of quantitative testing, flow and pressure was collected and analyzed. In testing the hollow-fiber harvest probe's perfusion capabilities, spent reactor fluid from a previous run that was stored in the cold room for 8 days was used. The control of the syringe

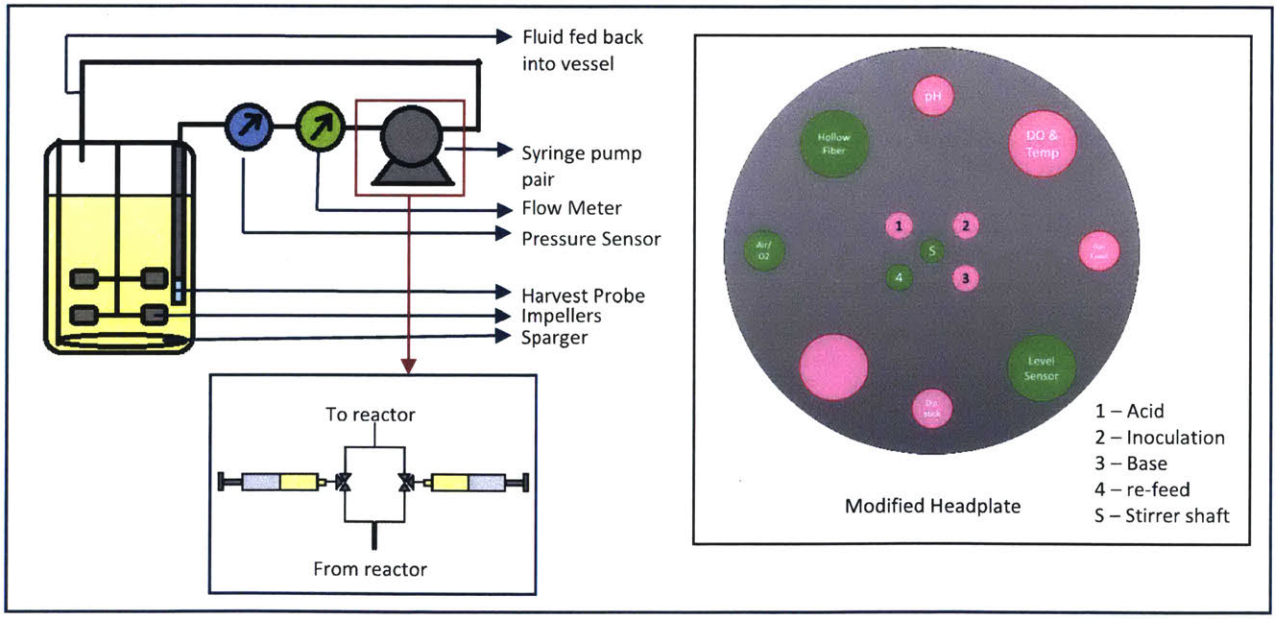


***Figure 4- 3* Harvest Probe Experimental Testing Setup** Schematic of physical test setup for the harvest probe prototype testing; the syringe pump assembly is controlled by 3-way valves, where one syringe pulls media from the reactor while the other simultaneously pushes previously pulled fluid back into the reactor. The roles of the syringes switch at the end of the stroke, as controlled by the self-developed MATLAB code. The modified headplate of the Infors 2 reactor is shown on the right. The green ports were used during testing while the pink ports were not used for the purpose of this test.

pumps was done using a syringe pump controller for the first round, and using self-developed MATLAB code to run the syringes in the second round of testing.

The first round of testing is shown in Table 4-1. Positive flow rate is perfusion, whereas negative flow rate indicates a backwash mechanism. The design of experiments was based on typical operating conditions that the bioreactor will experience during the course of a production run, based on previous runs conducted in the lab.

| Stirrer Speed (rpm) | Sparge Rate (SLPM of $O_2$) | Flow Rate (ml/min) | Notes |
|---|---|---|---|
| 0 | 0 | 0.5 | Clean; no air bubbles, no cells |
| 400 | 0 | 0.5 | Clean; no air bubbles, no cells |
| 800 | 0 | 0.5 | Clean; no air bubbles, no cells |
| 800 | 0 | 1 | Clean; no air bubbles, no cells |
| 800 | 0.04 | 2 | Some air bubbles |
| 800 | 0.1 | 2 | Some air bubbles |
| 800 | 0.2 | 2 | More air bubbles |
| 800 | 0.04 | 4 | Some air bubbles |
| 800 | 0.1 | 4 | Some air bubbles |
| 800 | 0.2 | 4 | Tubing crushed due to vacuum; possible fouling here |
| 800 | 0.1 | -4 | Initialized backwash; tubing recovered |
| 800 | 0.1 | -8 | Higher backwash |
| 800 | 0.1 | 2 | Perfusion post-backwash; no cells |
| 800 | 0.1 | 4 | Higher perfusion; no cells, some air bubbles |

***Table 4-1* Harvest Probe Experimental Test Results** Qualitative testing of hollow-fiber harvest prototype to determine functionality and viability

From the results, it is apparent that the harvest probe performed well at the desired flow rates. Under typical operating conditions, the bioreactors conditions experience an impeller rate of 800 rpm at an oxygen sparge rate of 0.04 standard liters per minute (SLPM). The FISP perfusion rate is 0.5 ml/min average (2 ml/min for $1/4^{th}$ period, followed by no-

flow for 3/4$^{th}$ period) when in forward flow, and 8 ml/min backwash (constant). At 800 rpm, 0.04 SLPM oxygen feed, and a forward flow rate of 2 ml/min, the harvest probe experienced very minor air bubbles – an indication that there were no leaks or loss of integrity. Additionally, the clear nature of the removed fluid confirmed the lack of cells allowed through the membrane. After multiple repeated runs at these conditions, the membrane operated as expected under typical operating conditions, with fouling occurring at the higher flow rates, that was corrected with a backwash cycle.

The existence of a few air bubbles can be explained by air trapped in the hollow-fiber structure prior to testing. Once the flow rate was further ramped up beyond operating conditions, for a lengthy period of time, the tubing started getting crushed due to the vacuum created. This indicates the initialization of possible fouling within the membrane inside the reactor, and the backwash cycle was immediately initiated. Backwashing seemed to have been successful, as after the cycle, further perfusion seemed to proceed without fault.

However, a concern that arose from testing was the fragility of the membranes in the agitated environment, as at some point, the membrane suddenly lost integrity and allowed cells to pass through it. This was evident from the yellow appearance of the fluid (Figure 4-4). Upon ending the run, the dislocation of one of the fibers from its groove was evident, and attributed as the cause of the loss of integrity. However, a Scanning Electron Microscope (SEM) image of the fibers indicated a tear along the length of a fiber, which would also explain the loss of integrity (Figure 4-4). While this was not conclusive evidence that fracture occurred as a result of operating the fibers under test conditions, as opposed to improper handling of the membrane, this reiterated the need for structural strength testing of the fibers to withstand operating conditions going forward.

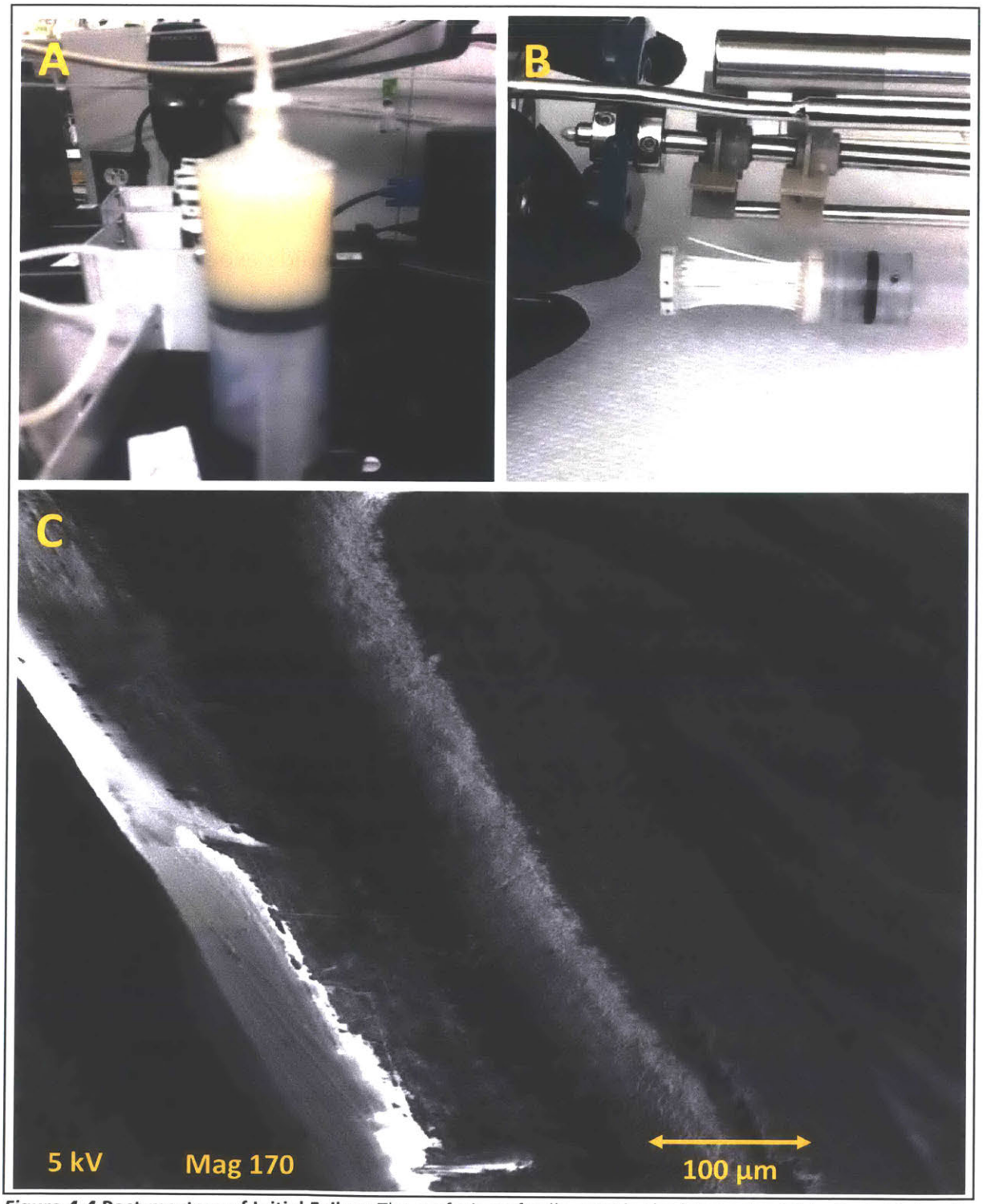


***Figure 4-4* Post-mortem of Initial Failure** The perfusion of cells outside the bioreactor (A) indicated integrity failure of the hollow-fiber membranes. Initial investigation (B) indicated a fiber may have been dislodged leading to the breach. However, upon further investigation using a Scanning Electron microscope (C), the potential of fiber fracture was made apparent.

With the moderate success of the initial qualitative prototype testing, and the 2D CFD simulations guiding the design parameters, the move to a more complete design for a scaled-up design was undertaken. To get a picture of the most extreme conditions experienced by the harvest probe at any point, in regards to any process parameter, a full 3D simulation of the bioreactor was undertaken, as outlined below. The 3D study can be used to understand the forces acting on the fibers, so as to guide experimental testing of the fibers during the design process.

## 4.3 3D Computational Fluid Dynamics Study

With the moderate success of the initial qualitative prototype testing, and the 2D CFD simulations guiding the design parameters, the move to a more complete design for a scaled-up design was undertaken. To get a picture of the most extreme conditions experienced by the harvest probe at any point, in regards to any process parameter, a full 3D simulation of the bioreactor was undertaken, as outlined below. The theory and equations that underlie the CFD simulation model solver is not reproduced here, although it the setup conditions are explained, for which the equations are available online. ANSYS Fluent is used for the solution.

### 4.3.1 Methodology and Design of Experiments

The 3D solution portrayed in the steps below were evaluated at 4 different impeller speeds (300 rpm, 600 rom, 900 rpm, 1200 rpm) so as to encompass the operating range of a typical bioreactor production run, and provide enough intermediate points for fairly accurate interpolation. A SolidWorks model of the complete bioreactor with every probe, fitting, etc. was used in the model, with one exception. The actual harvest probe with the numerous (48) hollow-fibers was modeled as a single cylinder in the 3D flow. This was done to aid with the success of convergence of the simulation, by making the valid (and testable) assumption that the bulk flow properties of the bioreactor would not be affected by the switch. This was later validated in the next 2D simulation.

The 3D approximate solution acts as a good half-way point towards leveraging more results. In the case of the getting flow properties (and shear, stagnation points, etc.) around the hollow-fibers, the 3D bulk flow solution was used in this way: the flow properties at an appropriate distance away (so as to ensure that the flow vectors along this boundary are independent of the local flow caused by switching the harvest probe cylinder to an actual representation of the hollow-fibers) from the harvest probe cylinder were exported, and these values were appropriately used in a 2D infinite flow field simulation to determine the

local properties experienced by the hollow-fibers. The major motivation of the study is threefold:

(1) Determine shear experienced by the hollow-fibers in order to enable experimental structural integrity testing
(2) Develop an understanding of bulk fluid flow profiles in the bioreactor to ensure appropriate mass transfer and mixing, as well as enable future studies
(3) Determine the fouling properties based on the microscopic flow profiles in the vicinity of the harvest probe

### 4.3.2 Geometry

The geometry of the bioreactor used in the simulation mimics the scaled-up concept of the 5-liter vessel set for development for use in the lab (Figure 4-5). As noted previously, the only notable difference was the change from the actual hollow-fibers to a cylinder that would have enclosed all the fibers if they were present. As explained, this is only done in

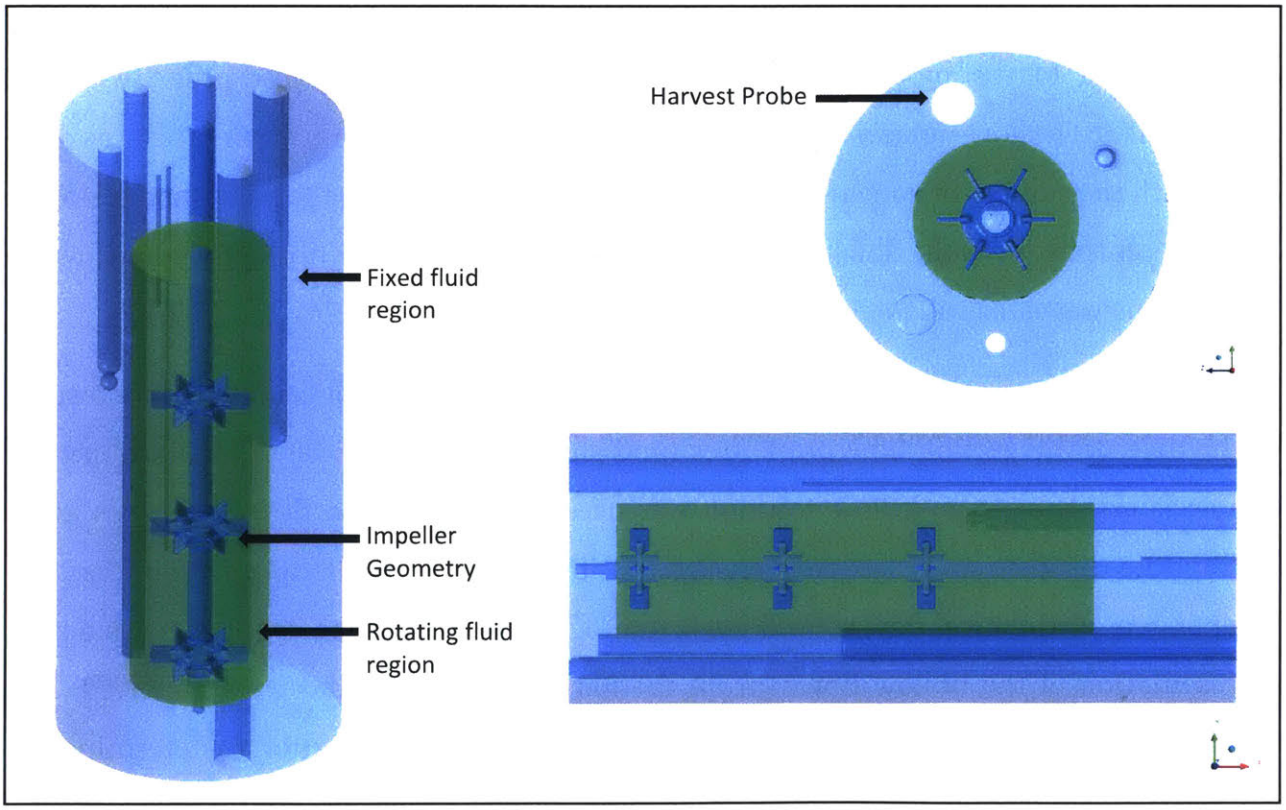


***Figure 4-5* Geometry and MRF Regions of the 3D Study** with the rotating region shown in green

the 3D simulation, and is a valid assumption in solving bulk flow profiles, as multiple fibers arranged cylindrically have the same bulk flow pattern as flow around a cylinder. This is later validated in the 2D analysis. The geometry was modeled in SolidWorks and exported to ANSYS Design Modeller. An area enclosing the three impeller shafts was defined as the *Rotating Fluid Region*, while the rest of the bioreactor was defined as the *Fixed Fluid Region*. This was done so as to use the Multiple Reference Frame model in simulating the 3D solution. The top surface of the bioreactor was defined separately as a named selection called *Static Free Surface*, so as to assign it different boundary properties.

### 4.3.3 Meshing

The geometry was then meshed using the in-built ANSYS Meshing Software. The mesh was divided into 3 regions – the impellers blades, the probes/shafts, and the bulk (rest of the geometry). Region 1 (impeller blades) was meshed using the Mesh Sizing option. It consisted of 735 faces (highlighted in blue in Figure 4-6) soft meshed with an element size of 2 e-03 m and a minimum size of 1 e-03 m. Region 2 (probes and shafts) was also meshed using the Mesh Sizing

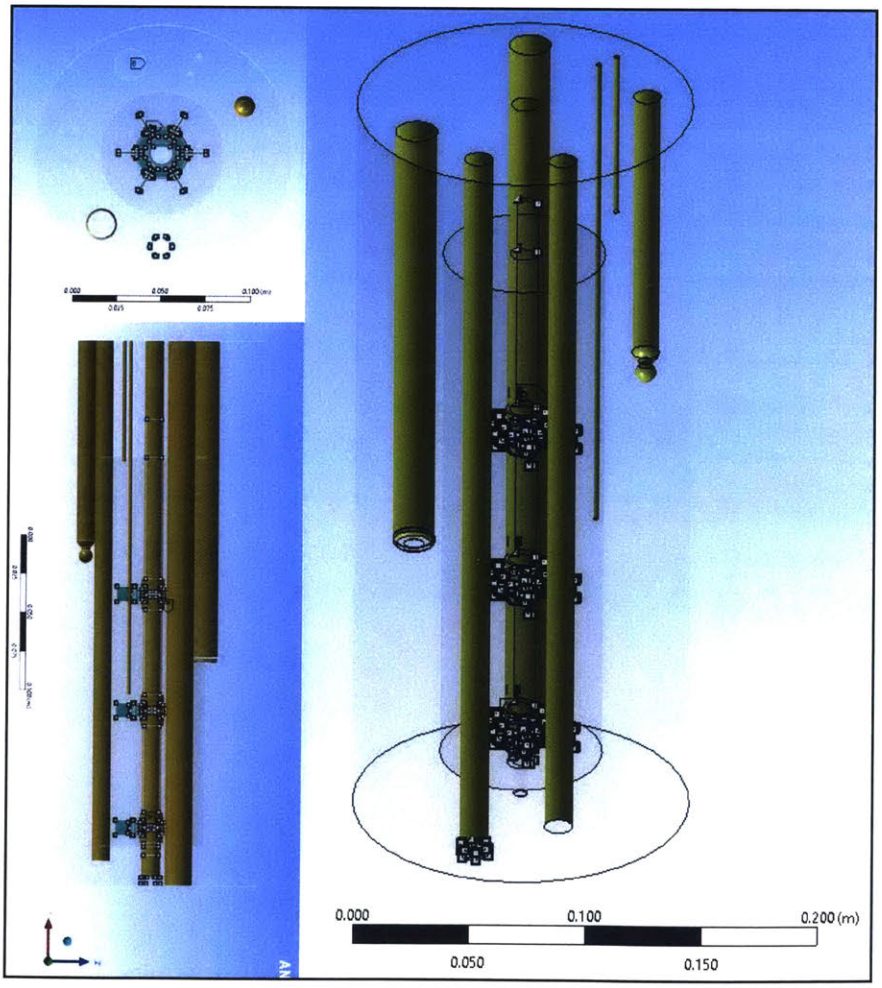


***Figure 4-6* Mesh Sizing in the 3D Study** was used to separately mesh the regions of expected sharp gradients – one group is shown in blue and the other is shown in yellow

option. It consisted of 24 faces (highlighted yellow in Figure 4-6) soft meshed with an element size of 2 e-03 m and a minimum size of 1 e-03 m. In this case, both Region 1 and 2 were meshed with the same Mesh Sizing options. However, to aid with future projects using this geometry, there were separated into distinct regions because convergence may often depend on refining the mesh of one of the regions, depending on where the gradients are highest. Region 3 (the rest of the geometry) was sized using the Cut Cell Assembly Meshing Method. A curvature size function was used, with medium relevance center, high smoothing, a minimum size of 1 e-03 m, and a maximum tetrahedral size of 8 e-03 m. The overall mesh of the geometry resulted in 567,764 nodes, and 506,233 elements. The total

mesh can be seen in Figure 4-7, including with some section cuts to show the internal meshing.

### 4.3.4 Setup

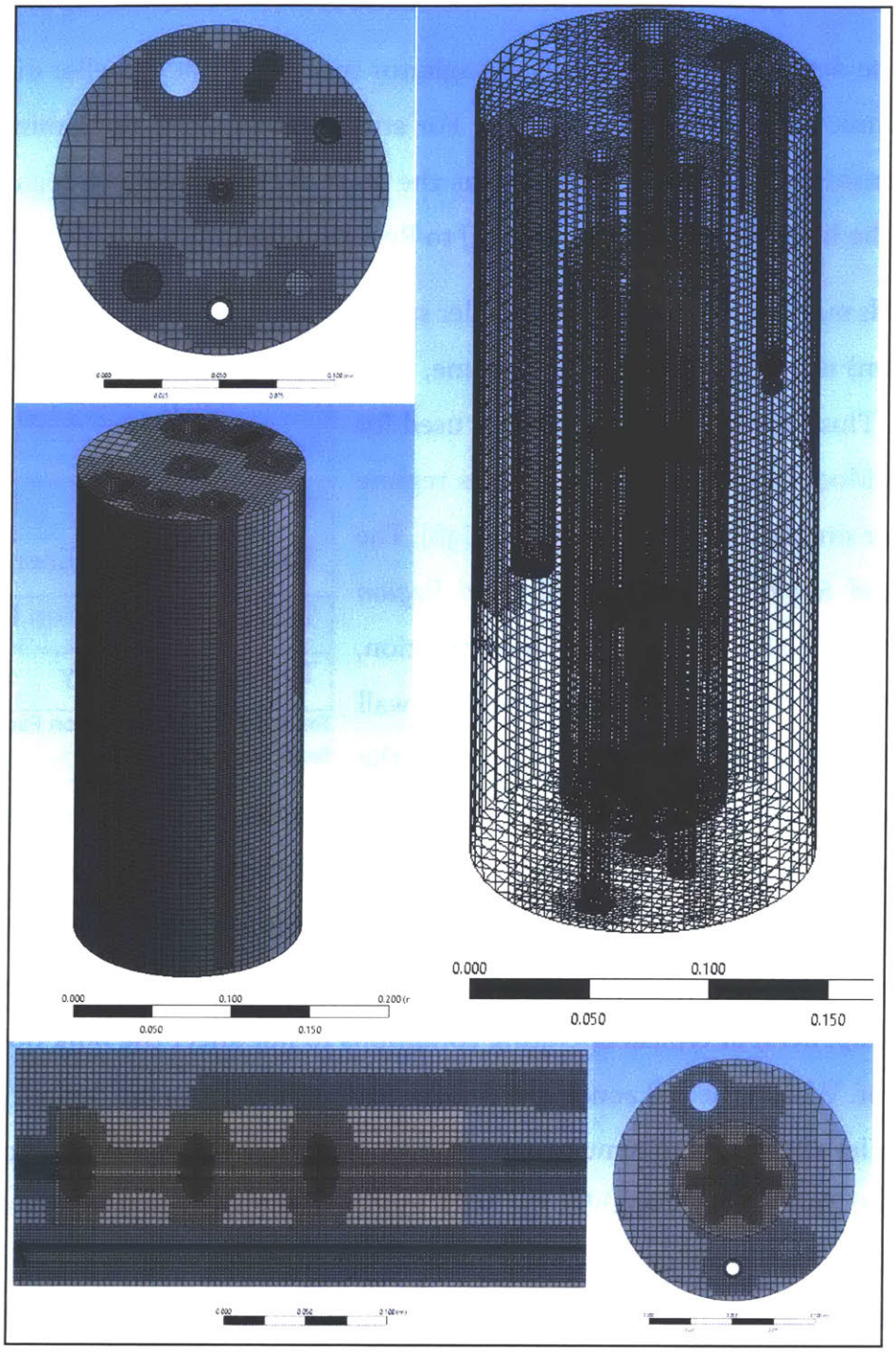


***Figure 4-7* Mesh of the 3D Study** The entire mesh is shown in the top three images. The bottom two images are cross-sections of the mesh to display the interior meshing.

The mesh was then imported into the ANSYS Fluent Solver. For a stirred tank, the Reynolds number is defined as:

$$Re = \frac{\rho N D^2}{\mu}$$

where ρ is the density of the fluid, N is the agitator speed, D is the impeller diameter, and μis the dynamic viscosity of the fluid [32]. For stirred bioreactors, the laminar region is generally considered when Re < 10, whereas the start of the turbulence region has wide variance in the literature, from Re > 480 [33] to Re > 1200 [34].

The Reynolds number for the slowest impeller speed case (300 rpm) is in the fully turbulent regime, with Re = 14,000. Thus, the k-epsilon model was used for the Viscous Model, commonly used in this regime for bioreactor simulations [32] [37] [28] [25] [38]. The *Rotating Fluid Region* and the *Fixed Fluid Region* were defined as walls with a "No Slip" condition, whereas the *Static Free Surface* was defined as a wall with zero-shear conditions to properly simulate the boundary constraints within the working of the MRF model. Although the harvest probe (hollow-fibers) is actually pulling protein product and therefore have minor mass and velocity flow associated with it, it is modeled as a wall. This is because the outflow velocity from the fibers is negligibly slow (on the order of $10^5$ to $10^7$ times slower than the velocities around the impellers) at typical operating conditions to not affect the bulk flow profile of the bioreactor. Within the cell zones, the rotational zone was set to the desired rpm (based on the impeller speeds being simulated), whereas the other zones were set to having no frame motion. This properly enables the MRF model to simulate impeller rotation within the vessel. The fluid in all zones was set to water at standard temperature and pressure (STP) conditions, which has properties that are fairly similar to the fluid mix within the bioreactor.

| | |
|---|---|
| Pressure | 0.3 |
| Density | 1 |
| Body Forces | 1 |
| Momentum | 0.1 |
| Turbulent Kinetic Energy | 0.1 |
| Turbulent Dissipation Rate | 0.1 |
| Turbulent Viscosity | 1 |

***Table 4-2* Under-relaxation Factors in the 3D Study Simulation**

The SIMPLE pressure-velocity coupling solver was used, with a Least Squares Cell Based gradient, second order pressure and momentum equations, and first order turbulent equations. The under-relaxation factors to achieve convergence are shown in Table 4-2. A Standard Initialization was used with default settings, and the solution was accepted as having converged when all the residuals were below 10 e-04.

### 4.3.5 Results

After the solution converged, the results were exported to CFD-Post, the post-processing toolbox in ANSYS Fluent. The 1200 rpm case is used as an example to display all the studies conducted for various parameters in this section, whereas the full results are available in Appendix C. From Figure 4-8, which plots the static pressure in the reactor, it is evident that the impellers have clear regions of leading high-pressure edges, and low-pressure lagging edges, which is consistent with the literature and theory.

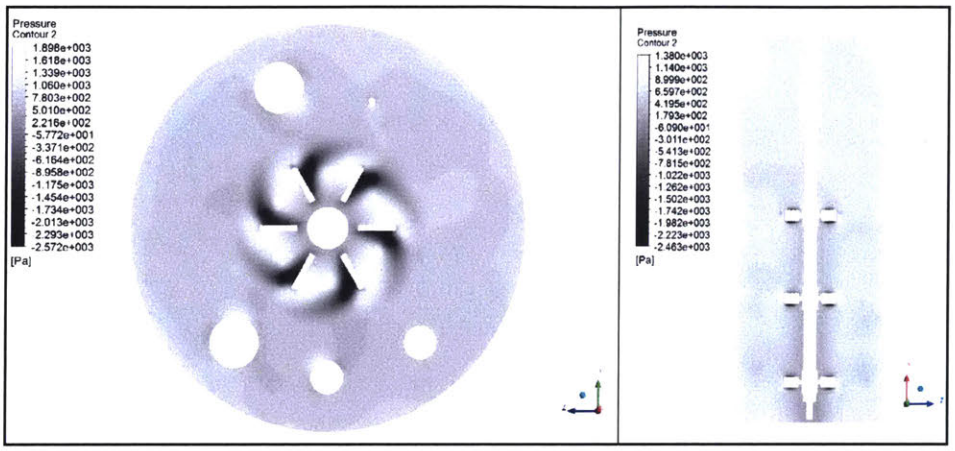


***Figure 4-8* Pressure Profile Results in the 3D Study** The static pressure gradients for the 1200 RPM case in the vertical and horizontal planes.

Next, the turbulence eddy dissipation was plotted on two vertical planes that bisect each other and the impeller shaft, as well a horizontal plane that intersects one of the impeller blades. The results are shown in Figure 4-9. It can be seen that the regions of high turbulence eddy dissipation are around the probes generating velocity as well as around the probes that obstruct fluid flow.

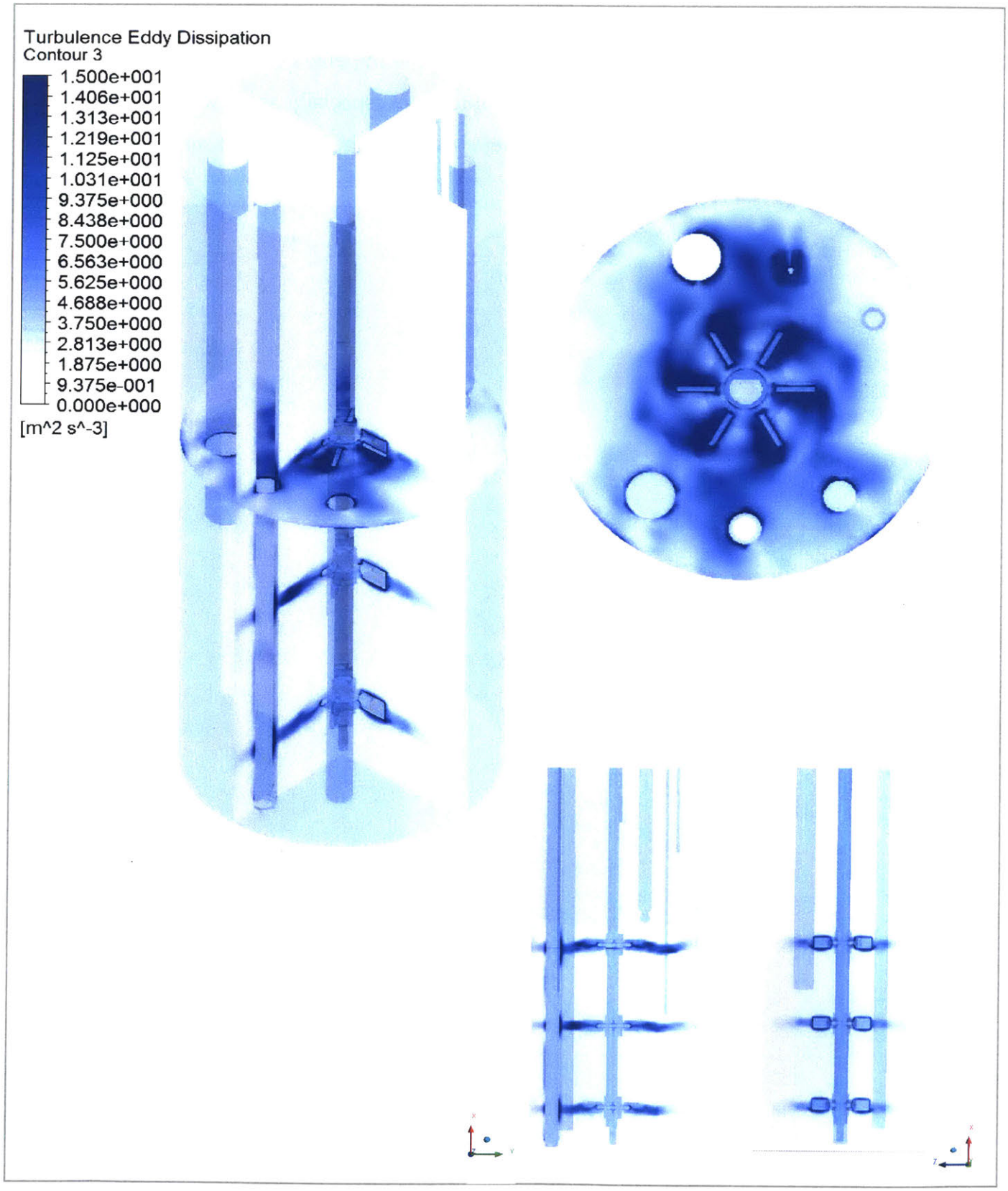


***Figure 4-9*** **Turbulence Eddy Dissipation Profile Results in the 3D Study** in the horizontal and vertical planes of the bioreactor in the 1200 RPM case

The wall shear experienced by the solid parts in the bioreactor vessel are shown in Figure 4-10. The probes that are in-line with the height of the impellers experience the highest shear on those parts, as expected. These values are especially vital when designing reinforcements on the harvest probe, and other structural, shear-resistant modifications.

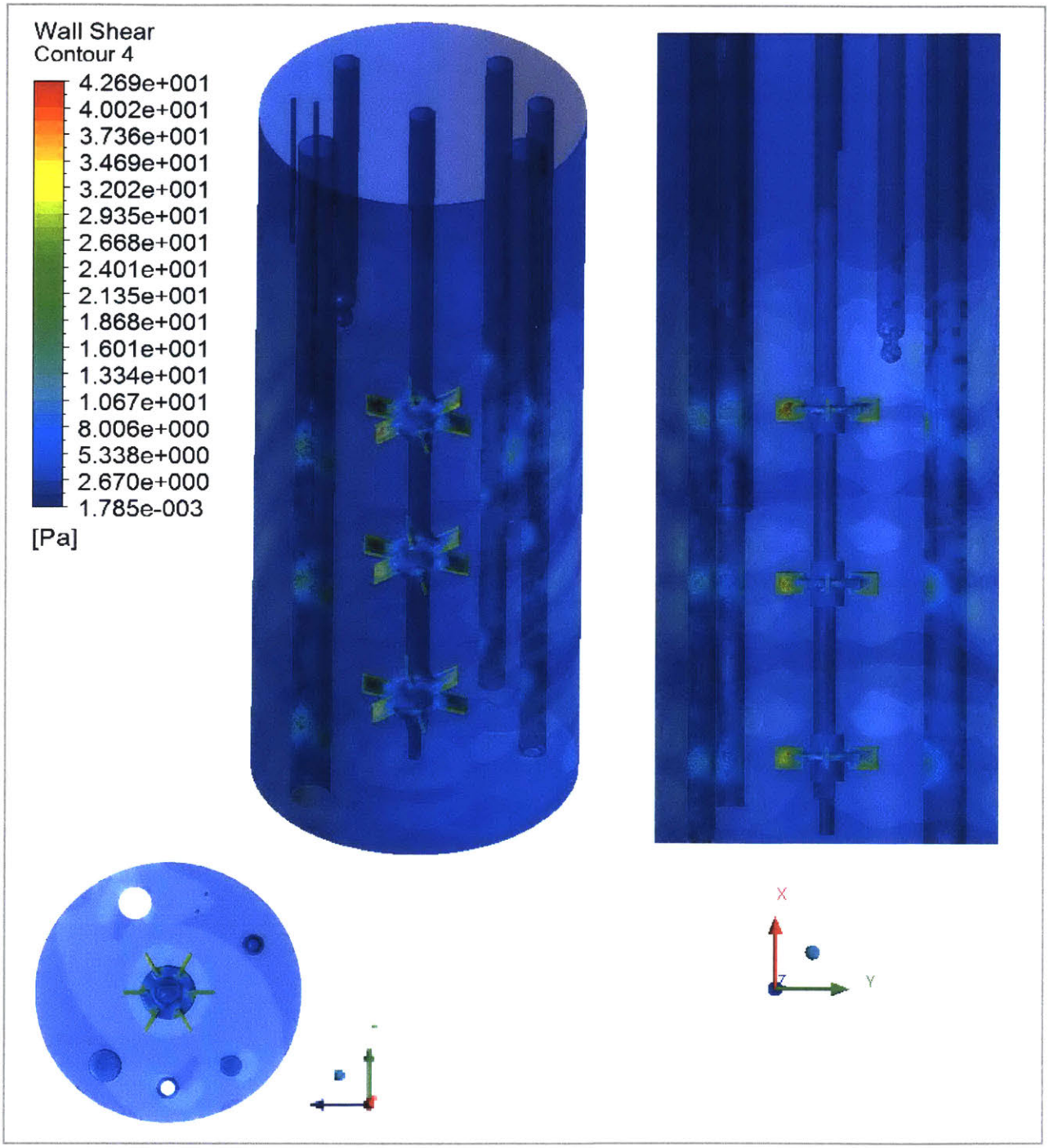


***Figure 4-10* Wall Shear Results in the 3D Study** The wall shear on every wall of the vessel shown isometrically, from above, and from the side, for the 1200 RPM case

The velocity profiles in the two bisecting vertical planes and the horizontal plane, along with a volume rendering of the velocity at every point within the reactor are shown in Figure 4-11. Additionally, streamlines using 50 starting seed points are generated. The streamlines show that solid-body rotation is avoided (that is seen when there are no probes in the vessel). The velocity magnitude profiles are as expected, with the highest regions velocities around the impellers. The region near the surface experience very low velocities. The max velocities in the vessel in this 1200 rpm case is 4.833 m/s.

Three distinct flow pattern regions develop in the vertical planes, which is similar to some to the "parallel flow" pattern seen in the literature [44]. The velocity vectors can be seen in Figure 4-12. The analysis of the velocity profiles and bulk flow patterns are conducted in detail in Chapter 2 of this thesis, and is avoided here. The purpose of this Chapter is to investigate flow affecting the harvest probe, and thus will commence investigating it without re-characterizing the flow in the vessel.

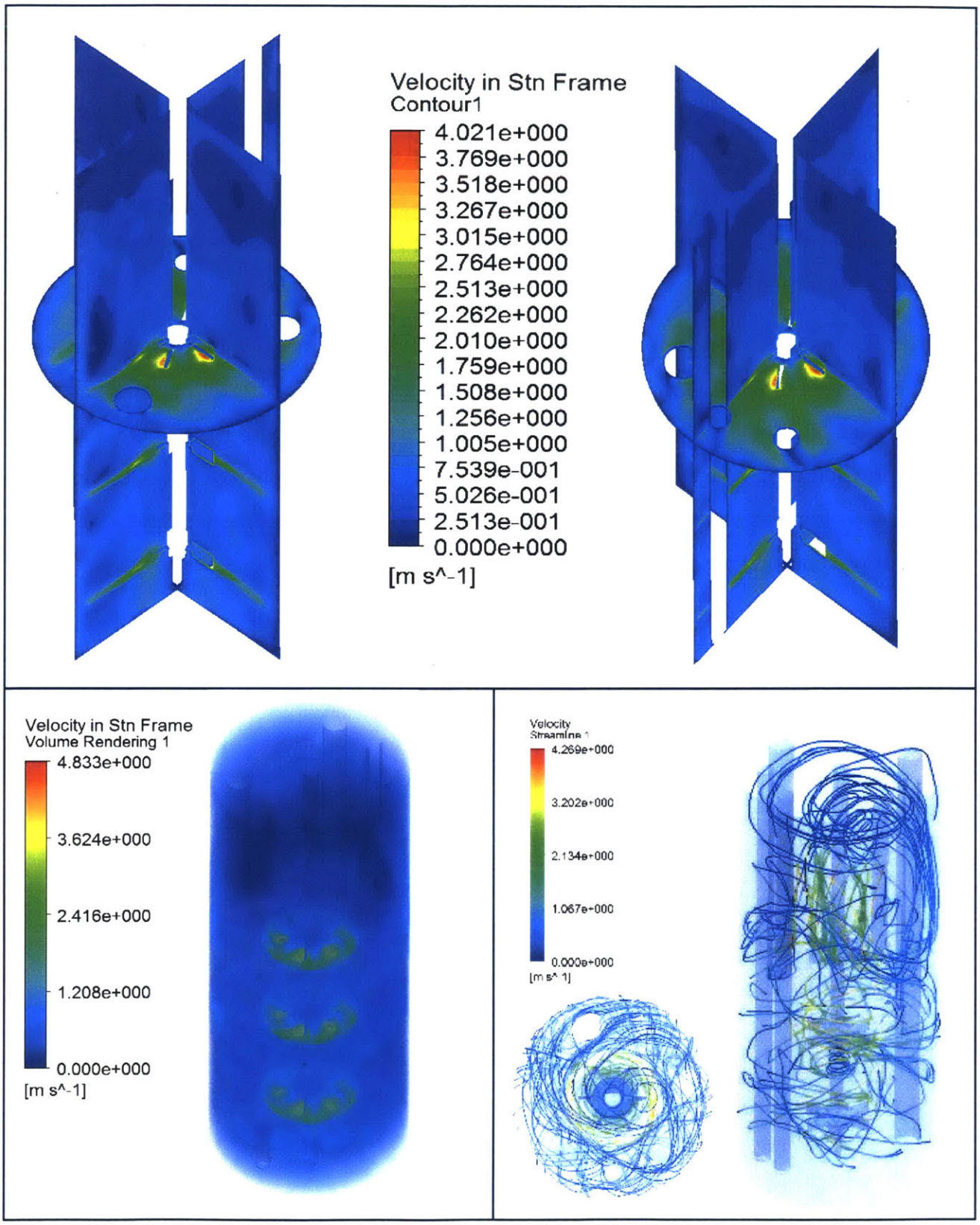


***Figure 4-11* Velocity Profile Results in the 3D Study** Top: The velocity contours displayed on the horizontal and vertical planes; Bottom-left: velocity volume rendering; Bottom-right: velocity streamlines

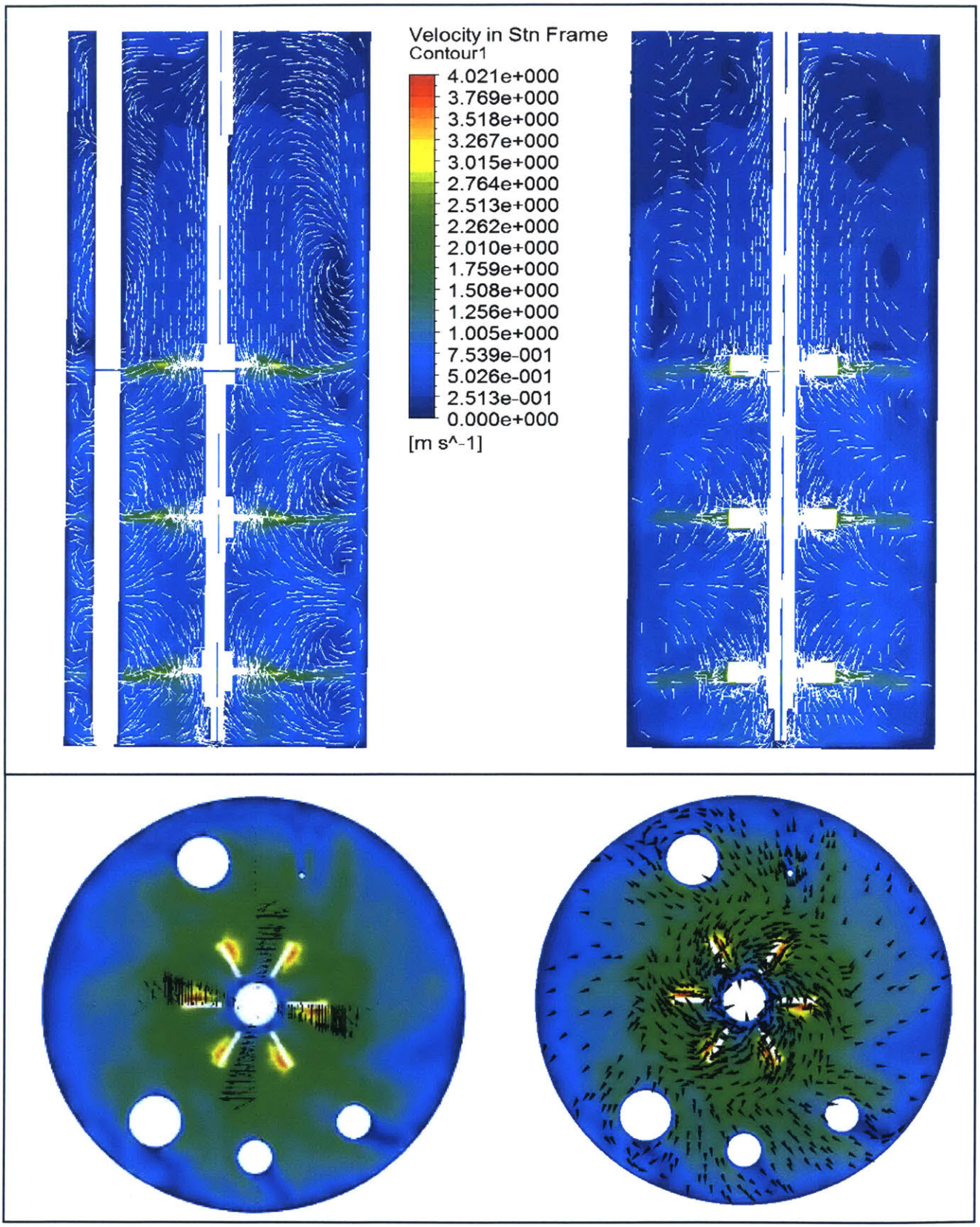


***Figure 4-12* Flow Vector Results in the 3D Study** Top: flow vectors of horizontal slices with total velocity magnitude, and direction vectors in the vertical direction; Bottom-left: flow vectors of vertical planes viewed from above; Bottom-right: flow vectors in the horizontal plane viewed from above

### 4.3.6 Exporting Values

For this scenario, in order to determine the shear and flow properties around the individual hollow-fibers, the bulk 3D model values were manipulated. A Surface of Revolution (SOR) at a distance 35 mm away from the center of the harvest probe cylinder was created, as shown in Figure 4-13. The velocity vector values (in each x, y, and z directions) were then exported at each node of the SOR. The assumption is that at this distance away from the harvest probe, the bulk flow should be sufficiently representative of the bulk flow even in

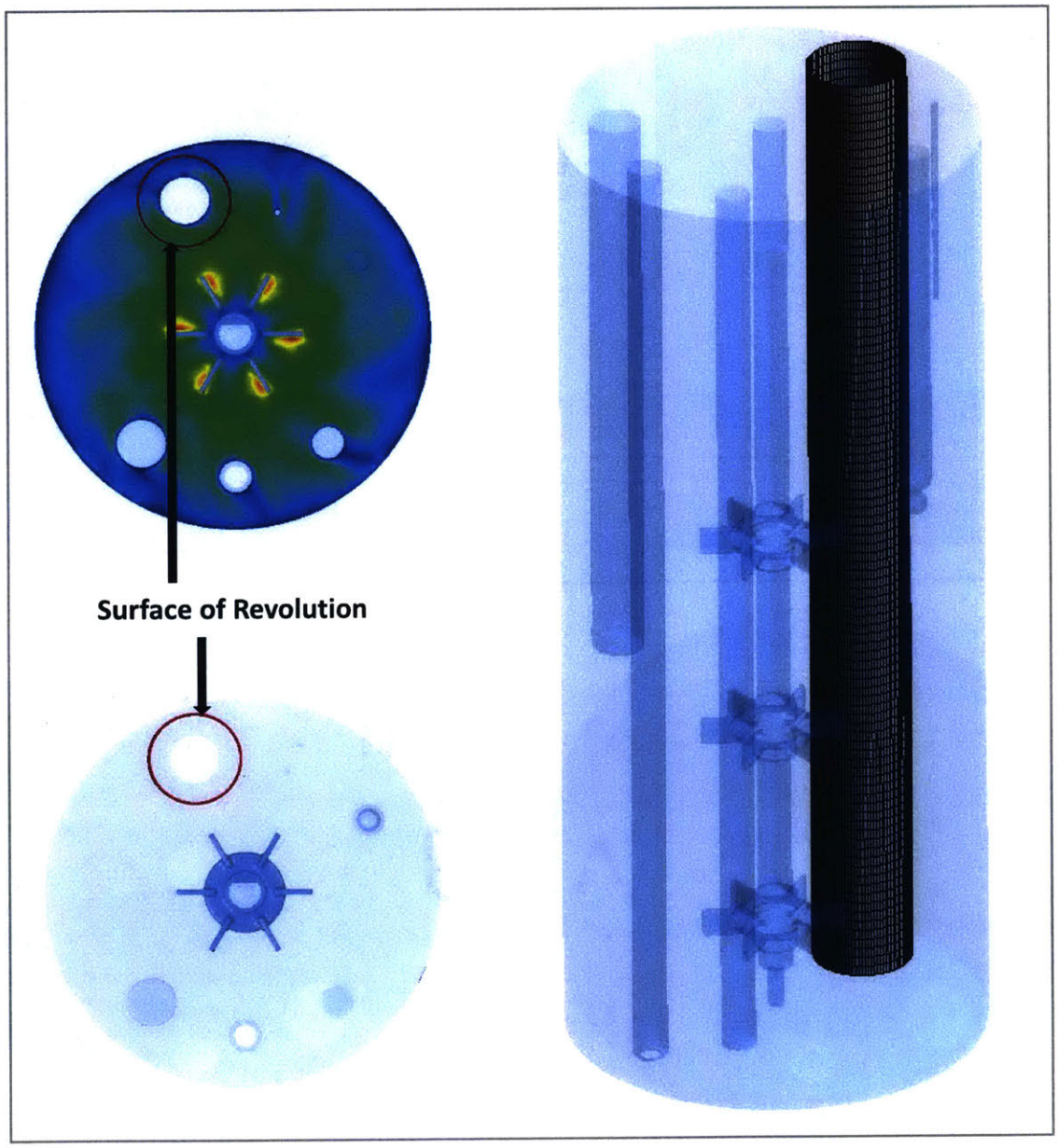


***Figure 4-13*** **Surface of Revolution** used to export values from the solution

the case when the harvest probe cylinder was modeled as individual hollow-fibers. In other words, the flow parameters are independent of local effects at the harvest probe location. This assumption is validated in the following 2D simulation.

The velocity vectors were broken into their x, y, and z components. Ignoring the velocity vectors of the z-direction (vertical), the x-velocity and y-velocity at every point was used to compute the corresponding velocity vector towards the probe center by normalizing the vector (see Box 4-1). This enables the determination of the maximum velocity magnitude (positive or negative) that the harvest probe faces normal to its surface at every height. For every ring around the SOR (i.e., at every discretized height), there are 100 nodes. The maximum absolute velocity vector at each ring was found. This allows for determining the flow and shear experienced by the harvest probe along the length of the vessel. The results of this can be seen in in the 2D analysis conducted using the SOR results.

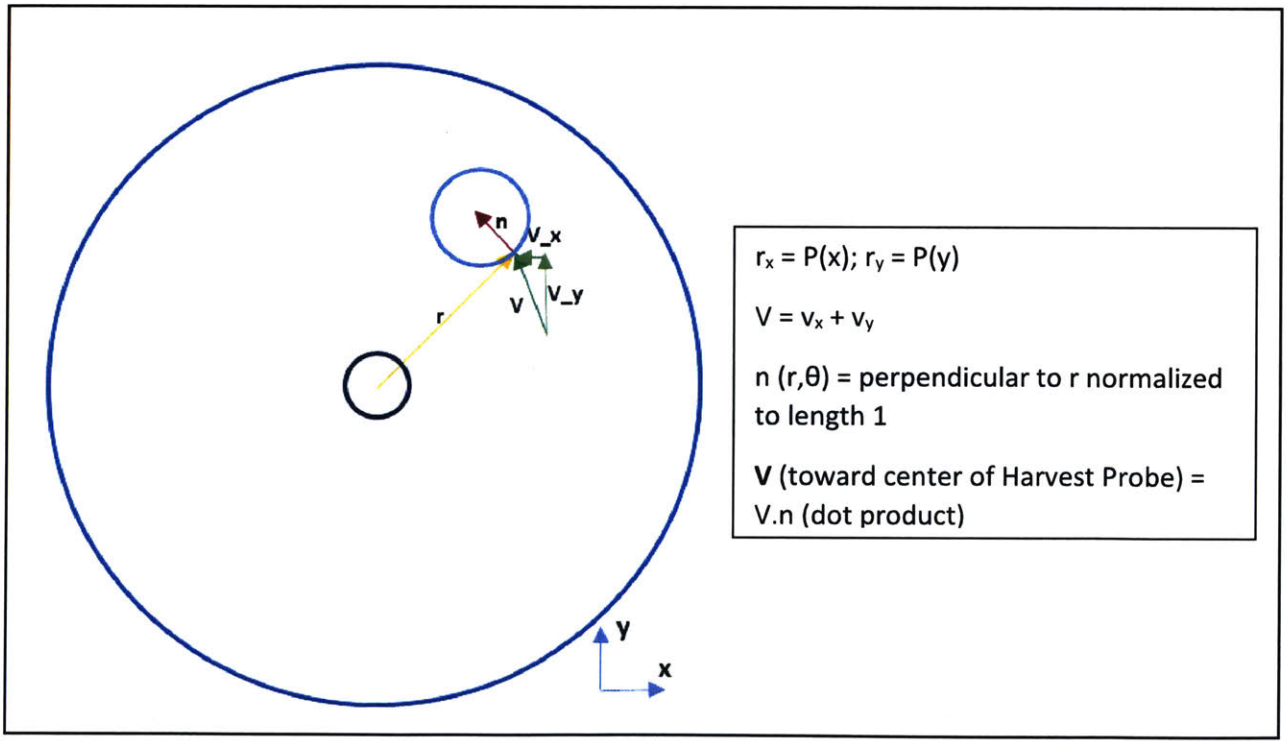


***Box 4-1*** **Geometric conversion of velocity vectors into required domain**

This analysis is an example of how the 3D simulation acts as a good half-way point towards further learning. Decoupling the study allows for rapid iteration, optimization, and smart

resource allocation. This aligns with a futuristic workflow approach and easy transfer of labor in unexpected applications. The 3D bulk flow result can be used in myriad ways to glean information on a smaller scale, by coupling it to a downstream 2D solver, or a different microscopic 3D analysis of a certain part of the fluid flow. Furthermore, structural analysis using ANSYS Finite Element Analysis and other such software can be conducted. Keeping in mind that the initial model was created using SolidWorks, and the amount of modifiable parameters that go into the input as a design or process parameter, as well as the numerous studies that can be done in a post-processing study, this type of analysis lends itself well to a Parametrized and Optimized approach somewhere down the line.

### 4.3.7 Surface of Revolution Results

The maximum absolute velocity plotted around the SOR at each ring (height) was plotted using MATLAB for each impeller speed. The results are shown in Figure 4-14. It was found that the maximum absolute flow velocity crossing the SOR at any point was found in the 1200 RPM case, as expected. This velocity was determined to be 2.1 m/s, and will be used in the 2D infinite flow field simulations with the exact individual hollow-fibers geometry. The location was at the height in line with the second impeller. In all four impeller speed cases, it can clearly be seen that the SOR experiences maximum flow inline of each of the three impellers, as signified by the peaks. This gives insight into the flow affecting the harvest probe as a function of height, and can aid qualitatively with design tweaks such as reinforcements at the height of the impellers.

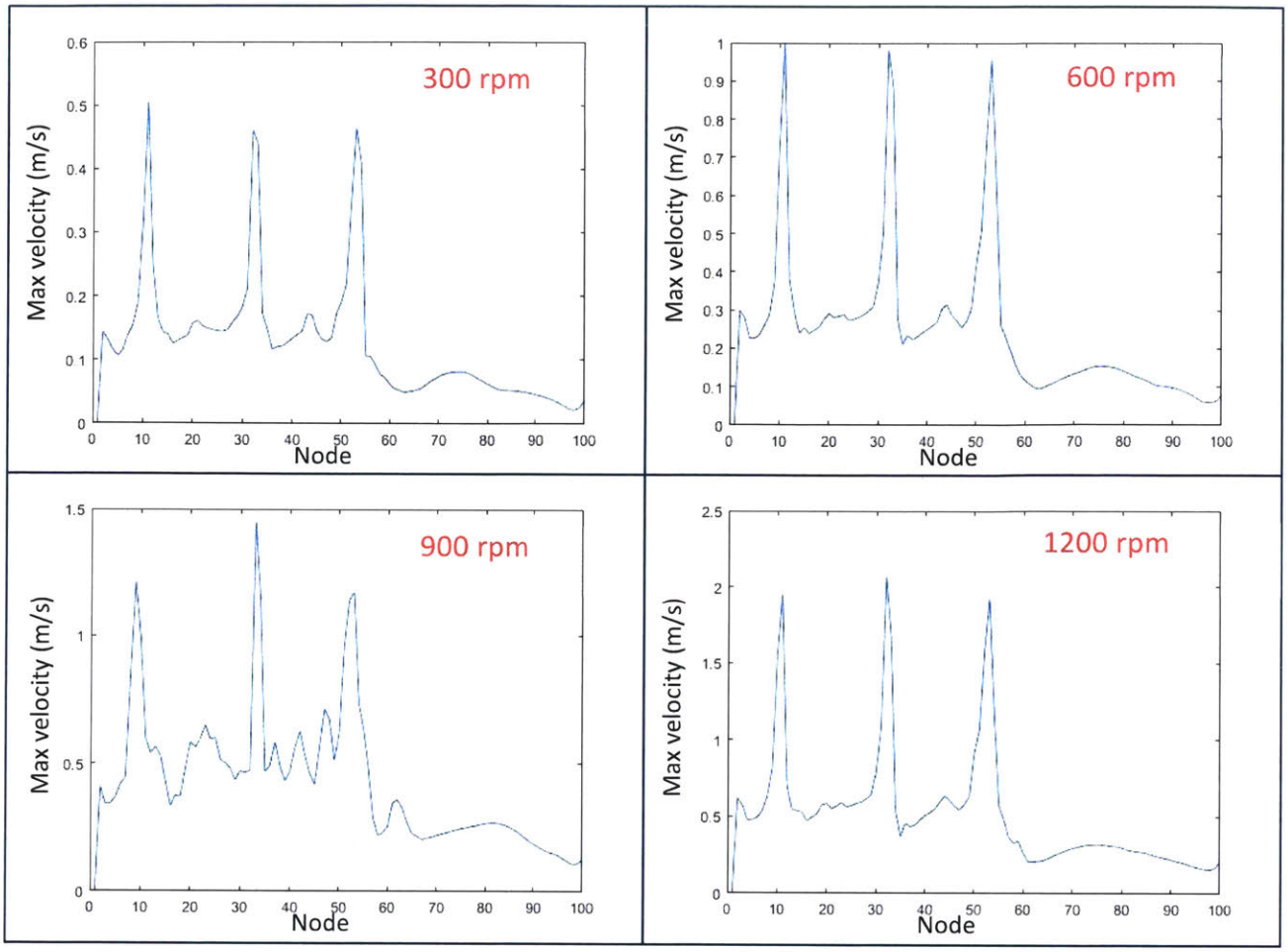


***Figure 4-14*** **Maximum Velocity Results in the Surface of Revolution** plotted against the height for each of the four cases

Histograms plotted in MATLAB of the maximum velocity at each height data are shown in Figure 4-15. What is evident is that at most heights, the max velocities experienced by the harvest probe are on the lower end. In the 1200 RPM case, with the maximum velocity of 2.1 m/s, the histogram indicates that 80% of the 100 rings (heights) experience a max absolute velocity of below 0.6 m/s passing through the SOR towards the harvest probe.

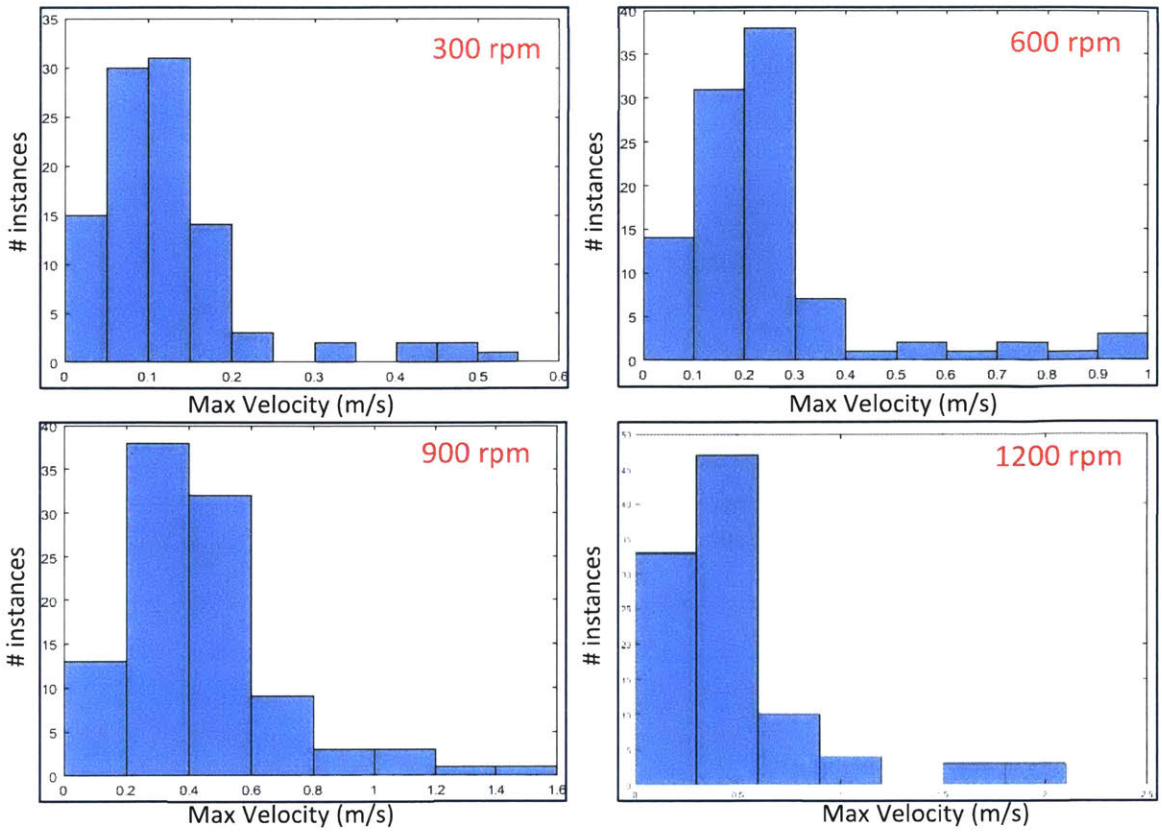


***Figure 4-15* Maximum Velocity Histograms in the Surface of Revolution** plotted for each of the four cases

These results offer a good insight into the bulk flow at regions surrounding the harvest probe. Similarly, any other region of the bioreactor can also be studied in detail, with results that can lead to further analysis and exploitation.

The 3D interpolated velocity profile (along the vertical axis of the bioreactor) on the SOR with increasing RPM, is shown in Figure 4-16. Table 4-3 characterizes the velocity at different vertical heights along the surface of revolution.

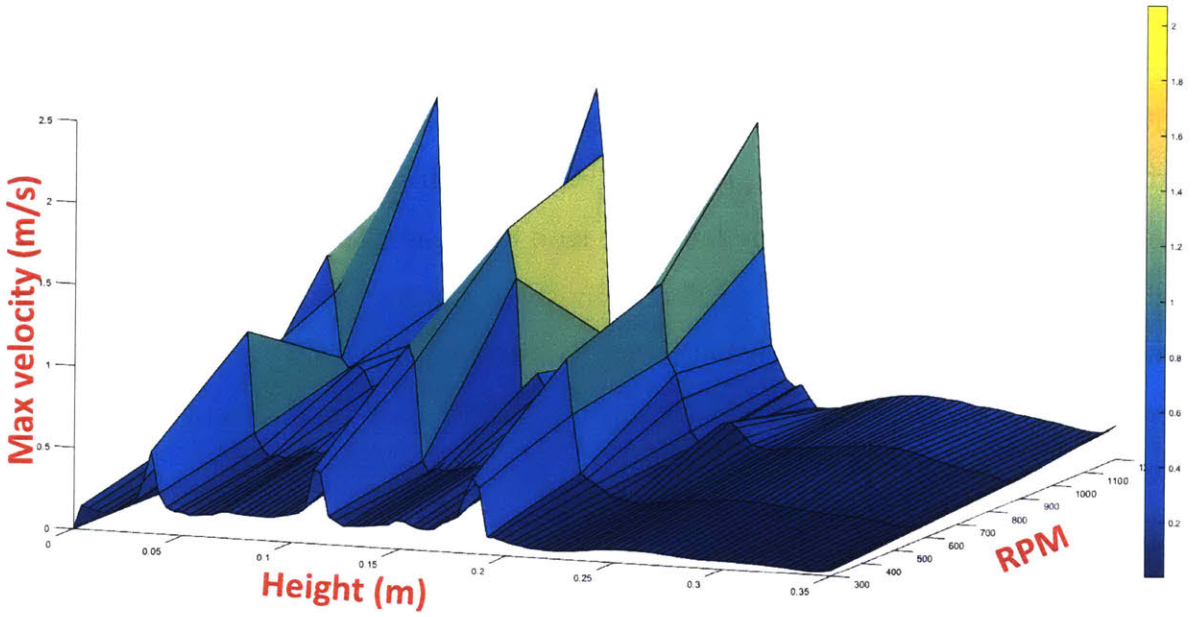


***Figure 4-16* 3D Surface Plot of Maximum Velocity along the Surface of Revolution** with vertical height in bioreactor and increasing RPM

| | 300 RPM | 600 RPM | 900 RPM | 1200 RPM |
|---|---|---|---|---|
| SOR – max normalized velocity at impeller 1 height (m/s) | 0.51 | 1.00 | 1.24 | 1.93 |
| SOR – max normalized velocity at impeller 2 height (m/s) | 0.46 | 0.98 | 1.46 | 2.08 |
| SOR – max normalized velocity at impeller 3 height (m/s) | 0.47 | 0.96 | 1.22 | 1.90 |
| SOR – range of >60% of instances of max velocity (m/s) | 0.05-0.15 | 0.1-0.3 | 0.2-0.6 | 0-0.6 |

***Table 4-3* Velocity Characterization along the Surface of Revolution**

## 4.4 2D Infinite Flow Field Simulation

The post-processed results from the Surface of Revolution provided the maximum absolute velocity that passed through the SOR. When normalized to ensure the effective velocity towards the center of the harvest probe, the maximum absolute velocity was found to be 2.1 m/s in line with the middle impeller in the 1200 RPM case. This value will be used in the 2D infinite flow field simulation to determine how the harvest probe (with individual hollow fibers accurately modeled) will react to incoming flow of that velocity. This is a conservative model, since the velocity towards the fibers will be different (and lower) at different places.

### 4.4.1 Geometry, Meshing, and Setup

The harvest probe geometry modeled by Goddard in SolidWorks is shown in an engineering drawing format in Figure 4-17. For the purpose of the infinite flow field simulation, a flat plate was drawn in SolidWorks, with the hollow-fiber geometry within the flat plate. The distance between the leading edge of the plate to the center of the hollow-fiber geometry was the same as the distance from the Surface of Revolution to the center of the harvest probe cylinder. This region was determined to be sufficient to achieve independence from local flow. Additionally, this allows for validation of the previous assumption. The flat plate with the hollow-fiber geometry was then bisected horizontally, since symmetry effects can be applied within the simulation. The

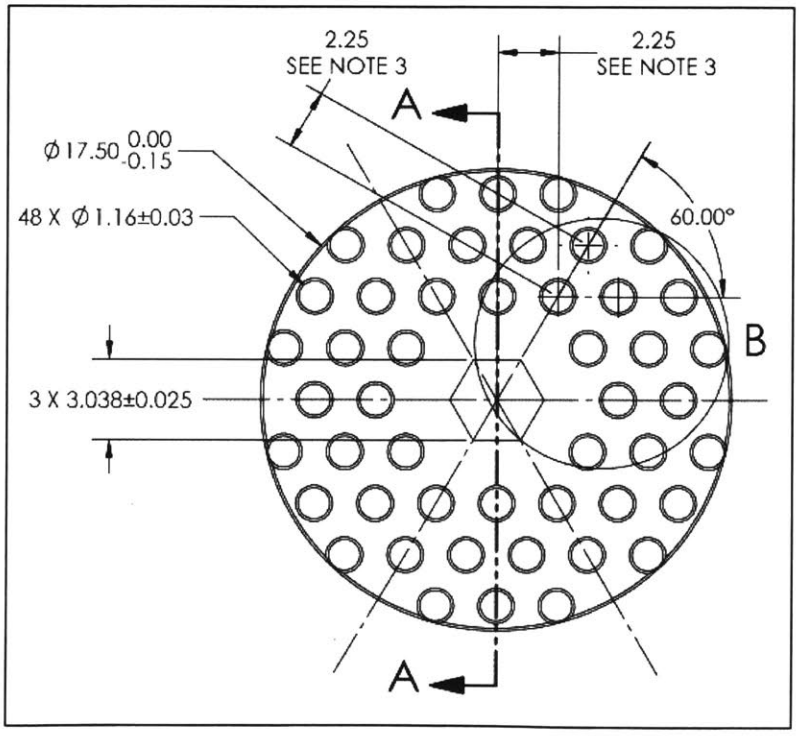


***Figure 4-17* 2D Geometry of the Harvest Probe** (Image Credit: Goddard Technologies)

geometry was recreated as a 2D drawing in SolidWorks and defined as a Surface. The surface was then imported into the ANSYS Design Modeller.

The surface was then exported to the meshing software. In there, through Named Selections, the leading edge of the surface was defined as the *Inlet*, the rear edge was defined as the *Outlet*, the upper edge defined as *Upper*, and the lower edge defined as *Symmetry*. Further, edges of the fibers were defined as *Tubes*. The reasons for separating the definitions of these parts are so as to allow different Boundary Conditions in the setup downstream in the analysis.

The mesh was defined so as to ensure the mesh was very fine near the hollow-fibers, as that region is expected to experience high gradients. A fine relevance center was used, with medium smoothing, and the curvature size function. A total of 21,894 nodes were created, and 21,056 elements. The mesh can be seen in Figure 4-18, as well as a zoom-in of the mesh on the hollow-fiber region.

In the ANSYS Setup module, the *Inlet* boundary conditions were set to 2.1 m/s as a constant velocity-inlet. The *Outlet* was set as a pressure-outlet. The *Upper* and *Symmetry* boundaries were set as lines of symmetry. The *Tubes* were set as a "No Slip" wall. Enabling the Viscous model, the Realizable RNG model was used as a solver, with a default Hybrid Initialization, with default solver settings and under-relaxation factors.

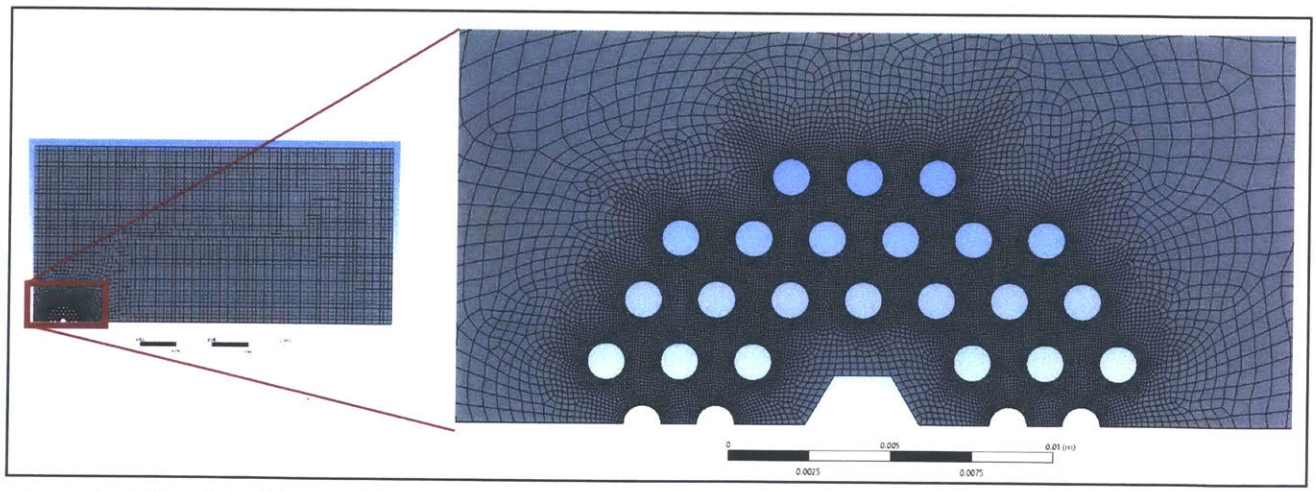


***Figure 4-18* 2D Infinite Flow Field Study Mesh** The mesh generated for the 2D infinite flow field simulation of the hollow-fiber harvest probe

## 4.4.2 Velocity Profile

The results of the simulation were viewed in CFD-Post. The macroscopic flow profile of the simulation closely resembles flow past a cylinder. This validates the previous assumption about bulk flow at the appropriate distance away from the harvest probe being independent of the local geometry. It is important to note that modeling the fibers as a no-slip wall is just an approximation, as in reality, the fibers will be a suction to remove protein from the reactor, or (in backwash mode) send fluid back into the reactor. However, the approximation is a good one, as the same simulation was conducted by modeling the fibers as a velocity-inlet, and assigning them very low flow. The results were almost identical.

As can be seen from Figure 4-19, the flow accelerates past the harvest probe on either side, similar to if the probe was a solid cylinder. The highest velocity reached is 3.45 m/s with the input of 2.1 m/s. Behind the harvest probe, a low-flow wake develops.

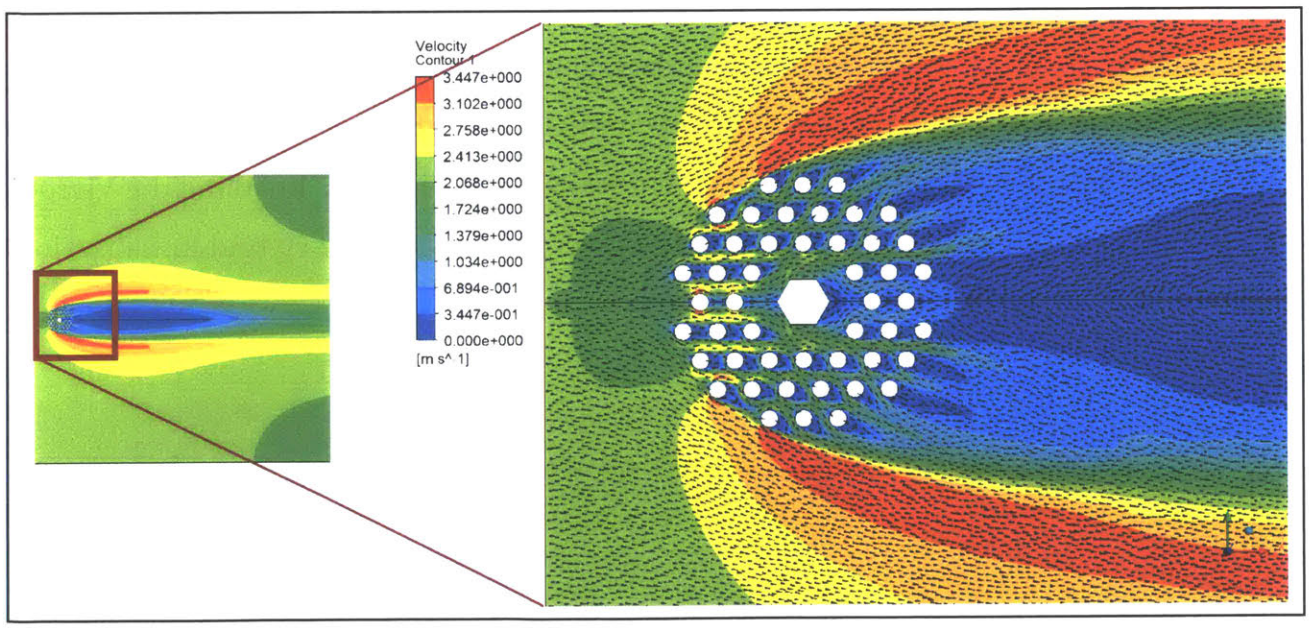


***Figure 4-19* Velocity Profile Results of the 2D Infinite Flow Field Study** The velocity profile of the harvest probe under flow; zoomed in on the hollow-fibers with flow vectors

For further insights into the flow field, the velocity scale was contour plotted logarithmically. This will allow a more microscopic look into the low-flow wake. The max velocity to be shown was set to 2.1 m/s (the same as the inlet velocity) where everything above that was shown as the max. The logarithmic plot can be seen in Figure 4-20. An emergence of a stagnation point can be seen in this scenario, at a distance of approximately 50 mm away from the center of the harvest probe. The flow vectors in this region are reversed. However, since the distance of the point is far enough away from the fibers, the proclivity for fouling is reduced. In fact, this point will not occur in the bioreactor because the vessel wall behind the probe is closer than the distance required for the formation of a stagnation point. However, at lower velocities and in cases with different geometry, the stagnation point can move closer to the hollow-fibers, and must be considered in design.

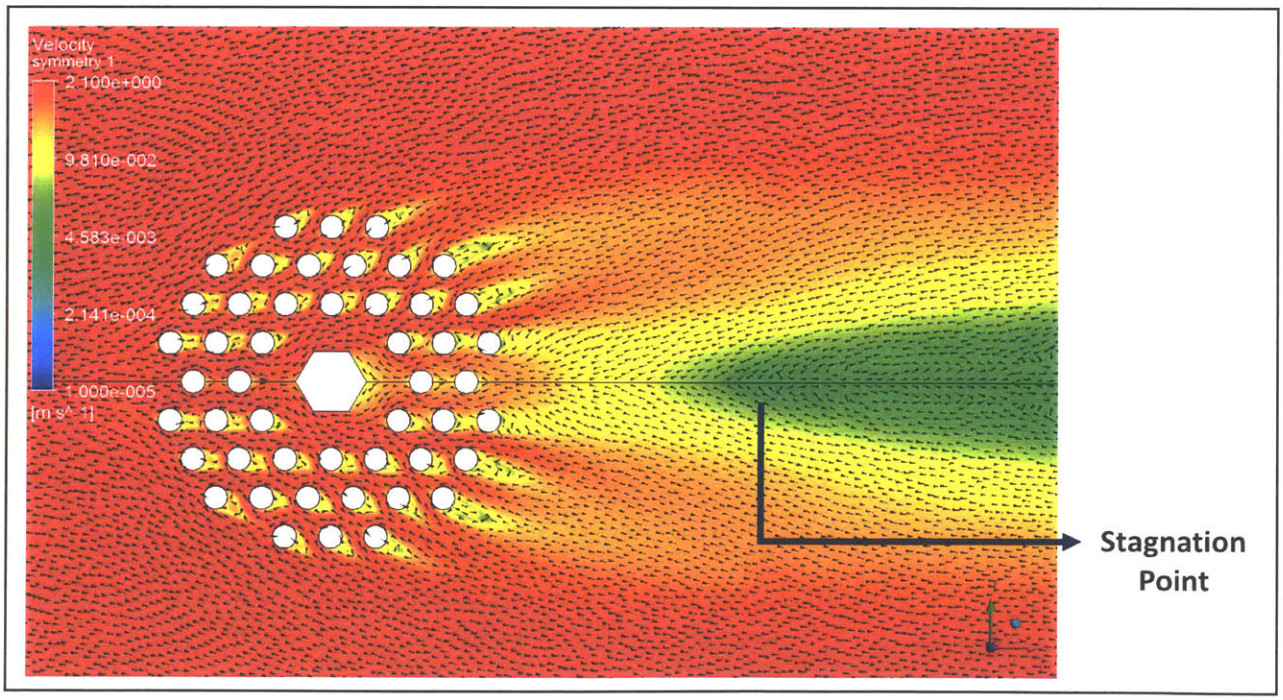


***Figure 4-20*** **Stagnation Point Results of the 2D Infinite Flow Field Study** Logarithmic contour plot of the velocity flow field of the harvest probe under flow, with the emergence of a stagnation point downstream of the flow

### 4.4.3 Wall Shear and Turbulence

The wall shear on the fibers were exported at every node on the fibers. A contour representation of these values are shown in Figure 4-21. The localized wall shear at some of

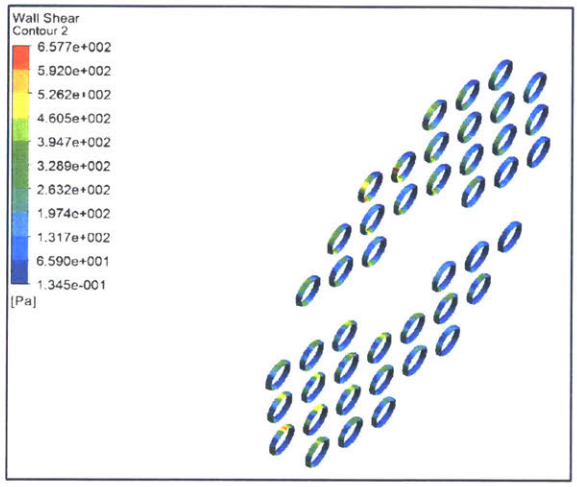


***Figure 4-21*** **Wall Shear Results of the 2D Infinite Flow Field Study** Wall shear on the fibers

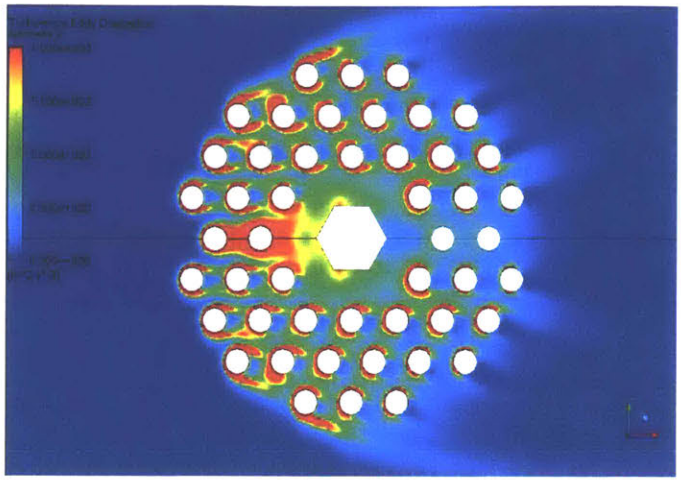

***Figure 4-22*** **Turbulence Eddy Dissipation in the 2D Infinite Flow Field Study**

the points was higher than expected if the harvest probe was modeled as a single cylinder in the 2D analysis. The localized flow accelerations within the fibers could be the reason for the high localized shear. The outer edges of the outer fibers experience lower wall shear. The maximum local wall shear of 658 Pa (0.7% of 1 atm) is felt by the fibers. The average wall shear was found to be 130 Pa.

The turbulence eddy dissipation is shown in the contour plot in Figure 4-22. As expected, the higher values are seen around the fibers, which act as obstructions to the flow.

The wall shear associated with each mode of each fiber in the 2D simulation is show in Figure 4-23. A histogram of these values is also show in Figure 4-23. Most of the nodes have wall shears clustered towards the lower end of the spectrum, with about a third of the values less than 30 Pa.

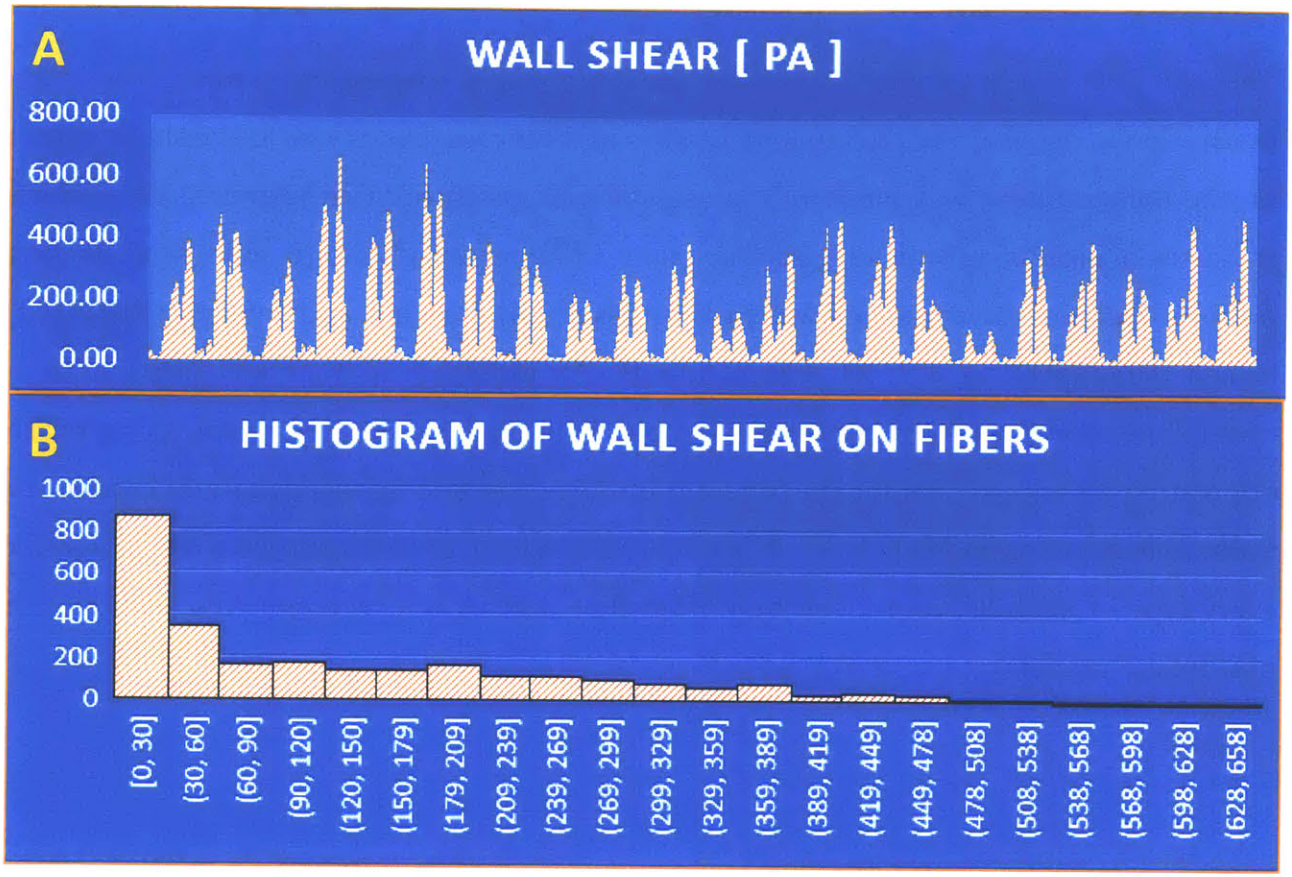


***Figure 4-23* Wall Shear Detailed Data in the 2D Infinite Flow Field Study** (A) Wall shear at every node on the fibers plotted (B) Histogram of the wall shear on the fibers

These values are used to inform testing downstream in the development process. The shear and velocity profiles are used to construct experimental testing procedures to ensure that the fibers are able to structural withstand the flow in the bioreactor. The testing of the harvest probe was successful and revealed the ability of the hollow-fibers to withstand operating conditions. Further, the velocity flow profiles gave an understanding of the mixing conditions in the bioreactor, while the stagnation study allowed for an understanding of the fouling propensity of the setup, and can be used in the future to inform design iterations and operating conditions.

## 4.5 Conclusions

The 3D CFD study of the bioreactor provided many interesting results. The main motivation in determining the velocity profiles of the bioreactor, as well as the shear impact on the hollow-fibers, was ultimately successful and insightful. Furthermore, the analysis indicates a promising way of gleaning many different insights into fluid flow, mixing profiles, and reactor dynamics within the vessel. This can aid and inform geometrical design parameters, as well as process inputs. An extended analysis will incorporate a multiphase model, with oxygen (or air) bubbles being sparged into the vessel, along with a population-balance-model for the different bubble sizes, and bubble dynamics to account for bubble bursting and cell death. However, these advanced methods are not required for every type of analysis, as a lot of bulk fluid flow studies can be conducted without the multiphase model.

# Chapter V
# Market Research

# Executive Summary

Recent developments in the growing biotechnology industry have shown biosimilars to be a viable option going forward. While the upside of the biopharma industry is massive, the increased complexity, cost of goods sold, and regulatory concerns make the cradle-to-grave process a quite multi-layered and difficult one. Cold chain logistics account for a significant portion of this journey, and the market for cold chain itself is about $13 billion annually, compared to the $163 billion in sales by the biopharmaceutical industry. These numbers portray an immense opportunity for landscaping the biopharma industry, potentially by adding tools to circumvent the cold chain and the problems (and cost) associated with it, by distributed single-use manufacturing, or at least significantly reducing the required cold chain capacity.

A few options were explored in order to pinpoint the cost of cold chain logistics. The macro-economic approach is a simplistic model focusing on comparing cold chain costs to overall product costs on a very high level. The vaccine approach explored mining the vast amount of data available regarding simple vaccine cold chains (which is not available for most biologics) and using that data to extrapolate reasonable numbers. The financial report approach looked at specific companies' annual and quarterly reports, to stratify costs and profits based on different sectors, drugs, logistics, overhead, etc. All of these methods lacked complete enough information to give anything more than a qualitative feel of the costs of cold chain, either due to simplicity, lack of transparency, or non-comparable scenarios. The problems associated with cold chain, such as a theft, loss of stability, counterfeiting, increased costs, increased time, etc. make it imperative that a solution is found.

The latter part of the report delves into more detail about the major distributor and wholesale companies, namely, McKesson, AmerisourceBergen, and Cardinal Health. Complete SWOT analyses of these three companies reveal that the stranglehold they have on the industry in terms of market share is their major advantage, as well as a comprehensive network that includes multiple sister companies and subsidiaries.

However, quite a few smaller distribution companies exist, and cater to niche regions or specialty drugs, as well as serving as redundancy outlets for manufacturers. Upon assessing manufacturers' (Gilead's and Amgen's in this report) Authorized Distributors of Record, it was found that each biotech company had myriad ADRs subscribed to contracts, all including the "Big 3" companies. But the regional or niche distributors present opportunities to inquire into the logistics of the cold chain space.

The major markets for distributors include warehouse supercenters, chain pharmacies, specialty pharmacies, hospitals, clinics, mail-order, etc. These front-end drug dispensers are potential target markets for distributed manufacturing, as well as possible resources of information regarding market needs, costs of purchasing, and other such questions.

## 5.1 Introduction

Following the development of a disposable bench-top bioreactor for biologic drug manufacturing, a go-to-market (GTM) strategy for successful commercial penetration is the obvious next step. In order to commercialize the product, understanding the market is necessary. Thus, a market research analysis was conducted with that in mind. In the following market analysis, two major sections exist. The first part aims to establish the benefits of avoiding the cold chain process in traditional biomanufacturing, and attempts to quantify the value proposition of the bench-top alternative by avoiding the cold chain. Additionally, it explores the recent trends in biotechnology, including the increased prevalence of biosimilars and their potential to create a market for alternative manufacturing. The second part looks at the current distribution systems for biologic drugs across the United States, and attempts to glean as much information as possible regarding these wholesale companies, in order to understand the costs, benefits, and weaknesses of such a distribution network.

# Chapter V
# Part I
# Biotechnology Trends & Cold Chain

## 5.2 Biopharmaceutical Industry and the case for Biosimilars

Biopharmaceutical drugs are any drug products manufactured in, extracted from, or synthesized from biologic sources. Complex advances in recombinant DNA technology has led to the growth of this exciting field of biologics. Currently, generating global revenues of $163 billion, biopharmaceuticals make up around 20 percent of the pharmaceutical market [3]. With the conventional pharma market growing at about 4% annual, and biologics seeing upwards of 8% growth, it is expected to become the cornerstone of the pharma market [3]. In 2015, 6 of the top 10 grossing drugs were biologics [97].

Biosimilars are biologic drugs which are almost identical copies of products originally manufactured by a different company, whose patent has expired. Due to increased complexity of biosimilars as compared to small molecule drugs, the regulatory approval pathway is different, and requires more testing as compared to small molecule generics [98]. The patents of a number of blockbuster biologics is expected to expire from now until 2019 [5]. In fact, EvaluatePharma reports than biologics with an estimated $80 billion in sales will lose patent protection through 2020. In March 2015, Sandoz's Zarxio became the first biosimilar to gain FDA approval in the US.

Rand Corporation predicts a $44.2 billion decrease in direct spending toward innovator biologic drugs between 2014 and 2024, due to the emergence of biosimilars [99]. Although the cost of developing a new drug, from preclinical research to clinical trials, has reached an average of $2.6 billion [100], with sales (with an assumption of high profit margin) for many blockbuster drugs reaching several billion a year, there is definite room for the emergence of a competitive market, where natural supply-and-demand economics will drive costs down.

## 5.3 Opportunities and Challenges in Biopharmaceuticals

Due to the efficacy, safety, and ability to treat previously untreatable problems, the upside in biopharmaceuticals is exciting. However, with added complexity of product, increased cost of goods sold, and regulatory scrutiny, there are a few challenges that need to be streamlined for the industry going forward.

Improvement in affordability of biologics is a key aspect of the field going forward, especially as emerging markets will tend to pursue alternatives of their own. This cost pressure will lead to the further importance of biosimilars, which in turn are expected to drive down costs as the age-old supply-and-demand tug-o-war ensues. Lower costs, increased innovation across the board, qualitative competition, and other consequences of a more open-market in the biopharma industry, may require an overhaul of current biologics paradigm. This need for adaptability, agility, and efficiency in the cradle-to-grave process of producing biologic products, is an immense opportunity for rethinking the current status quo, and can foster development in sectors such as single-use bioreactors to produce biosimilars as well as new biologic drugs.

> *"Large-scale biotech-manufacturing facilities require $200 million to $500 million or more to build, compared with similar-scale small-molecule facilities that may cost just $30 million to $100 million, and they can take four to five years to build. These facilities are costly to run, too, with long process durations, low yields, expensive raw materials, and, not least, the need for a team of highly skilled experts to operate them. There are myriad reasons the rapid growth and increasing importance of the industry is producing new challenges and opportunities. To keep pace, biopharma players must revisit and fundamentally reassess many of the strategies, technologies, and operational approaches they currently use."*
> – *McKinsey Report* [125]

Due to the requirements of patients, as well as extended insurance coverage, the demand for biologic drugs remains highly price-inelastic. This allows companies to avoid a marginal pricing strategy, and reap exorbitant profits of certain biologics. The restructuring of the biopharmaceutical industry could incorporate strategies so as to avoid this problem, and let the free market drive the cost to the right price points.

## 5.4 Introduction to the Cold Chain

The fragility of biopharmaceuticals, where both chemical and physical instability may contribute to loss of activity, require proper storage and handling throughout the process, giving rise to cold chain logistics. The cold chain associated with biologics refers to the controlled temperature storage and handling of the product, from start of production, through the supply storage, and right until the first point of shipment. There are strict regulations and guidelines in place to oversee this process, but beyond that point, it's more up to local distributors and consumers to follow directions to properly store and handle the products.

According to Pharmaceutical Commerce's Annual Biopharma Cold Chain Sourcebook, managing the transportation of temperature-controlled products will total $12.6 billion in 2016, in line with the 8-9% year over year trend [101]. Non cold-chain logistics for biologics meanwhile accounts for a $66.2 billion market, and is continuing at a slower growth rate of 4-5% [101]. The major drivers for growth are the increased global adoption of cold-chain products, continued development of new drugs, and overall growth of the larger market [102]. Drugs requiring a cold supply chain accounted for 24 of the top 50 drugs in 2013, and the global market for biopharma requiring cold-chain is expected to breach $350 billion by 2019 [102].


***Figure 5-15* Cold Chain Market Size Distribution** (Data From: [102])

The cold supply chain needs to be maintained from production to point-of-delivery. A typical distribution network will start at the manufacturer, include international transportation, repackaging, domestic transportation, wholesaling, and further local transportation, before finally begin delivered to the intended point [103].

Clearly, the massive and growing size of the cold-chain logistics market, coupled with the complexity and problems associated with it, gives rise to immense opportunity to

alternative technologies, including complete circumvention of the cold-chain. There is a case to be made for the overall positive effect of this strategy giving rise to alternative manufacturing processes, including the increasing prevalence of single-use, on-site bioprocessing.

## 5.5 The Cost of Cold Chain Logistics

Estimating the cost per weight/volume of cold chain logistics that companies are facing per specific drug is extremely difficult to do reasonably, if not impossible. This is likely a result of closed-door decisions and pricing strategies that the public are not privy to. With multi-billion-dollar R&D costs for successful drugs, hedging against sunk costs for drugs that fail to gain regulatory approval, profit margins, overhead, and so many other factors, the cost of cold chain logistics if smothered in the mix. The issue is further complicated when the reality of a case-to-case basis is understood. The cold chain logistics differs from company to company, and possibly between biologics as well. Different distribution models lead to different costs associated with it, as well as vast differences in market size and location. That said, it is probable that corporations have internal numbers regarding the cost of specific cold chains. Some models that may yield estimates are provided below in brief, which could unearth more information with further digging.

### *Macro-economic Approach*

The overall size of the pharmaceutical cold chain industry was $12.6 billion, compared to the size of the market of drugs that relied on cold chain being $260 billion [8]. A macroeconomic approach of determining the cost of the cold chain for individual drugs on a per-weight or volume basis may be possible. It would require detailed knowledge of the distribution chain, as well as the income chain. The price of a drug the consumer pays comes through many channels, such as drug developers, insurance companies, pharmacies, etc. Often they vary between drugs. Deeper reconnaissance of these models could help estimate how much the value of a certain drug is in terms of price sold by the company to the next merchant. Unfortunately, due to options for outsourcing of cold chain and transportation, further transparency is lost to find the cost of the cold chain to the pharmaceutical company itself.

### *Vaccine Approach*

Despite the massive differences between most administered vaccines and biologics, especially regarding costs, there is some merit towards pursuing information relating their similarities. Globally, around half of all vaccines are exposed to inappropriate temperatures to the point that they lose their efficacy, and the cold chain accounts for 80% of the cost of a vaccine [104]. After understanding the detailed distribution model, and exploring the breakdown of cold chain costs, it may make sense to delve into this approach so as to extrapolate the similar costs associated with biologics. Note that the differences regarding how widespread a distribution model is, target market, requirements of the drugs/vaccine, etc. are all factors in determining the difference between the two costs.

### *Financial Reports*

The annual or quarterly financial reports of biopharmaceutical companies provides significant information. Unfortunately, despite the vast amounts of data present in these reports, the real breakdown for costs of goods sold is obscure and varies with accounting principles. To understand each companies' accounting principles and financial reports may not be possible as they are often nebulous.

### *Personal Approach*

Interviews and conferences could be a major contributor towards understanding the nuances of cold chain costs. The key to success in this area would be preparation of a variety of questions, and a knowledge of the broader picture. Consultants such as McKinsey or PwC could help directly approach this problem as well, or alternatively, more biopharma-specific consultants. This is the approach with the highest chance of getting an accurate number regarding the cost of a cold chain in general, and specific to drug products.

## 5.6 Problems associated with Cold Chain

There are myriad problems associated with maintaining a successful cold chain. Foremost, the complexity and sensitivity of biologics requires very strict temperature-controlled environments. This leads to many costs, from equipment, to transportation, to training and employing skilled workers. The globalization of the biopharma market also leads to further problems in establishing cold chain lanes in emerging markets, which has its own implications. With the high prices of biologics, certain consignments may alone be worth millions of dollars. Thus, it is imperative that the cold supply chain also has measures to deal with theft and counterfeiting. Furthermore, with the increased globalization of the biopharmaceutical market, the cold chain has to meet an ever-increasing number of governmental and organizational regulations [105].

> *"Because drugs are manufactured in specialized locations, these temperature-controlled products frequently traverse the world on their way to market. They move through a sometimes extreme range of climactic zones while en route, and travel via multiple modes with numerous hand-offs." – Inbound Logistics* [105]

According to a recent Georgia Institute of Technology study, 90% of cold chain failures are caused by human error [106]. This makes the problem even harder to solve, as technology and innovation could keep improving, but would still require human error to be mitigated. This leads to added costs of training skilled workers in appropriate handling and storage of product, shipping, etc.


***Figure 5-2* Cold Chain Issues** Problems associated with the biopharmaceutical cold chain

The wide range of temperatures a drug faces by the time it reaches a consumer's hands, from airport cool rooms to outside climates that themselves range drastically depending on the location, cold chain management leads

to another plethora of problems. Attacking cold chain logistics from the managerial and optimization headache it causes is another opportunity.

# Chapter V
# Part II
# Biotechnology Distribution

## 5.7 Overview of Biotechnology Distribution

Most major biologic drug manufacturers outsource distribution to third party logistics companies (3PLs) and wholesalers. This is so manufactures can reduce added costs of infrastructure, equipment, wages, and other associated costs of storage and distribution, and instead contract these services to companies built for that, for whom the associated costs are cheaper as a result of economies of scale (multiple clients). Traditionally, in the US, the biotech companies have been dependent on wholesale distributors to inventory and sell products. There is a fine distinction to be made between wholesalers that purchase the product and assume responsibility, and 3PLs that simply provide the service of distribution. The major players today may be merging these business models within their parent company.

The competition in distributors has dwindled since the 1970s. From over 200 distributors, today there are less than 50 such companies, and 3 companies hold over 90% of the market share in the United States [107]. This is disadvantageous to manufacturers due to simple supply vs. demand economics, as the monopolistic nature of distribution means manufacturers have reduced leverage of negotiation, leading to reduced profit margins, increased prices for consumers, or some combination of both.

Currently, the major distribution model changes in structure have led to a fee for service structure (where the manufacturer retains ownership but outsources stocking, selling, and distribution), incremental commission incentive structure (where manufacturers also commission the sales force as well as subsidize the distributor), and the direct product sales model (where the manufacturers sells directly to pharmacies or hospitals, typically for a limited product) [107]. These are in addition to the model where wholesales assume ownership of the product and buy it from the manufacturer, effectively absolving responsibility downstream of the sale.

The three major distributors in the U.S. (with over 90% of market share) are AmerisourceBergen Corp., Cardinal Health Inc., and McKesson Corporation [107].

## 5.8 Major Distributors in Biotechnology

An overview of the major distributors in the biotech distribution space. It is difficult to get statistics of companies decoupling cold chain from the regular supply chain, so most of the data here is combined for the company. Even the annual and quarterly reports of the companies failed to discretize the incoming sales into sectors to be able to make the distinction.

### AmerisourceBergen Corporation

AmerisourceBergen Corporation (ABC) is one of the Big Three distributors of biologics in North America, operating primarily in Canada and the USA. It acts as a middle man between drug manufacturers and pharmacies, doctors' offices, hospitals, and other drug dispensaries. A specialty distribution unit focuses on sensitive and complex biopharmaceuticals, assumed to necessitate the need for a widely distributed cold chain.

*Company Snapshot*

ABC had $135.9 billion in sales in 2015, with operating income of $386 million. As of 27$^{th}$ June 2016, ABC has a market capitalization of $15.44 billion [108]. ABC currently has 17,500 employees [109]. The company also has 187 family members including branches and subsidiaries, the whole list of which can be found at OneSource [110].

*SWOT Analysis*

For full coverage on each point in the SWOT Analysis diagram, visit [111].


***Figure 5-3* SWOT Analysis of AmerisourceBergen** (data courtesy of OneSource) [111]

## Cardinal Health Incorporation

Cardinal Health (CH) provides a pharmaceutical distribution service from manufacturers to pre-consumer dispensaries such as hospitals, pharmacies, and so on, for all kinds of pharmaceuticals, including branded drugs, generics, OTC, and biologics. CH also caters to international markets including China.

*Company Snapshot*

ABC had $102.5 billion in sales in 2015, with operating income of $2.1 billion. As of 27th June 2016, ABC has a market capitalization of $23.12 billion [112]. ABC currently has 34,500 employees [113]. The company also has 926 family members including branches and subsidiaries, the whole list of which can be found at OneSource [113].

*SWOT Analysis*

For full coverage on each point in the SWOT Analysis diagram, visit [114].

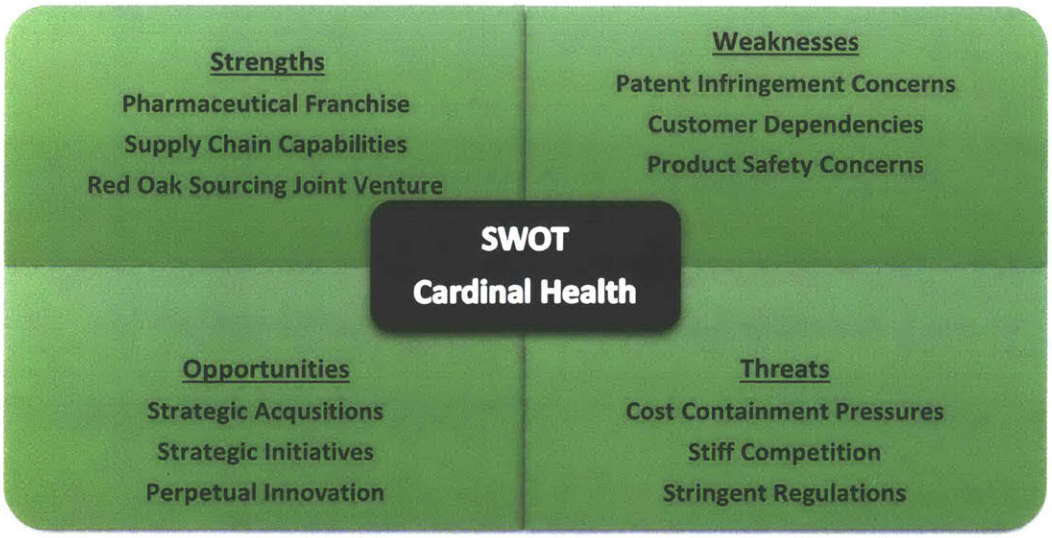


***Figure 5-4* SWOT Analysis of Cardinal Health** (data courtesy of OneSource) [114]

## McKesson Corporation

McKesson Corporation (MC) moves medicine between manufacturers and dispensers. They cater to over 40,000 retail and institutional pharmacies throughout the U.S. The company also wholesales medical and surgical equipment, and has quite a vast portfolio in general.

*Company Snapshot*

ABC had $179 billion in sales in 2015, with operating income of $2.96 billion. As of 27$^{th}$ June 2016, ABC has a market capitalization of $37.49 billion [115]. ABC currently has 70,400 employees [116]. The company also has 2443 family members including branches and subsidiaries, the whole list of which can be found at OneSource [117].

*SWOT Analysis*

For full coverage on each point in the SWOT Analysis diagram, visit [118].

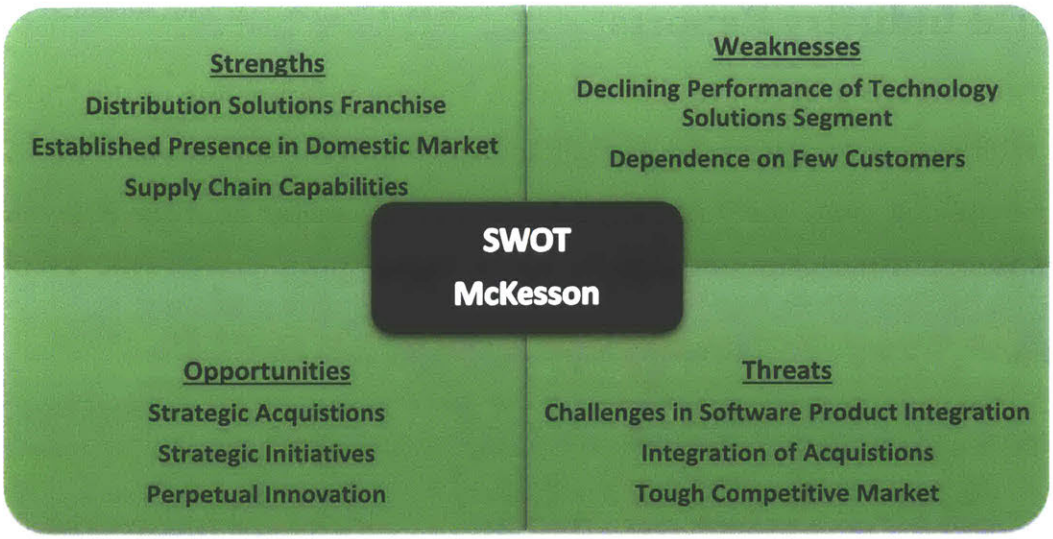


***Figure 5-5* SWOT Analysis of McKesson Corporation** (data courtesy of OneSource) [118]

## 5.9 IBIS World Industry Reports

IBIS World Industry Reports groups "Drug, Cosmetic & Toiletry Wholesaling in the US" as one industry in their extensive reports. Looking at an overview of the supply chain for the industry may be helpful at some point of our venture. Here is a snapshot of the overview provided by IBIS World, with the interesting sectors highlighted [119]:

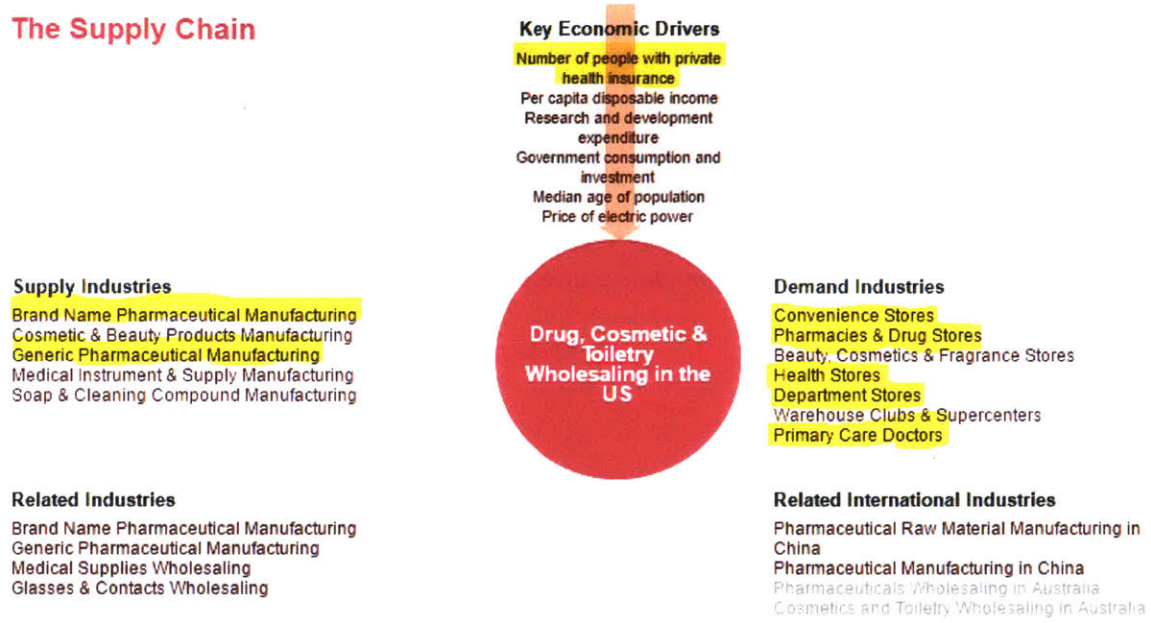


***Figure 5-6* IBIS Report on the Supply Chain in Drug Wholesaling** IBIS World Industry Report on the supply chain in Drug, Cosmetic & Toiletry Wholesaling in the US (Image Modified from: [119])

Noteworthy are the same three major players at the bottom, validating the industry report. The key economic drivers include number of people with private health insurance, which changes the dynamics of drug distribution by diversifying the distribution channels. Furthermore, with the advent of a strong healthcare reform through the Patient Protection and Affordable Care Act, and the Healthcare and Education Reconciliation Act, the number of people with access to health insurance will increase, thereby increasing demand for biologics [120]. However, it is imperative that the complex dynamics of the insurance financials is not overlooked, since with added pressure, they are subject to change in the future as well, and the number of people without insurance could rapidly fluctuate. This could lead to the growth of an unsatisfied group of consumers that are dependent on

biologics looking to cut costs and cut the middle man (i.e. the distributors). Keeping that in mind, a global map based on insurance coverage was developed in Appendix D.

Walmart now buys almost all its generics directly from the manufacturers, as increasing reliability of 3PLs allows for cutting out the distributors in some cases. With the growth of that industry, other drug dispensers will look to further cut costs by circumventing the major wholesalers. However, especially regarding biologics, the 3PLs would still cost companies like Walmart a substantial amount of money, and bypassing even them could be enticing. This presents a potential opportunity for distributed manufacturing, where the cold chain is take out of the equation, or rather, reduced to cold storage.

The increase in partnerships between major players is a concerning factor. Two 10-year contracts from 2013, one between ABC and Walgreens, and the other between Cardinal Health and CVS, points to a future of exclusivity in the supply chain [120]. This could be an issue with regards to distributed manufacturing strategies, although it is more likely that these partnerships involve generics, and not biologics. However, the trend of the emergence of these exclusive contracts is one of concern.

## 5.10 Authorized Distributors of Record

According to the FDA, Section 203.3(b) of the Federal Food, Drug, and Cosmetic Act defines an "authorized distributor of record" (ADR) as any distributors with whom a manufacturer has established an "ongoing relationship" to distribute its products.

Looking at some authorized distributors of record for major biopharma companies will offer insight into distribution networks, as well as act as leads for potential contacts to be made in order to establish connections who can be interviewed for information. It seems like companies rely on multiple distributors for each drug product, although the Big Three may do the bulk of the moving. Below is an example of two biopharmaceutical companies and their ADRs.

### Gilead Sciences [121]

Gilead's blockbuster drug Sovaldi, as well as Harvoni, is distributed through 13 wholesalers, including the Big Three. A wide range of their drugs – Atripla, Complera, Descovy, Emtriva, Genvoya, Hepsera, Odefsey, Ranexa, Stribild, Truvada, Tybost, Viread, Viteka – are distributed through 25 distributors, again including the Big Three. Cayston is only distributed through 6 specialty pharmacies, including an off-shoot of McKesson. Letairis is only distributed through 9 specialty pharmacies, while Zydelig is also distributed through 9 non-identical specialty pharmacies. Overall, this shows that there is a massive diversity in the drug distribution network, in spite of the supposed monopoly of a few companies. Manufacturers seems to hedge against contract breakdown, as well as account for the fact that certain distributors and wholesalers are cheaper in certain regions or for certain types of products with different needs.

### Amgen [122]

Amgen's best-selling drug (Enbrel) has 22 ADRs, whereas their second-best (Neupogen) has 21 ADRs. Neuplasta, on the other hand, has different allowances to distributors depending on whether the drug will be purchased through 340B (drug pricing program) or non-340B purchases. Similarly, Nplate is segregated by clinic and non-clinic purchases of

the drug. All in all, Amgen is catered to by 28 ADRs (some are sister companies of each other). This again demonstrates the diversification in order to create a large network that encompasses regions and cold chain capabilities. Amgen also stratifies their distributors by the segment they are authorized to service – oncology, nephrology, hospital/retail, and PCP/non-oncology/non-nephrology. Similarly, they have different distributors for US States and US Territories.

## 5.11 Major Markets

Understanding the major markets of operation for the major distributors and wholesalers may provide insight into the market space. 85% of all prescription medicines sold in the US are stored, managed, and delivered by drug wholesalers between manufacture and a healthcare setting [123]. Although this includes non-biologics, this number demonstrates the huge market potential of cutting out the cold chain. However, a contrarian view is that since such a vice-like grip exists in the market, it will be hard to shake off, due to existing contracts, trust, and dependence fostered by wholesalers and distributors.

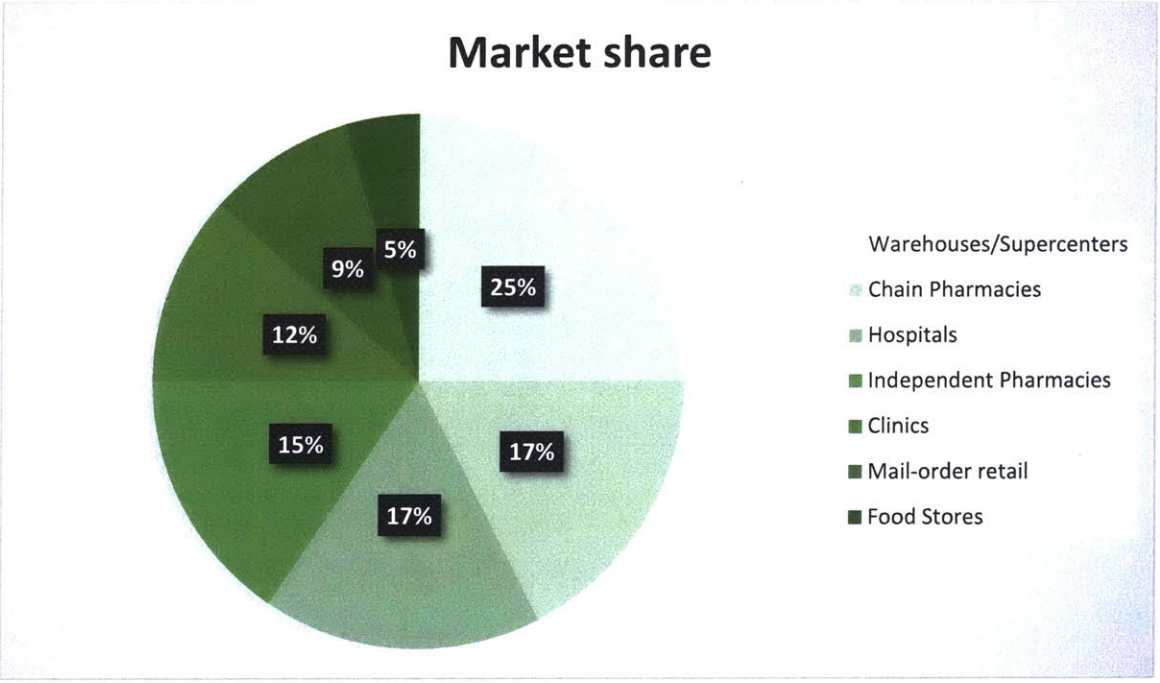


***Figure 5-7* Market Share of Drug Distribution** (Data From: [123])

About a quarter of the sales from distributors and wholesalers go to warehouse stores (such as Walmart, Target, and Costco). Chain pharmacies (e.g. Walgreens, CVS), hospitals, independent pharmacies, and clinics are also important customers in the views of the distributors. It is important to keep in mind that not all the distributed drugs are biologics, and not all the drugs require a cold chain distribution either. This variance can be explored in more detail if necessary, from the point-of-view of which market segment tends to stock which kind of drugs.

### *Network of locations*

A proper distribution network allows for efficient cold chain distribution and reduced costs associated with it. Analyzing one of the Big Three's distribution center locations (ABC), it is noticeable that they have done a good job of aggregating distribution facilities in states with higher population, which makes intuitive sense – California, southern Ontario, and cities along the East Coast [124]. These regions also all have at least 10% of the population over the age of 65, making the demand for biologics likelier.

Consolidating data from IBIS World and individual company websites, the distribution scene across the US was be mapped on the basis of percentage of business locations by state in Figure 5-9.

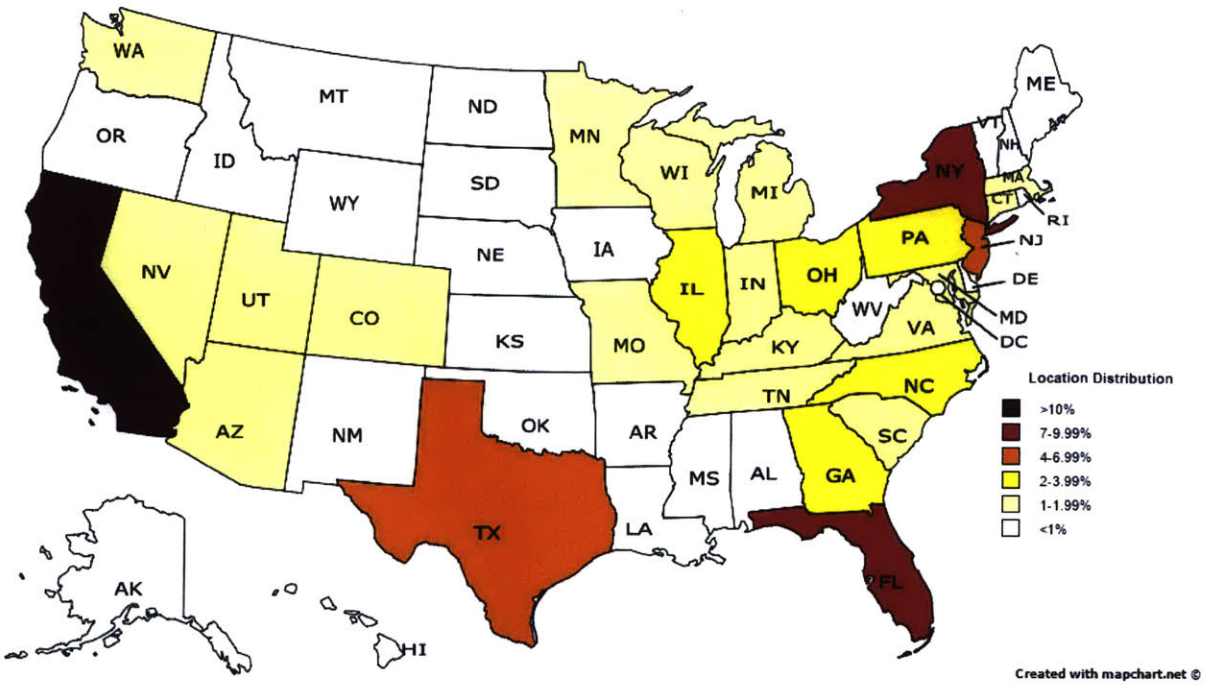


***Figure 5-8*** **Percentage by State of the Total Distribution Business Locations**

## 5.12 Conclusions

A market research of the Drug Distribution in the United States revealed that the cold chain logistics regarding distribution was a significant portion of costs. However, it is extremely difficult to determine the exact cost cold chain contributes towards the total cost, on a per-drug basis, due to many factors. The current cold chain for biologic drug distribution has multiple problems associated with it, including loss of stability, theft, and high costs. A distributed manufacturing approach will certainly be beneficial with regards to removing some of these issues. A review of the drug distribution network revealed that three major corporations – AmerisourceBergen, Cardinal Health, and McKesson Corporation, hold a dominant share of the market, and have distribution facilities throughout the country. Further, there is an increasing trend of partnerships forming between these corporations and smaller wholesalers. Large pharmaceutical companies have Authorized Distributors of Record (ADRs) that always include these corporations, as well as some of their sister organizations, although for specific drugs and regions, companies do tend to have ADRs that are outside of the network of the major three corporations.

# Appendix A

## Impeller Study Velocity Profiles

### A.1 Radial Velocity vs Radial Distance Profiles

Radial velocity profiles – absolute (top) and dimensionless (bottom) for the four impellers in the impeller study, in the plane at a height of 0.056 m.

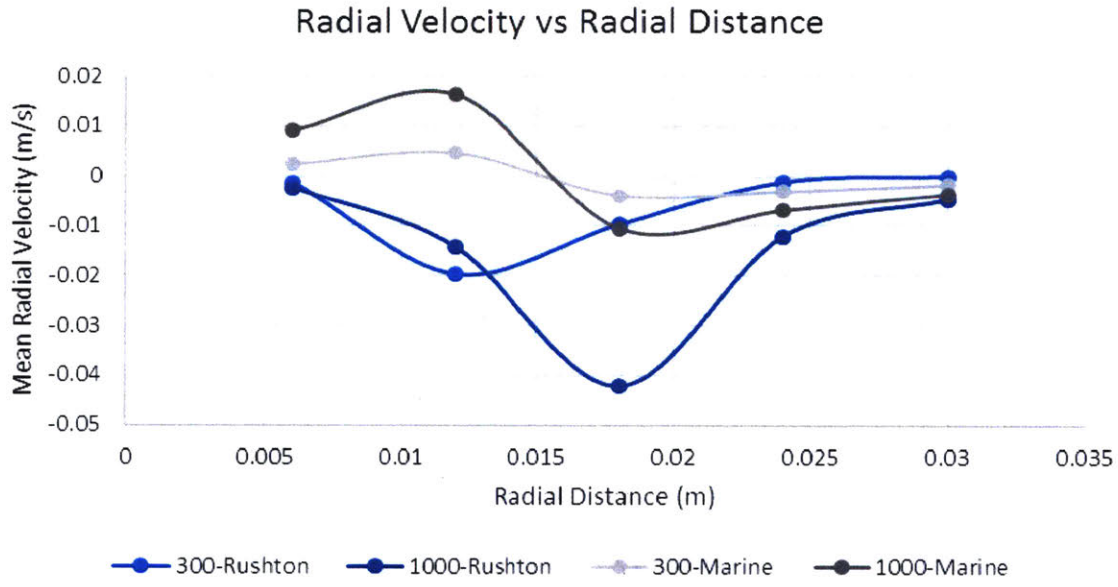


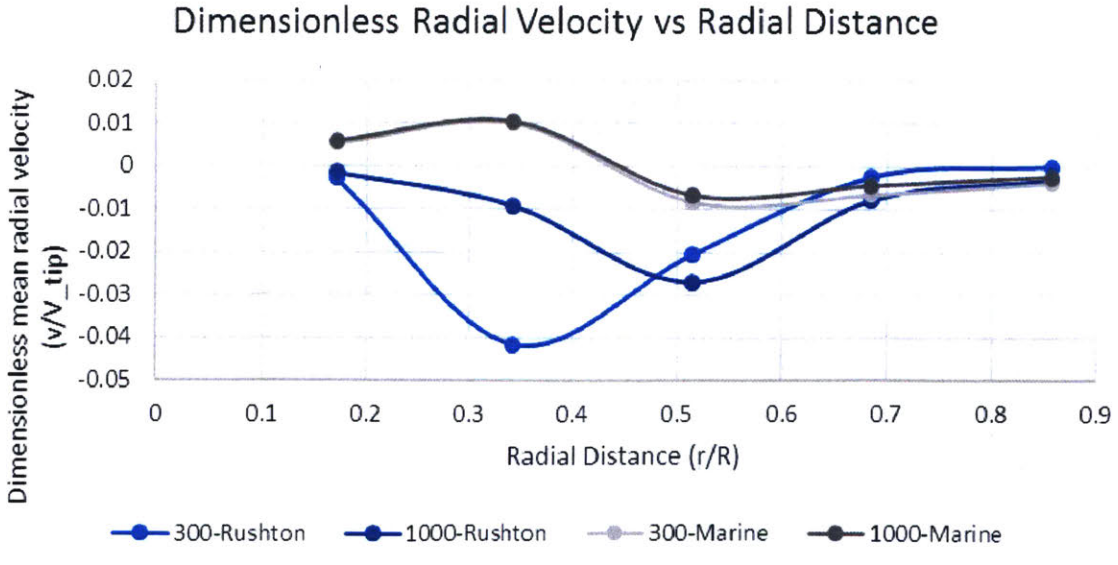

## A.2 Axial Velocity vs Radial Distance Profiles

Axial velocity profiles – 7 mm above (top) and 7 mm below (bottom) the top impeller, for the four impellers in the impeller study.

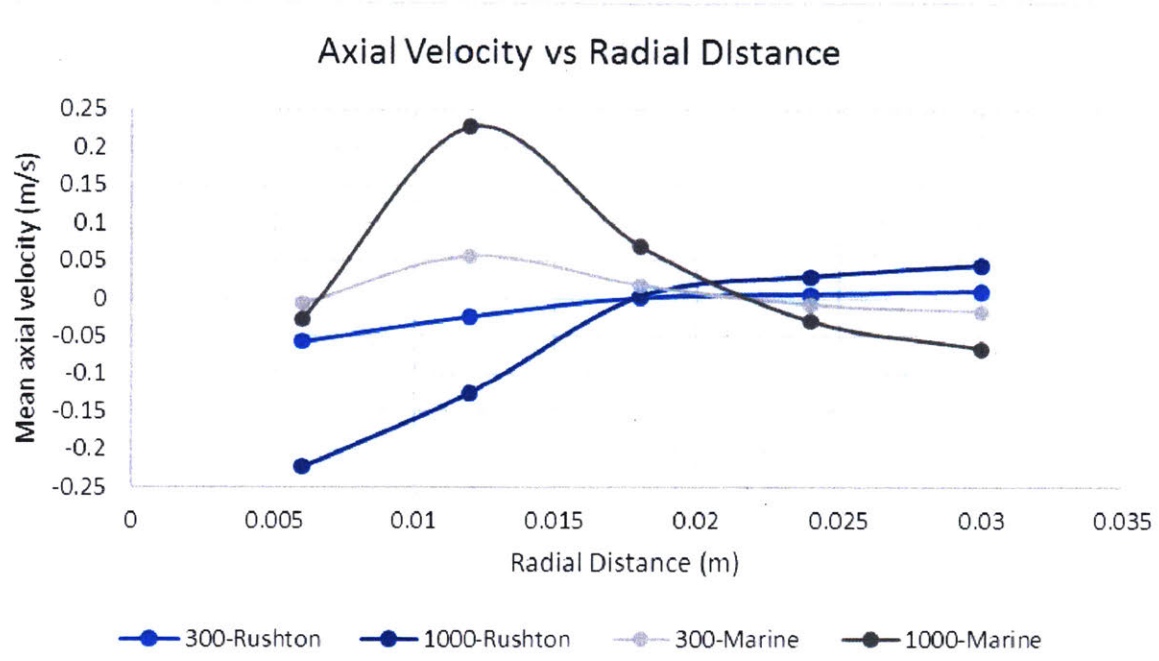


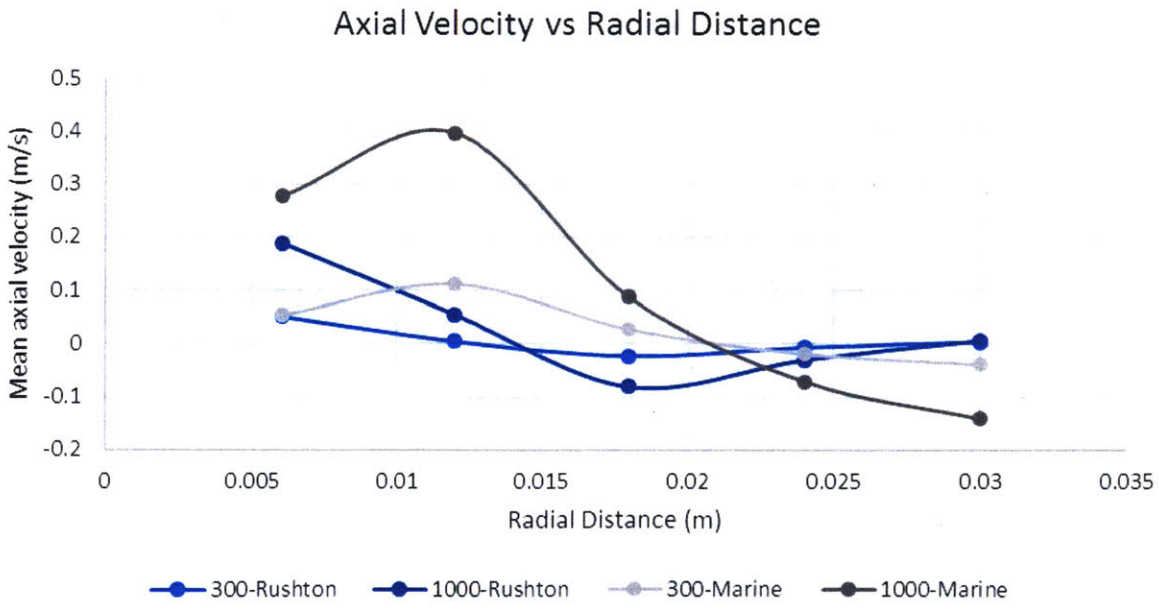

# Appendix B

## 5-liter Vessel Study Velocity Profiles

### B.1 Velocity vs Axial Distance Profile

Velocity profile as a function of axial distance, at a radial distance 0.03 m from the center, of the 4 impeller speeds in the 5-liter vessel study.

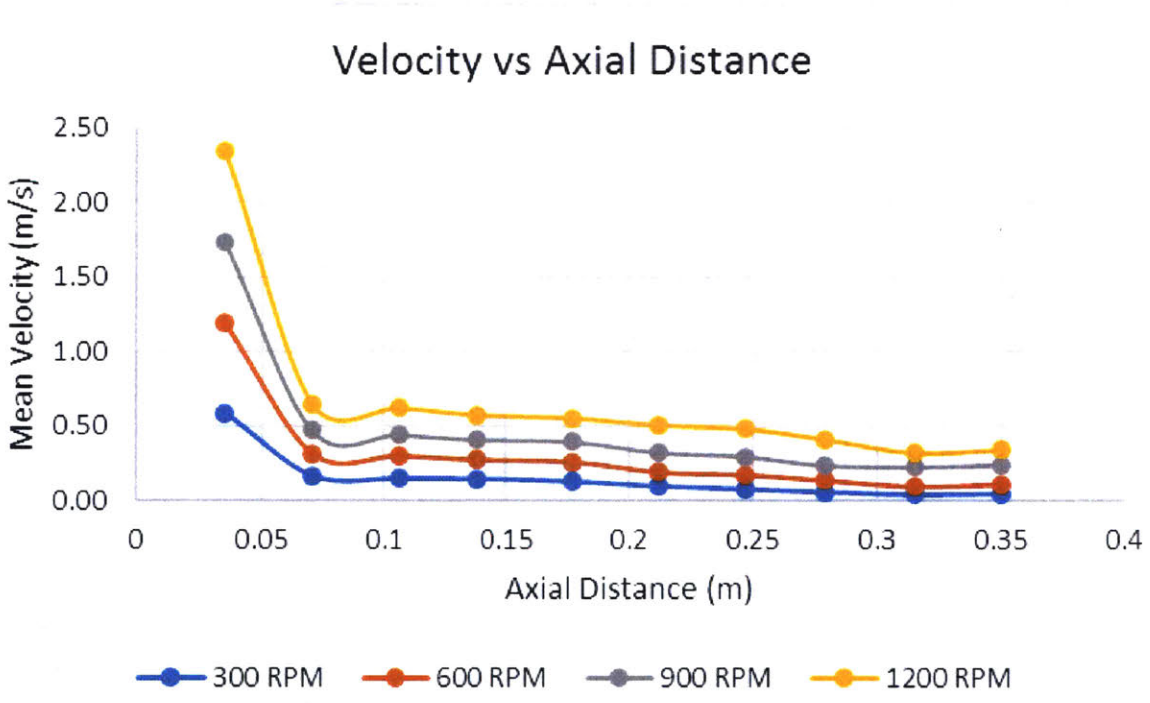

## B.2 Axial Velocity vs Radial Distance Profiles

Axial velocity profiles 7 mm above (top) and 7 mm below (bottom) the top impeller, as a function of radial distance, of the 4 impeller speeds in the 5-liter vessel study.

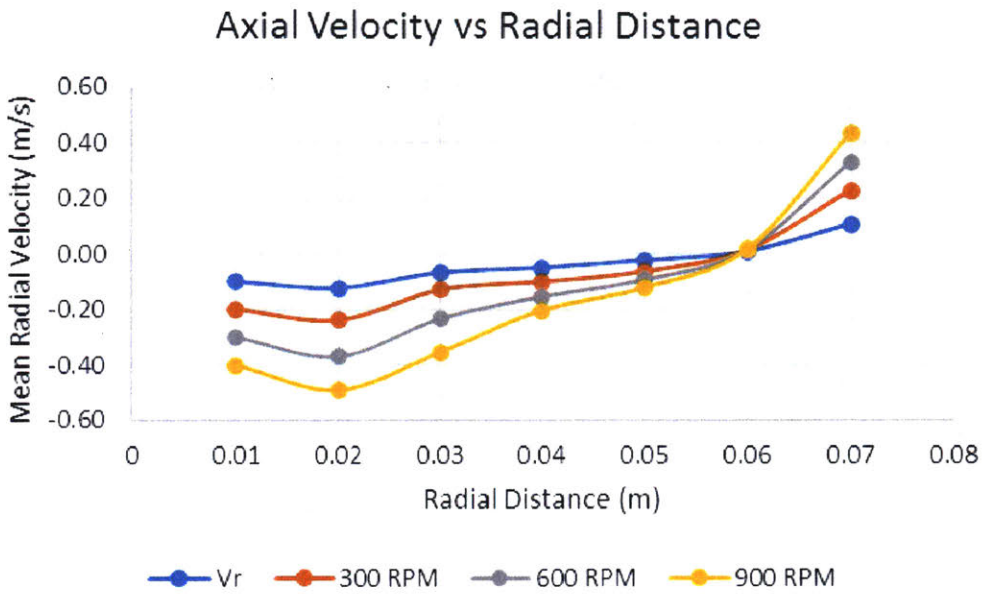


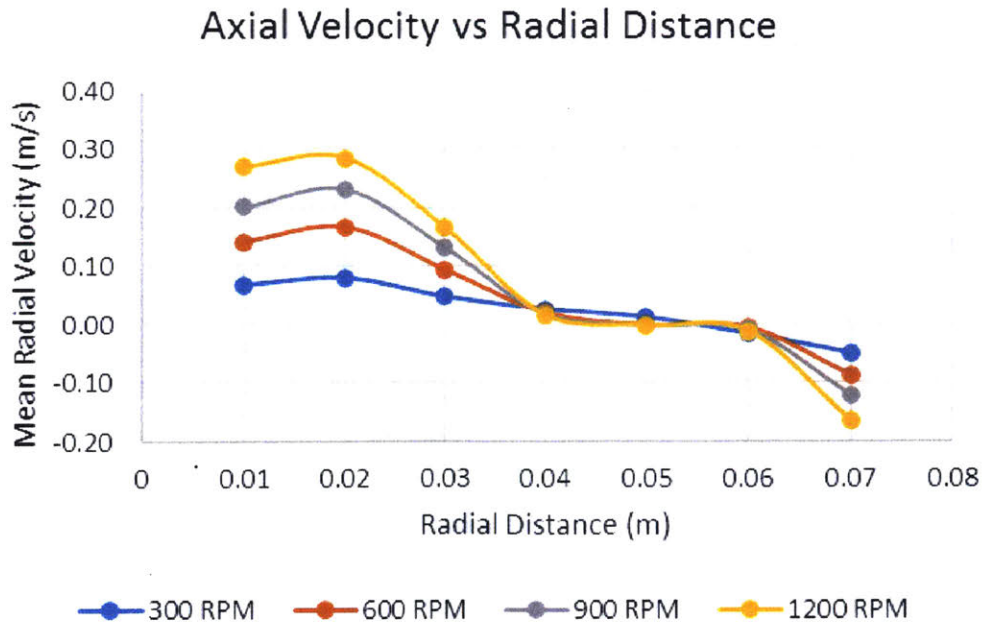

### B.3 Tangential Velocity vs Radial Distance Profiles

Tangential velocity profiles – absolute (top) and dimensionless (bottom) – as a function of radial distance, at a height of 0.0318 m from the bottom of the vessel, of the 4 impeller speeds in the 5-liter vessel study.

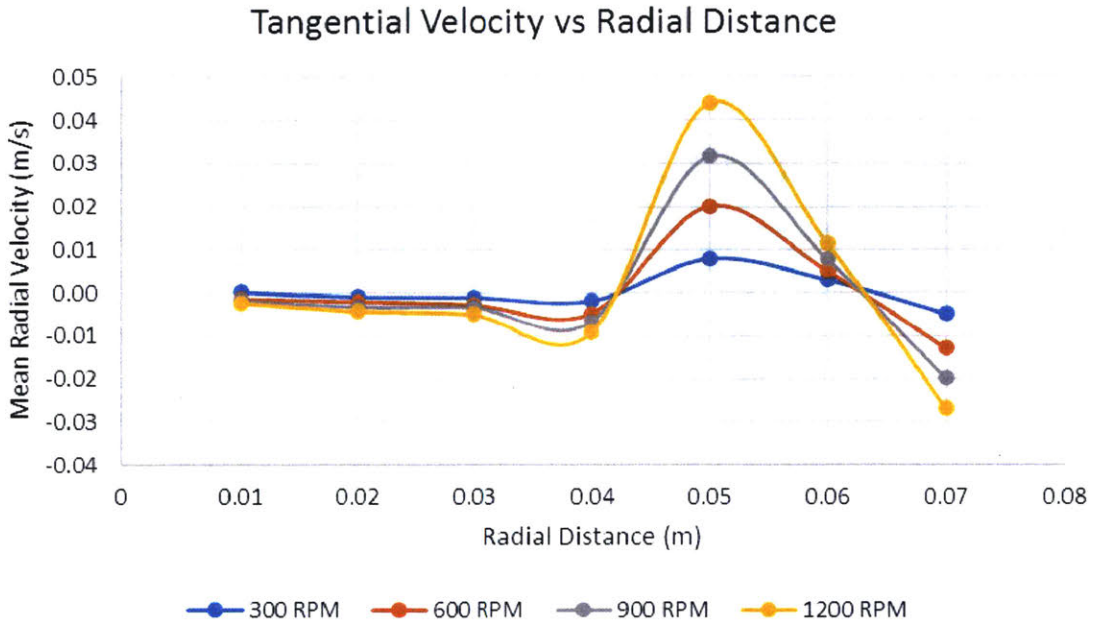


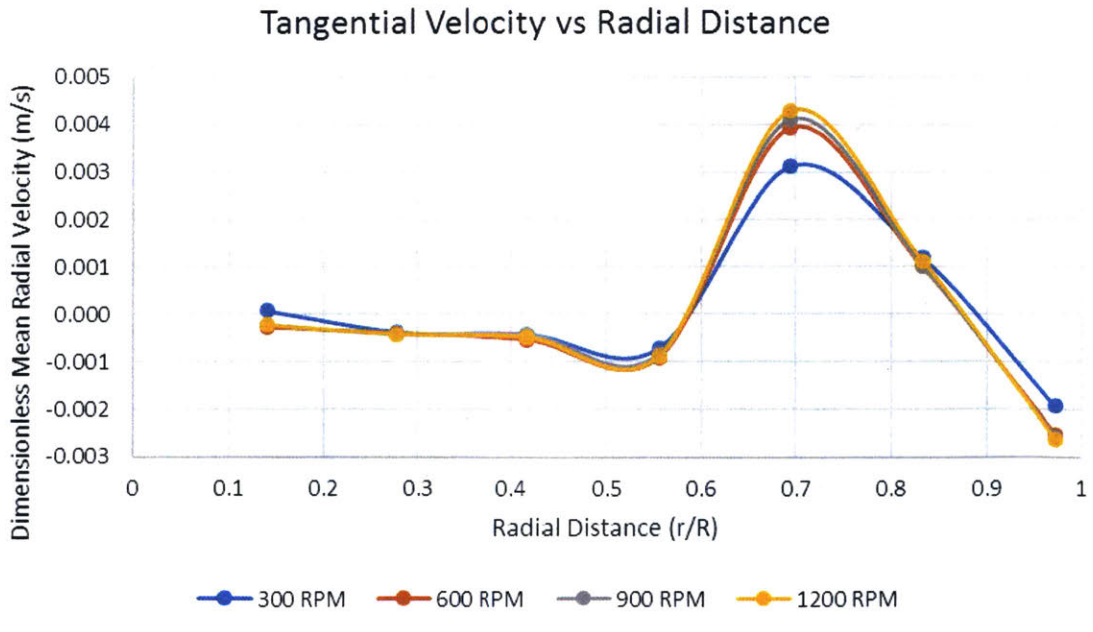

# Appendix C

## 3D CFD Study Results – 300, 600, 900 RPM cases

### C.1 Pressure Profiles

Pressure profiles for the three other impeller speeds from above at a height of 0.186 m.

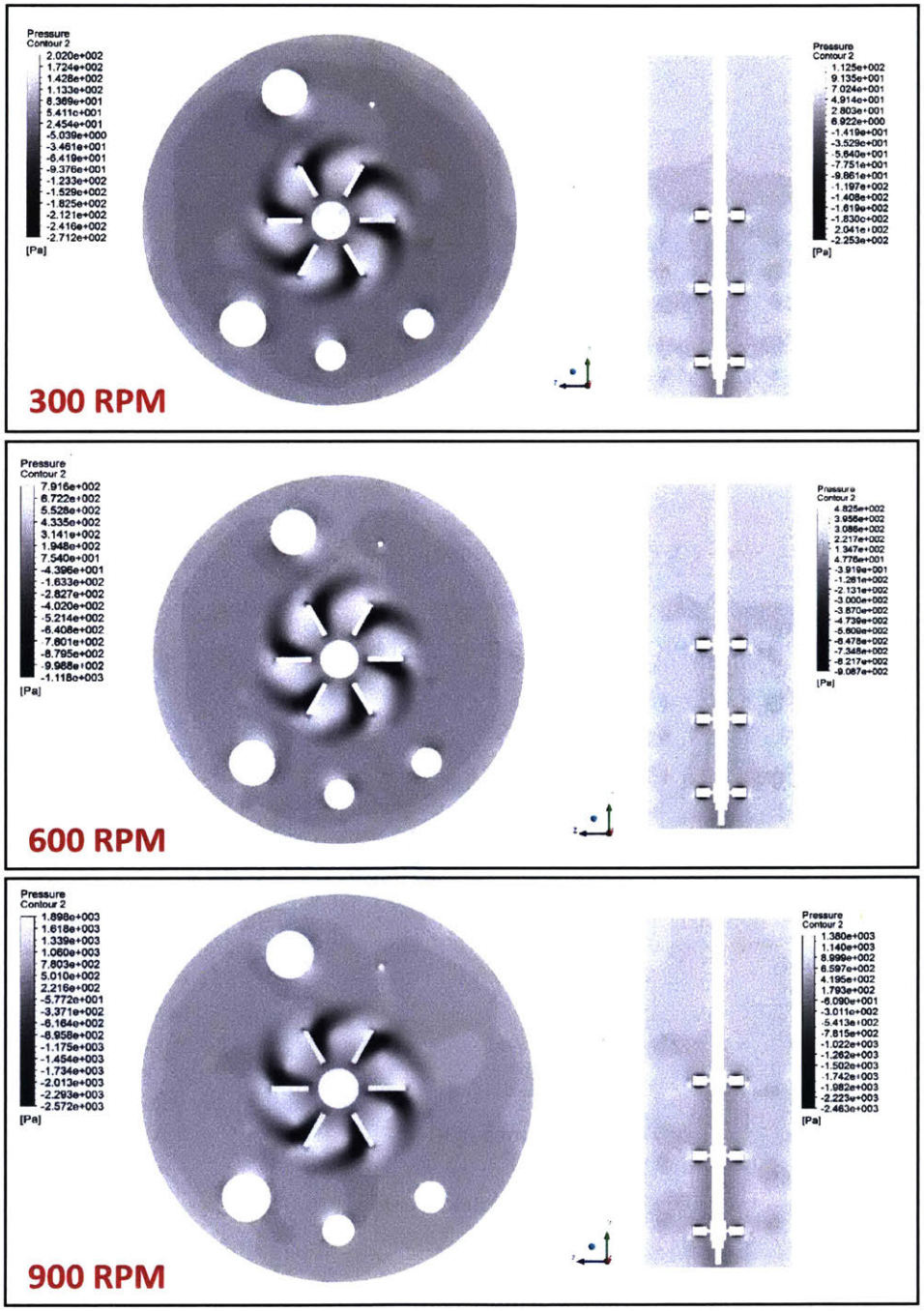

## C.2 Turbulence Eddy Dissipation Profiles

Turbulence Eddy Dissipation profiles of the three other impeller speeds.

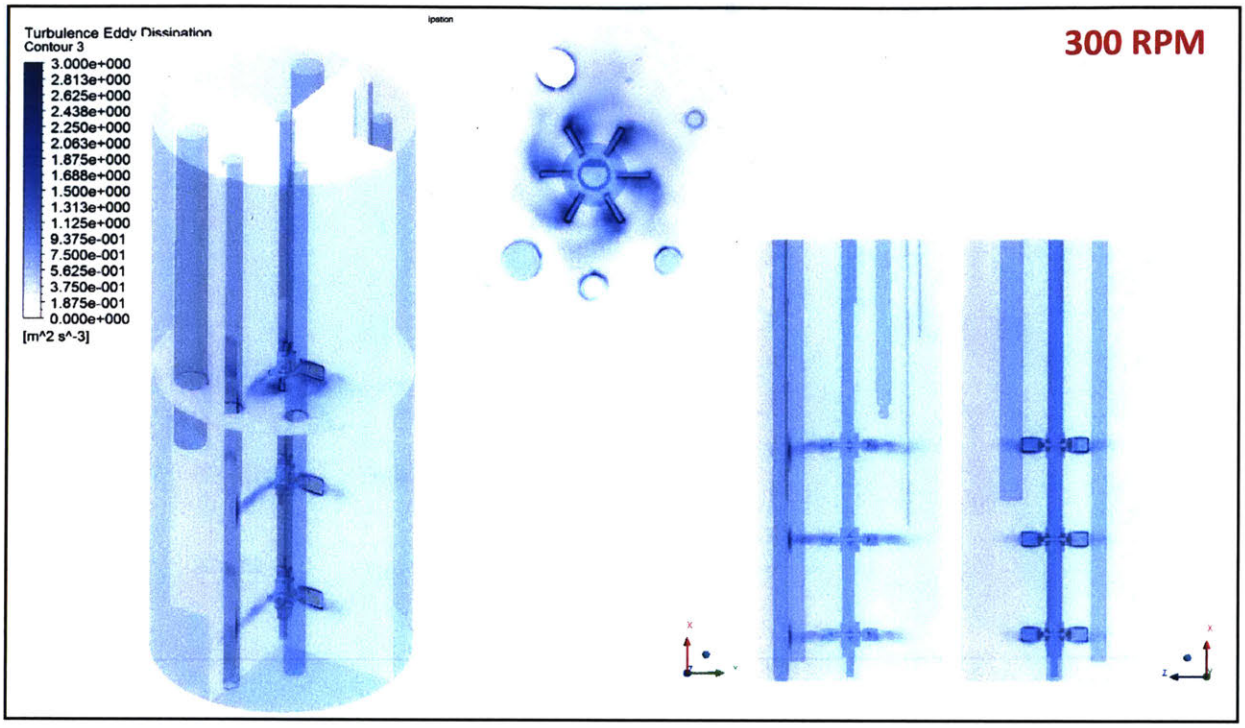


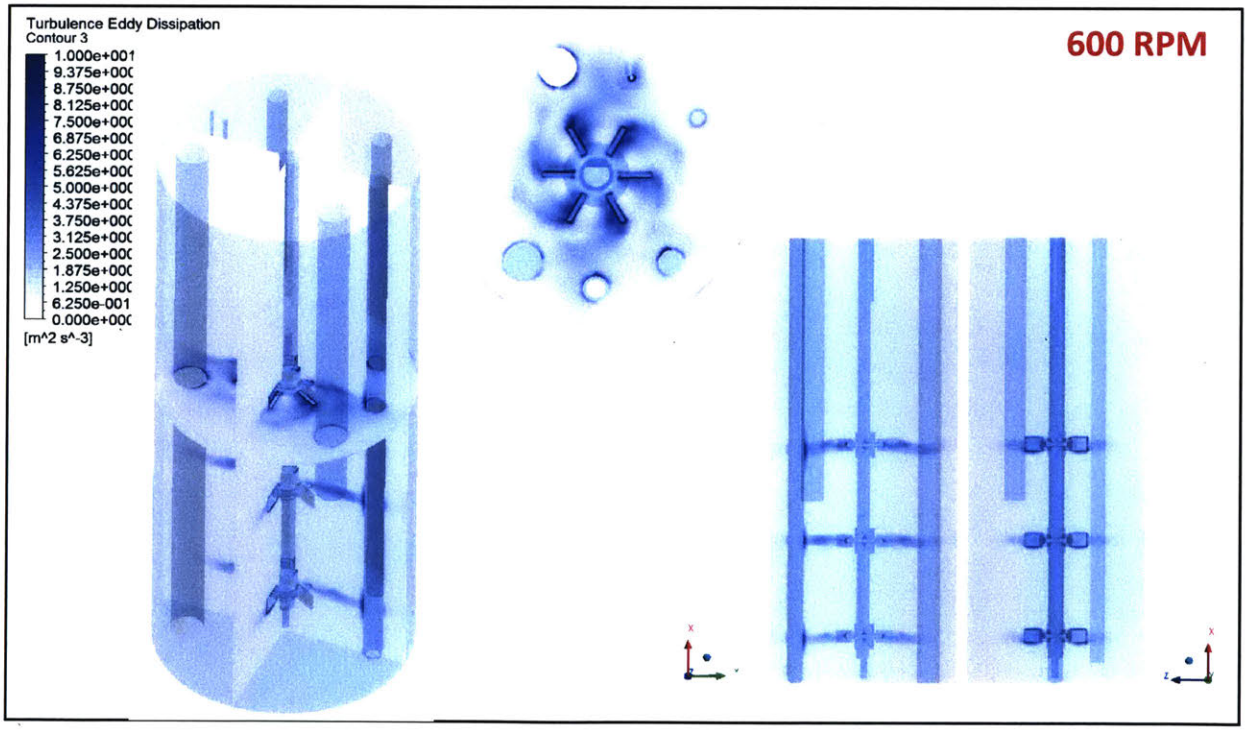

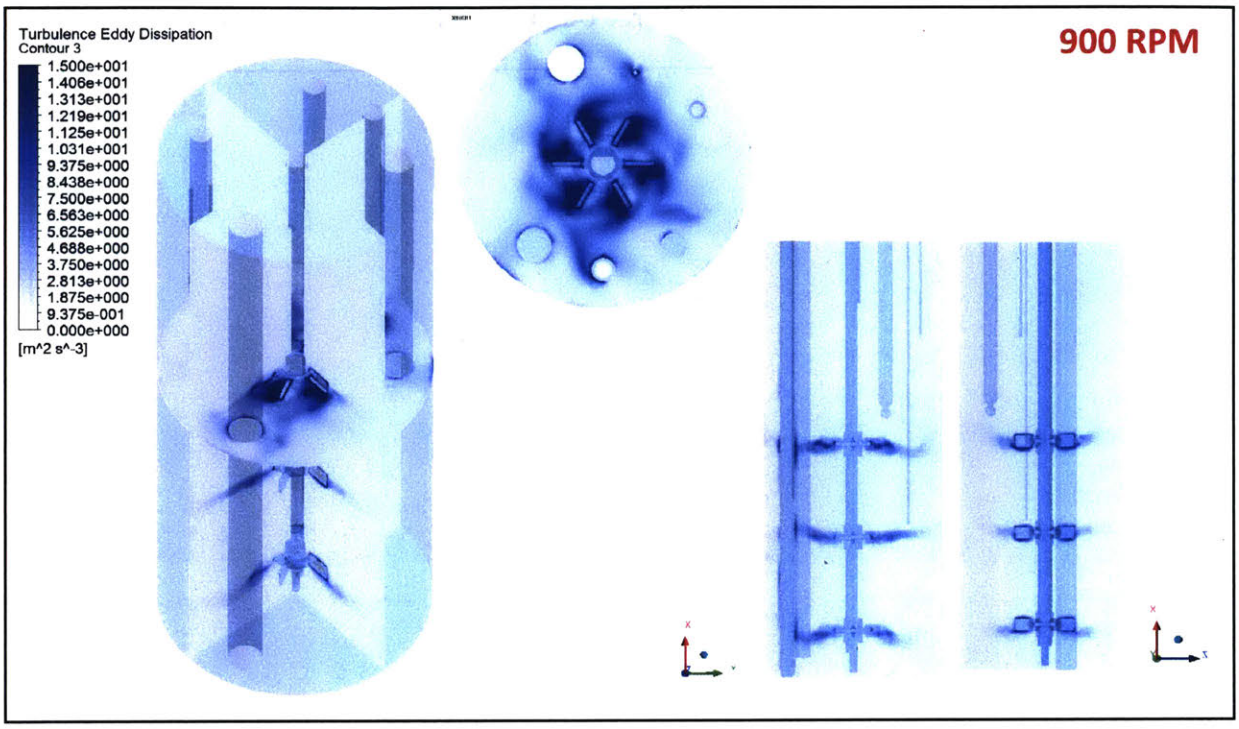
Turbulence Eddy Dissipation
Contour 3
1.500e+001
1.406e+001
1.313e+001
1.219e+001
1.125e+001
1.031e+001
9.375e+000
8.438e+000
7.500e+000
6.563e+000
5.625e+000
4.688e+000
3.750e+000
2.813e+000
1.875e+000
9.375e-001
0.000e+000
[m^2 s^-3]
900 RPM

## C.3 Wall Shear Profiles

Wall shear profiles of the three other impeller speeds.

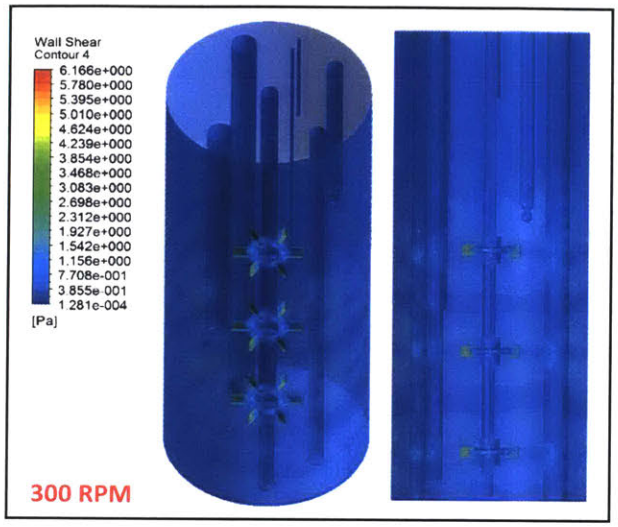


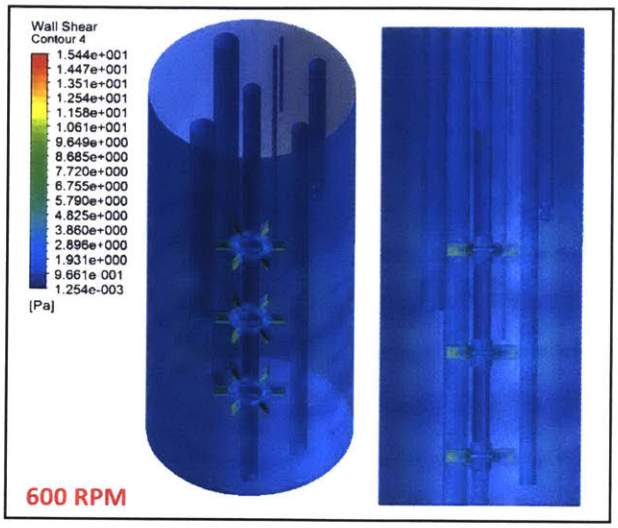


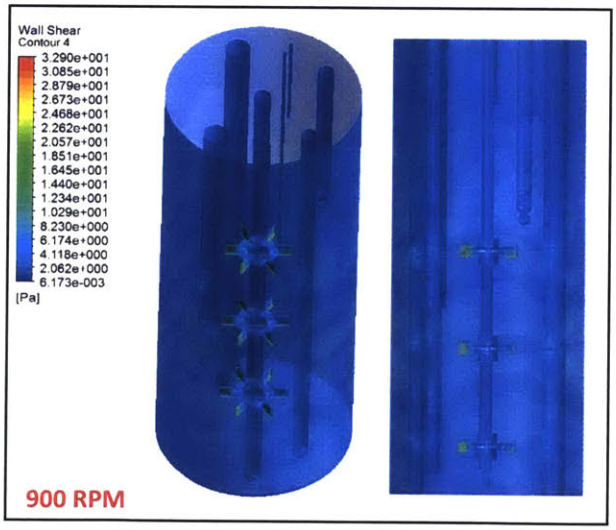

## C.4 Velocity Profiles

Velocity profiles in different planes of the three other impeller speeds.

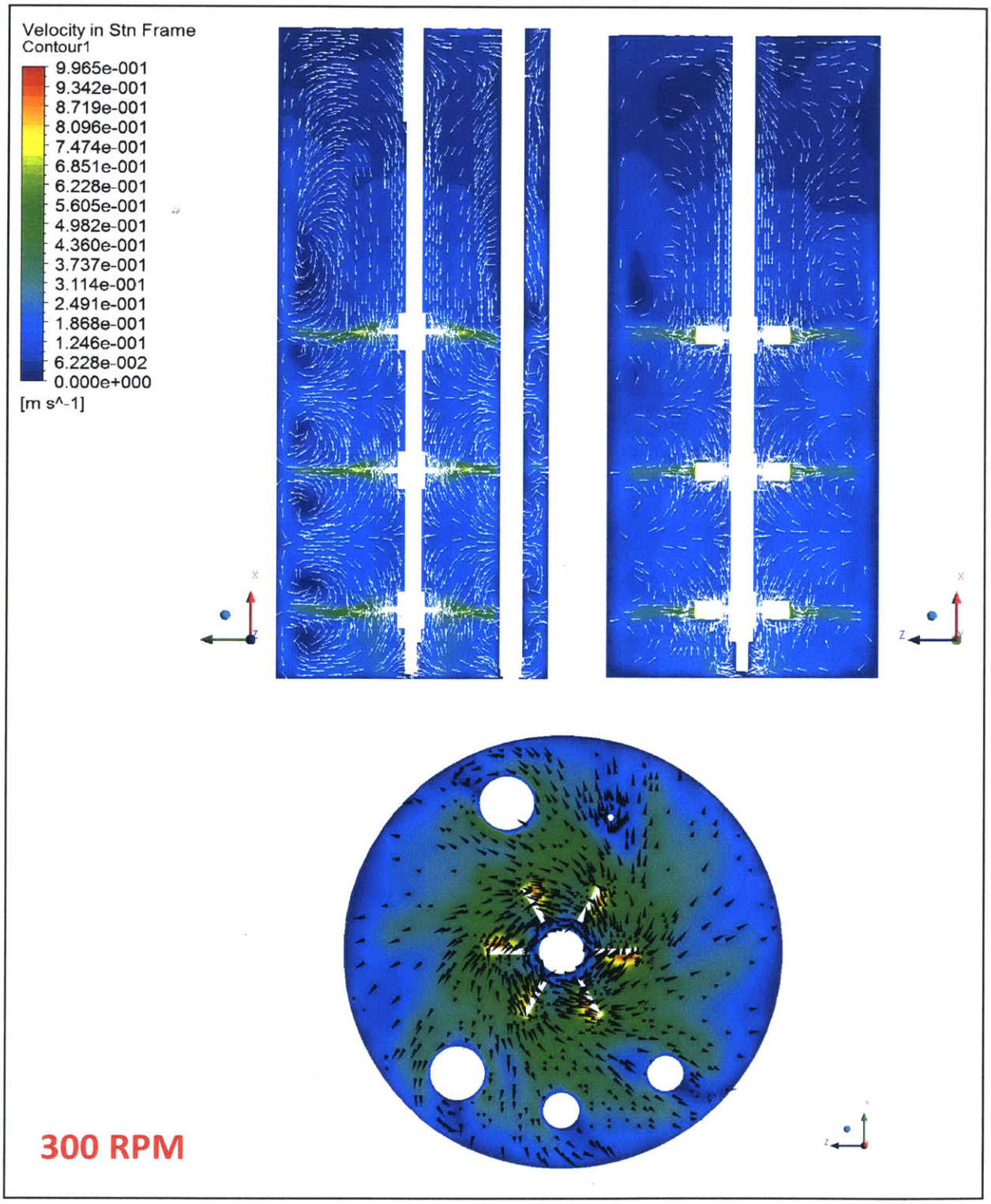

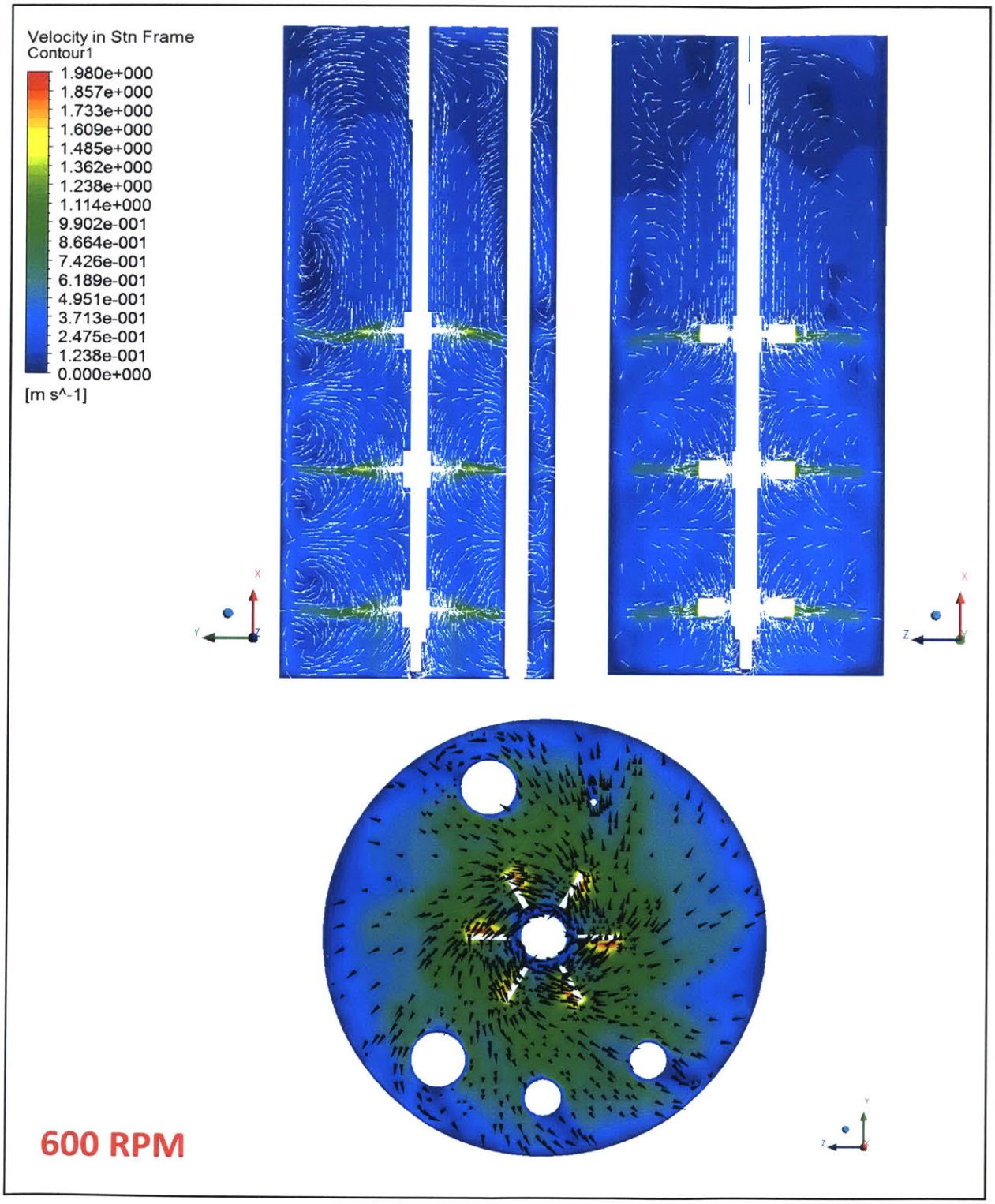
Velocity in Stn Frame
Contour1
1.980e+000
1.857e+000
1.733e+000
1.609e+000
1.485e+000
1.362e+000
1.238e+000
1.114e+000
9.902e-001
8.664e-001
7.426e-001
6.189e-001
4.951e-001
3.713e-001
2.475e-001
1.238e-001
0.000e+000
[m s^-1]
600 RPM

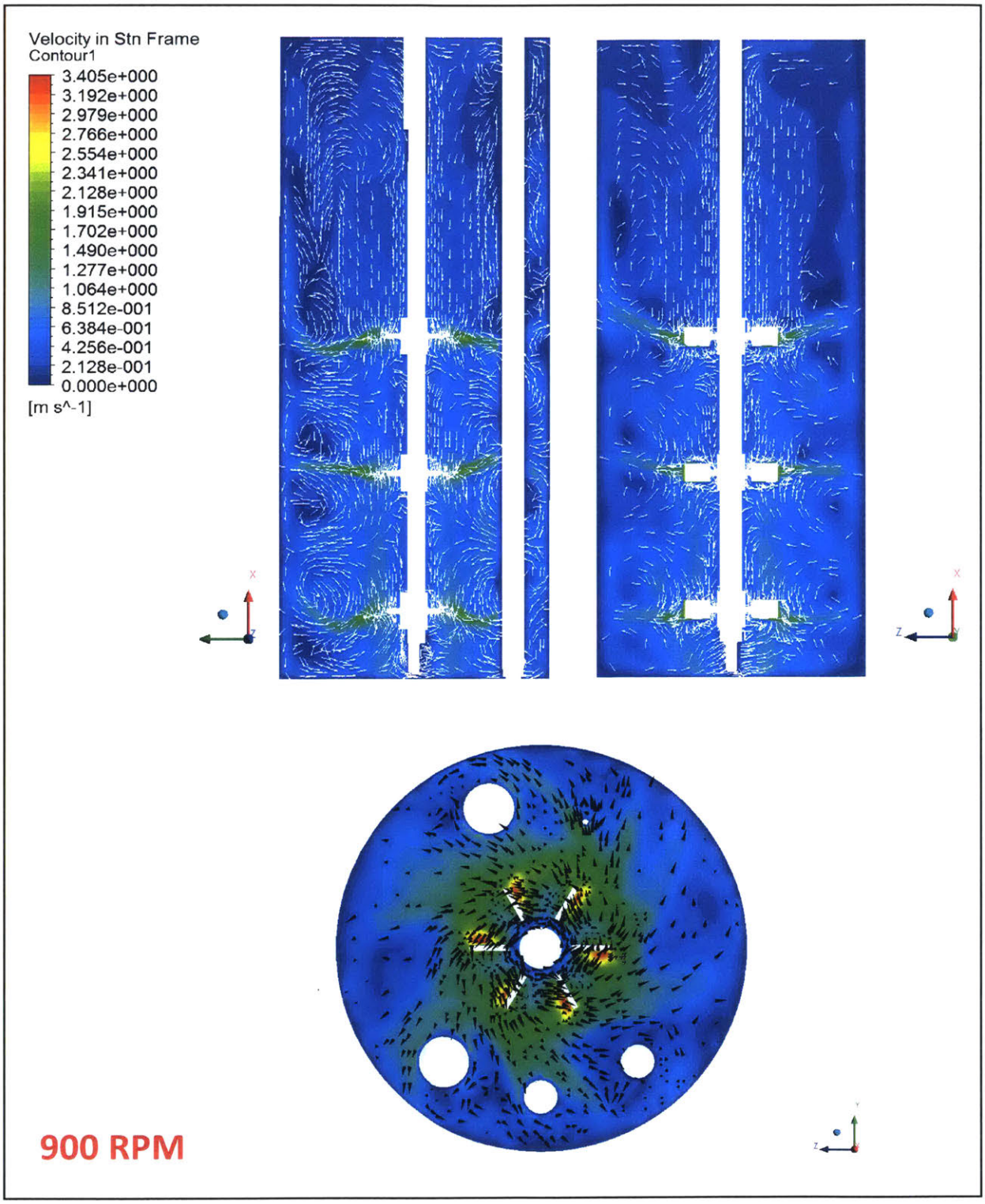
Velocity in Stn Frame
Contour1
3.405e+000
3.192e+000
2.979e+000
2.766e+000
2.554e+000
2.341e+000
2.128e+000
1.915e+000
1.702e+000
1.490e+000
1.277e+000
1.064e+000
8.512e-001
6.384e-001
4.256e-001
2.128e-001
0.000e+000
[m s^-1]
900 RPM

# Appendix D

## Market Research

### D.1 Number of Uninsured People

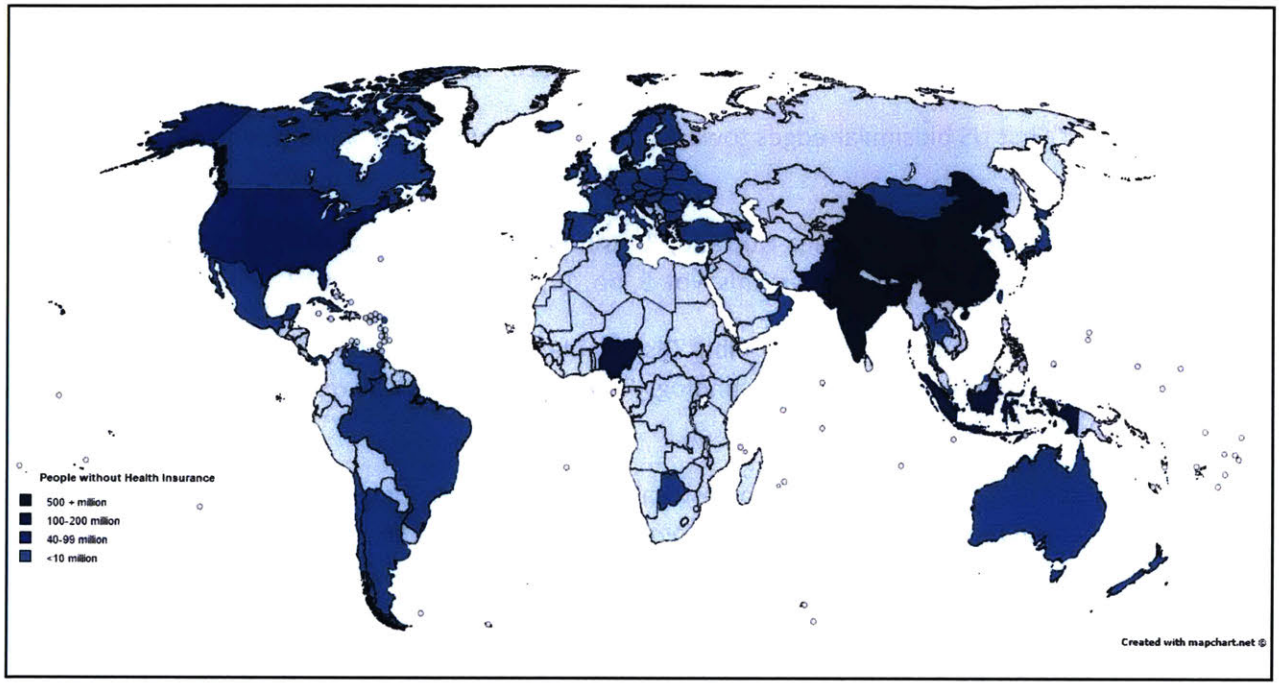

# Bibliography


[1] A. E. Raj and N. G. Karanth, "Fermentation Technology and Bioreactor Design," in *Food Biotechnology, Second Edition*, Taylor & Francis Group, 2006, pp. 33-77.

[2] Massachusetts Institute of Technology, *10.03x Making Biologic Medicines for Patients: The Principles of Biopharmaceutical Manufacturing.*

[3] EvaluatePharma, "World Preview 2015, Outlook to 2020," 2015.

[4] M. Senior, "First US biosimilar edges towards market," *Nature Biotechnology,* vol. 33, pp. 222-223, 2015.

[5] B. Calo-Fernandez and J. Martinez-Hurtado, "Biosimilars: company strategies to capture value from the biologics market," *Pharmaceuticals,* vol. 5, no. 12, pp. 1393-1408, 2012.

[6] R. Eibl, S. Kaiser, R. Lombriser and D. Eibl, "Disposable bioreactors: the current state-of-the-art and recommended applications in biotechnology," *Applied Microbiology and Biotechnology,* vol. 86, no. 1, pp. 41-49, 2010.

[7] D. Eisenkraetzer, "Upstream and Downstream Process Technology: Bioreactors for Animal Cell Culture," in *Animal Cell Biotechnology, Biologics Production*, Berlin, Germany, Walter de Gruyter GmbH & Co KG, 2015.

[8] D. L. Hacker, M. De Jesus and F. M. Wurm, "25 years of recombinant proteins from reactor-grown cells - Where do we go from here?," *Biotechnology Advances,* vol. 27, pp. 1023-1027, 2009.

[9] N. Jones, "Single-use Processing for Microbial Fermentations," 14 April 2015. [Online]. Available: http://www.bioprocessintl.com/upstream-processing/fermentation/single-use-processing-for-microbial-fermentations/.

[10] S. S. Mostafa and X. Gu, "Strategies for Improved dCO2 Removal in Large-Scale Fed-Batch Cultures," *Biotechnology Progress,* vol. 19, no. 1, pp. 45-51, 2003.

[11] W. J. Kelly, "Using computational fluid dynamics to characterize and improve bioreactor performance," *Biotechnology and Applied Biochemistry,* pp. 225-238, 2008.

[12] F. Garcia-Ochoa and E. Gomez, "Bioreactor scale-up and oxygen transfer rate in microbial processes: An overview," *Biotechnology Advances,* vol. 27, pp. 153-176, 2009.

[13] R. Higbie, "The rate of absorption of a pure gas into a still liquid during short periods of exposure," *Institution of Chemical Engineers,* pp. 36-60, 1935.

[14] Y. Kawase, B. Halard and M. Moo-Young, "Theoretical prediction of volumetric mass transfer coefficients in bubble columns for Newtonian and non-Newtonian fluids," *Chemical Engineering Science,* pp. 1690-1617, 1987.

[15] P. Wilkinson, Haringa H and L. Van Dierendonck, "Mass transfer and bubble size in bubble column under pressure," *Chemical Engineering Science,* pp. 1417-1427, 1994.

[16] M. Tobajas, E. Garcia-Calvo, M. Siegel and S. Apitz, "Hydrodynamics and mass transfer prediction in a three-phase airlift reactor for marine sediment biotreatment," *Chemical Engineering Science,* pp. 5347-5354, 1999.

[17] F. Kudrewizki, "Zur Berechung des gasgehaltes in begasten Ruhrkesseln," *Chem Technol,* pp. 247-249, 1982.

[18] F. Kudrewizki and P. Rabe, "Model of the dissipation of mechanical energy in gassed stirred tanks," *Chemical Engineering Science,* pp. 2247-2252, 1986.

[19] S. Bhavaraju, T. Russell and H. Blanch, "The design of gas sparged devices for viscous liquid systems," *Advances in Chemical Engineering,* vol. 24, pp. 454-66, 1978.

[20] J.-D. Y. R. C. K.-C. C. Nam Sun Wang, "Unified modeling framework of cell death due to bubbles in agitated and sparged bioreactors," *Journal of Biotechnology,* vol. 33, pp. 107-122, 1994.

[21] R. Cherry and C. Hulle, "Cell Death in the Thin Films of Bursting Bubbles," *Biotechnology Progress,* vol. 8, pp. 11-18, 1992.

[22] A. H. D. I. W. Steven Meier, "Cell Death from Bursting Bubbles: Role of Cell Attachment to Rising Bubbles in Sparged Reactors," *Biotechnology and Bioengineering,* vol. 62, no. 4, pp. 468-478, 1999.

[23] H. Luo and H. F. Svendsen, "Theoretical Model for Drop and Bubble Breakup in Turbulent Dispersions," *American Institute of Chemical Engineers Journal,* vol. 42, no. 5, pp. 1225-1233, 1996.

[24] J. A. Jr., "Governing Equations of Fluid Dynamics," in *Computational Fluid Dynamics: An Introduction (3rd Edition)*, Springer Berlin Heidelberg, 2009, pp. 14-51.

[25] F. Kerdouss, A. Bannari, P. Proulx, R. Bannari, M. Skrga and Y. Labrecque, "Two-phase mass transfer coefficient prediction in stirred vessel with a CFD model," *Computers & Chemical Engineering,* vol. 32, no. 8, pp. 1943-1955, 2008.

[26] D. H. Noorman, "An industrial perspective on bioreactor scale-down: What we can learn from combined large-scale bioprocess and model fluid studies," *Biotechnology Journal,* vol. 6, no. 8, pp. 934-943, 2011.

[27] B.-H. Um and T. R. Hanley, "A CFD model for predicting the flow patterns of viscous fluids in a bioreactor under various operating conditions," *Korean Journal of Chemical Engineering,* vol. 25, no. 5, pp. 1094-1102, 2008.

[28] R. Gelves, A. Dietrich and R. Takors, "Modeling of gas–liquid mass transfer in a stirred tank bioreactor agitated by a Rushton turbine or a new pitched blade impeller," *Bioprocess and Biosystems Engineering,* vol. 37, no. 3, pp. 365-375, 2014.

[29] S. C. Kaiser, C. Loffelholz, S. Werner and D. Eibl, "CFD for Characterizing Standard and Single-use Stirred Cell Culture Bioreactors," in *Computational Fluid Dynamics Technologies and Applications*, InTech, 2011, pp. 97-122.

[30] ANSYS Fluent, "10.3.1 The Multiple Reference Frame Model," [Online]. Available: https://www.sharcnet.ca/Software/Fluent6/html/ug/node419.htm. [Accessed 2017].

[31] J. Y. Luo, R. I. Issa and A. D. Gosman, "Prediction of Impeller-induced flows in mixing vessels using multiple frames of reference," in *Institution of Chemical Engineers Symposium Series*, 1994.

[32] L. Yu, J. Ma and S. Chen, "Numerical simulation of mechanical mixing in high solid anaerobic digester," *Bioresource Technology,* vol. 102, no. 2, pp. 1012-1018, 2011.

[33] S. Murthy Shekhar and S. Jayanti, "CFD study of power and mixing time for paddle mixing in unbaffled vessels," *Chemical Engineering Research and Design,* vol. 80, pp. 482-498, 2002.

[34] A. Bakker, R. D. LaRoche, M. H. Wang and R. V. Calabrese, "Sliding Mesh Simulation of Laminar Flow in Stirred Reactors," *Chemical Engineering Research and Design,* vol. 75, no. 1, pp. 42-44, 1997.

[35] D. M. Koerich and L. M. Rosa, "Numerical evaluation of the low Reynolds turbulent flow behaviour in a bioreactor," *International Journal of Simulation and Process Modelling,* vol. 11, no. 1, pp. 66-75, 2016.

[36] S. Bruning and D. Weuster-Botz, "CFD analysis of interphase mass transfer and energy dissipation in a millimeter-scale stirred-tank reactor for filamentous microorganisms," *Chemical Engineering Research and Design,* vol. 92, pp. 240-248, 2014.

[37] G. Montate, M. Coroneo, J. A. Francesconi, A. Paglianti and F. Magelli, "CFD Modelling of a Novel Stirred Reactor for the Bioproduction of Hydrogen," in *14th European Conference on Mixing*, Warsaw, 2012.

[38] M. Jahoda, L. Tomaskova and M. Mostek, "CFD Prediction of liquid homogenisation in a gas-liquid stirred tank," *Chemical Engineering Research and Design,* vol. 87, pp. 460-467, 2009.

[39] A. Bakker, K. J. Myers, R. W. Ward and C. K. Lee, "The Laminar and Turbulent Flow Pattern of a Pitched Blade Turbine," *Institution of Chemical Engineers,* vol. 74, pp. 485-491, 1996.

[40] I. Naude, C. Xuereb and J. Bertrand, "Direct prediction of the flows induced by a propeller in an agitated vessel using an unstructured mesh," *Canadian Journal of Chemical Engineering,* vol. 76, no. 3, pp. 631-640, 1998.

[41] J. Aubin, D. F. Fletcher and C. Xuereb, "Modeling turbulent flow in stirred tanks with CFD: the influence of the modeling approach, turbulence model and numerical scheme," *Experimental Thermal and Fluid Science,* vol. 28, no. 5, pp. 431-445, 2003.

[42] K. Ng and M. Yianneskis, "Observations of the Distribution of Energy Dissipation in Stirred Vessels," *Chemical Engineering Research and Design,* vol. 78, pp. 334-341, 2000.

[43] C. Sturesson, H. Theliander and A. Rasmuson, "An Experimental (LDA) and Numerical Study of the Turbulent Flow Behavior in the Near Wall and Bottom Regions in an Axially Stirred Vessel," *American Institute of Chemical Engineers Symposium Series,* vol. 91, pp. 102-114, 1995.

[44] K. Rutherford, K. C. Lee, S. M. S. Mahmoudi and M. Yianneskis, "Hydrodynamic Characteristics of Dual Rushton Impeller Stirred Vessels," *American Institute of Chemical Engineers,* vol. 42, no. 2, pp. 332-346, 1996.

[45] J. A. Sachez Perez, E. M. Rodriguez Porcel, J. L. Casas Lopez, J. M. Fernandez Sevilla and Y. Chisti, "Shear rate in stirred tank and bubble column bioreactors," *Chemical Engineering Journal,* vol. 124, pp. 1-5, 2006.

[46] B. Robertson and J. J. Ulbrecht, "Measurement of shear rate on an agitator in fermentation broth," in *Biotechnology Processes: Scale-up and Mixing*, New York, American Institute of Chemical Engineers, 1987, pp. 72-81.

[47] W. Kelly and B. Gigas, "Using CFD to predict the behavior of power law fluids near axial-flow impellers operating in the transitional flow regime," *Chemical Engineering Science,* vol. 58, pp. 2141-2152, 2003.

[48] F. Fakheri and J. Moghaddas, "Compartment Mixing Model in a Stirred Tank Equipped Dual Rushton Turbine," *Iranian Journal of Chemical Engineering,* vol. 9, no. 3, pp. 14-21, 2012.

[49] P. Vrabel, R. Van Der Lans, Y. Q. Cui, K. Luyben and A. M. Ch, "Compartment model approach: Mixing in large scale aerated reactors with multiple impellers," *Chemical Engineering Research and Design,* vol. 77, pp. 291-302, 1999.

[50] Y. Q. Cui, R. Lans, H. J. Noorman and K. Luyben, "Compartment mixing model for stirred reactors with multiple impellers," *Japanese Journal of Chemical Engineering,* vol. 34, pp. 1499-1505, 2001.

[51] G. R. Kasat and A. B. Pandit, "Mixing time studies in multiple impeller agitated reactors," *Canadian Journal of Chemical Engineering,* vol. 82, pp. 892-904, 2008.

[52] J. M. T. Vasconcelos, S. S. Alves and J. M. Barata, "Mixing in gas-liquid contractors agitated by multiple turbines," *Chemical Engineering and Science,* vol. 50, pp. 2343-2354, 1995.

[53] K. Ng, J. Fentiman, K. C. Lee and M. Yianneskis, "Assessment of Sliding Mesh CFD Predictions and LDA Measurements of the Flow in a Tank Stirred by a Rushton Impeller," *Institute of Chemical Engineers,* vol. 76, pp. 737-747, 1998.

[54] R. Zadghaffari, J. S. Moghaddas and J. Revstedt, "A mixing study in a double-Rushton stirred tank," *Computers and Chemical Engineering,* vol. 33, pp. 1240-1246, 2009.

[55] A. O. O. Odeleye, D. T. J. Marsh, M. D. Osborne, G. J. Lye and M. Micheletti, "On the fluid dynamics of a laboratory scale single-use stirred bioreactor," *Chemical Engineering Science,* vol. 111, no. 100, pp. 299-312, 2014.

[56] R. Kunert and D. Reinhart, "Advances in recombinant antibody manufacturing," *Applied Microbiology and Biotechnology,* vol. 100, pp. 3451-3461, 2016.

[57] K. R. Love, K. A. Shah, C. A. Whittaker, J. Wu, M. C. Bartlett, D. Ma, R. L. Leeson, M. Priest, J. Borowsky, S. K. Young and J. C. Love, "Comparative genomics and transcriptomics of Pichia pastoris," *BMC Genomics,* 2016.

[58] A. E. Lu, J. A. Paulson, N. J. Mozdzierz, A. Stockdale, A. N. F. Versypt, K. R. Love, J. C. Love and R. D. Braatz, "Control systems technology in the advanced manufacturing of biologic drugs," in *Proceedings of the IEEE Conference on Control Applications*, Sydney, Australia, 2015.

[59] D. Jenke, "Evaluation of the Chemical Compatibility of Plastic Contact Materials and Pharmaceutical Products; Safety Considerations Related to Extractables and Leachables," *Journal of Pharmaceutical Sciences,* vol. 96, no. 10, pp. 2566-2581, October 2007.

[60] G. Rao, A. Moreira and K. Brorson, "Disposable Bioprocessing: The Future Has Arrived," *Biotechnology and Bioengineering,* vol. 102, no. 2, pp. 348-356, 1 Februrary 2009.

[61] A. A. Shukla and U. Gottschalk, "Single-use disposable technologies for biopharmaceutical manufacturing," *Trends in Biotechnology,* vol. 31, no. 3, pp. 147-154, March 2013.

[62] J. Bonham-Carter and J. Shevitz, "A Brief History of Perfusion Biomanufacturing," *Bioprocess International,* vol. 9, no. 9, pp. 24-31, 1 October 2011.

[63] E. S. Langer, "Trends in Perfusion Bioreactors: The Next Revolution in Bioprocessing?," *Bioprocess International,* vol. 9, no. 10, pp. 18-22, November 2011.

[64] V. Vojinovic, J. Cabral and L. Fonseca, "Real-time bioprocess monitoring: Part I: In situ sensors," *Sensors and Actuators B: Chemical,* vol. 114, no. 2, pp. 1083-1091, 26 April 2006.

[65] A. J. Brennan, J. Shevitz and J. D. Macmillan, "A perfusion system for antibody production by shear-sensitive hybridoma cells in a stirred reactor," *Biotechnology Techniques,* pp. 169-174, September 1987.

[66] R. J. Wojciechowski, D. P. Page, K. P. Bongers, S. T. Waniger, B. Norris, M. D. Hirschel, T. C. Duong Wong, M. P. Crep, M. J. Gramer and G. Adams, "Method and system for the production of cells and cell products and applications thereof". United Sates Patent US8383397 B2, 26 February 2013.

[67] Applikon Biotechnology, "Cultivation Systems from Discovery to Production," 18 May 2014. [Online]. Available: http://www.reseachem.ch/de-wAssets/docs/downloads/SIP-Catalog-2014.pdf.

[68] K. A. McDonald and A. P. Jackman, "Bioreactor studies of growth and nutrient utilization in alfalfa suspension cultures," *Plant Cell Reports,* pp. 455-458, 1989.

[69] R. M. Matanguihan, K. B. Konstantinov and T. Yoshida, "Dielectric measurement to monitor the growth and the physiological states of biological cells," *Bioprocess Engineering,* pp. 213-222, 1994.

[70] J. P. Carvell and J. E. Dowd, "On-line Measurements and Control of Viable Cell Density in Cell Culture Manufacturing Processes using Radio-frequency Impedance," *Cytotechnology,* pp. 35-50, March 2006.

[71] P. Hauptmann, N. Hoppe and A. Puttmer, "Application of ultrasonic sensors in the process industry," *IOP Science,* vol. 13, no. 8, pp. 73-83, 1 July 2002.

[72] D. Ghimire and J. Lee, "Color Image Enhancement in HSV Space Using Nonlinear Transfer Function and Neighborhood Dependent Approach with Preserving Details," in *Image and Video Technology (PSIVT), 2010 Fourth Pacific-Rim Symposium on*, Hsinchu, Taiwan, 2010.

[73] R. Fergus, B. Singh, A. Hertzman, S. T. Roweis and W. T. Freeman, "Removing Camera Shake from a Single Photograph," *ACM Transactions on Graphics (TOG) - Proceedings of ACM SIGGRAPH 2006,* vol. 25, no. 3, pp. 787-794, July 2006.

[74] D. H. Brainard and B. A. Wandell, "Analysis of the retinex theory of color vision," *Journal of the Optical Society of America A,* vol. 3, no. 10, pp. 1651-1661, 1986.

[75] E. S. Langer and R. A. Rader, "Continuous Bioprocessing and Perfusion: Wider Adoption Coming as Bioprocessing Matures," *Bioprocessing Journal: Trends & Developments in BioProcess Technology,* pp. 50-55, 2014.

[76] R. Eibl, S. Kaiser, R. Lombriser and D. Eibl, "Disposable bioreactors: the current state-of-the-art and recommended applications in biotechnology," *Applied Microbiology and Biotechnology,* vol. 86, no. 1, pp. 41-49, March 2010.

[77] Ocean Optics, "pH Sensing," [Online]. Available: https://oceanoptics.com/measurementtechnique/ph-sensing/. [Accessed 2017].

[78] Mason Technology, "Non-invasive pH Sensors," [Online]. Available: http://www.masontechnology.ie/files/documents/PreSens_NoninvasivepHSensors.pdf. [Accessed 2017].

[79] BioProcess Online, "Datasheet: Non-Invasive pH Sensors," [Online]. Available: https://www.bioprocessonline.com/doc/non-invasive-ph-sensors-0003. [Accessed 2017].

[80] Sensorland, "Understanding pH measurement," [Online]. Available: http://www.sensorland.com/HowPage037.html. [Accessed 2017].

[81] Finesse Solutions, "TruFluor pH Single-use Optical pH Sensors," [Online]. Available: http://www.finesse.com/products/sensors/single-use-sensors/trufluor-ph/. [Accessed 2017].

[82] F. Bernard, E. Chevalier, J.-M. Cappia, M. Heule and T. Paust, "Disposable pH Sensors," BioProcess International, [Online]. Available: http://www.bioprocessintl.com/upstream-processing/upstream-single-use-technologies/disposable-ph-sensors-184073/. [Accessed 2017].

[83] D. Guenther and Y. Mattley, "Noninvasive, Real-Time Monitoring of Oxygen and pH During E. coli Fermentation Using Optical Sensors," [Online]. Available: https://oceanoptics.com//wp-content/uploads/App-Note-NoninvRealTimeMonitoringofOxandpHduringEcoliFermentation1.pdf. [Accessed 2017].

[84] Scientific Bioprocessing, "pH and DO Flask w/ Patches," 2017. [Online]. Available: http://www.scientificbioprocessing.com/none-invasine-ph-do-monitoring/flasks. [Accessed 2017].

[85] S. Arain, "Noninvasive Oxygen and pH Sensors," Genetic Engineering & Biotechnology News, 15 September 2011. [Online]. Available: http://www.genengnews.com/gen-articles/noninvasive-oxygen-and-ph-sensors/3815?page=1. [Accessed 2017].

[86] Center for Microcomputer Applications, "Dissolved Oxygen Sensor," [Online]. Available: http://labfiz.uwb.edu.pl/labfiz/siec/info/dokumentacja_oeiizk/manuals/d0376.pdf.

[87] Erlich Industrial Development, Corp., "DO Theory," [Online]. Available: http://www.eidusa.com/Theory_DO.htm. [Accessed 2017].

[88] Finesse Solutions, "Dissolved Oxygen Sensor Primer," [Online]. Available: http://finesse.com/media/121732/Finesse.TruDO.primer.ApNote.pdf. [Accessed 2017].

[89] Mettler Toledo, "Dissolved Oxygen Sensors: High performance optical and polarographic in-line probes," [Online]. Available: http://www.mt.com/us/en/home/products/Process-Analytics/DO-CO2-ozone-sensor/dissolved-oxygen-meter.html#Question-1. [Accessed 2017].

[90] PendoTech, "Temperature Sensors & Monitors," [Online]. Available: http://www.pendotech.com/pendotech-products/sensors-and-monitors/temperature-sensors-monitors/. [Accessed 2017].

[91] C. Card, K. Clark and J. Furey, "Adoption of Single-Use Sensors for BioProcess Operations," BioProcess International, 1 May 2011. [Online]. Available: http://www.bioprocessintl.com/2011/adoption-of-single-use-sensors-for-bioprocess-operations-315211/. [Accessed 2017].

[92] Finesse Solutions, "TruFluor DO Single-use Optical Dissolved Oxygen Sensors," [Online]. Available: http://www.finesse.com/products/sensors/single-use-sensors/trufluor-do/. [Accessed 2017].

[93] Applikon Biotechnology, "BugLab Biomass Sensor: Measure OD in your bioreactor non-invasively," [Online]. Available: https://www.applikon-biotechnology.us/en/buglab. [Accessed 2017].

[94] T. Reinecke, P. Biechele, V. Schulte, T. Scheper and S. Zimmermann, "Low-cost Sensor System for Non-invasive Monitoring of Cell Growth in Disposable Bioreactors," *Procedia Engineering,* vol. 120, pp. 548-551, 2015.

[95] C. Perley, J. Swartz and C. Cooney, "Measurement of Cell Mass Concentration with a Continuous-Flow," *Biotechnology and Bioengineering,* vol. 21, no. 3, pp. 519-523, 1978.

[96] Flownamics, "FISP," Flownamics, [Online]. Available: http://www.flownamics.com/cell_free_sampling_FISP.html. [Accessed 2017].

[97] A. M. Thayer, "Leading Drugs Under Fire In 2015 - Biologics: Biosimilar competition emerged for the first time in U.S. market," Chemical & Engineering News, 7 December 2015. [Online]. Available: http://cen.acs.org/articles/93/i48/Leading-Drugs-Under-Fire-2015.html. [Accessed 2017].

[98] C. Nick, "The US Biosimilars Act: Challenges Facing Regulatory Approval," *Pharmaceutical Medicine,* vol. 26, no. 3, pp. 145-152, 2012.

[99] A. W. Mulcahy, Z. Predmore and S. Mattke, "The Cost Savings Potential of Biosimilar Drugs in the United States," Rand Corporation, 2014.

[100] R. Mullin, "Cost to Develop New Pharmaceutical Drug Now Exceeds $2.5B," Chemical & Engineering News, 24 November 2014. [Online]. Available: https://www.scientificamerican.com/article/cost-to-develop-new-pharmaceutical-drug-now-exceeds-2-5b/. [Accessed 2017].

[101] Pharmaceutical Commerce, "Pharmaceutical cold chain logistics is a $12.6-billion global industry," Pharmaceutical Commerce, 16 April 2016. [Online]. Available: http://pharmaceuticalcommerce.com/supply-chain-logistics/pharmaceutical-cold-chain-logistics-is-a-12-6-billion-global-industry/. [Accessed 2017].

[102] Pharmaceutical Commerce, "The 2015 Biopharma Cold Chain Landscape," Pharmaceutical Commerce, 27 August 2015. [Online]. Available: http://pharmaceuticalcommerce.com/special-report/the-2015-biopharma-cold-chain-landscape/. [Accessed 2017].

[103] A. Hoffman, "Challenges of Cold Supply Chain," July 2013. [Online]. Available: http://eipg.eu/wp-content/uploads/2013/07/seminar-armin-presentation-eipg-madrid.pdf. [Accessed 2017].

[104] cSafe Global, "The Cost of a Broken Vaccine Cold Chain Part Two, Financial Cost," 17 September 2014. [Online]. Available: http://csafeglobal.com/the-cost-of-a-broken-vaccine-cold-chain-part-two-financial-cost-1. [Accessed 2017].

[105] L. Terry, "The Big Chill: 10 Trends in Cold Chain Logistics," Inbound Logistics, July 2015. [Online]. Available: http://www.inboundlogistics.com/cms/article/the-big-chill-10-trends-in-cold-chain-logistics/. [Accessed 2017].

[106] BioPharm Internaional Editors, "Challenges in Managing the Cold Chain," BioPharm International, 1 November 2013. [Online]. Available: http://www.biopharminternational.com/challenges-managing-cold-chain-0. [Accessed 2017].

[107] J. Bagalay, "Marketing & Distribution of Biotech Products in the United States," 2012. [Online]. Available: http://www.launchinus.com/wp-content/uploads/2012/07/Marketing-Distribution-of-Biotech-Products-in-the-United-States.pdf. [Accessed 2017].

[108] Google Finance, "Amerisource Bergen Corp. (NYSE: ABC)," 2016.

[109] Mergent Intellect, "03-927-7590. AMERISOURCEBERGEN CORPORATION," 2016. [Online]. Available: http://www.mergentintellect.com/index.php/search/companyDetails/39277590. [Accessed 2017].

[110] OneSource, "Amerisource Bergen Summary," 2017. [Online]. Available: https://globalbb.onesource.com/Web/Reports/ReportMain.aspx?KeyID=420562&Process=CP&Report=UNIFIEDSUMMARY. [Accessed 2017].

[111] OneSource, "Amerisource Bergen SWOT," 2017. [Online]. Available: https://globalbb.onesource.com/Web/Reports/ReportMain.aspx?KeyID=420562&Process=CP&CIK=1140859&Report=STRENGTHWEAKNESS#3. [Accessed 2017].

[112] Google Finance, "Cardinal Health Inc," 2016. [Online]. Available: https://www.google.com/finance?cid=86352.

[113] OneSource, "Cardinal Health Summary," 2017. [Online]. Available: https://globalbb.onesource.com/web/Reports/ReportMain.aspx?KeyID=5533&Process=CP&FtrID=UNIFIEDSUMMARY. [Accessed 2017].

[114] OneSource, "Cardinal Health SWOT," 2017. [Online]. Available: https://globalbb.onesource.com/web/Reports/ReportMain.aspx?KeyID=5533&Process=CP&CIK=721371&Report=STRENGTHWEAKNESS. [Accessed 2017].

[115] Google Finance, "McKesson Corporation," 2016. [Online]. Available: https://www.google.com/finance?cid=22611. [Accessed 2017].

[116] Mergent Intellect, "17-766-7227. MCKESSON CORPORATION," 2017. [Online]. Available: http://www.mergentintellect.com/index.php/search/companyDetails/177667227. [Accessed 2017].

[117] OneSource, "McKesson Corporation Summary," 2017. [Online]. Available: https://globalbb.onesource.com/web/Reports/ReportMain.aspx?KeyID=376341&Process=CP&FtrID=UNIFIEDSUMMARY. [Accessed 2017].

[118] OneSource, "McKesson Corporation SWOT," 2017. [Online]. Available: https://globalbb.onesource.com/web/Reports/ReportMain.aspx?KeyID=376341&Process=CP&CIK=927653&Report=STRENGTHWEAKNESS. [Accessed 2017].

[119] IBIS World, "Drug, Cosmetic & Toiletry Wholesaling in the US," August 2016. [Online]. Available: http://clients1.ibisworld.com/reports/us/industry/default.aspx?entid=964. [Accessed 2017].

[120] IBIS World, "Industry Outlook: Drug, Cosmetic & Toiltetry Wholesaling," 2016. [Online]. Available: http://clients1.ibisworld.com/reports/us/industry/industryoutlook.aspx?entid=964. [Accessed 2017].

[121] Gilead Sciences, "Authorized Distributors of Record," 2017. [Online]. Available: http://www.gilead.com/medicines/authorized-distributors. [Accessed 2017].

[122] Amgen, "Amgen Authorized Distributors of Record," 2017. [Online]. Available: http://www.amgen.com/~/media/amgen/full/www-amgen-com/downloads/partners/amgen_us_authorized_wholesalers.ashx?la=en. [Accessed 2017].

[123] IBIS World, "Products & Markets: Drug, Cosmetic & Toiletry Wholesaling," 2017. [Online]. Available: http://clients1.ibisworld.com/reports/us/industry/productsandmarkets.aspx?entid=964. [Accessed 2017].

[124] Amerisource Bergen Corporation, "Amerisource Bergen DC Map," 2016. [Online]. Available: http://www.amerisourcebergendrug.com/abcdrug/PDFs/Retail_Pharmacies/AmerisourceBergen_DC_Map_abcwebsite.pdf. [Accessed 2017].